A NEW MODEL FOR THE SUBSTORM GROWTH PHASE

By

Min-Shiu Hsieh

RECOMMENDED:

Dr. William Bristow

Dr. Chung-Sang Ng

Dr. Hui Zhang

Dr. Antonius Otto
Advisory Committee Chair

Dr. Curt Szuberla
Chair, Department of Physics

APPROVED:

Dr. Paul Layer
Dean, College of Natural Science and Mathematics

Dr. John Eichelberger
Dean of the Graduate School

8/15/14
Date

A NEW MODEL FOR THE SUBSTORM GROWTH PHASE

A

DISSERTATION

Presented to the Faculty

of the University of Alaska Fairbanks

in Partial Fulfillment of the Requirements

for the Degree of

DOCTOR OF PHILOSOPHY

By

Min-Shiu Hsieh, B.S., M.S.

Fairbanks, Alaska

August 2014

Abstract

The physics of geomagnetic substorms has been under debate for a long time. In particular, the formation of a thin current sheet (CS) is a central unresolved problem because it provides the magnetotail conditions for the expansion phase onset. This dissertation presents a new CS thinning mechanism based on midnight magnetic flux depletion (MFD), which is caused by sunward convection to balance dayside reconnection during periods of southward interplanetary magnetic field. The results demonstrate that MFD is a highly efficient mechanism to generate a very thin CS in the near-Earth tail. This study also examines CS formation under the influence of adiabatic lobe compression in combination with MFD and proposes a double-current sheet evolution at distinct locations in the near-Earth region and mid-tail region. The results suggest that substorm expansion onset is associated only with near-Earth onset of magnetic reconnection, while mid-tail reconnection causes bursty bulk flows. In addition, this dissertation investigates the changes of the auroral morphology associated with the magnetotail evolution. An ionospheric map is constructed based on Tsyganenko 96 magnetic field model corrected by magnetic flux conservation. By employing MFD, the mapping results such as the equatorward expansion of the open/closed field boundary, the convergent motion of strong field-aligned currents, and the location of electron and ion isotropy boundaries are consistent with typical ionospheric observations. These results demonstrate that MFD is the first model that can consistently explain and predict the typical magnetotail and ionospheric evolution during the substorm growth phase and shed light on the physics of the growth phase aurora.

Table of Contents

List of Figures

List of Tables

Page

List of Appendices

Acknowledgements

After four years of Ph.D. study, I have finally reached this point.

At first, I would like to express the deepest appreciation to my advisor, Professor Antonius Otto. I am grateful for his advice and support. I thank him for his trust, patience, and understanding. I thank him for everything he has done for me. It is my extreme fortune to be his student, and I am also proud of being his student.

I would like to thank my committee members: Professor Chung-Sang Ng, Professor William Bristow, and Professor Hui Zhang. Thanks for all their help, for their useful comments and suggestions, and for their careful reading of my dissertation.

Thanks to Professor Curt Szuberla for his careful reading and useful comments on my dissertation.

Thanks to Professor Joseph Kan for his discussion of substorm physics.

Thanks to Professor Hui Zhang for listening and encouraging me during my Ph.D. study.

I would like to thank my Taiwan Professors: Professor Jih-Hong Shue, Professor Ling-Hsiao Lyu, Professor Ya-Hui Yang, and Professor Sunny W. Y. Tam. Thanks for all their help that let me have the chance to study at University of Alaska Fairbanks.

I would like to thank my Taiwan Professor Huo-Ming Jiang. Thanks for his expectation, care, and encouragement. Thanks to him for being my mentor when I was lost. Thanks for his suggestions that inspire me to pursue my Ph.D. in the United States. Although it is too late, I still hope that he can know of my accomplishments in heaven.

I would like to thank my friends at UAF: Sunhee Lee, Christina Chu, Xuanye Ma, Tapas Bhattacharya, Srikamal Soundararajan, Ting Xiao, Robin Whittier, etc. Thanks for all their help, care, and friendship.

I would like to thank many Taiwan friends for their friendship that enriches my life. I have a special thanks to my friends in "NFT". Thanks for being with me for many years.

Finally, I want to say sorry to my parents. Sorry for the worries. I thank them for their love, encouragement, and understanding. Thanks to them for forever being my backup. Thanks to them for respecting whatever decisions I have made.

Chapter 1
Introduction

This dissertation investigates the magnetotail and ionospheric evolution during the substorm growth phase. The physics of substorms has been under debate for a long time. The physics of the expansion phase onset and of the growth phase is not well understood. Although the growth phase has received less attention than the spectacular expansion phase, the state of the magnetotail at the end of the growth phase, i.e., a thin current sheet (CS) formation is of central importance for substorms because it provides the magnetotail conditions for the expansion phase onset. It is also important to note that no model to date can predict the typical ionospheric evolution of the substorm growth phase and shed light on the role of the growth phase arc.

Several numerical approaches have been proposed to study mechanisms that can cause the formation of thin CSs, e.g., lobe deformation and anti-entropy diffusion. This dissertation proposes a new CS thinning mechanism based on midnight magnetic flux depletion (MFD) which is caused by slow sunward convection to balance dayside magnetic reconnection during the periods of southward interplanetary magnetic field. This study demonstrates that MFD is a highly efficient mechanism to generate a very thin CS in the near-Earth tail. This study also examines the CS formation under the influence of adiabatic lobe compression during the growth phase contrasted and in combination with MFD. By combining MFD and lobe compression, this dissertation presents a double-current sheet evolution at distinct locations in the near-Earth region and mid-tail region and suggests that substorm expansion onset is associated only with near-Earth onset of magnetic reconnection, while mid-tail reconnection causes bursty bulk flows.

Another important aspect of this dissertation is to examine the changes of the magnetotail structures mapped into the auroral ionosphere. This study illustrates that sunward convection is a central element for the evolution of field-aligned current and for the equatorward motion of these currents during the growth phase, demonstrating the importance of MFD for the growth phase auroral evolution.

1.1 Magnetospheric Structure

The magnetosphere is a large plasma cavity caused by the interaction between solar wind plasma and Earth's intrinsic dipole field. The stream of solar wind plasma with the embedded interplanetary magnetic field (IMF) flows out from the sun, as it compresses the dayside portion of the Earth's magnetic field, and stretches the nightside portion into a long tail. Figure 1.1 shows a three-dimensional sketch of the magnetosphere, where it is composed of some basic elements: the magnetopause, the magnetotail, the plasma sphere, and overall current systems.

Serving as the outer boundary of the magnetosphere, the magnetopause is a current layer (called Chapman-Ferraro currents) which is an important region for the entry of plasma, momentum, and magnetic energy from the solar wind into the magnetosphere, particularly during periods of southward IMF. The stand-off distance R_{mp} of the dayside magnetopause is determined by the force balance

between the normal component of the solar wind dynamic pressure and Earth magnetic pressure as

$$R_{mp} = (\frac{\kappa B_E^2}{2\mu_0 m_p n_{sw} u_{sw}^2}), \tag{1.1}$$

where the typical value for the solar wind density n_{sw} is 5 cm^{-3}, the solar wind velocity u_{sw} is 400 km/s, the Earth's equatorial magnetic field B_E is 3×10^4 nT, and κ is 2. R_{mp} is usually found near $x = 10R_E$ but can be found inside of geosynchronous distances ($x = 6.6\,R_E$) for strongly enhanced solar wind dynamic pressure [*Shue et al.*, 1998].

The magnetotail is a long portion of Earth's magnetic field stretching hundreds of Earth radii ($R_E \sim 6400$ km) on the nightside, which contains the mantle, lobes, the plasma sheet boundary layer (PSBL), and the plasma sheet. The mantle represents as a boundary to the magnetotail and is usually filled with particles originating from the solar wind plasma. Serving as the boundary that separates the lobes and plasma sheet, the PSBL is characterized by the existence of oppositely directed field-aligned ion and electron beams [*Williams*, 1981]. The plasma sheet is located in the center of the magnetotail and contains dense plasma with a ratio of thermal to magnetic pressure (plasma $\beta = p/(\frac{B^2}{2\mu_0})$) greater than 100 in the central plasma sheet. Here p is the thermal pressure and $\frac{B^2}{2\mu_0}$ is the magnetic pressure. Figure 1.1 shows a strong westward-directed crosstail CS in the center of the plasma sheet because this region is surrounded by closed magnetic field lines, which point toward the Earth in the northern hemisphere and away from the Earth in the southern hemisphere. This region is also known as the neutral sheet because the magnetic field strength is very weak ($B_x \sim 0$ nT) in the center. Many observations demonstrate that the CS thickness can change dramatically particularly during periods of southward IMF.

The plasmasphere, located in the inner magnetosphere, is filled with the dense but cold plasma. The size of the plasmasphere is determined by the region in which low energy particles conduct closed orbits around the Earth (trapping) under the influence of Earth's corotating electric field and dawn-dusk convection electric field. Outside the plasmasphere, the ring current is caused by the magnetic gradient and curvature drift of energetic particles. A partial ring current develops and increases in intensity during geomagnetic storms, and the circuit is closed through the so-called region 2 (R2) field-aligned current. The field-aligned current system (Birkeland currents) couples Earth's magnetosphere and high latitude ionosphere.

Field-aligned currents were first predicted by Kristian Birkeland in 1908 [*Birkeland*, 1908]. Figure 1.2 (a) and (b) sketch the field-aligned currents and electric fields distributed in the northern hemisphere. The region 1 (R1) current locates poleward of the R2 current, flowing down into the ionosphere on the dawnside and up on the duskside. The R2 current has an opposite current direction compared to the R1 currents. The R1 and R2 currents are closed through the horizontal currents, i.e., Pederson currents, in the ionosphere. The location of upward field-aligned current represents the region where electrons can precipitate and generate the auroral borealis in the high latitude ionosphere. Typical ionospheric convection is likely the result of plasma motions subject to the induced electric fields and

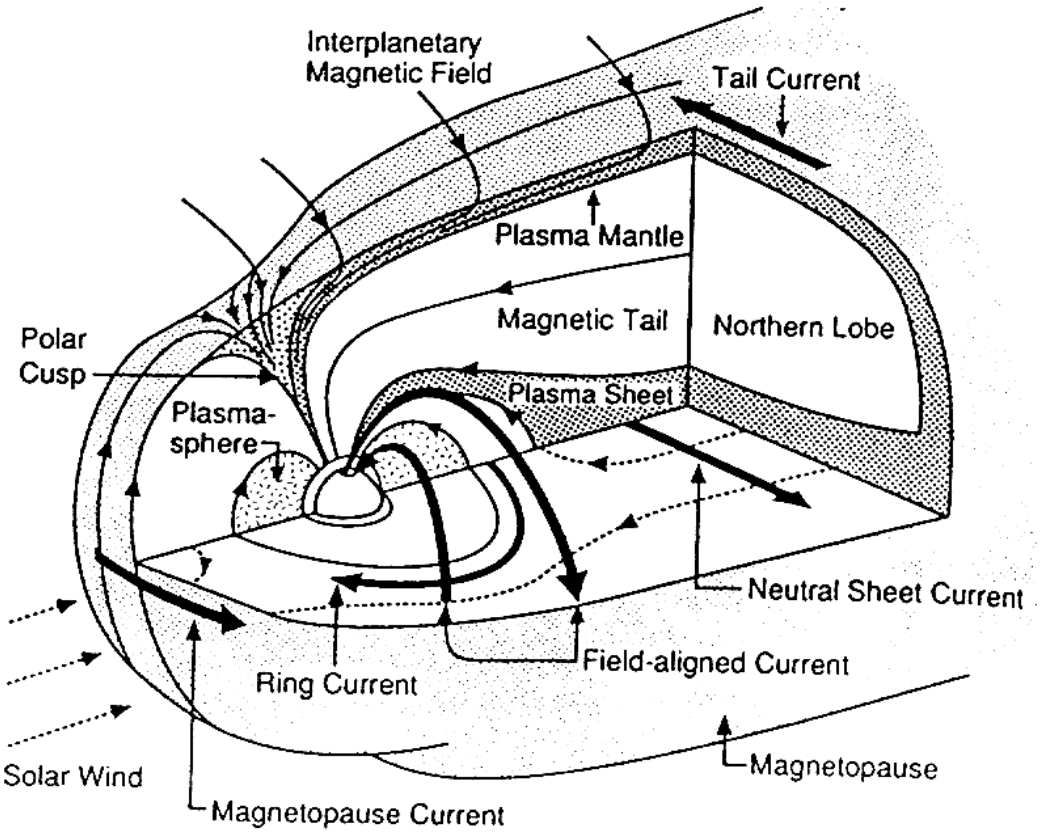

Figure 1.1. Sketch of Earth's magnetosphere [*Russell and Luhmann*, 1997].

Earth's downward magnetic field, which is also called the two-cell disturbance polar 2 (DP2) current system as illustrated in the bottom panel of Figure 1.2. This convection pattern changes in response to the variation of the IMF B_y and B_z components.

1.2 Substorm Dynamics

The morphology that in the southward IMF condition magnetic energy is stored and released in the magnetotail is indicative that the magnetotail is a highly dynamic system [*Dungey*, 1963; *Baker et al.*, 1985]. This sequence of storage-and-release of magnetic energy is called a "magnetospheric substorm". The concept of (auroral) substorm was originally described by *Akasofu* [1964]. The auroral substorm begins with the breakup of the most equatorward discrete auroral arc and ends when the auroral activity diminishes to the quiet phase level characterized by the absence of the aurora. The beginning of the auroral breakup is called the onset of the expansion phase. Later, *McPherron et al.* [1973] noted that many phenomena precede the onset of the expansion phase; therefore, a growth phase was added prior to the expansion phase. Nowadays it is well known that a typical substorm consists of three different phases: the growth phase, the expansion phase, and the recovery phase.

The growth phase is generally believed to start with the southward turning of the IMF and the erosion of magnetic flux at the dayside magnetopause through magnetic reconnection [*McPherron et al.*, 1973]. The typical duration of the growth phase is about 30 to 60 minutes. In this stage, open magnetic flux is transported to the nightside and accumulated in the magnetotail lobes, which serve as a reservoir of the magnetic energy. There are several ionospheric and magnetotail properties characterized by the growth phase. In the ionosphere: (a) intensification of the ionospheric convection [*Coroniti and Kennel*, 1973]; (b) gradual increase of the polar cap size [*Clausen et al.*, 2012]; (c) slow intensification of the field-aligned current (FAC) systems [*Baumjohann et al.*, 1981]; (d) equatorward motion of the growth phase arc [*Aikio et al.*, 2002]; (e) convergent motion of the most equatorward discrete arc and the diffuse aurora equatorward of the energetic particle isotropy boundaries [*Mende et al.*, 2001]. In the magnetosphere: (a) slow increase of lobe magnetic fields [*Wang et al.*, 2004]; (b) reduction of the dipolar field near geosynchronous distances [*Kokubun and McPherron*, 1981]; (c) thin CS formation between $x = -8$ and $x = -15\,R_E$ [*Sergeev et al.*, 1990]; (d) enhancement of crosstail currents [*Petrukovich et al.*, 2007].

The stored magnetic energy is released after the onset of the expansion phase. The expansion phase onset is characterized by large scale auroral intensifications and by strong high latitude magnetic perturbations. It has also been characterized by the disruption of crosstail currents in the near-Earth tail. This diversion of crosstail currents, the so-called the substorm current wedge (illustrated in Figure 1.3), links to the field-aligned current that closes through the ionosphere. Figure 1.3 illustrates the ionospheric portion of the current system flows into the enhanced conductivity channels that are called auroral electrojets, i.e., disturbance polar 1 (DP1) current system. Early studies argue that the expansion phase onset can be occasionally triggered by the northward turning of the IMF [*McPherron*

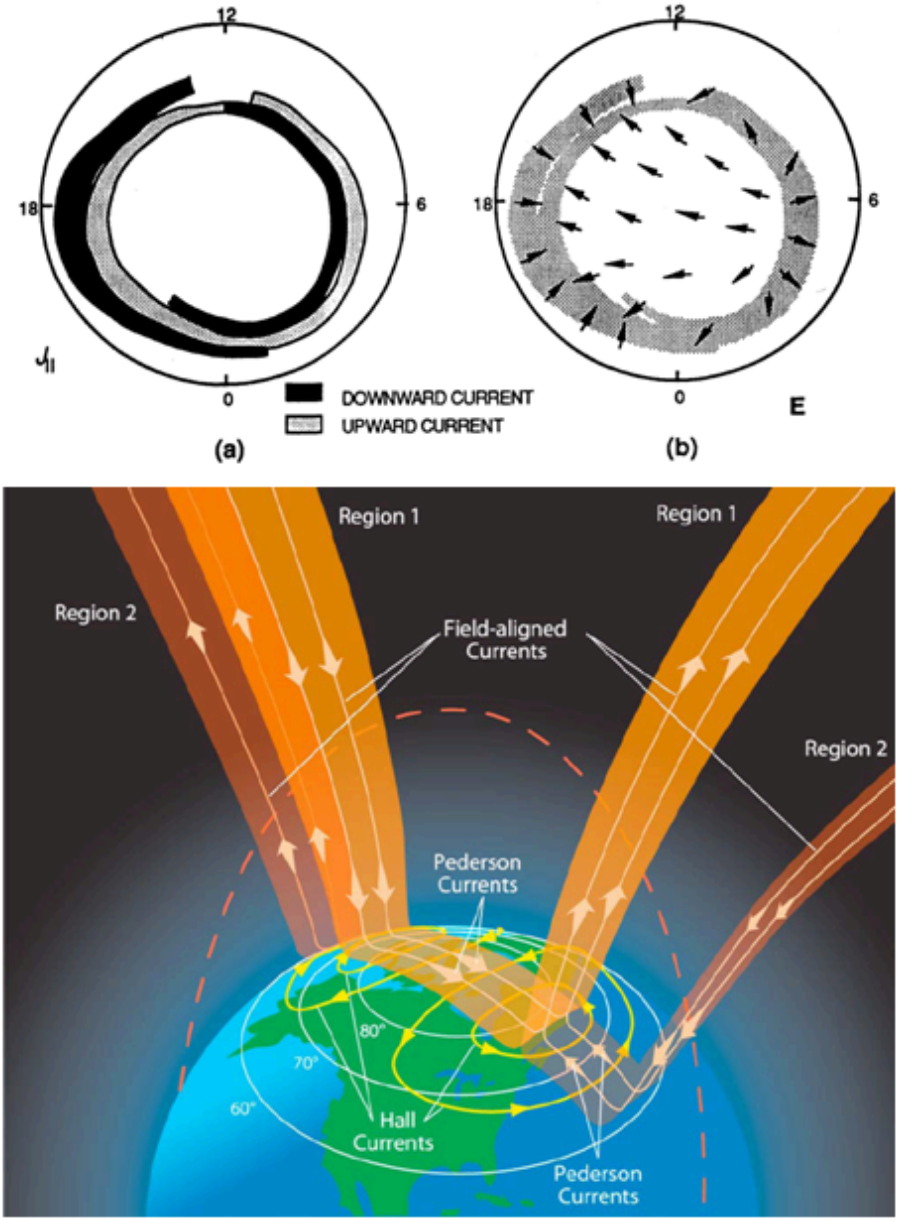

Figure 1.2. Sketch of (a) Birkeland currents, (b) electric fields in the northern hemisphere [*Wolf*, 1995]. The bottom panel illustrates the three-dimensional field-aligned currents [*Le et al.*, 2010].

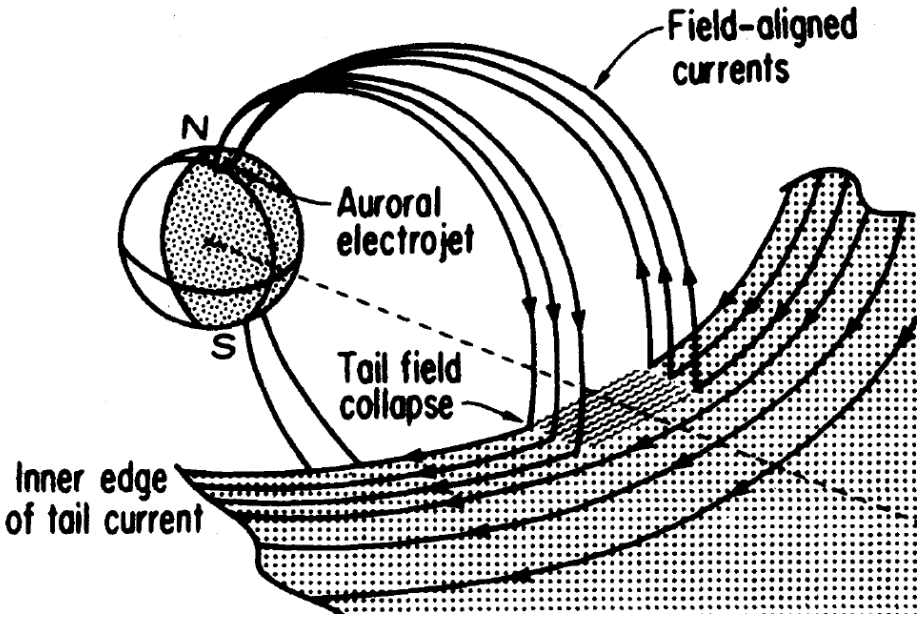

Figure 1.3. Sketch of the substorm current wedge [*Mcpherron*, 1997].

et al., 1986; *Lyons et al.*, 1997; *Russell*, 2000]. During the expansion phase, ground magnetometers and satellites observe: (a) auroral poleward expansion [*Nakamura et al.*, 1993]; (b) enhancement of the westward auroral electrojet [*Wiens and Rostoker*, 1975]; (c) Pi2 pulsations [*Hsu and McPherron*, 2004]; (d) local magnetic reconnection associated with fast tail- or Earth-ward flows [*Nagai and Machida*, 2013]; (e) dipolarization in the near-Earth region [*Ohtani et al.*, 1999]; (f) rapid tailward plasmoid and traveling compression regions (TCR) [*Hones et al.*, 1984; *Slavin et al.*, 1984]; (g) plasma injections at geosynchronous distances [*Birn et al.*, 1997].

Figure 1.4 presents the change of AU and AL indices, i.e., eastward and westward electrojets during the period of a particular substorm. AU and AL are auroral electrojet indices obtained from a number of stations distributed in the auroral zone [*Davis and Sugiura*, 1966]. The superposition of north-south magnetic perturbation H measured for each station constructs a lower bound for H, which is called AL index. Similarly, an upper bound in the H is called AU index. The growth phase starts with slowly growing AU and AL indices. This magnetic perturbation is caused by the DP2 current system. The beginning of the expansion phase onset is characterized by a suddenly increasing slope of AL index ($\sim 10:54$ UT). Subsequent increases of the AL magnitude are called intensifications. The strong AL perturbation is the result of the intensification of westward electrojet in the DP1 current system. Eventually the AL index reaches a minimum and starts to recover. During the recovery phase, geomagnetic activity reduces and the magnetospheric configuration returns to its quiet state with a moderately stretched tail [*Mcpherron*, 1997]. The recovery phase lasts about 60 to 90 minutes.

The physics of substorm onset has been highly debated for some time, e.g., near-Earth neutral line (NENL) and current disruption (CD) models [*Baker et al.*, 1996; *Lui*, 1996]. These are also known as the outside-in and inside-out models. Figure 1.5 illustrates the substorm scenario of each model.

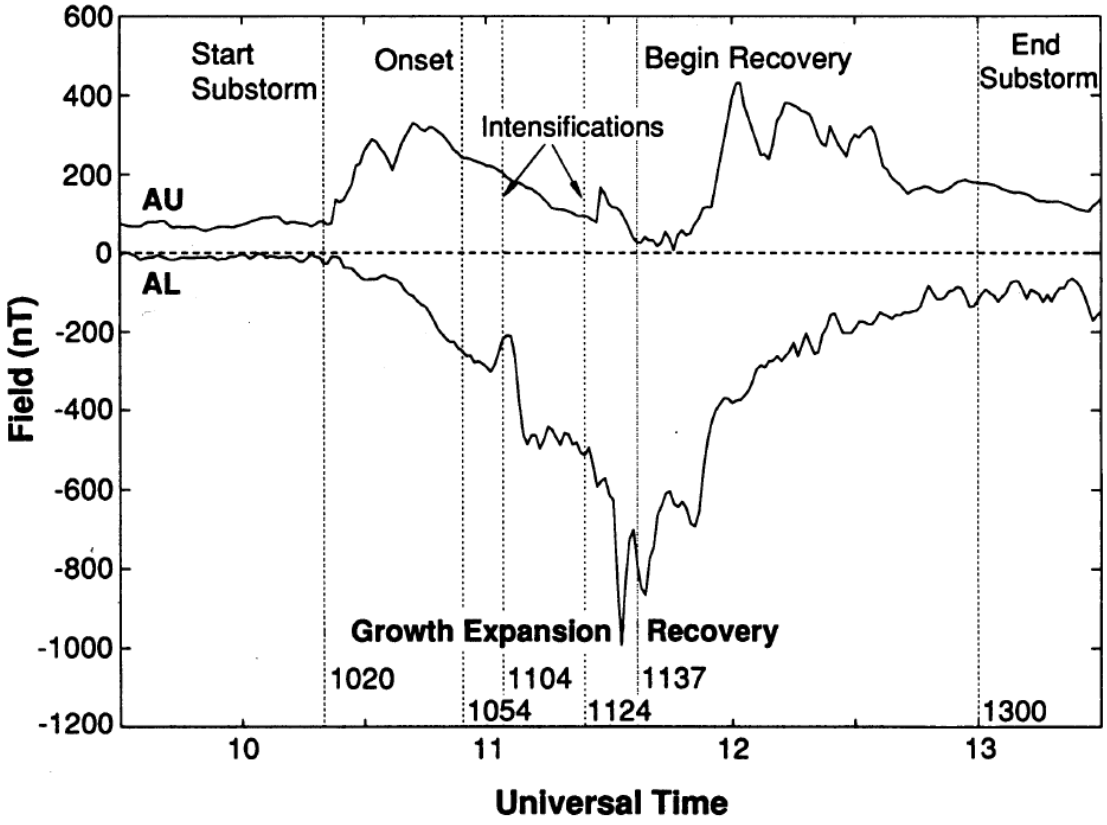

Figure 1.4. AU and AL indices for a typical substorm [*Mcpherron*, 1997].

Figure 1.5 (a) depicts the outside-in model that proposes the near-Earth tail reconnection triggers the substorm onset and expansion by the injection and rapid Earthward deceleration of fast flows. Another competition model is the inside-out model, as illustrated in Figure 1.5 (b). The inside-out model suggests that a near-Earth instability triggers substorm onset such that auroral expansion could proceed before the arrival of earthward-directed fast flows, at the boundary to the dipolar magnetosphere.

The detailed observational confirmation of either model is not easy and depends heavily on the exact relative locations of satellites and ground observations. It is also not unambiguous because of the incomplete knowledge of the magnetospheric configuration which determines the mapping. This dissertation constructs ionospheric maps of magnetotail properties, suggesting that the distinction between the inside-out and outside-in hypotheses is even more challenging than conventionally assumed.

1.3 Review of Prior Works- Thin Current Sheet Formation

1.3.1 Satellite Observations

Several magnetospheric and ionospheric properties are characteristic of the growth phase. Particularly, the evolution of strong thin CSs are critical to the understanding of the mechanism that leads to the expansion phase onset. This strong enhancement of the current density can increase kinetic instabilities and lead to a possible loss of equilibrium or onset of instability [*Schindler and Birn*, 1993; *Birn et al.*,

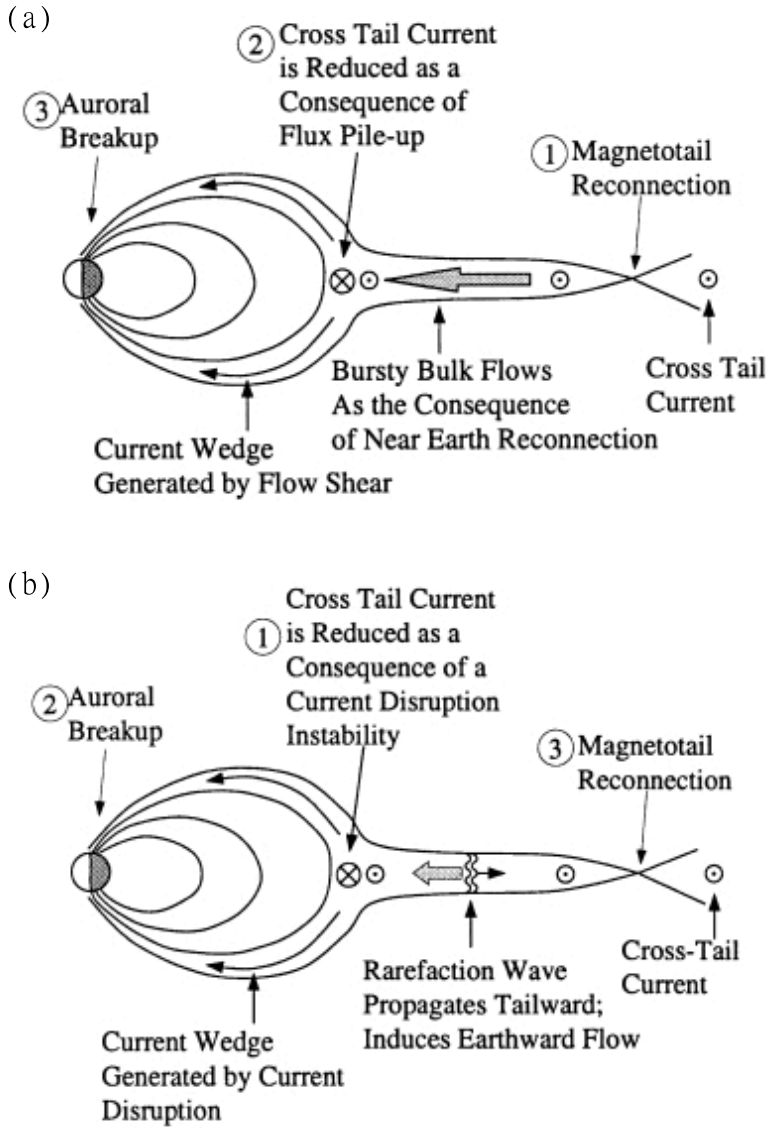

Figure 1.5. Sketch of substrom models [*THEMIS Scientific Aims*, 2007]. Panel (a) depicts the Near-Earth neutral line model, and panel (b) shows the current wedge disruption model.

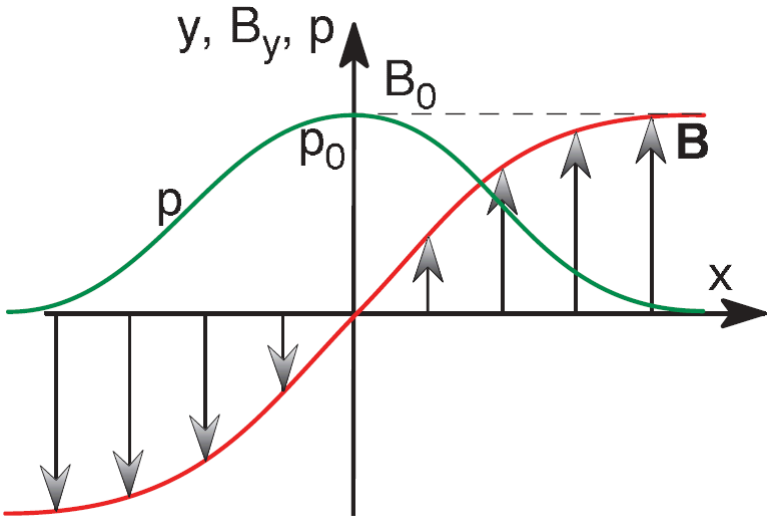

Figure 1.6. Sketch of the one-dimensional Harris sheet model.

1998; *Lee et al.*, 1998]. Thin CSs are often observed at a radial distance of about 15 R_E with a thickness decreasing from several R_E down to hundreds of kilometers [*Sergeev et al.*, 1990; *Baker et al.*, 1993; *Sanny et al.*, 1994].

A simple self-consistent and kinetic equilibrium state called Harris sheet model [*Harris*, 1962] has been widely accepted as the standard magnetic field profile to calculate the CS thickness. Figure 1.6 illustrates the one-dimensional Harris sheet profile. The Harris sheet considers the thermal equilibrium with the distribution function

$$f_s(\vec{r},\vec{v}) = F_s(H_s, P_{ys}) = c_s \exp(-\alpha_s H_s + \beta_s P_{ys}) \tag{1.2}$$

that solves the collisionless Boltzmann equation, which is justified by assuming $\partial/\partial t = 0$ and $\partial/\partial y = 0$. With

$$H_s = m_s v^2/2 + q_s\phi \quad \text{and} \tag{1.3}$$

$$P_{ys} = m_s v_y + q_s A_y, \tag{1.4}$$

equation (1.2) transforms into

$$f_s(\vec{r},\vec{v}) = c_s \exp\left\{-\alpha_s[\frac{m_s}{2}(v_x^2+v_z^2)+q_s\phi] - \alpha_s\frac{m_s}{2}[(v_y-\frac{\beta_s}{\alpha_s})^2] + \frac{m_s}{2}\frac{\beta_s^2}{\alpha_s} + \beta_s q_s A_y\right\}, \tag{1.5}$$

where ϕ is the electric potential, A_y is the y component of the vector potential, c_s is the normalization constant, m_s is the mass of a species, and q_s is the charge species. This illustrates $\alpha_s = 1/(k_B T_s)$ for the Maxwell distribution (local thermodynamic equilibrium). Here k_B is the Boltzmann constant (1.38×10^{-23} J/K) and T_s is the temperature of a species. Note that β_s/α_s should be interpreted as a constant velocity u_y that shifts the distribution in the v_y direction. By solving the Poisson equation and Ampére's law, it yields

$$-\nabla^2 A_y = \mu_0 e n_0 u_i (1+\frac{T_e}{T_i})\exp\{\frac{A_y}{\kappa}\} = -\lambda\exp\{\frac{A_y}{\kappa}\}. \tag{1.6}$$

This is called Grad-Shafranov equation [*Grad and Rubin*, 1958]. Solving equation (1.6), A_y is represented as

$$A_y = A_0 \ln \cosh(\frac{x}{L_0}). \tag{1.7}$$

Therefore, the magnetic field, the pressure, and the current density are given as

$$b_z = \frac{dA_y}{dx} = b_0 \tanh(\frac{x}{L_0}), \tag{1.8}$$

$$p = \frac{b_0^2}{2\mu_0} \mathrm{sech}^2(\frac{x}{L_0}), \quad \text{and} \tag{1.9}$$

$$j_y = \frac{b_0}{\mu_0 L_0} \mathrm{sech}^2(\frac{x}{L_0}). \tag{1.10}$$

Here b_0 is the lobe magnetic field and L_0 is the width of Harris Sheet. This Harris sheet describes the profile of the magnetic field, the thermal pressure, and the current density of a one-dimensional collisionless equilibrium serving as a model for the plasma sheet during quiet periods in the magnetotail. The Harris solution further implies

$$\nabla^2 \tilde{A} = \exp\{-2\tilde{A}\} \quad \text{and} \tag{1.11}$$

$$\tilde{p} = \exp\{-2\tilde{A}\}, \tag{1.12}$$

with $\tilde{p} = p + \frac{b_z^2}{2\mu_0}$ and $\tilde{A} = A_y/A_0$. A_0 is a normalization constant. For the derivation of Harris sheet profile, see Appendix A.

In observations a major difficulty for employing the Harris sheet to calculate the CS thickness is the lack of multiple satellites distributed vertically along the plasma sheet. The lobe magnetic field strength b_0 is often estimated from a single satellite located in the neutral sheet based on the assumption of pressure balance

$$p_0 = \frac{b_0^2}{2\mu_0}, \tag{1.13}$$

where p_0 is the thermal pressure in the neutral sheet. Here a weak magnetic field strength in the neutral sheet and a small thermal pressure at the lobes are motivated by typical observations. Figure 1.7 depicts a CS thinning event found by *Petrukovich et al.* [2007]. This event is observed at the radial distance $\sim -18\,R_E$ from cluster satellites during a period of southward IMF. The small B_x value (~ 0 nT) in the first panel indicates that the satellite is located very close to the neutral sheet. Panel *c* shows the reduction of B_z implying that the plasma sheet is thinning. The increase of the current density (panel *g*) and the decrease of the CS thickness (panel *h*) are typical magnetotail features during the growth phase. The CS thickness is estimated based on the Harris sheet profile with the sheet width at $B \sim 0.5B_0$ (B_0 is the lobe magnetic field). In this event the CS thickness is down to 3000 km before the local onset (13 : 00 UT).

Other characteristics associated with thin CSs have been observed:

• a large increase of the current density by a factor up to 10 over the course of the growth phase [*Sergeev et al.*, 1993a];

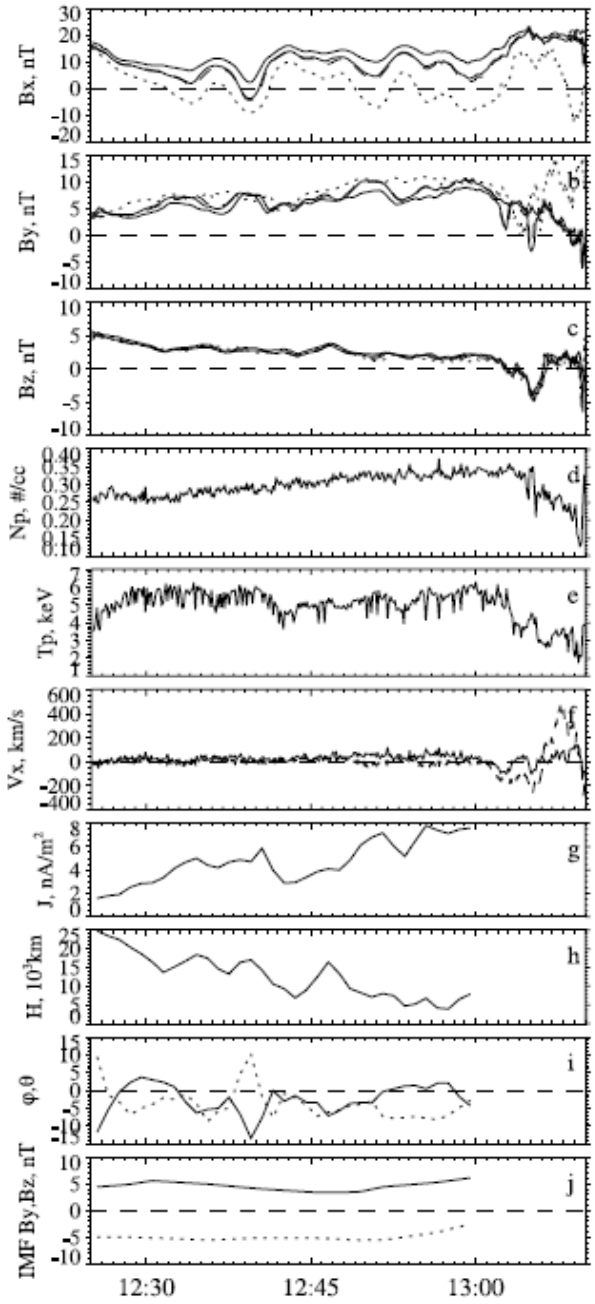

Figure 1.7. A CS thinning event on 12 September 2001 [*Petrukovich et al.*, 2007]. (a-c) the magnetic field B_x, B_y, and B_z components, (d) the plasma density N_p, (e) the temperature T_p, (f) the velocity v_x, (g) the crosstail current density, (h) the CS thickness, (i) the azimuthal and polar angles, and (j) the IMF B_y and B_z components.

• a thin CS structure extends from the near geosynchronous distances into the mid-tail region [*Pulkkinen et al.*, 1999];

• a bifurcated CS structure [*Nakamura et al.*, 2002];

• a dramatic CS thinning occurs with the onset of a tail instability and fast flows in the late growth phase and early expansion phase [*Asano et al.*, 2003].

1.3.2 Numerical Simulations

Although the characteristics of thin CSs are supported by many observations, the physical mechanism of CS thinning during the substorm growth phase is still not well understood. Several numerical approaches have been proposed and can simulate the formation of thin CSs. The first class of methods employs boundary deformation through a perturbed or driving boundary condition, as illustrated by *Wiegelmann and Schindler* [1995], *Ma et al.* [1995], *Birn et al.* [1998], and *Becker et al.* [2001].

Wiegelmann and Schindler [1995] examined thin CS formation based on a two-dimensional ideal magnetohydrodynamics (MHD) simulation with an adiabatic pressure law. With the assumptions of weak time-dependence and weak x-dependence, the governing equations can be expressed in the form

$$\frac{1}{2\mu_0}(\frac{\partial A}{\partial z})^2 + p(A,t) = \frac{1}{2\mu_0}{B_0}^2(x,t) \quad \text{and} \tag{1.14}$$

$$\frac{d}{dt}(p(A,t)V(A,t)^\gamma) = 0, \tag{1.15}$$

where A is magnetic flux function, and γ is the ratio of specific heats, which is 5/3 in the adiabatic assumption. The initial pressure condition at time $t = 0$ is

$$p(A,0) = \exp(-2A), \tag{1.16}$$

which is the standard Harris sheet solution (equation (1.12)). The magnetic field B_0 represents the B_x component, which is assumed to vary slowly in time and is described by the function

$$B_0(x,t) = \sqrt{2}(1+t)(1+\Lambda(1+t)^2x)^{-\frac{n}{2}}, \tag{1.17}$$

which simulates an increase of the lobe magnetic field. This mimics the magnetic flux transport from the dayside magnetopause to the tail region during the growth phase. The choice of Λ and n is motivated by observations. With $\Lambda = 0.036$ and $n = 1.1$, the magnetic field profile implies the stronger lobe compression close to the Earthward boundary. By increasing the lobe magnetic field strength by a factor of up to 2 at the time $t = 1$, they found that the innermost magnetic field line strongly stretches tailward. The reorganized system forms a thin CS with maximum current density increasing close to the Earthward boundary, as shown in Figure 1.8. The results indicate that a thin CS formation can be regarded as a consequence of strong tail stretching and is associated with the gradient of flux tube volume, the so-called gradient of flux volume mechanism.

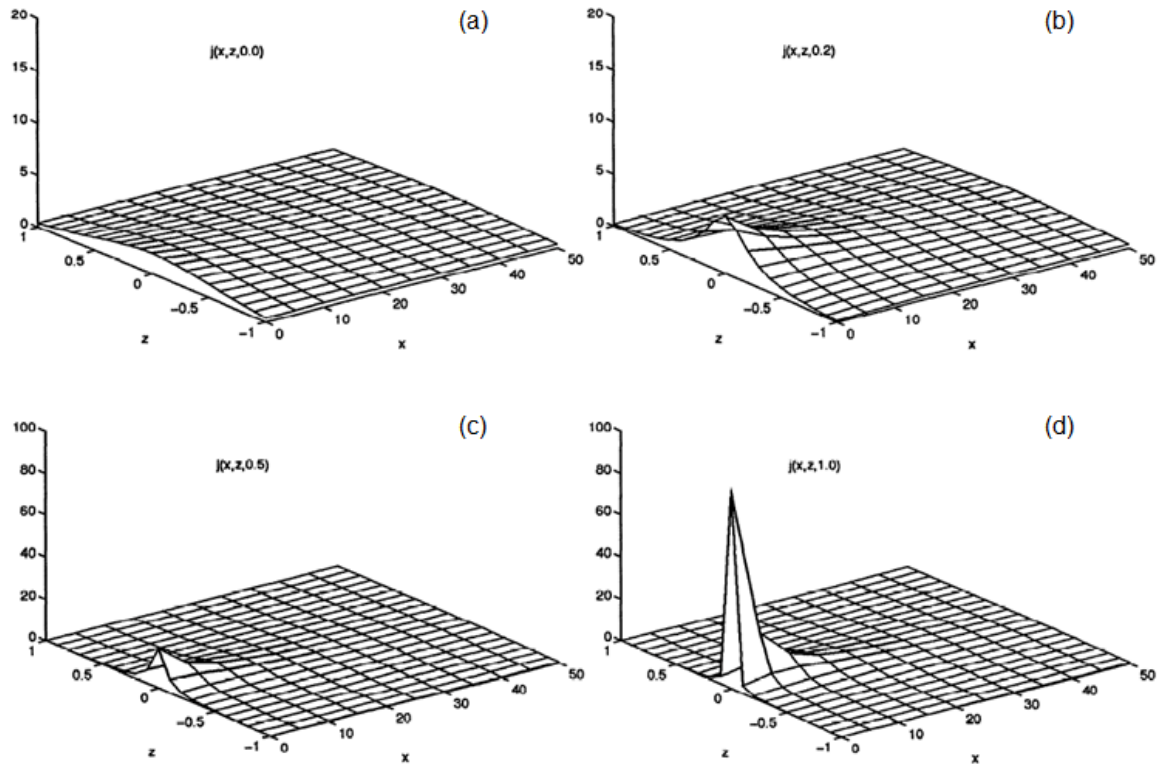

Figure 1.8. Current density $j(x, z, t)$ at times (a) $t = 0.0$, (b) $t = 0.2$, (c) $t = 0.5$, and (d) $t = 1.0$ in the near-Earth magnetotail [*Wiegelmann and Schindler*, 1995].

Birn and Schindler [2002] studied the influence of a finite boundary deformation at the lobe on magnetotail equilibria. They demonstrated that a local deformation of the lobe boundary produces a local increase of the current density and a local reduction of the magnetic field component B_z in the center of the plasma sheet when the deformation approaches a critical threshold. Such a boundary perturbation might be caused by a suitable change of the boundary electric field. In other words, this boundary deformation approach indicates that the magnetic energy accumulated in the lobes can play an role for the formation of a thin CS.

Instead of the boundary deformation, *Lee et al.* [1998] proposed the entropy anti-diffusion instability as a mechanism for thin CS formation in a two-dimensional global MHD simulation. This approach employed a thermal pressure diffusion at the edges of the plasma sheet and demonstrated that the growth rate of maximum current density increases linearly with the diffusion coefficient. Pressure diffusion at the plasma sheet boundary is assumed to be caused by the lower-hybrid drift instability, which is stabilized by the high plasma beta in the central plasma sheet. In two-dimensional equilibrium

$$\vec{B} = \nabla A_y \times \hat{e_y}, \tag{1.18}$$

where the equilibrium conditions

$$p = p(A_y) \quad \text{and} \tag{1.19}$$

$$j_y \sim dp/dA_y \tag{1.20}$$

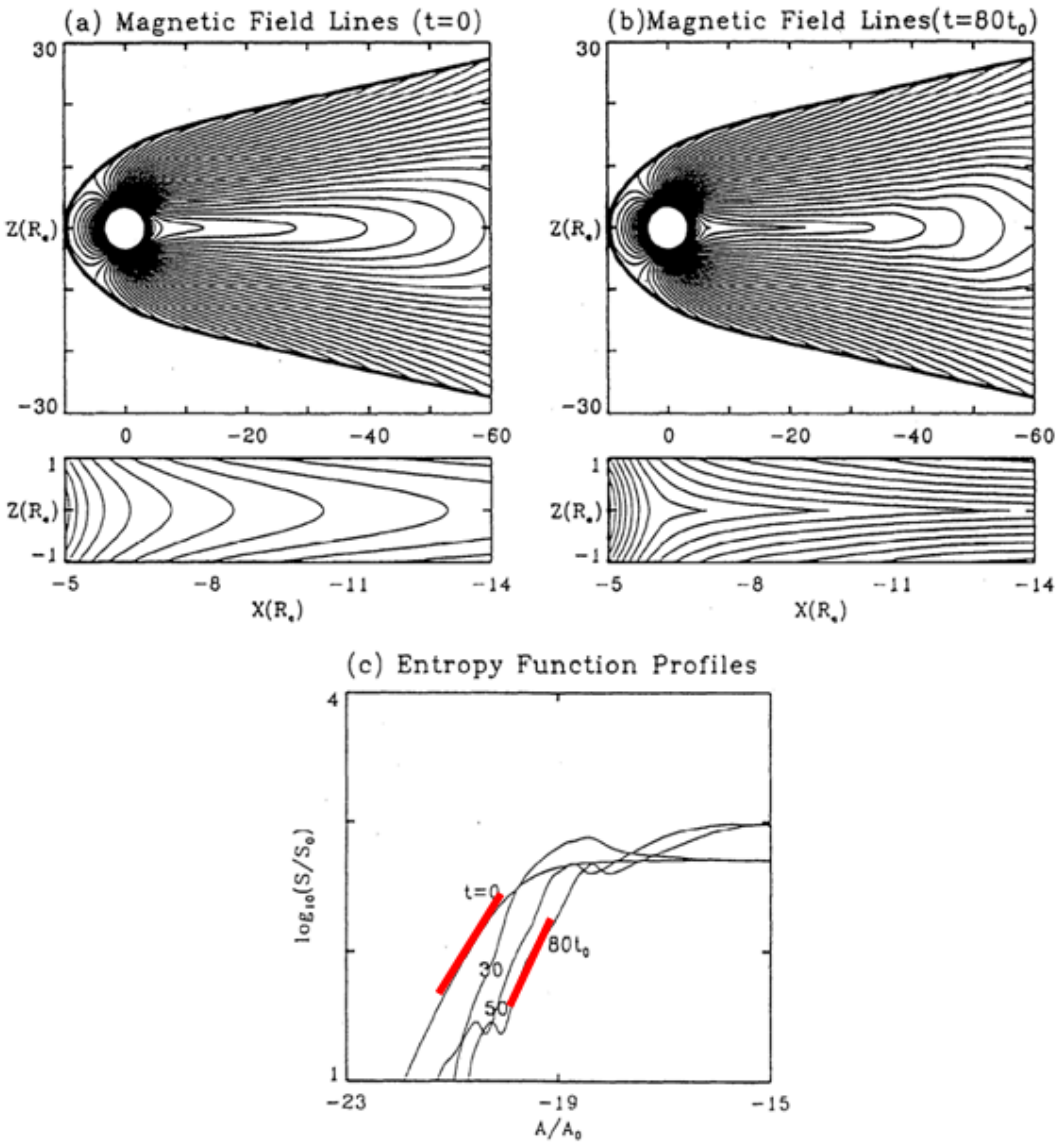

Figure 1.9. A thin CS formation caused by the entropy anti-diffusion in a global MHD simulation [*Lee et al.*, 1998]. Panels (a) and (b) illustrate the magnetic field lines at times $t_0 = 0$ and $t = 80t_0$. Panel (c) shows the flux tube entropy. The red straight lines indicate the gradient of the entropy.

are implied. Pressure diffusion redistributes the pressure by the increase of a local perturbation $\delta p(A_y)$, thereby introducing a modification of the current density $\delta j_y \sim d\delta p/dA_y$. The modified current density is associated with a steeper profile of the flux tube entropy $S = pV^\gamma$ (red straight lines in Figure 1.9) and lead to the thinning of the CS. Here ds is the flux tube length and γ is the ratio of specific heats (γ is 5/3 for the adiabatic case).

1.4 Dissertation Scope

1.4.1 Motivation

Although the proposed models of the previous section can cause thin CS formation, they do not address other typical growth phase properties. For instance, it is not clear why the lower-hybrid drift should operate only after a southward turning of the IMF. Also none of these CS formation mechanisms can easily predict the duration of the growth phase or the particular location of the CS that develops in the substorm growth phase. This dissertation first investigates the magnetotail evolution during the substorm growth phase by employing a new CS thinning mechanism, the midnight magnetic flux depletion (MFD). This study demonstrates that MFD is closely related to dayside reconnection during periods of southward IMF, which can also predict the growth phase duration. At the end of this section a table comparing different CS thinning mechanisms is provided.

This dissertation also investigates the influence of the thin CS formation on the auroral ionosphere. A highly important question is whether or not the thin CS is associated with the expansion phase onset. It is generally believed that energetic particle injection at geosynchronous distances is indicative of the substorm expansion. The source region of the injected plasma is still highly debated and strongly depends on the location of the onset of reconnection in the magnetotail, or the location of the thin CS formation. This evolution of thin CS formation can be associated with changes of the auroral morphology during the growth phase. Therefore, it is of particular importance to examine the magnetotail features mapped into the auroral ionosphere.

1.4.2 Background and Goals

The presented model of CS thinning is based on MFD in the near-Earth tail, which is caused by sunward convection to replenish magnetic flux that is eroded on the dayside by magnetic reconnection during periods of southward IMF. An important aspect of this model is the constraint imposed by adiabatic magnetotail convection.

Magnetotail evolution is slow during the growth phase compared to the fast break-up process, and the associated tail convection is considered as a quasi-static process. Early ideas that the dayside reconnection can cause slow sunward convection in the magnetosphere through fast rarefaction waves go back to *Mozer* [1971], *Coroniti and Kennel* [1973], *Coroniti* [1985], and *Kan* [1990]. The associated sunward magnetic flux transport can balance the dayside reconnection and depletes the tail region of

closed magnetic flux. This convection is slow and therefore should conserve adiabatic invariants during the slowly evolving growth phase, that is, the flux tube entropy S of any particular magnetic tube should remain constant during convection. The flux tube entropy is derived utilizing the first law of thermodynamics and the ideal gas law (Appendix B). If one considers the entropy for a plasma parcel

$$dS = \frac{dQ}{T}, \tag{1.21}$$

where dQ is the differential heat added to the parcel and T is temperature. Here dQ should be represented as

$$dQ = nC_v T d[\ln(pV^\gamma)]. \tag{1.22}$$

For adiabatic changes, $dS = 0$ such that

$$nC_v d[\ln(pV^\gamma)] = 0. \tag{1.23}$$

Since nC_v is generally non-zero, pV^γ is constant. That is, the flux tube entropy $S = pV^\gamma$ remains constant in the adiabatic change.

Erickson and Wolf [1980] argued that a steady, lossless, and adiabatic Earthward convection in the magnetotail cannot occur (the Erickson-Wolf problem). Figure 1.10 (a) illustrates the Erickson-Wolf problem when a flux tube convects Earthward from the point A to B. Considering the slow quasi-static evolution, the time-derivative $\partial/\partial t$ and velocity $\vec{u}$ are approximated to $O(\varepsilon)$, where ε is a very small value $\ll 1$ [*Schindler and Birn*, 1982]. Therefore, one can neglect the left two terms ($\sim \varepsilon^2$) of the momentum equation

$$\frac{\partial \rho \vec{u}}{\partial t} + \nabla \cdot \rho \vec{u}\vec{u} = -\nabla p + \vec{j} \times \vec{B} \tag{1.24}$$

and simplify equation (1.24) into the force balance equation

$$\nabla p = \vec{j} \times \vec{B}. \tag{1.25}$$

Note that the force balance equation implies

$$\vec{B} \cdot \nabla p = 0 \quad \text{and} \tag{1.26}$$

$$\vec{j} \cdot \nabla p = 0, \tag{1.27}$$

which means the thermal pressure and the perpendicular current density are constant along the magnetic field lines. *Erickson and Wolf* [1980] examines the variations of thermal pressure when a flux tube convects adiabatically from $x = -60\,R_E$ in to $-10\,R_E$. When the flux tube convects toward Earth, the flux tube volume becomes much smaller such that the pressure needs a significant increase in order to keep the flux tube entropy constant. In this convection, the thermal pressure p_a increases much beyond the expected thermal pressure p_e calculated from the force balance equation (Figure 1.10 (b)). This pressure inconsistency indicates that time-independent, lossless, and adiabatic Earthward convection would lead to a pressure catastrophe. Such the inconsistency is the result of the large flux tube entropy

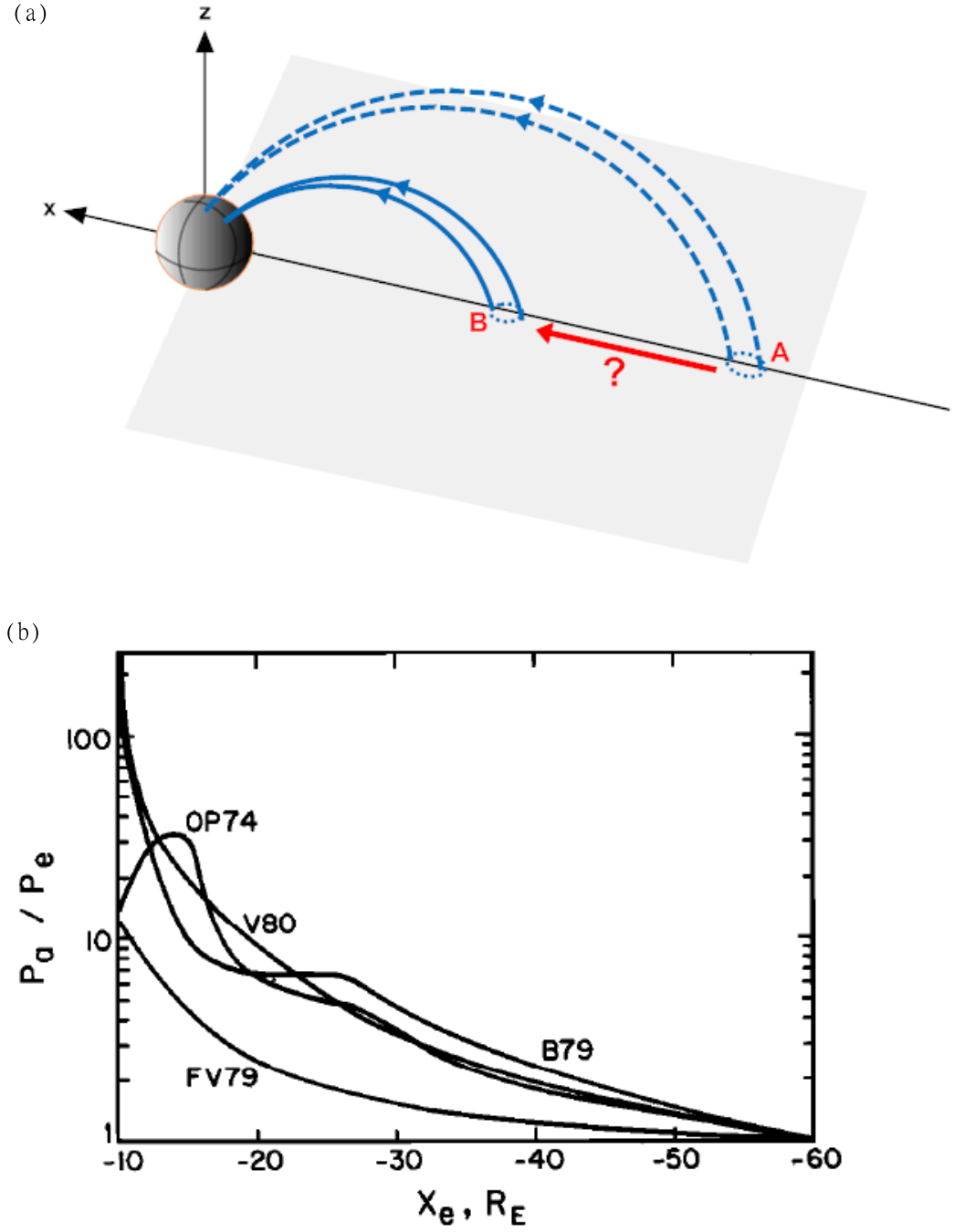

Figure 1.10. (a) Sketch of the Erickson-Wolf problem. (b) The pressure balance inconsistency for the adiabatic Earthward convection [*Erickson and Wolf*, 1980].

of flux tubes convected from the mid-tail into the near-Earth region, which suggests a strong increase of the thermal pressure and thereby leads to a strong force imbalance.

A contour map of specific entropy in the equatorial plane is displayed in Figure 1.11. The $S = 1.00$ contour at dayside corresponds to the magnetopause, and is extended to the region at $x \sim -10\,R_E$ in the magnetotail. The ringlike distribution of specific entropies implies that the magnetic flux tubes are likely to convect and divert around the Earth annularly, as the red arrows illustrated in Figure 1.11. This slow adiabatic convection is a major constraint of the evolution of the magnetotail during the growth phase, which confines the source of the magnetic flux for the convection to the dayside to a region of particular flux tube entropy in the near-Earth tail. This causes the magnetic flux depletion in this source region which explains the term midnight magnetic flux depletion as illustrated in Figure 1.12. This dissertation proposes a CS thinning model based on the MFD by assuming a particular sunward outflow condition to remove the closed magnetic flux in the near-Earth tail region.

It is well established that magnetic flux is added to the magnetotail lobes during the growth phase [*Caan et al.*, 1975; *Wang et al.*, 2004; *Petrukovich et al.*, 2007]. Therefore, this work also imposes a driving electric field at the lobe boundary to examine the influences of additional magnetic flux on the thin CS formation. This is done because the removal of closed magnetic flux in the near-Earth tail and the loading of energy and magnetic flux into the tail lobes are both important magnetotail features during the growth phase. The effects of both mechanisms on the magnetotail evolution are first discussed separately and then compared in detail in the later chapters.

An important ionospheric feature during the growth phase is the equatorward motion of the growth phase arc close to or even into regions of diffuse aurora characteristic of a dipolar magnetic field. According to *Akasofu* [1964], this growth phase (or onset) arc is the most equatorward discrete arc poleward of the diffuse aurora. Other important aspects of the auroral ionosphere are equatorward expansion of the growth phase arc, slow intensification of field-align currents, and convergent motion of the most equatorward discrete arc and the diffuse aurora. Therefore, the second important goal of this dissertation is to examine the near-Earth magnetotail changes mapped into the ionosphere during the growth phase. Of specific interest are the changes in magnetic flux, flux tube entropy, field-aligned currents, convection, and the size and location of the respective ionospheric footpoints of the magnetotail structure and properties. Our results demonstrate that many typical growth phase properties can be attributed to the depletion of near-Earth closed magnetic flux, which is associated with a thin CS formation. Note that such ionospheric properties cannot easily be explained by the previous CS thinning mechanisms listed in Table 1.1.

In summary, the dissertation examines the magnetotail and ionospheric evolution during the substorm growth phase. The typical magnetotail properties, including the removal of closed magnetic flux in the near-Earth tail and the loading of energy and magnetic flux into the tail lobes, are both considered. The goals of the dissertation are to examine:

(1) the physics of midnight magnetic flux depletion (MFD) on the magnetotail evolution;

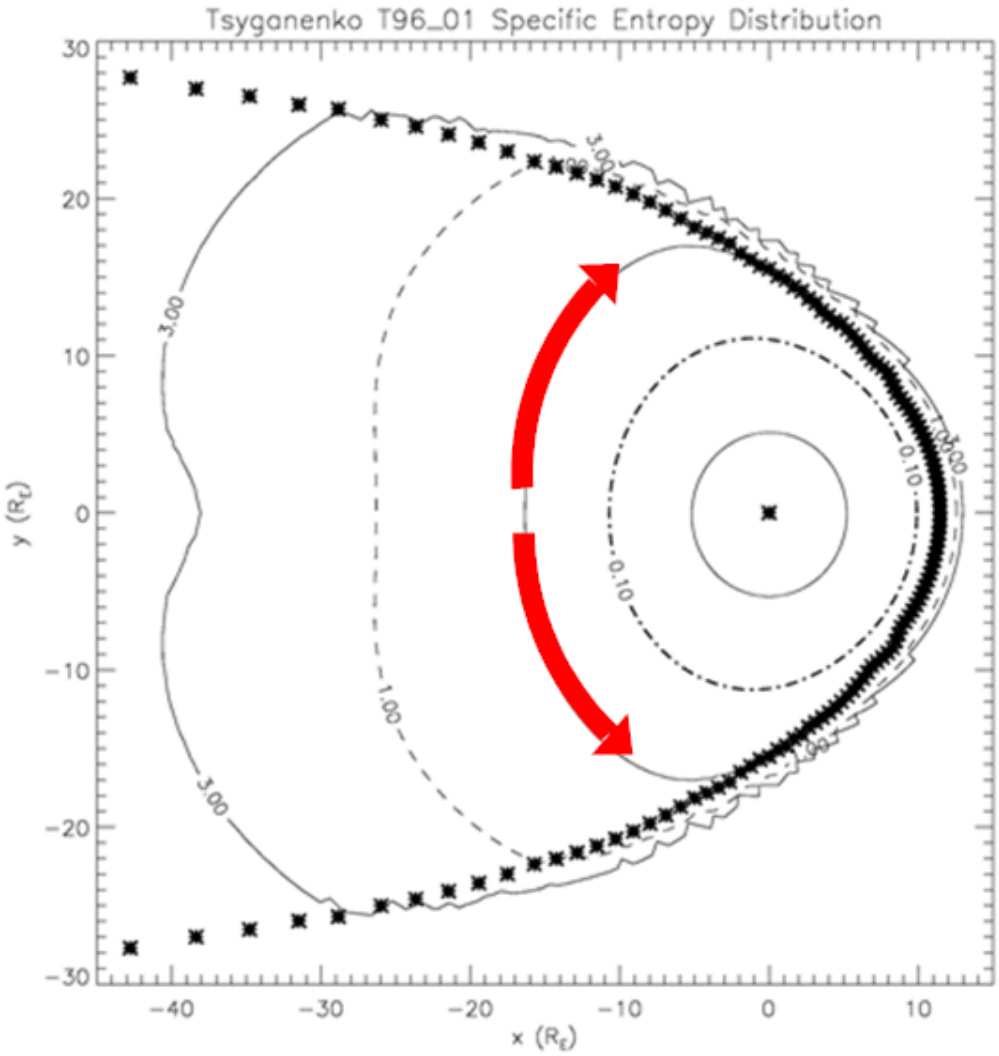

Figure 1.11. Specific entropy distribution in the equatorial plane constructed based on the Tsyganenko magnetic field model [*Hall*, 2006]. The asterisks represent the location of the magnetopuase. The red arrow illustrates sunward convection during the growth phase.

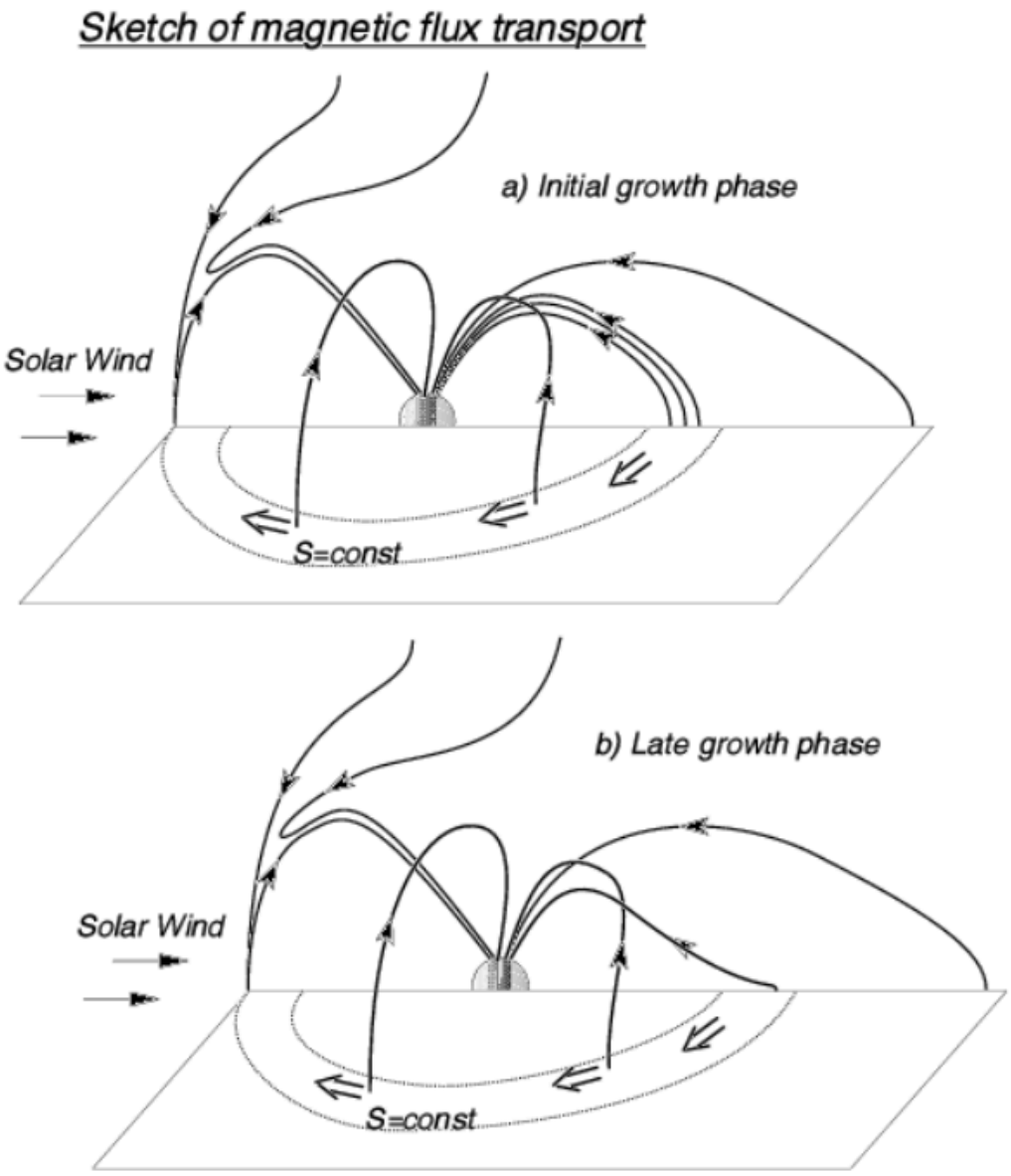

Figure 1.12. Sketch of midnight MFD. The top panel shows the initial growth phase and the bottom panel shows the late growth phase.

Table 1.1. Comparison of different CS thinning mechanisms, e.g., lobe deformation and entropy anti-diffusion. Several growth phase magnetotail and ionospheric properties are listed in the left column. The tick (question) mark represents the consistent (inconsistent) relation.

	Lobe deformation	Entropy diffusion
• Thin CS formation	√	√
• Strong relation with the southward IMF	√	?
• Thin CS location prediction	?	?
• Growth phase duration prediction	?	?
• B_z reduction near geosynchronous distances	?	?
• Equatorward motion of the growth phase arc • Gradual increase of the polar cap size • Reduction of the closed magnetic flux	?	?
• Convergent motion of the most equatorward discrete arc and the diffuse aurora	?	?

(2) the effects of adiabatic lobe compression (the energy loading process) on the magnetotail evolution; (3) the changes of the ionospheric morphology during the growth phase by mapping magnetospheric changes into the ionosphere.

This dissertation is organized into six chapters. Chapter 1 introduces the background of this work. Chapter 2 describes the numerical methods and boundary conditions of the simulation model. Chapter 3 addresses the first goal. The influence of lobe compression (goal 2) and the combined effects of sunward convection and lobe compression are presented in Chapter 4. Chapter 5 examines the aspects of ionospheric mapping and morphology (goal 3). A summary and discussion is presented in Chapter 6.

Chapter 2
Simulation Model Description

2.1 Introduction

This dissertation presents a model of CS thinning using a three-dimensional mesocale MHD simulations of the near-Earth tail. This model is developed based on the *Otto* [1990] three-dimensional MHD code, combined with T96 magnetic field model. The T96 model is an empirical magnetic field model based on a large number of satellite observations and on the modeling of magnetospheric current systems, which provides a statistical magnetic field parameterized by solar wind conditions. As noted, the T96 is not a equilibrium model because it only depicts the magnetic field configuration such that it cannot provide plasma pressure and density in the magnetosphere. The MHD equations are employed to include the plasma pressure and density to generate an equilibrium which is suitable for an initial magnetotail configuration in three-dimensional mesoscale MHD simulations.

This work applies the ballistic relaxation technique to remove the unbalanced magnetic force [*Hesse and Birn*, 1993], thereby constructing the initial configuration of the equilibrium magnetosphere which is used for the simulation study. Specific boundary conditions are chosen depending on particular goals of this study. Slightly different sets of boundary conditions are used for the case of relaxation, the study of MFD, and the simulation of lobe compression. This chapter is organized into five sections. The basic MHD equations are described in section 2.2. The numerical scheme employed in this simulation is introduced in section 2.3. Section 2.4 describes and summarizes the boundary conditions in separate regions of the simulation box. The relaxation technique and the equilibrium magnetotail are discussed in section 2.5.

2.2 MHD Equations

MHD theory can well describe the fluid dynamics of magnetized plasma in the length scale lager than the ion gyro radius, suitable to describe plasma behaviors in the magnetotail. The simulation model is govern by the resistive MHD equations normalized to the typical characteristic values as follows:

Continuity equation

$$\frac{\partial \rho}{\partial t} = -\nabla \cdot (\rho \vec{u}); \tag{2.1}$$

Momentum equation

$$\frac{\partial (\rho \vec{u})}{\partial t} = -\nabla \cdot \left[\rho \vec{u}\vec{u} + \left(\frac{1}{2} \right) (p + \vec{b}^2) \bar{I} - \vec{b}\vec{b} \right]; \tag{2.2}$$

Faraday's law

$$\frac{\partial \vec{b}}{\partial t} = \nabla \times (\vec{u} \times \vec{b} - \eta \vec{j}); \tag{2.3}$$

Energy equation

$$\frac{\partial h}{\partial t} = -\nabla \cdot (h\vec{u}) + \left\{ \left[\frac{(\gamma - 1)}{\gamma} \right] h^{1-\gamma} \eta \vec{j}^2 \right\}; \tag{2.4}$$

Ampére's law

$$\vec{j} = \nabla \times \vec{b}, \tag{2.5}$$

with

$$h = (\frac{p}{2})^{\frac{1}{\gamma}}. \tag{2.6}$$

Here ρ is the mass density, p is the thermal pressure, $\vec{u}$ is the plasma velocity, $\vec{b}$ is the magnetic field, $\vec{j}$ is the current density, η is the resistivity, and $\bar{I}$ is identity tensor. This dissertation presents the model based on the ideal MHD, that is, η and γ are set to 0 and 5/3 for all cases which address the growth phase evolution. Note that the energy equation is equivalent to the pressure equation (Appendix C). The factor of 1/2 is for the simplicity of the pressure balance representation.

All physical quantities in the simulation are normalized to the typical values, that is, the length scale is normalized by the Earth radius $L_0 = 1\,R_E$, the magnetic field is by $B_0 = 20$ nT, the velocity is by Alfvén speed $v_A = B_0(\mu_0\rho_0)^{-1/2} \sim$ 430 km/s, the pressure is by magnetic pressure ${B_0}^2/(2\mu_0) = 0.159$ nPa, the mass density ρ_0 is by $m_0 n_0 = 1.67 \times 10^{-24}$ g/cm^3 (m_0 is the mass of ion), the time is by Alfvén transit time $t_0 = L_0/v_A \sim$ 14.4 seconds, and the current density is by $B_0/(\mu_0 L_0) \sim$ 2.5 nA/m^2.

2.3 Numerical Scheme

All governing equations are solved by the leapfrog scheme and are completed by the Lax scheme. The leapfrog scheme is an explicit finite difference method that is a simple two-level scheme [*Fletcher*, 1988]. It has a second order accuracy for both time and space (truncation error is proportional to $(\Delta x)^2$) for uniform grids. It turns into a first order accuracy scheme for nonuniform grids, however, for a smooth resolution, the accuracy can be regarded as second order. To start the discussions of the numerical scheme, we first consider a continuous scalar quantity $f(x,t)$ in the one-dimensional discrete spatial grid and time increments. Figure 2.1 depicts the one-dimensional uniform grids of the space and time. It defines

$$f_i^n = f(x_i, t_n), \tag{2.7}$$

if f is at the position $x = x_i$ and at the time $t = t_n$.

Returning to the MHD equations, finite difference methods are employed to the partial derivative operator (for both space and time) of the various plasma quantities. The central difference approximation of the first partial derivative of f with respect to x at the position $x = x_i$ and time $t = t_n$ is given by

$$\left.\frac{\partial f}{\partial x}\right|_i^n = \frac{(f_{i+1}^n - f_{i-1}^n)}{2\Delta x}. \tag{2.8}$$

In a similar manner, the central difference approximation of the first partial derivative of f with respect to t at the position $x = x_i$ and time $t = t_n$ is given by

$$\left.\frac{\partial f}{\partial t}\right|_i^n = \frac{(f_i^{n+1} - f_i^{n-1})}{2\Delta t}. \tag{2.9}$$

As the first example, the one-dimensional continuity equation

$$\frac{\partial \rho}{\partial t} = -\frac{\partial(\rho v)}{\partial x} = -\frac{\partial s}{\partial x} \tag{2.10}$$

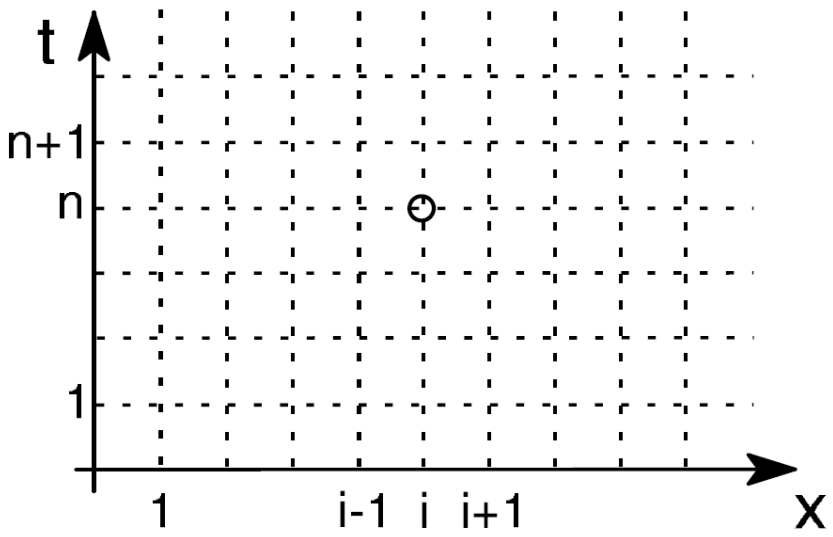

Figure 2.1. Uniform grids in the spatial (x) and time (t) domain. The index i represents the step of position, and the index n represents the step of time. The grid point (i,n) is indicated by a circle.

can be transformed as

$$\frac{(\rho_i^{n+1} - \rho_i^{n-1})}{2\Delta t} = -\frac{(s_{i+1}^n - s_{i-1}^n)}{2\Delta x}. \tag{2.11}$$

Here we denote $s = \rho u$ for simplicity. Rearranging equation (2.11), it becomes

$$\rho_i^{n+1} = \rho_i^{n-1} - \left(\frac{\Delta t}{\Delta x}\right)(s_{i+1}^n - s_{i-1}^n) \tag{2.12}$$

that is called the leapfrog scheme as illustrated in Figure 2.2. The leapfrog scheme only requires either the orange or the blue indicated grid points/time levels such that solutions develop independently on the alternating odd/even grid at any given time step. Since using both solutions does not increase accuracy only one, for instance on the orange gridpoints is computed, thereby save half of the computational resources (memory and time). Note, since the leapfrog scheme requires the information of the surrounding grid points, a mathematical boundary is to be used outside the physical boundary for von Neumann (derivative) boundary conditions. The time step $\Delta t_n = t_{n+1} - t_n$ is limited by the Courant−Friedrichs−Lewy (CFL) condition [*Courant et al.*, 1967]

$$\Delta t_n < \min\left(\left|\frac{x_i^n - x_{i-1}^n}{V_i^n}\right|\right), \tag{2.13}$$

where V_i^n is the group velocity at the grid point $x = x_n$ at $t = t_n$. The CFL condition requires the numerical scheme to resolve the transport of information along neighboring grid points which imposes a time step limitation consistent with (2.13).

Also, since the leapfrog scheme requires the information of plasma quantities at the previous time step, another numerical scheme such as Lax scheme must be used to initialize the Leapfrog integration at the beginning. To employ the Lax scheme, the first partial derivative with respect to time uses a forward difference approximation at position $x = x_i$ and time $t = 1$

$$\left.\frac{\partial f}{\partial t}\right|_i^1 = \frac{(f_i^1 - f_i^0)}{\Delta t}. \tag{2.14}$$

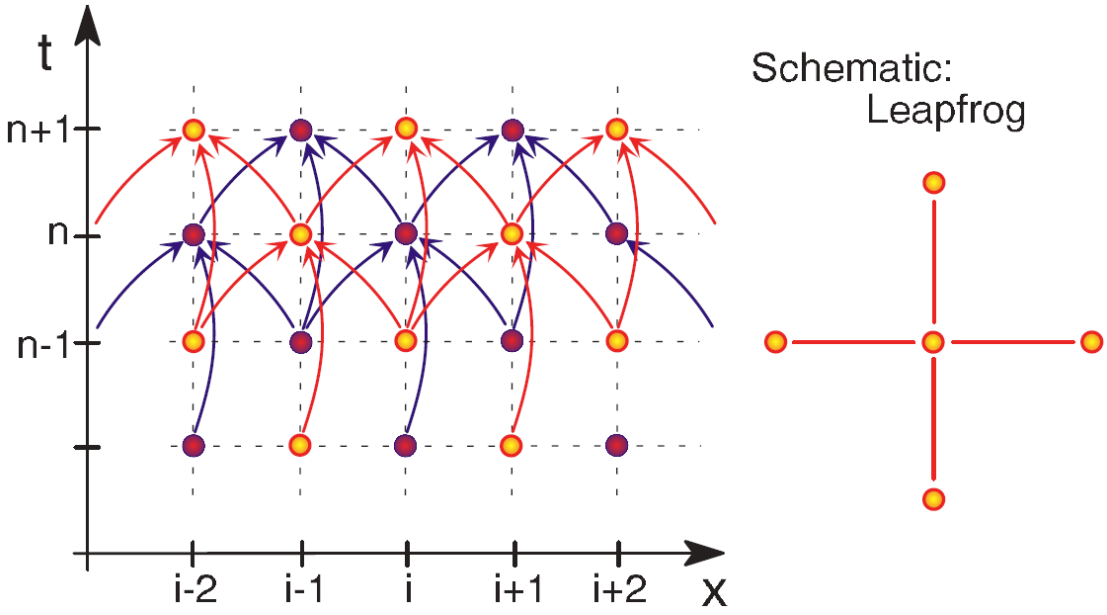

Figure 2.2. Illustration of the leapfrog integration scheme

Combining with the central difference approximation that is still used for the spatial partial derivatives, the continuity equation can be assumed as the form

$$\frac{\rho_i^1 - \rho_i^0}{\Delta t} = -\frac{(s_{i+1}^0 - s_{i-1}^0)}{2\Delta x}. \tag{2.15}$$

Rearranging equation (2.15), it turns into the form

$$\rho_i^1 = \rho_i^0 - \left(\frac{\Delta t}{2\Delta x}\right)(s_{i+1}^0 - s_{i-1}^0) \tag{2.16}$$

that the solution depends only on the plasma quantities at the initial step ($t = t_0$). The Lax scheme is also used to complete the solution and to move all gridpoints to the same time level at the end of the simulation run and everytime a full output data is generated.

2.4 Boundary Conditions

The model employs a three-dimensional mesocale MHD simulation of the near-Earth tail. The simulation domain is within the region of $-45\,R_E \le x \le -5\,R_E$, $-15\,R_E \le y \le 15\,R_E$, $0\,R_E \le z \le 12\,R_E$ in Geocentric Solar Magnetospheric (GSM) coordinate. Symmetry of the northern and southern lobes is assumed such that only the northern part of the magnetotail is simulated. The presented results use $83 \times 123 \times 123$ non-uniformly spaced grid points. The best resolution of this nonuniform grid is chosen to be $\Delta x = 0.07$, $\Delta y = 0.06$, and $\Delta z = 0.03$ corresponding to a resolution between 200 and 450 km at the Earthward boundary ($x = -5R_E$, $y = 0R_E$, $z = 0R_E$). The Earthward boundary is chosen at $x = -5\,R_E$ such that the ideal MHD equations are still applicable without considering the effects of ring currents.

The selection of appropriate boundary conditions is important and often challenging depending on the type of boundary condition and the characteristics of the physical system. In the three-dimensional

MHD simulation, the boundary conditions generally are uniquely defined only for information transport out of the system. However, even this represents an unresolved issue in three-dimensions because ideal MHD has three different and anisotropic wave modes. Therefore boundary conditions usually depend on physical intuition and experimentation or employing well defined symmetries or both. The boundary conditions are applied to all MHD quantities after each time step. In this simulation the boundary conditions can be separated into the following four different categories based on the manner in which boundary conditions are determined.

2.4.1 Equatorial Plane ($z = z_{min}$)

The magnetotail across the equatorial plane possess certain symmetries that make the selections of boundary conditions easier. If a quantity is symmetric across a certain plane, the values of the quantity are the same at both sides of the plane. For example, if v_x is symmetric across the equatorial plane, then $v_x(x, y, z)$ is equal to $v_x(x, y, -z)$, which implies the derivative of v_x is zero at the equatorial plane. On the other hand, if v_x is antisymmetric across the equatorial plane, then $v_x(x, y, z)$ is equal to the negative value of $v_x(x, y, -z)$ and $v_x(x, y, 0) = 0$.

We employ the boundary conditions at the equatorial plane with symmetries of the plasma and flow conditions (except the normal component v_z) between the northern and southern lobes. The v_z is set antisymmetric such that there is no in and out flows perpendicular to the equatorial plane. The advantage of the symmetry on the both hemispheres is the reduction of the computational effort by half. Note, if the dipole tilt angle or IMF B_y component is not zero it will destroy the properties of symmetry. At the equatorial plane, boundary conditions of magnetic field are chosen depending on the magnetotail configuration. Considering the magnetic field in the vector form

$$\vec{b} = b_x\hat{e_x} + b_y\hat{e_y} + b_z\hat{e_z}, \tag{2.17}$$

where b_x, b_y, and b_z are the components of the normalized magnetic field in the x, y, and z direction. Figure 2.3 illustrates the magnetic field lines from the south lobe to the north lobe in the magnetotail. The b_x and b_y components change the signs which implies the magnetic components b_x and b_y are antisymmetric across the equatorial plane. The b_z component is symmetric across the equatorial plane. The boundary conditions at the equatorial plane remain the same in the simulations for relaxation, MFD, and adiabatic lobe compression.

2.4.2 Side Boundaries ($x = x_{min}$, $y = y_{min}$, and $y = y_{max}$)

The simulation box with the boundaries at x_{min}, y_{min}, and y_{max} are chosen as a mesoscale system within the magnetosphere. In comparison to global MHD simulations that contain the entire magnetophere, the mesoscale system can provide a much higher resolution to model the dynamics of CS thinning. The appropriate boundary conditions at these boundaries require some experimentation based on the earlier numerical studies of relevance, e.g., *Otto* [1990] and *Hesse and Birn* [1993]. The boundary conditions at

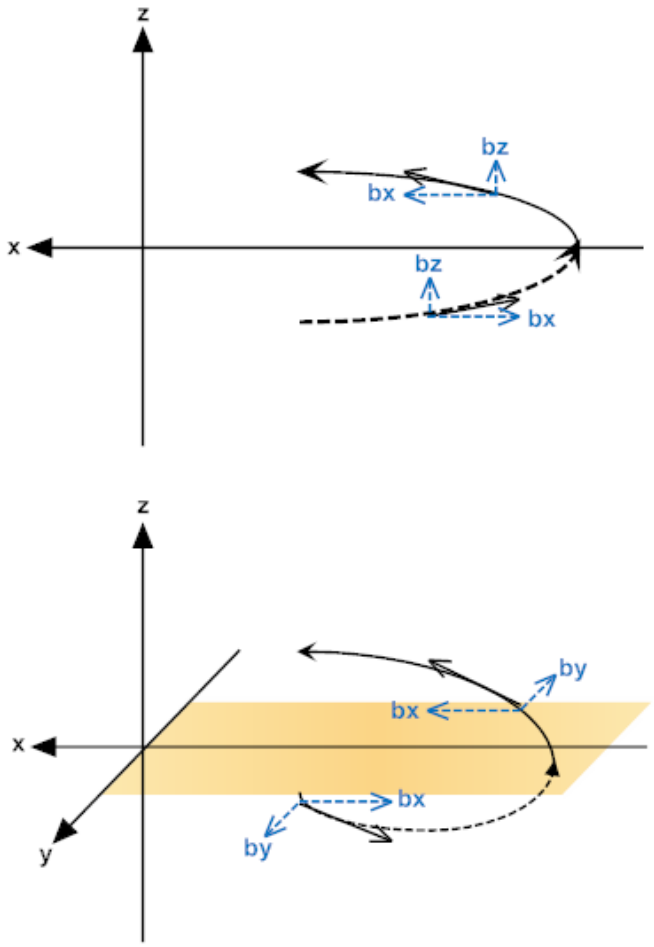

Figure 2.3. The configuration of magnetic field lines across the equatorial plane. The top figure shows a two-dimensional (x-z plane) sketch of the magnetic field line across the equatorial plane. The bottom figure shows a three-dimensional sketch of the magnetic field line across the equatorial plane.

the Earthward and top boundaries ($x = x_{max}$ and $z = z_{max}$) will be separately discussed later because their choice depends on the particular application.

Here we set all of the normal components of velocity to zero at the side boundaries x_{min}, y_{min}, and y_{max}, that is, v_x is antisymmetric at the x_{min} and v_y is antisymmetric at y_{min} and y_{max} boundaries. The tangential components of velocity, mass density ρ, and pressure function h are assumed symmetric across these boundaries. The tangential components of the magnetic field are all chosen symmetric, but the normal components of magnetic field are determined by the condition $\nabla \cdot \vec{b} = 0$ applied at the mathematical boundary. Note, that $\nabla \cdot \vec{b} = 0$ is also an initial condition in the simulation because the divergence of Faraday's law is zero

$$\frac{\partial(\nabla \cdot \vec{b})}{\partial t} = \nabla \cdot (\nabla \times (\vec{u} \times \vec{b})) = 0, \tag{2.18}$$

which implies that $\nabla \cdot \vec{b} = 0$ should be satisfied at all times. Here $\nabla \cdot \vec{b} = 0$ is well conserved in this simulation by the numerical method. Also, a diagnostic subroutine for $\nabla \cdot \vec{b} = 0$ is used periodically after integrations. Again, the boundary conditions at the planes $x = x_{min}$, $y = y_{min}$, and $y = y_{max}$ remain the same in the simulations addressing relaxation, MFD, and adiabatic lobe compression.

2.4.3 Top Boundary ($z = z_{max}$)

The general properties of boundary conditions at $z = z_{max}$ are the same as the boundary conditions described at the side boundaries x_{min}, y_{min}, and y_{max} in the relaxation and MFD simulations. However, in order to identify the importance of adiabatic lobe compression, a special inflow condition at the top boundary is specified by assuming a electric field driver (e_y) that is equivalent to the transport of magnetic flux into the lobe region. Thereby this boundary condition simulates the flux transport from the dayside magnetopause to the tail region during the substorm growth phase, as illustrated in Figure 2.4.

Figure 2.4 illustrates the electric field caused by the anti-sunward solar wind plasma for a southward IMF. In a steady state, one can assume the electric field to be uniform at the lobe boundary. Figure 2.4 illustrates that magnetic field lines are mostly parallel to the sunward direction (b_x) at the top of our simulation box, corresponding to an inflow v_z at the lobe boundary (the green shaded region). The tangential velocity v_x is very small and is assumed to be zero at the top boundary. The electric field is applied through the velocity as

$$(v_x)|_{top} = 0 \quad \text{and} \tag{2.19}$$

$$(v_z)|_{top} = -e_y/b_x. \tag{2.20}$$

Note, the frozen-in condition of ideal MHD is assumed here. The electric field is a direct measure of the rate at which open magnetic flux is added to the lobes.

2.4.4 Earthward Boundary ($x = x_{max}$)

In the relaxation the Earthward boundary conditions are the same as for the side boundaries, except that all components of the velocity are set to zero. After a well force-balanced magnetotail equilibrium is generated, the MFD simulations use a sunward outflow condition at the Earthward boundary by mapping an assumed azimuthal divergent flow profile from the equatorial plane. The sunward outflow condition is used to prescribe the rate of sunward magnetic flux transport in a manner that does not cause artificial strong boundary currents. At each boundary point a field line is traced into the simulation domain and, depending on its equatorial location in radial distance, an azimuthal divergent (from midnight) flow profile is assumed to specify the azimuthal velocity at the boundary point of the field line. This condition is dynamically updated during the simulation. The methodology is described follows:

We first assume the sunward outflow in the equatorial plane is

$$\vec{v} = v_\phi(r, \phi)\hat{e_\phi}, \tag{2.21}$$

where v_ϕ is the azimuthal component of velocity function with r and ϕ (the origin is at Earth's center). $\hat{e_\phi}$ is the unit vector in the azimuthal direction. No radial component of velocity is presented in the equatorial plane. The v_ϕ profile is chosen as

$$v_\phi(r, \phi) = 2v_0 f(r)\left[\frac{(\phi - \pi)}{\pi}\right], \quad \text{with} \tag{2.22}$$

$$f(r) = \tanh\left(\frac{r - r_0 + r_l}{r_w}\right) - \tanh\left(\frac{r - r_0 - r_l}{r_w}\right). \tag{2.23}$$

Here v_0 is the characteristic speed of the outflow, ϕ is the angle from the Sun-Earth line toward the y direction, r_l and r_w determine the width of flow channel, and r_0 is the radial distance of the flow channel from the Earth. Figure 2.5 illustrates the overall geometry of the simulation box and the sunward outflow profile (the red arrows).

We set the initial value of r_0 to 9.5, v_0 to 0.11, r_l to 1.0, and r_w to 0.5. All of the parameters can be adjusted to test the influence of different sunward outflow profile on the CS thinning. The function $f(r)$ provides the radial profile such as the channel width, and v_0 determines its magnitude. The velocity smoothly decreases to zero outside the outflow channel. Note that the assumed outflow profile is symmetric across the midnight meridian plane: however, one can easily break the symmetry of outflow profile by employing a slight change of the angular dependence. In Chapter 3 the effects of both symmetric and asymmetric sunward convection on the magnetotail evolution are examined.

To map the sunward outflow from the equatorial plane into the Earthward boundary, the azimuthal outflow is expressed in the Cartesian coordinates. The unit vector $\hat{e_\phi}$ can be decomposed into the Cartesian components

$$\hat{e_\phi} = -\sin\phi\hat{e_x} + \cos\phi\hat{e_y}, \tag{2.24}$$

where $\hat{e_x}$ and $\hat{e_y}$ are the unit vectors in the directions of x and y such that the outflow profile can be represented as

$$\vec{v} = v_x(r,\phi)\hat{e_x} + v_y(r,\phi)\hat{e_y}, \quad \text{with} \tag{2.25}$$

$$v_x(r,\phi) = -2v_0 f(r)\left[\frac{(\phi-\pi)}{\pi}\right]\sin\phi \quad \text{and} \tag{2.26}$$

$$v_y(r,\phi) = 2v_0 f(r)\left[\frac{(\phi-\pi)}{\pi}\right]\cos\phi. \tag{2.27}$$

In terms of

$$\sin\phi = \frac{y}{r}, \quad \cos\phi = \frac{x}{r}, \quad \text{and} \quad r = (x^2+y^2)^{1/2}, \tag{2.28}$$

one can represent the outflow profile in the Cartesian coordinate as

$$v_x(r,\phi) = -2v_0 f(r)\left[\frac{(\phi-\pi)}{\pi}\right]\left[\frac{y}{(x^2+y^2)^{1/2}}\right] \quad \text{and} \tag{2.29}$$

$$v_y(r,\phi) = 2v_0 f(r)\left[\frac{(\phi-\pi)}{\pi}\right]\left[\frac{x}{(x^2+y^2)^{1/2}}\right]. \tag{2.30}$$

Here x is equivalent to $x + x_{min}$ with $x_{min} = 5\,R_E$ in the tail (the Earthward boundary). The assumed flow profile (or better electric field) is then mapped along the magnetic field from the equatorial plane into the Earthward boundary. The mapping procedure assumes any individual magnetic field line connecting the equatorial plane and the Earthward boundary have the same angular velocity $\dot{\phi}$. The mapping procedure is outline below:

Starting from one point located at r_{eq} in the equatorial plane, the magnitude of azimuthal velocity is

$$(v_\phi)|_{eq} = r_{eq}\dot{\phi} \tag{2.31}$$

such that the angular velocity is

$$\dot{\phi} = \frac{(v_\phi)|_{eq}}{r_{eq}}. \tag{2.32}$$

Similarly, the magnetic conjugate point located at the Earthward boundary (radial distance r_b) has the azimuthal velocity

$$(v_\phi)|_b = r_b\dot{\phi} \tag{2.33}$$

which can be rewritten into

$$(v_\phi)|_b = r_b\left\{\frac{(v_\phi)|_{eq}}{r_{eq}}\right\} = (\frac{r_b}{r_{eq}})(v_\phi)\Big|_{eq}. \tag{2.34}$$

The azimuthal velocity $(v_\phi)|_{eq}$ can be decomposed into the x and y components as introduced such that the velocity at the Earthward boundary can be expressed as

$$\{(v_\phi)|_b\}_x = (\frac{r_b}{r_{eq}})\{(v_\phi)|_{eq}\}_x \quad \text{and} \tag{2.35}$$

$$\{(v_\phi)|_b\}_y = (\frac{r_b}{r_{eq}})\{(v_\phi)|_{eq}\}_y. \tag{2.36}$$

We emphasize that this condition is applied only at the Earthward boundary and there is no flow imposed in the equatorial plane. This sunward outflow is located at a radial distance of about $10\,R_E$ (the light red arrows in Figure 2.5) approximately consistent with adiabatic convection toward the dayside magnetopause. The color plot in Figure 2.5 (b) displays the velocity profile at the Earthward boundary after the sunward divergent outflow is switched on. Except for the specified sunward flow there is no normal component of the velocity at the Earthward boundary. Note that in the MFD runs, the normal velocity is set to 0 at other boundaries because of (1) the limited information for the in- and out-flow conditions at these boundaries, and because of (2) the minor effects of these boundaries for the near-Earth tail dynamics. This assumption should be reasonably satisfied during the slowly evolving growth phase unless there is a significant in- or out-flow through these boundaries.

2.4.5 Summary of the Boundary Conditions

This section summarizes all of the boundary conditions in this dissertation. The dynamic boundary conditions including the sunward convection and the electric field driver are applied on the equilibrium constructed from the relaxation technique. The relaxation technique will be discussed in the next section. All boundary conditions in this simulation are summarized in Table 1. Here we denote the value "1" as symmetry and the value "-1" as antisymmetry of the plasma quantities. The sunward convection is denoted as "s" for the MFD process and the driving electric field is denoted as "e" during the lobe compression.

2.5 Relaxation Technique

The relaxation procedure is a computational tool designed for a system evolving toward an equilibrium state. This work uses the "ballistic relaxation" method to generate the equilibrium configuration of the magnetotail. The relaxation method allows the system to evolve freely for a time period τ_d. During the relaxation period unbalanced forces relax and the associate energy is converted to kinetic and thermal energy mostly. At the end of each relaxation period, the plasma velocity is set to zero everywhere in the simulation domain, which results in the removal of plasma kinetic energy throughout the simulation domain. This sets the starting point for the next relaxation of the unbalanced force.

The relaxation period τ_d is set to several different values in this simulation. A small τ_d is efficient to reduce unbalanced forces on small scales for instance to achieve pressure equilibrium between the plasma sheet and the lobe magnetic field. However, employing the relaxation method with only small values τ_d leads to a very long relaxation time scale to remove the large scale unbalanced force. A large value of τ_d can reduce the large scale unbalanced forces for instance between the near-Earth boundary and the tail boundary. A quantitative measure of the unbalanced force is defined as

$$N = \int_V (-\nabla p + \vec{j} \times \vec{b})^2 dV, \tag{2.37}$$

where N is the unbalanced force integrated over the total volume V of the system and $\vec{j} \times \vec{b}$ is the local

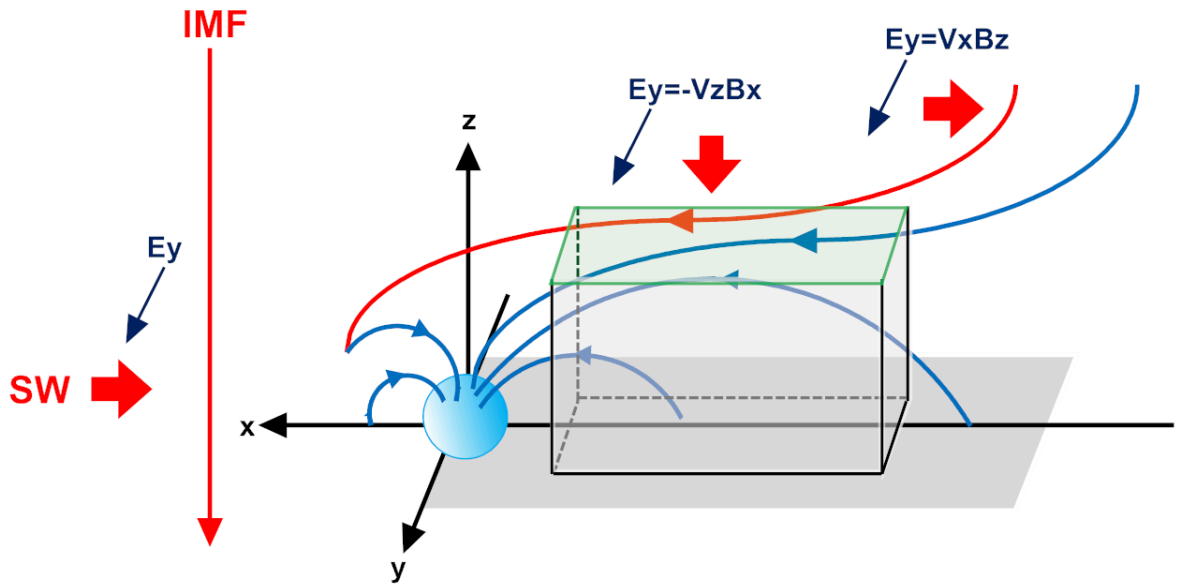

Figure 2.4. Illustration of the electric field transported from the solar wind into the tail region during the substorm growth phase. The red lines are the solar wind magnetic field lines, and the blue lines are the Earth intrinsic magnetic lines. The shaded green region is the top boundary of the simulation box. The red thick arrows indicate the solar wind flow directions.

Table 2.1. Summary of the boundary conditions in the relaxation, MFD, and the lobe compression simulations. The value "1" represents the symmetry of plasma quantities while the value "-1" represents the antisymmetry of plasma quantities at the certain boundaries. The symbol "s" denotes the sunward outflow condition, and the symbol "e" denotes the electric field driver.

	x_{min}	x_{max}	y_{min},y_{max}	z_{min}	z_{max}
ρ	1	1	1	1	1
h	1	1	1	1	1
b_x	$\nabla \cdot \vec{b} = 0$	$\nabla \cdot \vec{b} = 0$	1	-1	1
b_y	1	1	$\nabla \cdot \vec{b} = 0$	-1	1
b_z	1	1	1	1	$\nabla \cdot \vec{b} = 0$
v_x	-1	relaxation: -1; MFD: s	1	1	MFD: 1; compression: -1
v_y	1	relaxation: -1; MFD: s	-1	1	1
v_z	1	relaxation: -1; MFD: s	1	-1	MFD: -1; compression: e

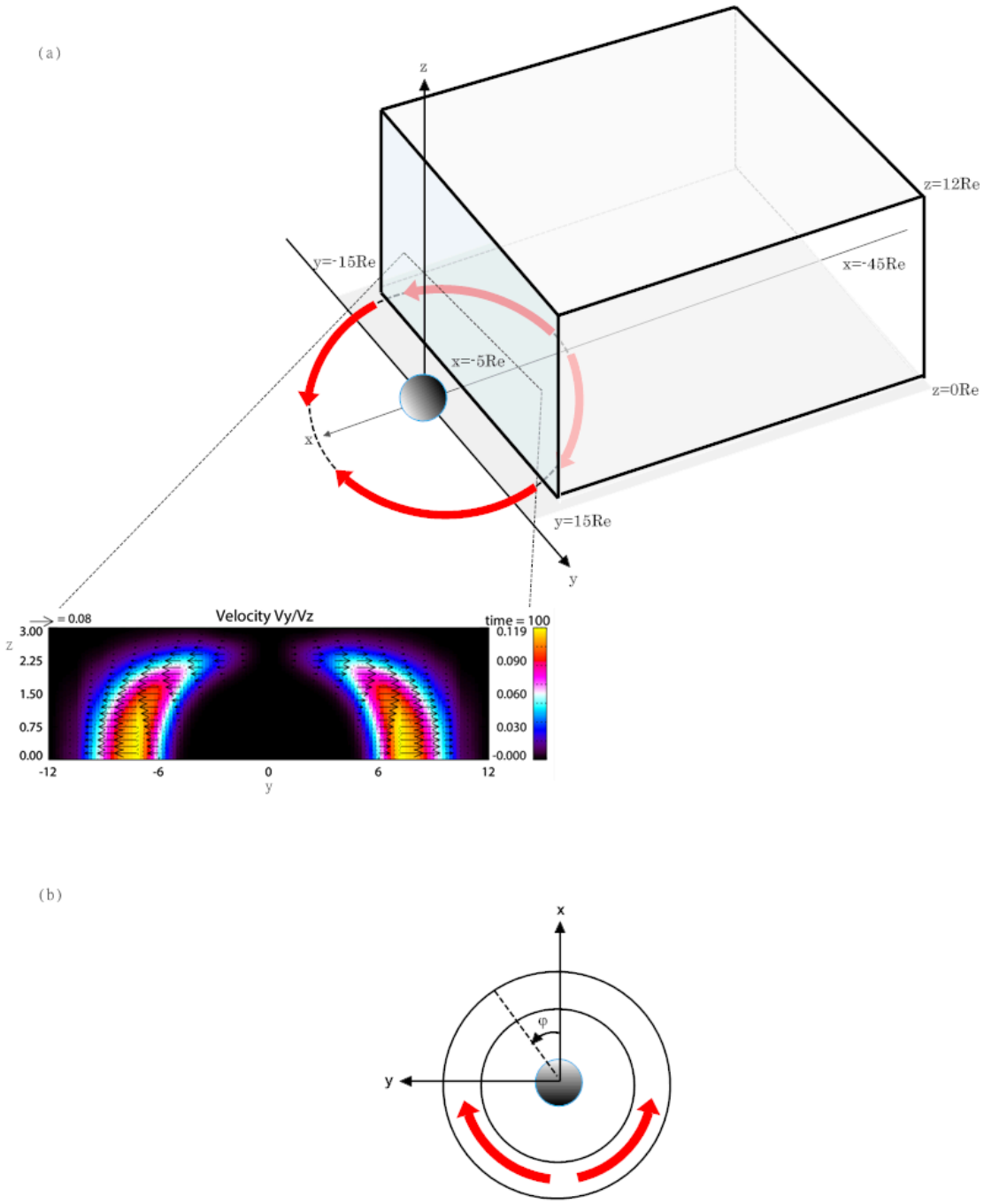

Figure 2.5. Sketch of the simulation model. (a) The simulation box and the applied Earthward boundary condition. A profile of the sunward divergent flow (the red arrows) is assumed in the equatorial plane. The rectangular panel shows the velocity mapped into the Earthward boundary ($x = -5R_E$) at $t = 20$ minutes, in which the color shows the normal component and arrow shows the tangential component of velocity. (b) ϕ is the angle from the Sun-Earth line toward the y direction.

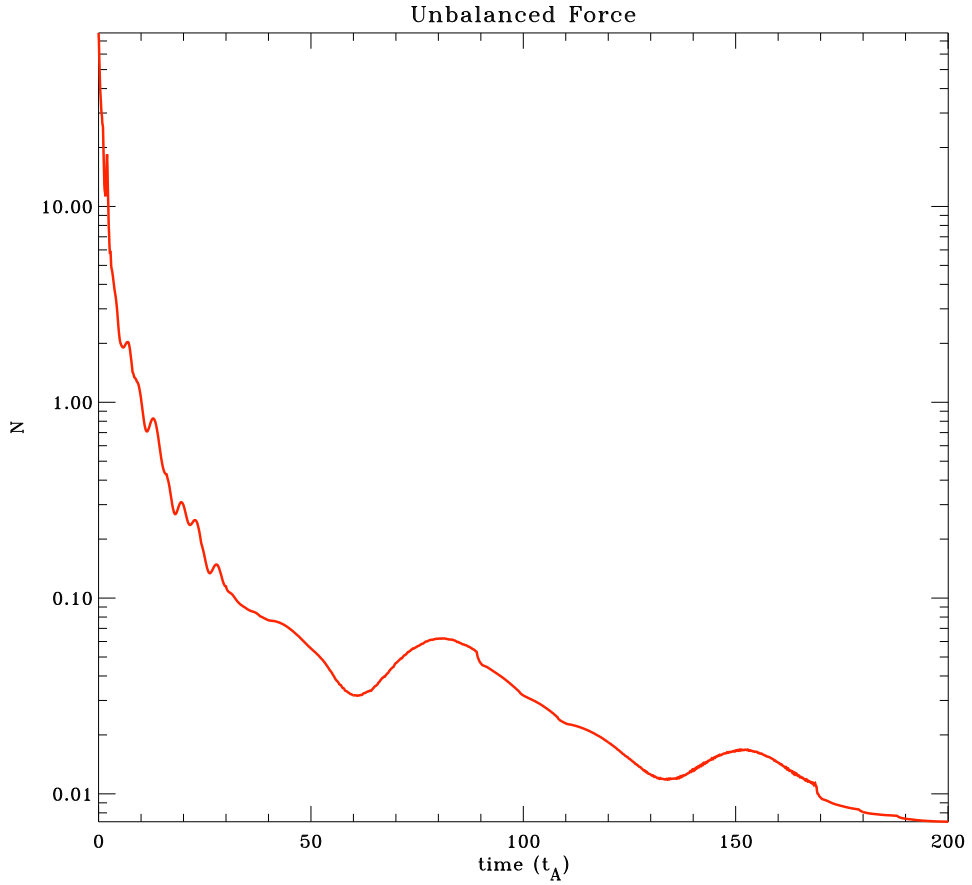

Figure 2.6. The variation of unbalanced force during the course of the relaxation. The x axis is the Alfvén time, and the y axis is the magnitude of the unbalanced force in the log scale.

magnetic force. The initial magnetic fields are obtained from T96 model under a particular solar wind and IMF condition. For all cases the solar wind dynamic pressure is assumed to be 1 nPa, the Dst is -15 nT, and the IMF B_z component is -1 nT (southward IMF condition). Tests with other values show that the results are rather robust and do not depend much on the choice of the parameters for the T96 model. Note, however, that larger negative values of B_z can cause local B_z minima including negative values of B_z in the tail which are an artefact of the statistical model because it does not differentiate between quiet and active times, during which reconnection operates in the tail. The IMF components B_x, B_y, and the dipole tilt angle are all set to zero, consistent with the symmetry of the simulation system. Figure 2.6 shows the variation of the unbalanced force during the entire course of a relaxation run. The unbalanced force sharply decreases during the first 30 Alfvén times by almost 3 orders of magnitude. The force starts to increase again around $t = 70$ because the relaxation period has been chosen large to allow the large distance relaxation. With several further relaxation periods the unbalanced force continuously decreases to a very small value less than 0.01 after 200 acceleration by Alfvén times, which can be used for a suitable equilibrium state of the initial magnetotail configuration. The average forces per gridpoint at this time is less than 10^{-4} N/m^3.

Here we present several plasma quantities before ($t = 0\,t_A$) and after ($t = 199\,t_A$) the relaxation

run. The first example is the magnetic field strength at the Earthward boundary presented in Figure 2.7. After the relaxation, the magnetic field configuration does not have any apparent change compared to the initial magnetic field generated from the T96 model. Figure 2.8 demonstrates that the relaxed magnetic field in the equatorial plane is also close to the initial T96 magnetic field configuration. Figure 2.9 presents the plasma density and pressure in the midnight meridian plane before the relaxation while Figure 2.10 shows the quantities after the relaxation. Here the temperature is assumed to be uniform such that the plasma density and pressure are equal. The results illustrate that the plasma density is more concentrated in the plasma sheet (the blue region) after the relaxation is applied. We also note that the plasma density and pressure is negative at some points near the Earthward boundary. A small constant value is added to avoid such negative values as shown in Figure 2.11.

Finally Figure 2.12 shows the current density in the midnight meridian plane. The initial high current density at around $x = -7\,R_E$ is slightly reduced after the relaxation. These results are expected because the system had been initialized with a pressure distribution, although not in equilibrium, that can only generate a relatively small force imbalance. Since the relaxation conserves the flux tube entropy, it is expected that the magnetic field does not change much. It is similarly expected that the largest changes are for the current density distribution because the initial current density is not constant along magnetic field lines. However, a two-dimensional equilibrium requires perpendicular current density to be constant along field lines (equations (1.26) and (1.27)). A large deviation from this condition can occur close to the Earthward boundary because this is the region with the largest three-dimensional effects (convergence of the magnetic field to Earth).

An equilibrium state of magnetotail is critical for the applications of the dynamic boundary conditions. Without such an initial state, the effect of the plasma outflow cannot be distinguished from the acceleration by non-equilibrium forces in the tail configuration. After a well force-balanced magnetotail is acquired, the dynamic boundary conditions can be applied to certain boundaries. The influences of the sunward convection on the magnetotail evolution will be presented in the next chapter.

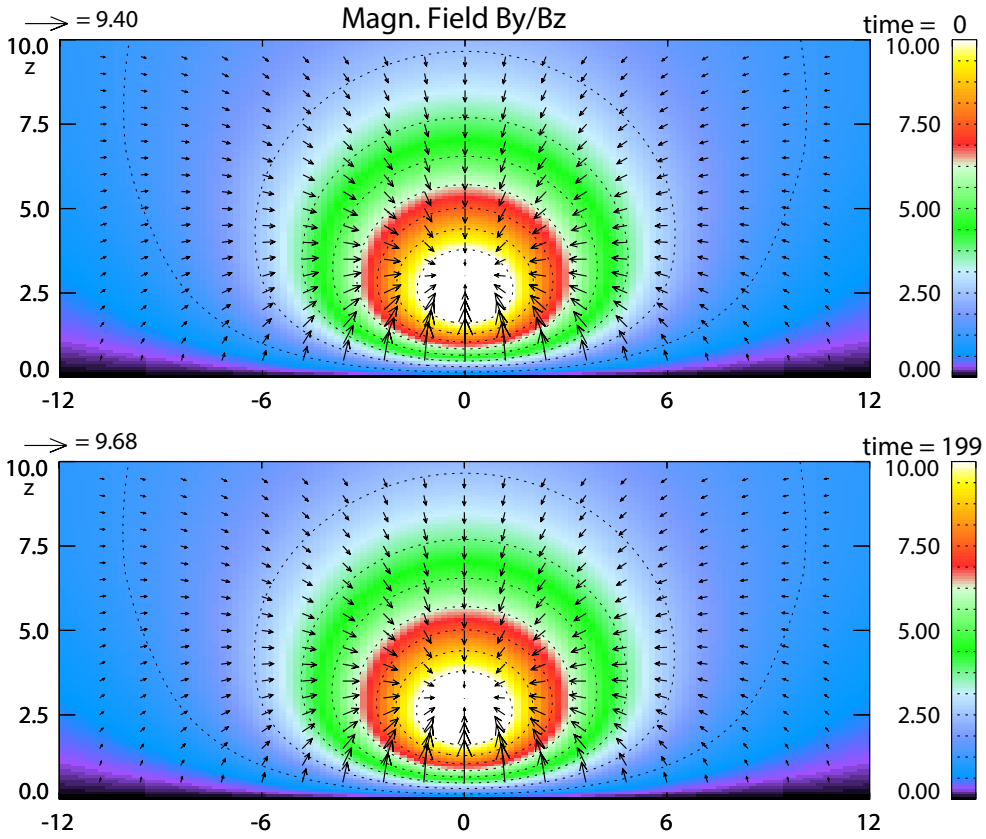

Figure 2.7. Magnetic field strength at the Earthward boundary (top) before the relaxation and (bottom) after the relaxation. The color shows the normal component of magnetic field (B_x). The title B_y/B_z represents the vector $B_y\hat{e_y} + B_z\hat{e_z}$, which indicates the tangential component of the magnetic field.

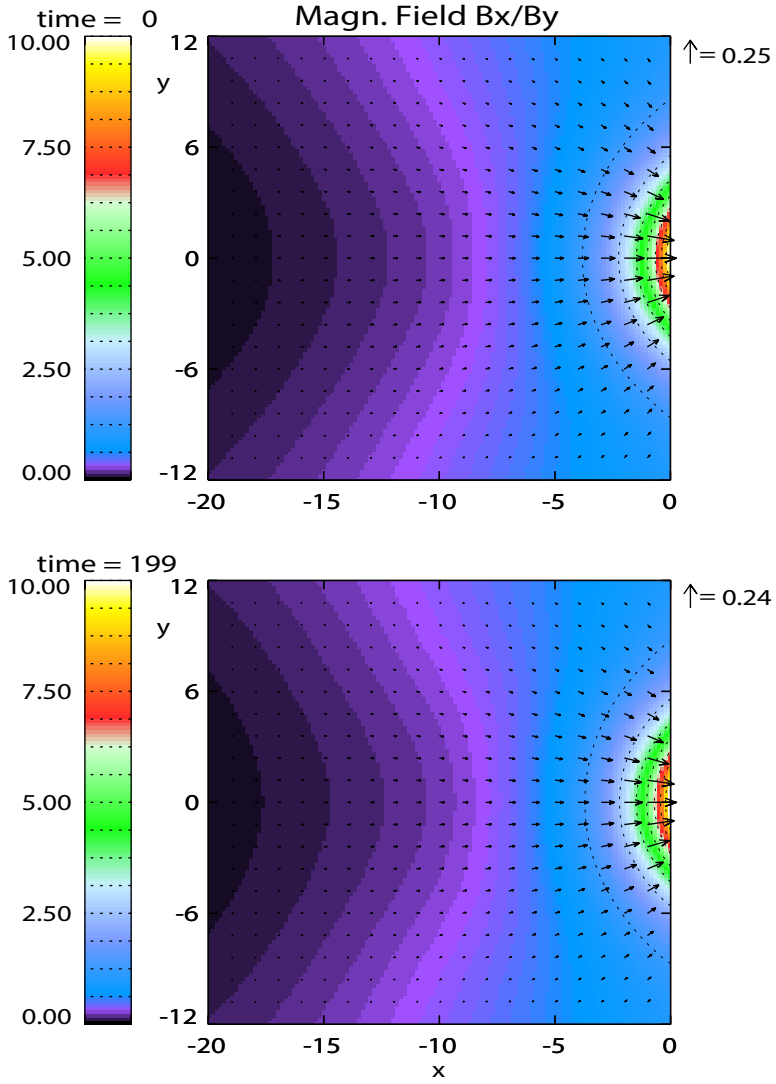

Figure 2.8. Magnetic field strength in the equatorial plane (top) before the relaxation and (bottom) after the relaxation. The color shows the normal component of magnetic field (B_z). The title B_x/B_y represents the vector $B_x\hat{e_x} + B_y\hat{e_y}$, which indicates the tangential component of the magnetic field.

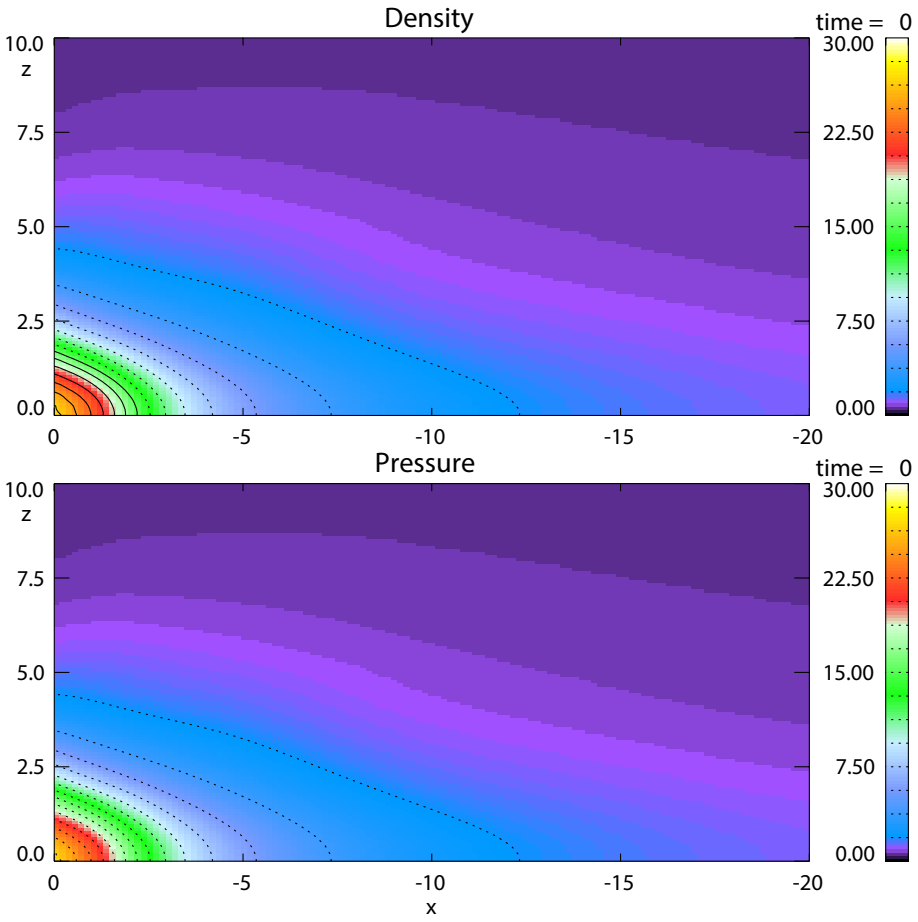

Figure 2.9. (top) Plasma density and (bottom) pressure in the midnight meridian plane before the relaxation.

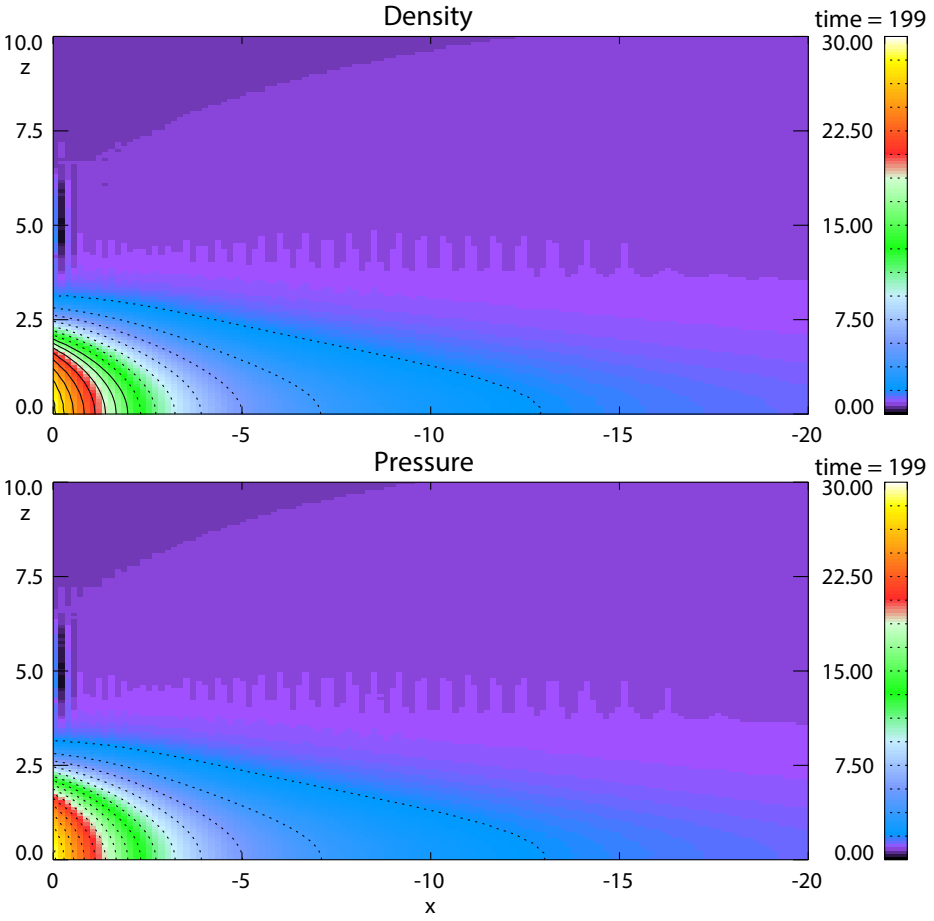

Figure 2.10. (top) Plasma density and (bottom) pressure in the midnight meridian plane after the relaxation.

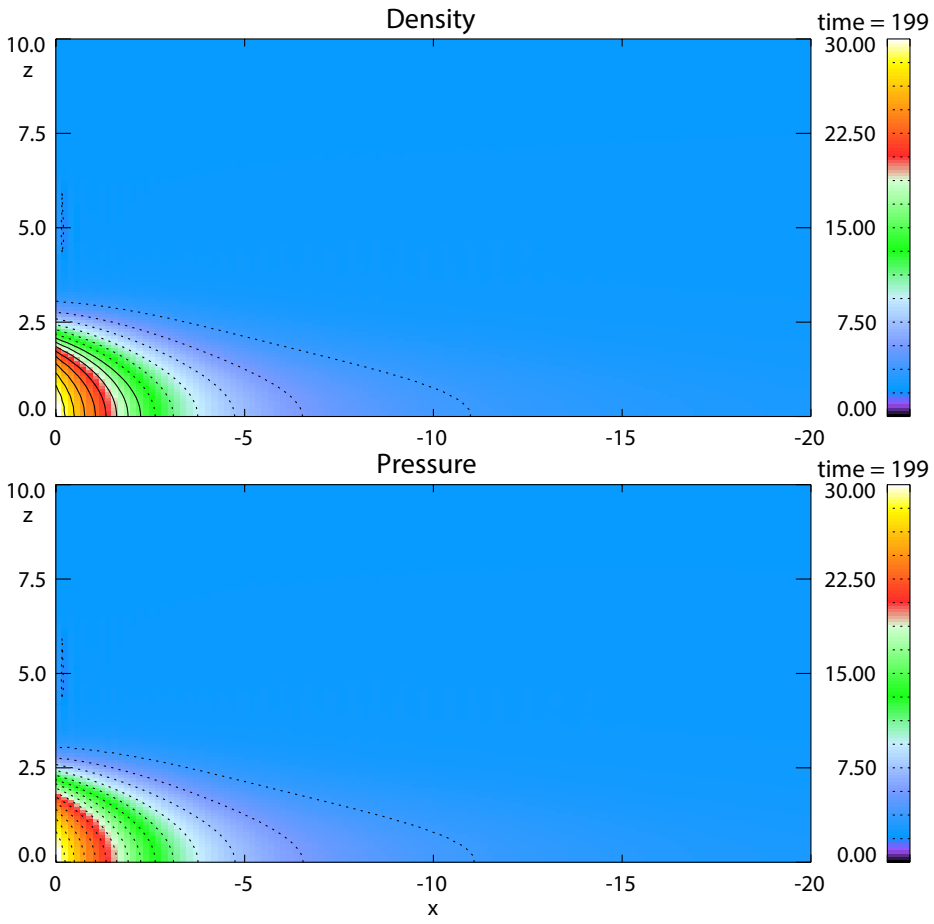

Figure 2.11. (top) Plasma density and (bottom) pressure in the midnight meridian plane after the relaxation. A small constant value is added to the case shown in Figure 2.10.

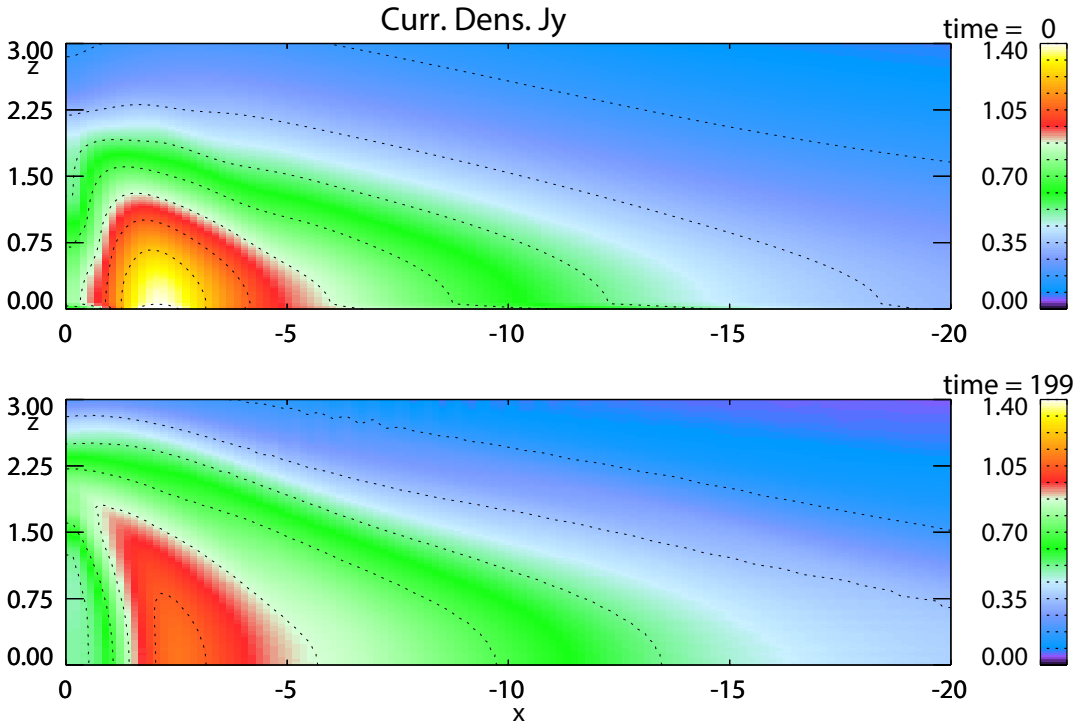

Figure 2.12. Crosstail current density in the midnight meridian plane (top) before the relaxation and (bottom) after the relaxation.

Chapter 3

The Influence of Midnight Magnetic Flux Depletion on the Magnetotail Evolution during the Substorm Growth Phase

3.1 Introduction

The growth phase of substorms is often initiated by the southward turning of the IMF and the erosion of magnetic flux at the dayside magnetopause through magnetic reconnection. The evolution of a thin CS is a particularly important magnetotail property characteristic of the growth phase, which is a critical process to understand the physics of magnetospheric substorms. It has been found that a thin CS forms preceding local magnetic reconnection, suggesting that the state of magnetotail in the late growth phase provides the conditions for an instability that leads to the expansion phase onset [*Asano et al.*, 2003; *Petrukovich et al.*, 2007]. Although observations detail many properties of CS thinning, the physical mechanism for thin CS generation is still not well understood. This chapter investigates a new mechanism of thin CS formation and demonstrates properties that agree well with the observed CS features during the substorm growth phase.

The presented study is based on magnetic flux depletion (MFD) in the near-Earth magnetotail. The MFD is caused by a divergent sunward outflow in the near-Earth tail to replenish magnetic flux which is eroded on the dayside by magnetic reconnection during periods of southward IMF. The sunward convection is slow and expected to be a quasi-static process during the slowly evolving growth phase. *Coroniti and Kennel* [1973] first proposed that the dayside reconnection can launch fast rarefaction waves which propagate into the magnetotail and enhance sunward convection across closed field lines, depleting the magnetic flux in the magnetotail. Similar ideas were also discussed by *Coroniti* [1985] and *Kan* [1990]. This sunward convection across closed field lines is expected to be enhanced within $x = -10\,R_E$ in the near-Earth plasma sheet, which maps to the diffuse auroral edge of low ionospheric conductance. However, the sunward transport of magnetic flux is not subject to any particular constraints in the earlier works.

An important aspect of the MFD model is the conservation of magnetic flux tube entropy during the slow quasi-static evolution in the magnetotail. This adiabatic invariant confines the depletion of magnetic flux in the tail to a region of specific flux tube entropy in order to avoid the pressure balanced inconsistency. As a result, magnetic flux tubes are likely to convect and divert around the Earth mostly along contours of constant flux tube entropy. The presented model for MFD specifies a sunward outflow condition at the Earthward boundary to prescribe the rate of sunward magnetic flux transport. The Earthward boundary condition is specified by mapping an azimuthal outflow profile at around $x = -10\,R_E$ from the equatorial plane through the magnetic field line integrations.

In order to identify the physics and importance of MFD for the substorm growth phase, this chapter does not include the addition of lobe magnetic flux which may contribute to a thin CS formation. A study including the additional influence of a lobe driver is presented in Chapter 4. The presented results employ a three-dimensional mesoscale MHD simulation of the near-Earth tail as described in Chapter

2. We first assume a sunward convection which is symmetrically diverted away from the midnight meridian, where one would expect the strongest thinning of the CS. However, observations indicate that the crosstail current density and the magnetic field depression often show a clear dawn-dusk asymmetry in the near-Earth magnetotail [*Nakai et al.*, 1997; *Newell et al.*, 1998], suggesting that the source region of the divergent convection might be occasionally off the midnight meridian. Therefore, it is interesting to examine the effects of an asymmetric sunward convection on the magnetotail evolution. The symmetric and asymmetric MFD cases will be studied in sections 3.2 and section 3.3 respectively. This chapter demonstrates that MFD is an efficient mechanism for thin CS formation by quantitatively examining the evolution of the crosstail current density, CS thickness, and other important magnetotail properties.

3.2 Symmetric Sunward Convection

This section investigates the symmetric MFD case, which assumes a symmetrically diverted convection pattern away from the midnight meridian. Figure 3.1 shows the azimuthal velocity at the Earthward boundary at times $t = 0\,t_A$, $130\,t_A$, and $270\,t_A$. The outflow boundary condition is slowly turned on in the MHD simulation at time $t = 0$ starting from the relaxed equilibrium state as outlined in section 2.5. This boundary condition is dynamically updated with time. The color in Figure 3.1 represents the normal or x component of velocity, and the vector represents the tangential component of velocity $(v_y\hat{e_y} + v_z\hat{e_z})$. In this figure and all other results distances are measured in Earth radii and velocity is measured in units of 430 km/s.

Figure 3.1 illustrates the azimuthal velocity at the Earthward boundary ($x = -5\,R_E$). The horizontal orientation of the velocity vectors indicates that there is no z component of velocity at the Earthward boundary. This figure shows that the sunward flow is confined to a region between $-12 < y < 12$ and $0 < z < 3$ at the sunward boundary consistent with the profile of the flow that is used to construct the outflow condition (see equations (2.22) and (2.23)). The outflow amplitude is not kept constant but updated with a function

$$f_t = 1 - \exp(-\text{time}/2) \tag{3.1}$$

parameterized by time. This function ramps the velocity up to a magnitude ~ 0.13 (~ 56 km/s) over a short time ($\sim t = 2\,t_A$) and then increase the velocity slowly during the rest time of the simulation. Figure 3.1 shows that the velocity is very small initially, because the outflow is switched on first with a small value. Then the velocity increases slowly up to a value $\sim$0.22 (~ 95 km/s) at $t = 270t_A$ (~ 1 hr) in attempt to maintain the outflow potential.

Figure 3.2 presents the magnetic fields (B_x) at the Earthward boundary. Again, three corresponding times are selected comparing with Figure 3.1. At the beginning of the simulation, there is still a strong dipole contribution at the region $1 < z < 3.5$ near the midnight meridian plane, which originates from the T96 magnetic field model. The dipolar field is strongly modified and reduced after the sunward convection is switched on. The region of strongest magnetic flux depletion is associated with the outflow

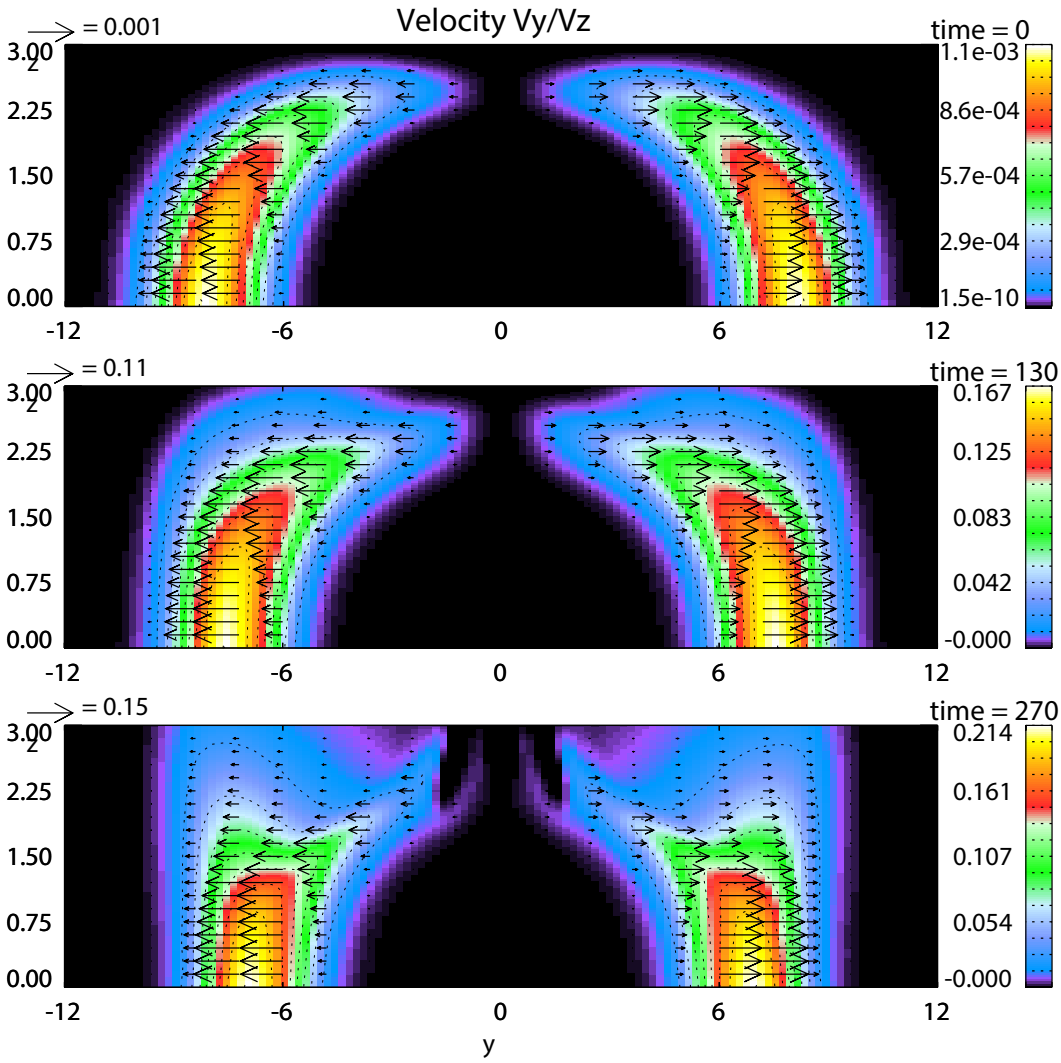

Figure 3.1. The sunward outflow at the Earthward boundary at times (top) $t = 0t_A$, (middle) $t = 130t_A$, and (bottom) $t = 270t_A$. The plane is cut within the range $-12 < y < 12$ and $0 < z < 3$. The color shows the normal component of velocity (v_x), and the arrows represent the tangential component of velocity ($v_y\hat{e_y}+v_z\hat{e_z}$).

channels. The depletion of magnetic flux is symmetric away from the midnight meridian because a symmetric divergent sunward outflow is assumed. Toward the end of growth phase, a major amount of magnetic flux through the sunward boundary is removed by the sunward flow. The strong dipole field splits into two parts with a local minimum of magnetic field in the center portion.

The most central property of this study is the current density in the near-Earth magnetotail. Figure 3.3 illustrates the current density (J_y) in the midnight meridian plane. It is shown that the CS density forms a sheet with a half width of about $3\,R_E$ along z direction at the beginning of the growth phase. The maximum current density is initially located near geosynchronous distances (note that $x = 0$ in the simulation corresponds to $x = -5R_E$ in GSM coordinate) when the magnetotail configuration is still close to the Tsyganneko magnetic field. The current density gradually increases and develops into the bifurcated current structure at $t = 130t_A$. After an hour ($t = 270t_A$), the initially wide CS is strongly

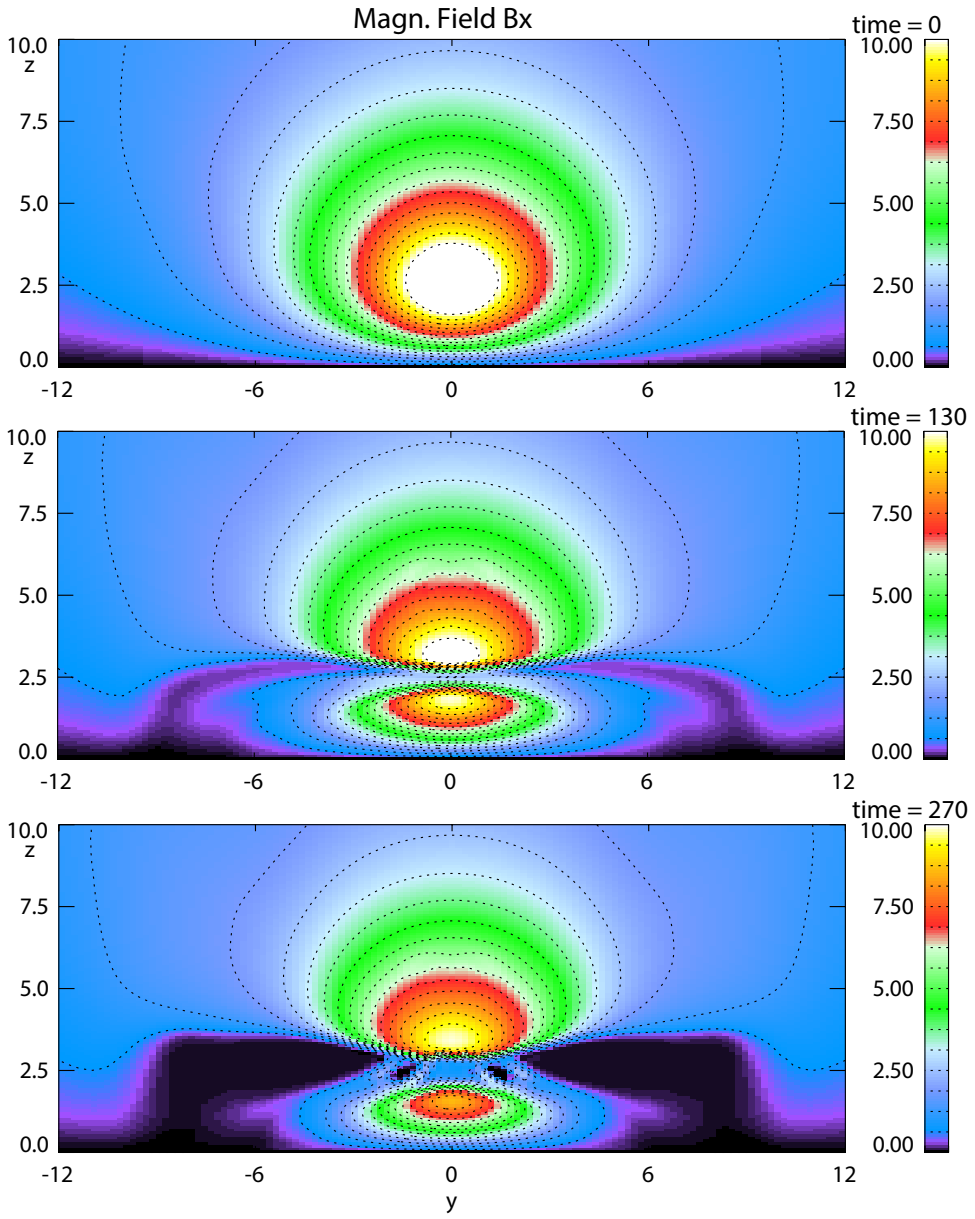

Figure 3.2. The format is the same as Figure 3.1, except for the magnetic field (B_x). The plane is cut within the range $-12 < y < 12$ and $0 < z < 10$.

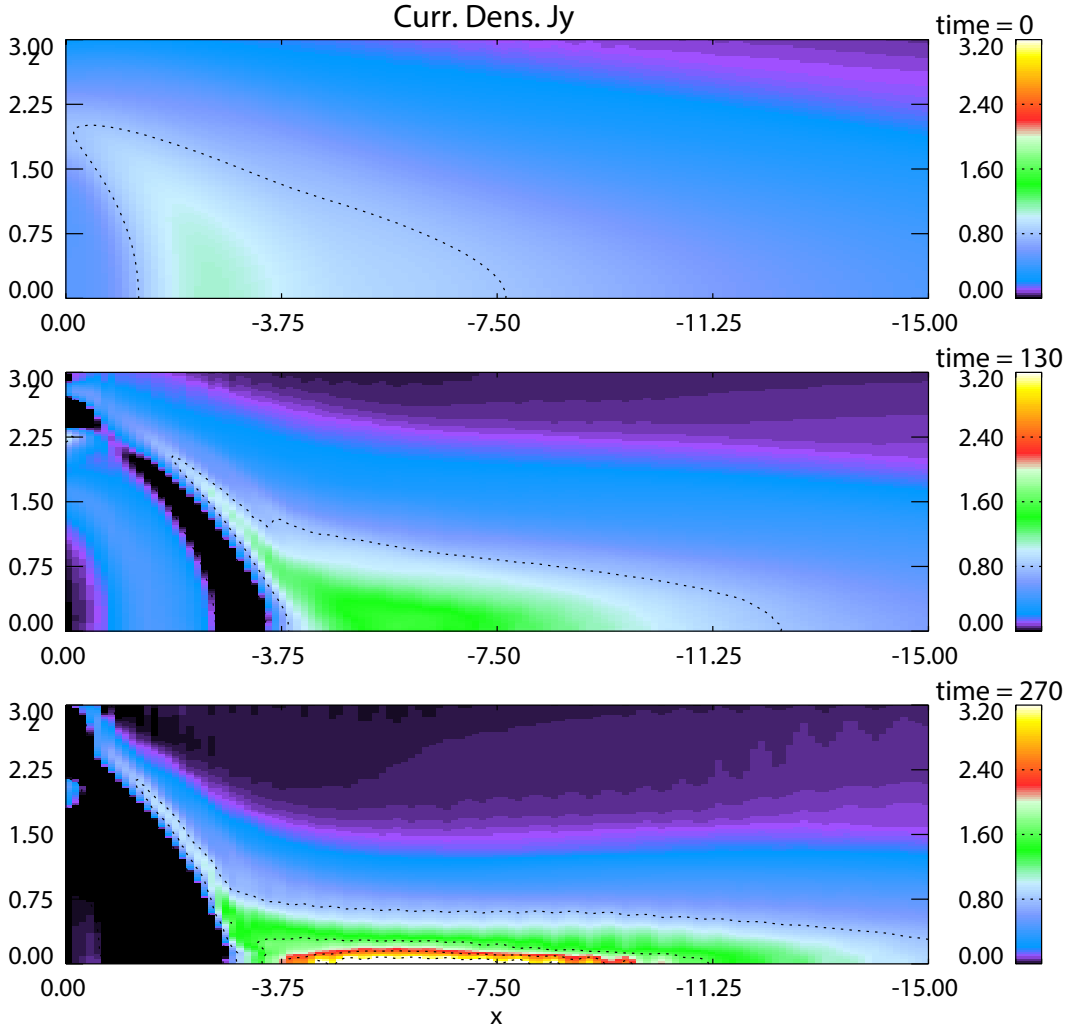

Figure 3.3. Crosstail current density in the midnight meridian plane at times (top) $t = 0t_A$, (middle) $t = 130t_A$, and (bottom) $t = 270t_A$. The color shows the current density J_y. The plane is cut within the range $-15 < x < 0$ and $0 < z < 3$.

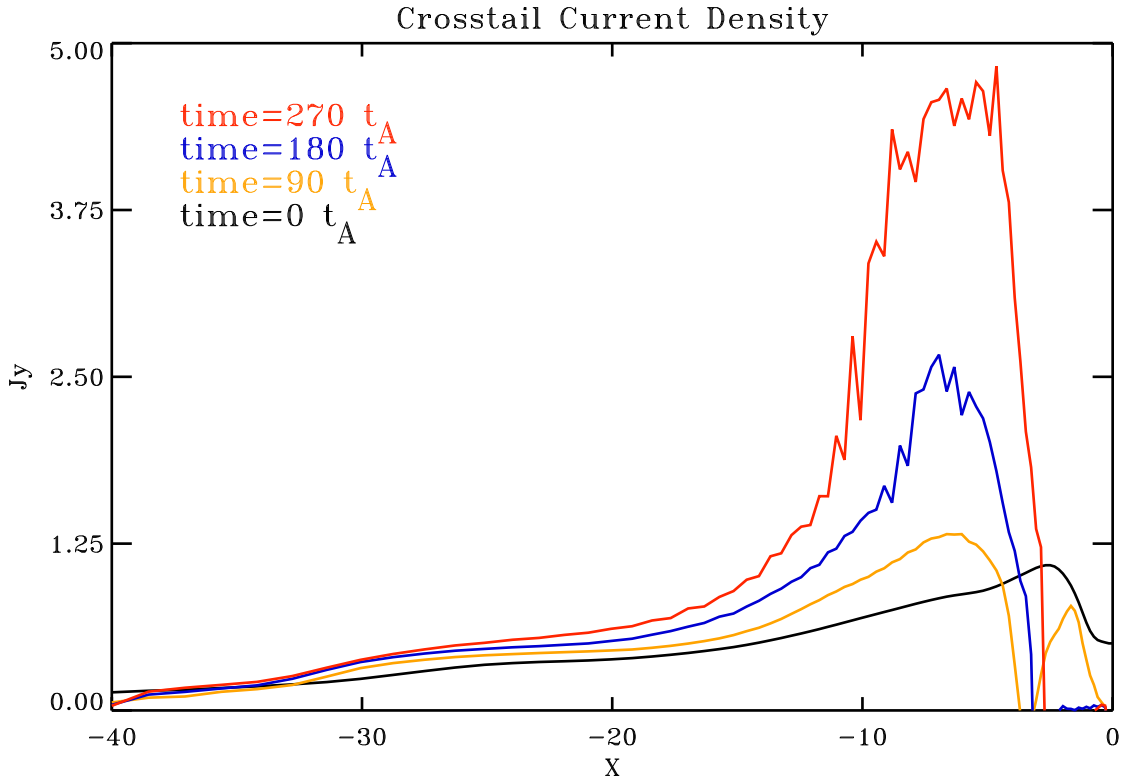

Figure 3.4. Equatorial crosstail current density in the midnight meridian plane at times (black) $t = 0t_A$, (orange) $t = 90t_A$, (blue) $t = 180t_A$, and (red) $t = 270t_A$.

concentrated into a thin and strong CS near the equatorial plane. This central result demonstrates a high efficiency of the divergent flow to generate a very thin CS with a strongly enhanced crosstail current density. The Earthward edge of the thin CS forms at about $x = -4$ and extends to $x = -11$, indicating that the thin CS structure is primarily confined to the near-Earth region.

Figure 3.4 shows the value of the equatorial crosstail current density in the midnight meridian plane at times $t = 0\,t_A$, $t = 90\,t_A$, $t = 180\,t_A$, and $t = 270\,t_A$. A bifurcated current structure is presented in the near-Earth region at $t = 90\,t_A$. The peak current density is retreating tailward by about 2 to $3\,R_E$ compared with its location at the beginning of the growth phase. The maximum crosstail current density increases about 4 fold toward the end of the growth phase. The strongest current density reaches close to $5j_0$ ($\sim$ 12 nA/m^2) and extends several R_E along the tail direction (around $x = -4$ to $x = -11$) after an hour. Such high current densities agree well with typical satellite observations during the growth phase, e.g., *Petrukovich et al.* [2007] and *Saito et al.* [2011].

Figure 3.5 examines the CS thickness and the associated tail properties in the midnight meridian plane. The CS thickness is computed from the Harris sheet model as introduced in the first chapter. By employing the Harris sheet model, the crosstail current density profile is assumed to be

$$j_y = j_0 \cosh^{-2} \frac{z}{L}, \tag{3.2}$$

where $j_0 = B_0/(\mu_0 L_0)$ represents the maximum current density in the CS. The integral of the current

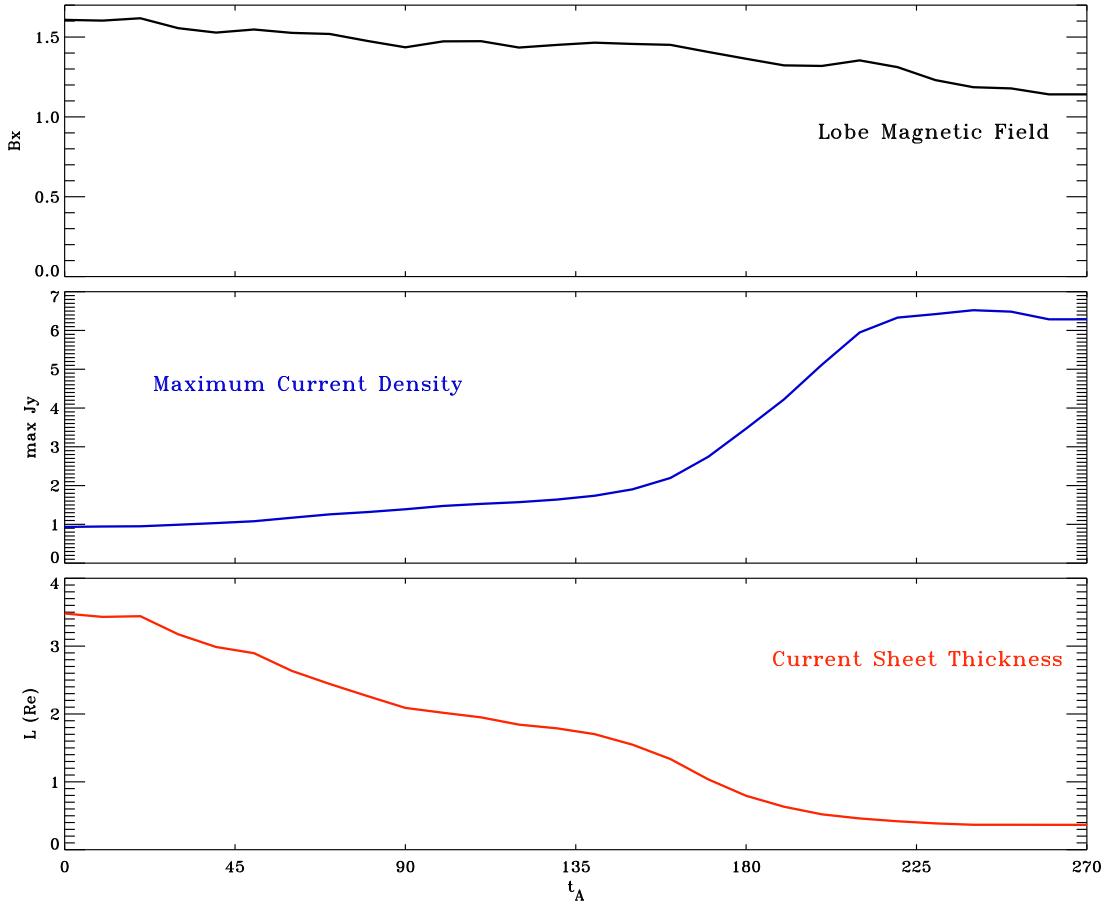

Figure 3.5. The magnetotail properties in the midnight meridian plane. The top panel shows the lobe magnetic field, the middle panel presents the maximum current density, and the bottom panel shows the CS thickness.

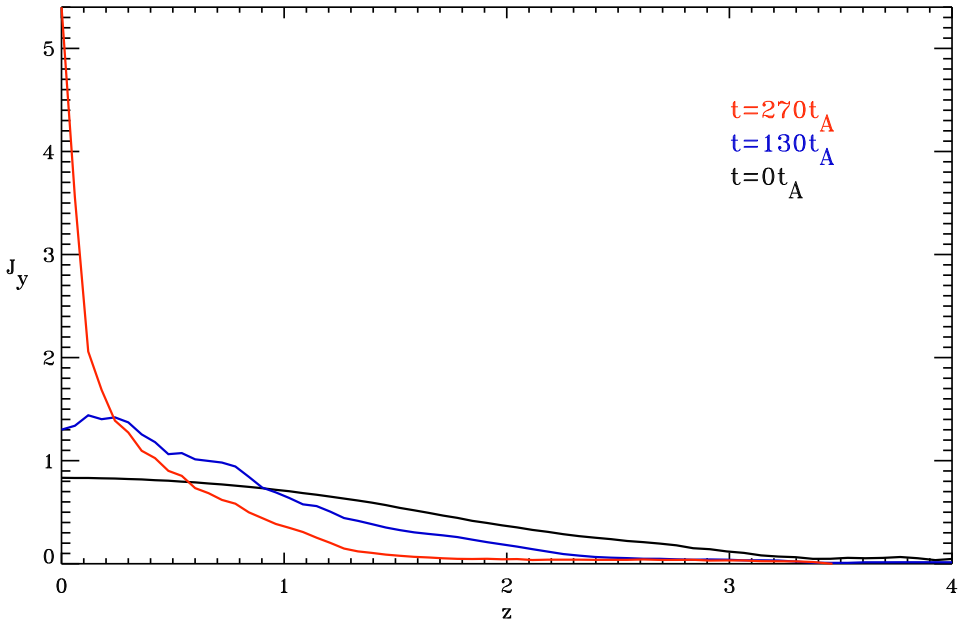

Figure 3.6. Current density distributed along z at times (black) $t = 0\,t_A$, (blue) $t = 130\,t_A$, and (red) $t = 270\,t_A$. The x position of the cut is about $-7\,R_E$.

density along the z axis is

$$\int_{z_{min}}^{z_{max}} j_0 \cosh^{-2}\frac{z}{L} dz = 2j_0 L, \tag{3.3}$$

which is approximately equivalent to the change of x component of the magnetic field from the southern to northern lobe, i.e., ΔB_x (note that the simulation assumes symmetry between the northern and southern lobes). Therefore, a typical CS thickness can be estimated from

$$L = \frac{\Delta B_x}{2j_0}. \tag{3.4}$$

The top panel of Figure 3.5 shows evolution of the lobe magnetic field over the course of the simulation. Without including any addition of lobe magnetic flux through a driving electric field, the lobe field decreases by about 30% (from 1.6 to 1.13) during the MFD process. The second panel shows the maximum current density in the midnight meridian plane (not at a specific radial distance). The current density increases by a factor of 6 and gradually saturates in the late growth phase. The last panel presents the CS thickness which is computed from equation (3.4). It is shown that the initial CS thickness is about $3.5\,R_E$ and decreases down to $0.4\,R_E$ after an hour. Note, Harris sheet theory assumes the particle distribution to be exponential as equation (1.2), however, it is not the case for an embedded CS. Figure 3.6 illustrates the current density distributed along z in the near-Earth region. The figure shows that there is a strong thin CS embedded into the background CS in the late growth phase. The half thickness of this embedded CS is about $0.1\,R_E$, which is much smaller than the thickness obtained from the Harris sheet profile. Figures 3.5 and 3.6 demonstrate again that MFD results in the strong thinning of the crosstail current and a large increase of the maximum current density. It is again emphasized that the presented results are obtained without any lobe compressions and in fact show a

reduction of the lobe magnetic field by 30%.

An important feature of the expansion phase onset is the magnetic reconnection in the magnetotail. Such reconnection likely requires current-associated instabilities which can easily operate in extremely thin CSs with high current density when the width decreases to less than the ion inertial or the gyro scale. Magnetotail reconnection is sometimes observed away from the midnight meridian plane. Therefore, the azimuthal current distribution can provide important information on the locations where magnetic reconnection is likely to start or operate. Figure 3.7 shows the magnetic field distributions in the equatorial plane. This figure demonstrates the drastic change of the magnetic field strength in the equatorial plane associated with the divergent azimuthal convection. The magnetic field is significantly reduced down to values of $B_z \sim 1$ nT and below in a large portion of the near-Earth plasma sheet in the region affected by the divergent (from midnight) convection at $10\,R_E$ distance which forms in response to the Earthward flow boundary condition. This reduction implies a major depletion of closed magnetic flux over the duration of the growth phase. Note, the reduction of the magnetic field at the Earthward boundary (Figure 3.1) and the reduction of the B_z component in the equatorial plane are consistent. The azimuthal extent of this reduction of closed dipolar magnetic field is not confined to a narrow region close to the midnight meridian plane but extends about hours away from midnight.

The equatorial plasma velocity is shown in Figure 3.8, which is subjected to the prescribed convection profile. No normal component of velocity is presented in the equatorial plane ($v_z = 0$). The overall flows are initially very small but increase slowly later. Note that different vector scales are used here. The fastest flows (~ 70 km/s) are diverted azimuthally (almost along contours of flux tube entropy) in order to avoid the pressure balance inconsistence as described in section 1.4. This sunward convection is seen as well associated with the azimuthal depletion of closed magnetic flux in the equatorial plane as shown in Figure 3.7. This slow divergent motion is the physical cause for the strong reduction of the equatorial B_z value.

Figure 3.9 presents the distribution of the azimuthal component of the current density (j_ϕ) in the equatorial plane. The figure illustrates the wide azimuthal section of the equatorial plane with thin CS formation. This is not unexpected in view of the relatively wide area with a strong depletion of the magnetic field B_z component. The enhanced plasma sheet current density is clearly associated with the region where the magnetic field B_z is reduced, and it spans an azimuthal area of about $\pm 40^\circ$ or approximately 3 hours from the local midnight. While the maximum current density is close to or at the midnight meridian, a similarly large current density can be found significant distances away from midnight, such that reconnection onset can occur up to 3 hours from the local midnight. Toward the end of the growth phase, the strongest current density indeed occurs away from the midnight meridian plane.

Figure 3.10 illustrates the source terms that contribute to the change of closed magnetic flux $\Phi = \int B_z dA$ in different sections of the equatorial plane. The x range is chosen between $x = -2$ and $x = -11$ that corresponds to the radial domain which is subject to the strong depletion of magnetic flux. The y

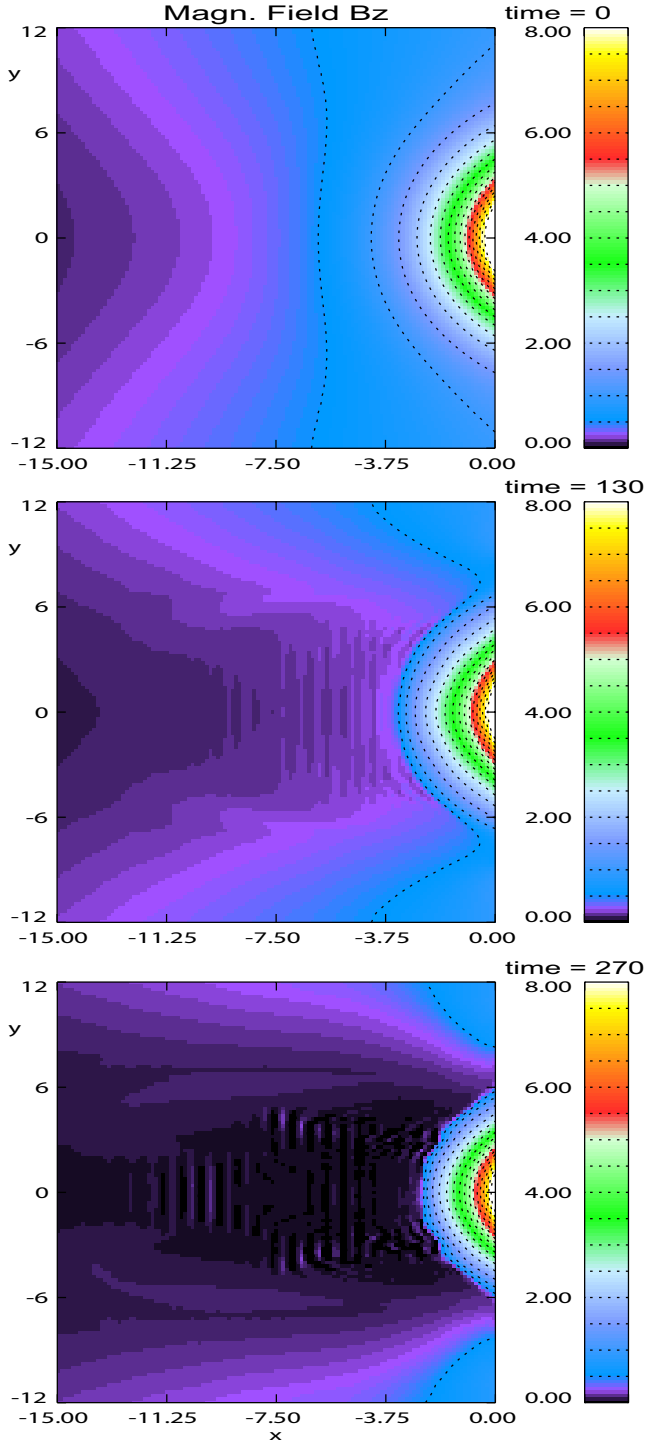

Figure 3.7. Magnetic field (B_z) in the equatorial plane at times (top) $t = 0t_A$, (middle) $t = 130t_A$, and (bottom) $t = 270t_A$. The plane is cut within the range $-15 < x < 0$ and $-12 < y < 12$.

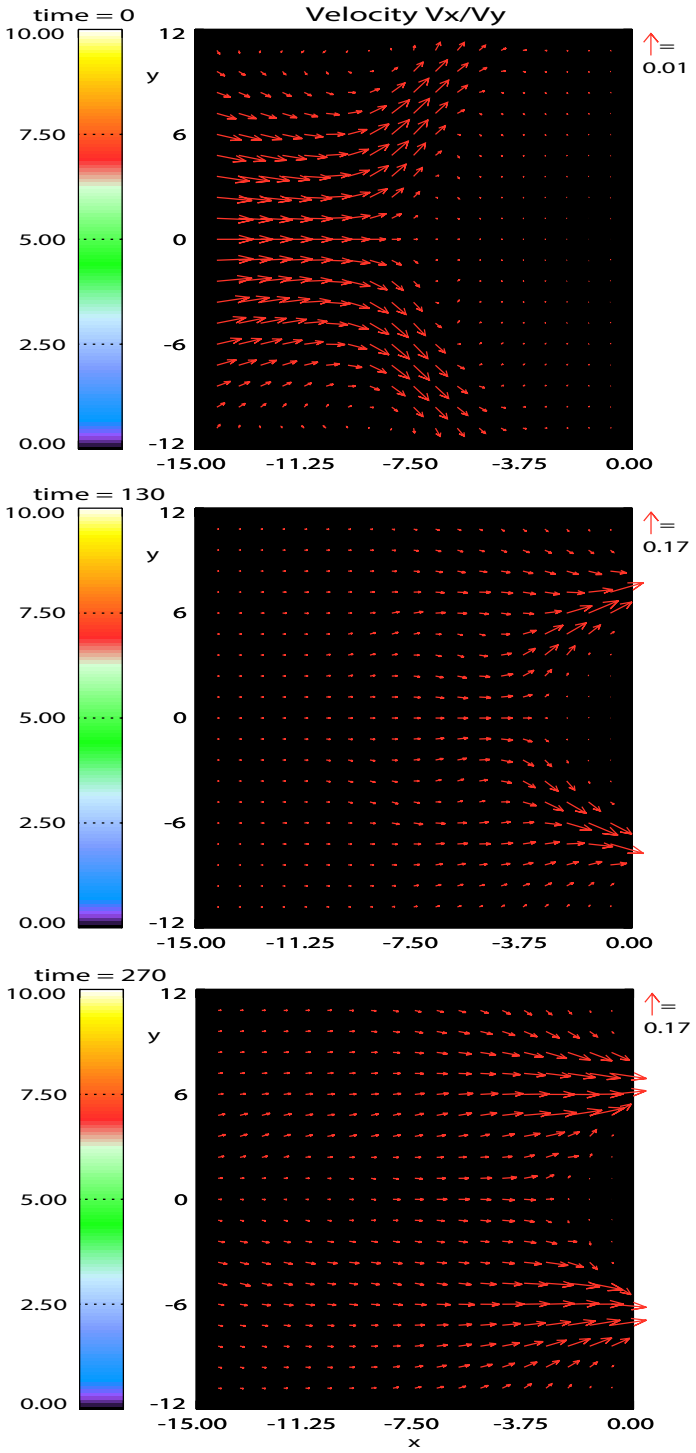

Figure 3.8. The format is the same as Figure 3.7, except for the plasma velocity. The color shows the normal component of velocity (v_z), and the arrow represents the tangential component of velocity ($v_x\hat{e_x}+v_y\hat{e_y}$).

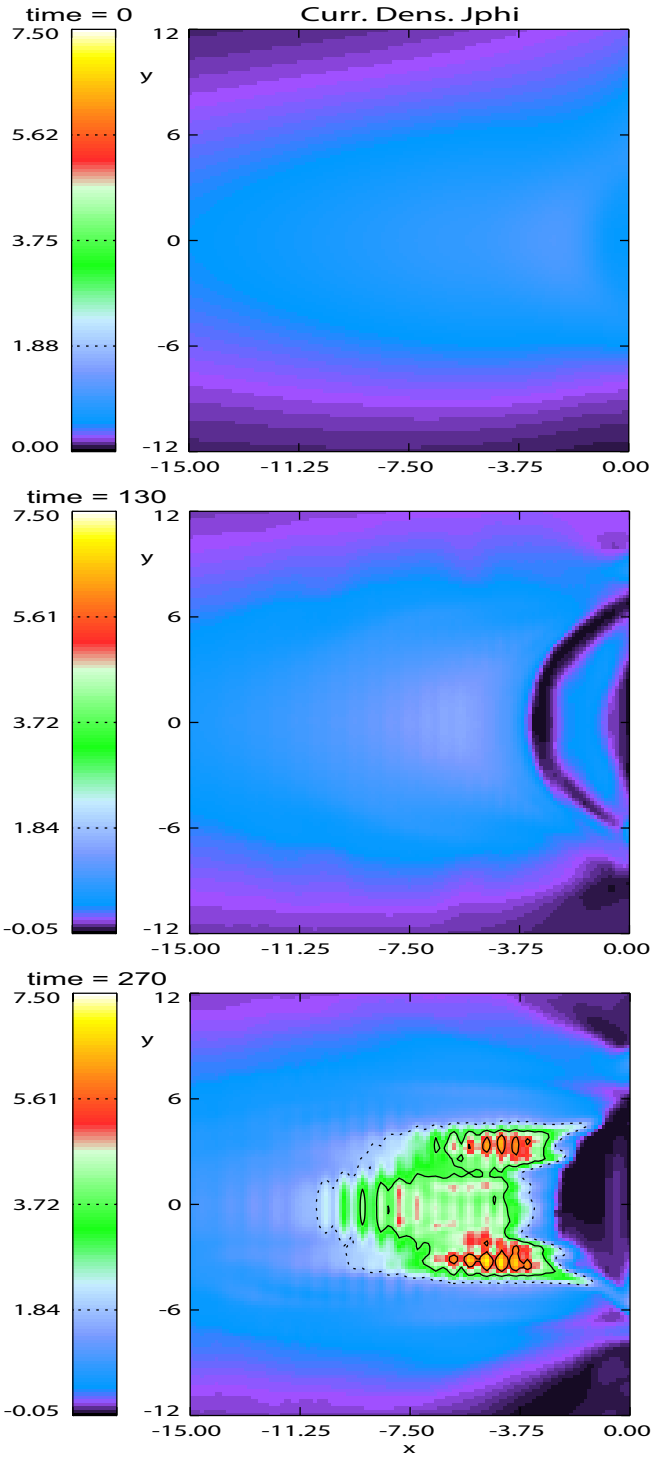

Figure 3.9. The format is the same as Figure 3.7, except for the azimuthal current density (j_ϕ).

range is chosen with 4 different sizes away from the midnight meridian plane. The first panel (top left) shows $\frac{d\Phi}{dt}$ only close to the midnight meridian plane, whereas the last panel (bottom right) presents $\frac{d\Phi}{dt}$ in the largest section of the midnight tail. Starting from Faraday's law combined with the frozen-in condition yields

$$\frac{\partial B_z}{\partial t} = \left[\nabla \times (\vec{u} \times \vec{B})\right]_z . \tag{3.5}$$

By decomposing the velocity $\vec{u}$ into $\vec{u}_{eq} + u_z \hat{e_z}$, equation (3.5) can be rewritten as

$$-B_z(\nabla \cdot \vec{u}_{eq}) - B_z \nabla_z u_z + B_z \nabla_z u_z - \vec{u}_{eq} \cdot \nabla B_z. \tag{3.6}$$

Therefore, we can express equation (3.6) as

$$\frac{\partial B_z}{\partial t} = -\nabla \cdot (B_z \vec{u}_{eq}). \tag{3.7}$$

Therefore, the magnetic flux transport through a closed surface dA in the equatorial plane can be regarded as

$$\frac{d\Phi}{dt} = \int \frac{\partial B_z}{\partial t} dA = -\int \nabla \cdot (B_z \vec{u}_{eq}) dA, \tag{3.8}$$

where the magnetic flux transport in the x direction is $\int \partial_x B_z u_x dA$ which is presented by black lines in Figure 3.10. The red lines of Figure 3.10 represent $\int \partial_y B_z u_y dA$ which is the y component of the magnetic flux transport. Here a positive value implies transport of flux into the chosen section of the equatorial plane and a negative value represent transport out of this section.

The first panel of Figure 3.10 shows the transportation of magnetic flux near the midnight meridian plane ($-1 < y < 1$). In the restricted region close to the midnight meridian plane, the magnetic flux transport is relatively small in the x direction. This is not unexpected because radial convection is limited by the constraint of flux tube entropy conservation. The dominant term that causes the decrease of closed flux is the divergent flow away from midnight in the y direction. Away from the midnight meridian plane ($-4 < y < 4$), the transport of magnetic flux out of the chosen domain increases for the y direction and the contribution from the x direction also becomes negative, i.e., contributes now to the depletion of magnetic flux. The bottom two panels illustrate the transportation of magnetic flux further away from the midnight meridian plane ($-7 < y < 7$ and $-10 < y < 10$). The result demonstrates that the magnetic flux transport is dominated by convection out of the region in the x direction for the larger domains. This implies the significant sunward magnetic flux transport in the large portion of the midnight tail. The stronger total depletion of magnetic flux is caused by the increasing velocity of the divergent azimuthal flow away from midnight. The larger contribution of the transport in x for the larger domains is caused by the sunward turning of the azimuthal convection with increasing distance from the midnight sector. The decreasing magnitude of flux transport in the late growth phase indicates a major amount of the magnetic flux has been depleted in the magnetic flux reservoir. Note that the outflow profile is kept the same. However, the magnetic field B_z component decreases such that the terms $B_z u_x$ and $B_z u_y$ decrease as the closed magnetic field flux is depleted.

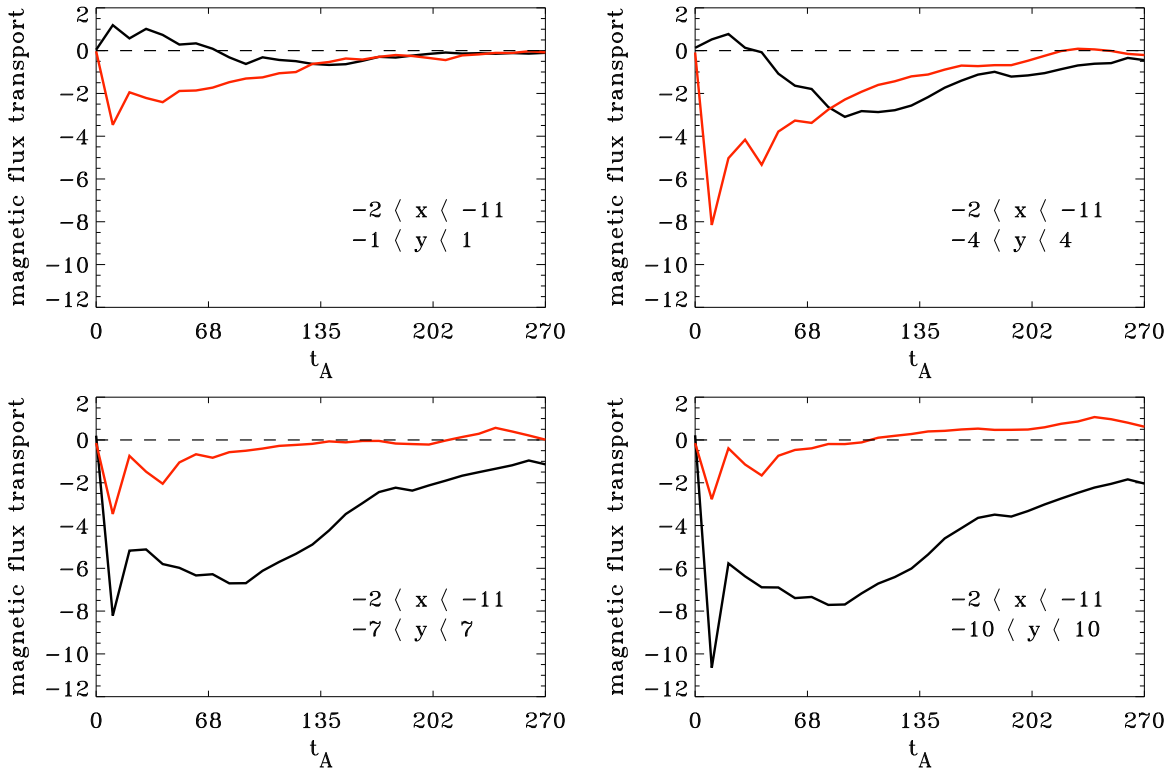

Figure 3.10. The magnetic flux transport $\frac{d\Phi}{dt}$ at different sections of the equatorial plane. The red (black) line represents the y (x) component of the transportation of magnetic flux.

These results indicate that the removal of near-Earth magnetic flux results in a major reconfiguration of the near-Earth magnetotail and the drastic thinning of the crosstail CS. This suggests that the rate of magnetic flux extraction from the near-Earth reservoir is related to the duration of the growth phase. However, a quasi-static evolution represents a sequence of magnetotail equilibria which is determined only by the total or integral change introduced by the boundary condition as long as the evolutions is slow. In other words, the current density profile should only depend on the total amount of magnetic flux and not on the specific flux transport rate.

This magnetic flux transport rate out of the simulation domain can be determined by the integral $\int E_y dl$ along the y axis at the sunward boundary of the system (similar to the expression in equation (3.8)). The total flux transport rate corresponds approximately to the polar cap potential and the following text will address the total flux transport rate as a potential (note that this is strictly not corrected because a potential implies $\nabla \times \vec{E} = 0$ which is inconsistent with $\frac{\partial \vec{B}}{\partial t} \neq 0$). This is carefully examined in Figure 3.11. The top panel of Figure 3.11 shows the variation of potential at the Earthward boundary during the MFD process. The three lines present the cases of different outflow magnitude $v_0 = 0.08$ (black), $v_0 = 0.11$ (blue), and $v_0 = 0.14$ (red). Obviously the lowest outflow magnitude (black) corresponds to the smallest potential at the Earthward boundary. Note, the potential is decreasing with time because the magnetic field B_z decreases strongly. Note that this reduction occurs even though the outflow velocity is moderately raised during the simulation to compensate for the decreasing B_z. The

middle panel shows that the MFD run with the lowest outflow potential reaches a certain magnitude of current density later than the faster outflow case. Here we define a term "$\Phi_{\rm d}$" (the depletion of magnetic flux) which is represented as the integration of potential presented in the last panel. Since the magnetic flux in a certain closed surface is represented as

$$\Phi_{\rm d} = \int \vec{B} \cdot d\vec{A} \tag{3.9}$$

which can be derived into

$$\frac{d\Phi_{\rm d}}{dt} = \int \frac{\partial \vec{B}}{\partial t} \cdot d\vec{A} = \int -(\nabla \times \vec{E}) \cdot d\vec{A} = -\oint \vec{E} \cdot d\vec{l} = \phi_{\rm t}. \tag{3.10}$$

This integral has contributions only from the sunward boundary because the normal velocity is 0 at all other boundaries. Therefore, the total amount of the removal of magnetic flux can be expressed as

$$\Phi_{\rm d} = \int_0^t \phi_{\rm t} dt, \tag{3.11}$$

which is equivalent to the integration of the potential at the Earthward boundary.

We can now represent the maximum current density as a function of $\Phi_{\rm d}$ for each MFD run. The result is presented in the bottom panel of Figure 3.11. This figure demonstrates that the current density gradually increases with increasing magnitude of MFD. The current density increases sharply after the $\Phi_{\rm d}$ reaches a critical value around 100. Here $\Phi_{\rm d}$ is normalized by about 7.9×10^5 wb. The three lines with different v_0 of the outflow condition almost overlap with each other before the critical value and are very similar even at larger values for large nonlinear changes. This demonstrates that the current density depends only on the amount of magnetic flux removed even if the temporal evolution is different in the considered cases. This result is remarkable because (1) it is obtained for a highly nonlinear and three-dimensional evolution, (2) numerical dissipation can have a considerable influence over a long simulation run, and (3) numerical inaccuracies (for instance grid oscillations) make a reliable determination of the maximum current density increasingly difficult.

This result also confirms the hypothesis of a quasi-static evolution of the magnetotail during the slowly evolving growth phase. We note that the current density linearly increases with the slight different slopes above the critical value of $\Phi_{\rm d}$. As the MFD increases, the magnetic field is strongly depleted such that the current density can be slightly oscillated due to the grid resolutions. This result also bears the question of the maximum current density possible for the considered process. Simulation runs with lower resolution show a lower maximum, indicating that the the maximum current density is determined only by the available numerical resolution. There is however also another physical limitation of the plasma description by the MHD equations. As shown in Figure 3.6, the half-width of the thinning CSs in the simulation is close to 600 km (for the embedded CS). This is close to the ion inertial scale and the ion gyro radius scale in these CSs. Therefore, the limitations presented by the MHD equations become critical in considering much higher numerical resolution.

It is interesting to examine if the CS formation and the quasi-static evolution depends much on the location of the outflow. Instead of the magnitude of the outflow velocity, Figure 3.12 shows two cases

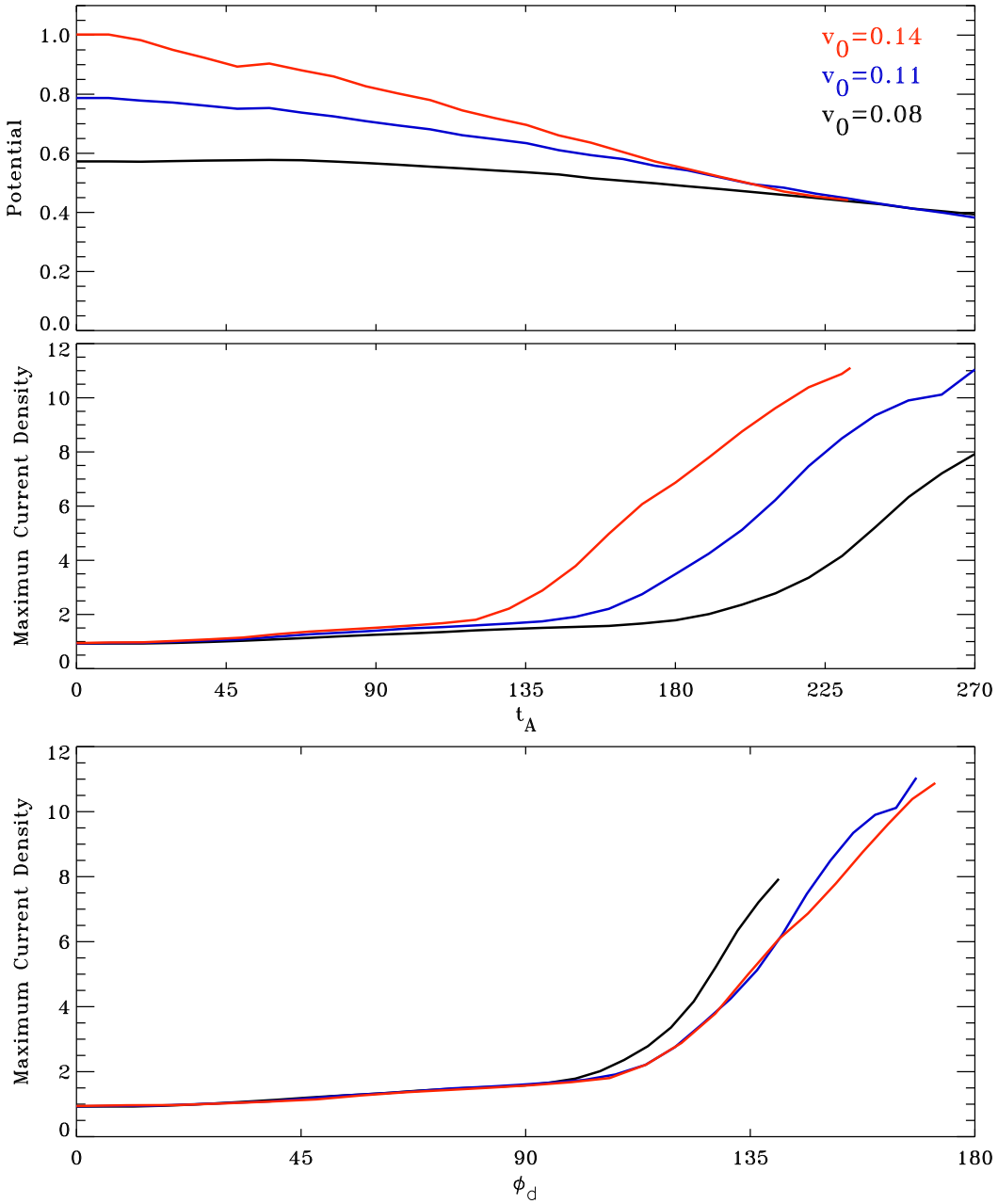

Figure 3.11. The MFD runs with three magnitudes v_0 of the outflows. The v_0 are chosen as (black) 0.08, (blue) 0.11, and (red) 0.14. The top (middle) panel shows the variations of potential (maximum current density) during the midnight MFD process. The last panel shows the correlation between the maximum current density and Φ_d.

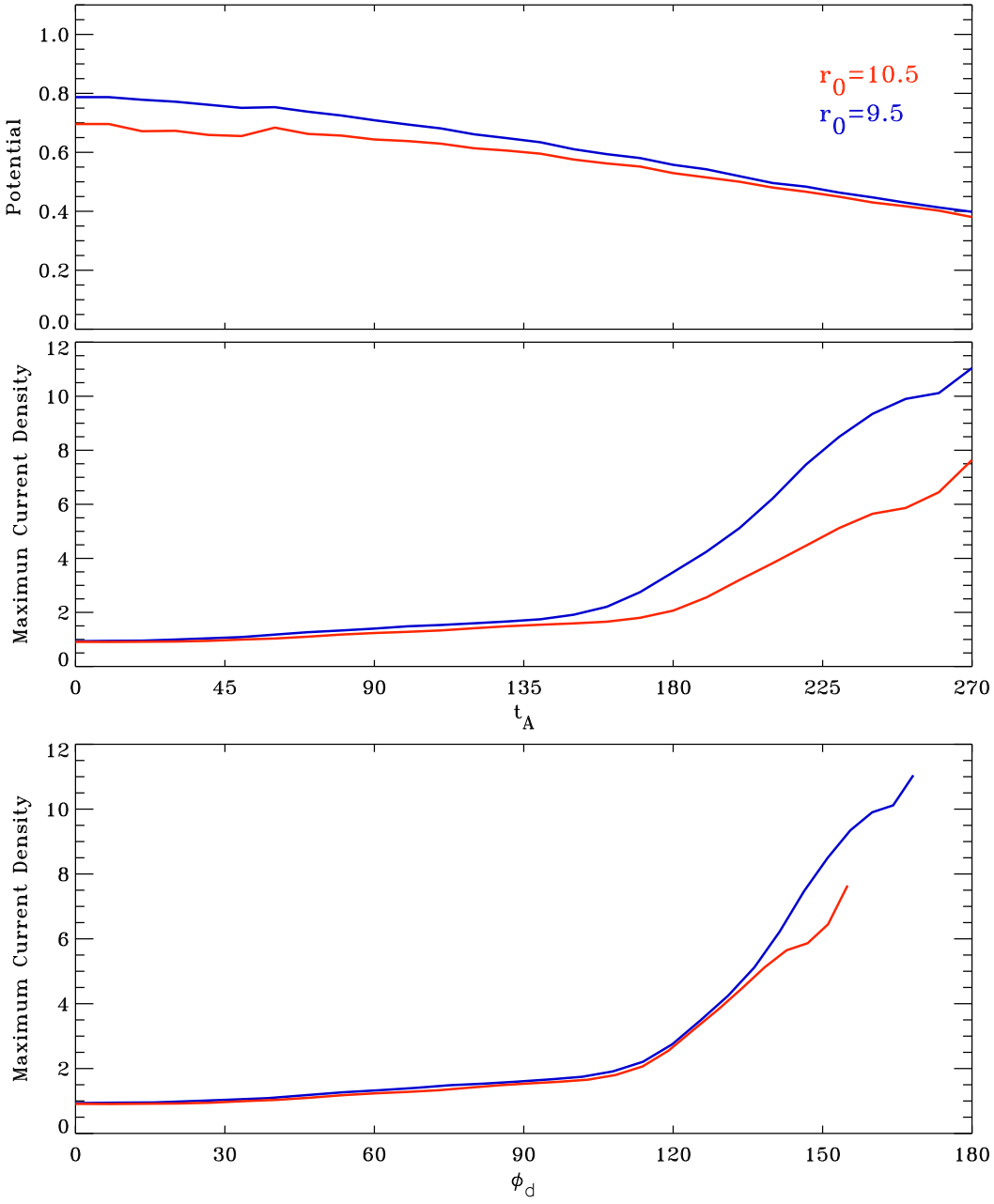

Figure 3.12. The format is the same as Figure 3.11, except for the MFD runs perturbed at the radial distances (blue) $r_0 = 9.5$ and (red) $r_0 = 10.5$. Here the outflow magnitude v_0 is set to 0.11.

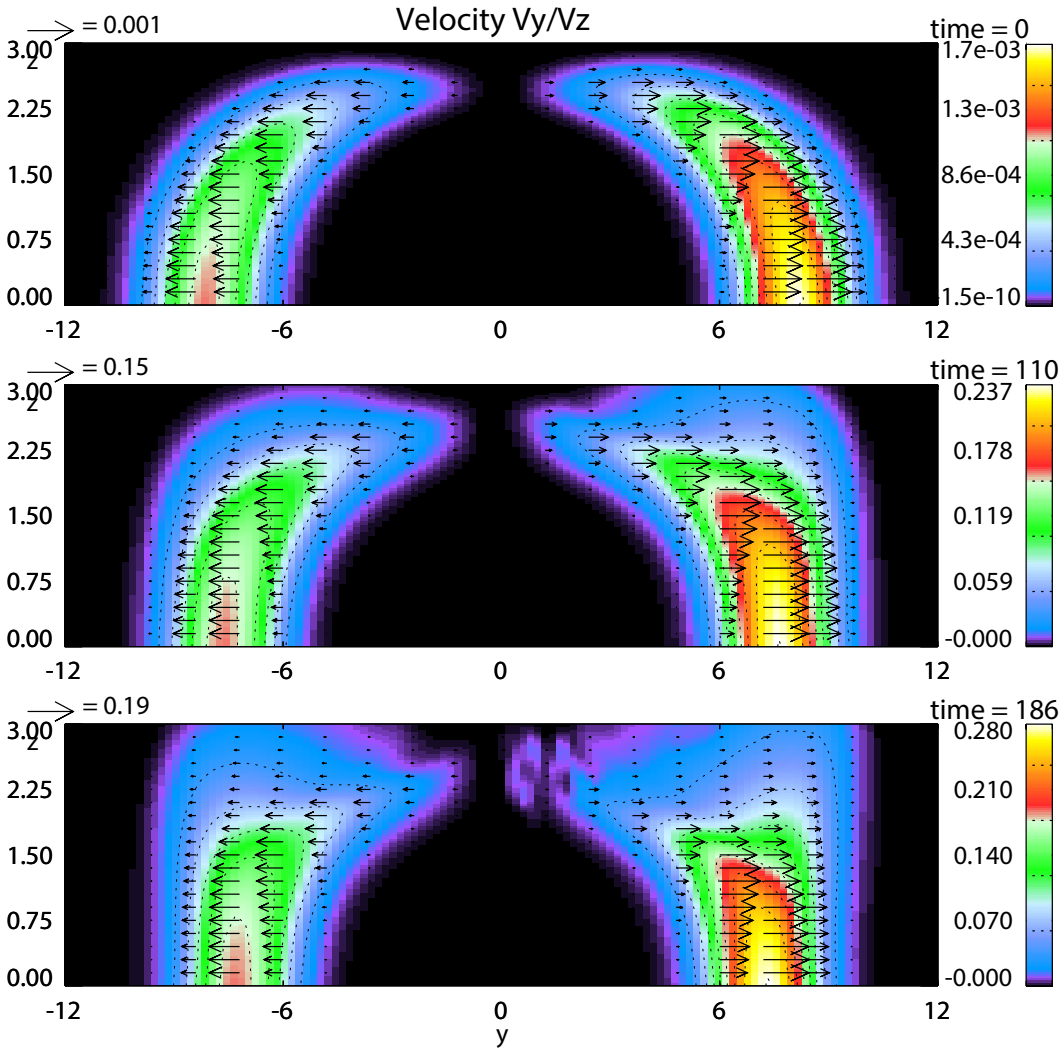

Figure 3.13. The format is the same as Figure 3.1, except for the asymmetric MFD run.

with the outflow applied at the different radial distances $r_0 = 9.5\,R_E$ (blue) and $r_0 = 10.5\,R_E$ (red)(see equations (2.22) and (2.23)). The magnitude of the velocity v_0 is fixed at 0.11 in both cases. It is shown that the case $r_0 = 9.5$ corresponds to a larger potential at the Earthward boundary. The current density increases faster as the stronger dipole field is depleted in the case $r_0 = 9.5$. The dependence of the maximum current density on the amount of depleted flux is shown in the last panel. Again, the two cases agree well with each other except for current densities larger than $6\,j_0$ close to the end of the growth phase. The total amount of MFD in the case $r_0 = 9.5$ is larger than that in the case $r_0 = 10.5$, indicating a stronger depletion of the near-Earth magnetic field which might explain the higher current density. Note that this result is remarkable also because the magnetic flux is removed not in the same location such that the respective equilibrium sequence should be slightly different. However, as our result demonstrates, the dependence of the maximum current density on the amount of removed flux is almost identical.

3.3 Asymmetric Sunward Convection

Observations indicate that current distribution and magnetospheric convection often show a dawn-dusk asymmetry. *Baumjohann et al.* [1990] presented a statistical study of magnetotail flows and found that the distribution of azimuthal sunward flow shows a dawn-dusk asymmetry in the central plasma sheet. Although such a dawn-dusk asymmetry could be due to the number of the sample data, the asymmetry of dawn-dusk crosstail current density was also observed. *Nakai et al.* [1997] found that the neutral sheet current maximizes in the region $-3\,R_E < y < 6\,R_E$, implying the associated tail properties might have a clear dawn-dusk asymmetry. In the inner magnetosphere the magnetic field rotates with the Earth leading to an asymmetric magnetic flux transport. Also, gradient and curvature drifts in the dipolar magnetic field region provide preference to ion convection opposite to the rotation of Earth. This scenario is supported by flow observations in the near-Earth magnetotail. Finally, the frozen-in condition strictly applies to electrons. The last effect becomes important for thin CSs where the dominant current carriers are electron (opposite to wide CSs where the current is mostly due to the diamagnetic drift of the ions).

Although the detailed physical cause for asymmetric convection is mostly a non-MHD effect, we can explore the results of such convection by appropriate asymmetric boundary conditions. This section presents the influence of asymmetric sunward convection on the crosstail current density. A larger magnitude of the sunward flow (by $\sim 50\%$) is employed for the duskside magnetotail boundary. Figure 3.13 displays a clear dawn-dusk asymmetry of the sunward velocity at the Earthward boundary. The simulation results also show a pronounced dawn-dusk asymmetry in the depletion of magnetic flux at the Earthward boundary and the equatorial plane as presented in Figure 3.14 and Figure 3.15. Note that the divergence of the azimuthal flow is not altered. However, the larger velocity at the dusk boundary results in the stronger transport of magnetic flux (small B_z) toward the duskside. Runs with such an asymmetric convection assumes large current densities earlier and terminate earlier because the region of small B_z values concentrate more on one side of the magnetotail and are more rapidly convected into the sunward boundary.

Figure 3.16 illustrates the distribution of azimuthal current density in the equatorial plane. The azimuthal current density shows a clear dawn-dusk asymmetry in the near-Earth tail, with a much larger current density on the dusk side particularly in the late simulation. The strong azimuthal current spans in the region around $-4 < y < 6$. The dawn-dusk asymmetry becomes dominant toward the end of the simulation when the strong asymmetric depletion of magnetic flux in the equatorial plane leads to a concentration of very small B_z values in a smaller region than obtained from the symmetric runs.

Figure 3.17 shows the crosstail current density along the dawn-dusk direction at the radial location close to the Earth (left panel) and a little further tailward (right panel). Initially the current density shows a local maximum in the midnight meridian plane, which is the result of the Tsyganenko field. However, a local minimum of current density near the midnight meridian plane develops once the thin CS starts to form as a result of sufficient magnetic flux removal by the sunward convection. Such local

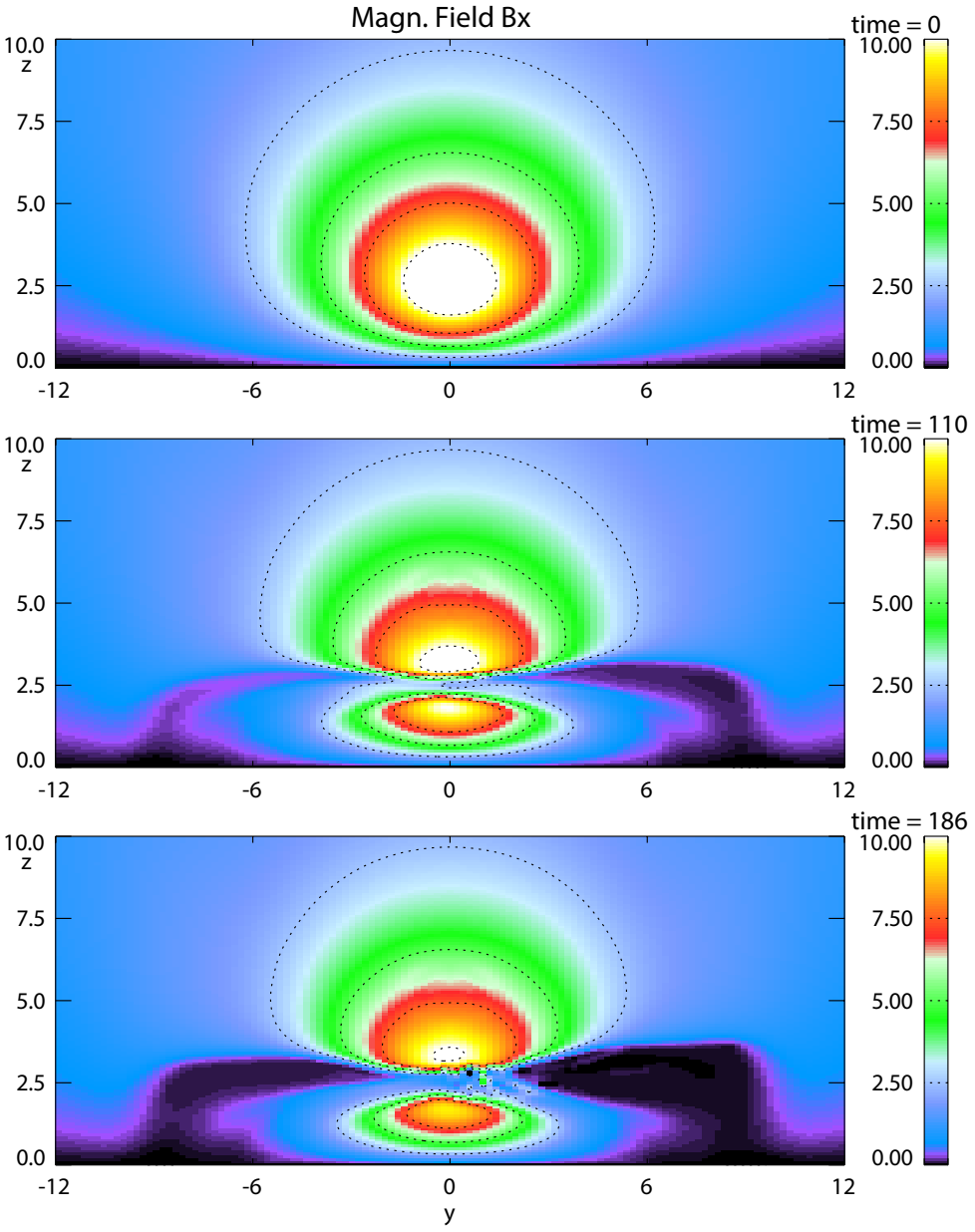

Figure 3.14. The format is the same as Figure 3.2, except for the asymmetric MFD run.

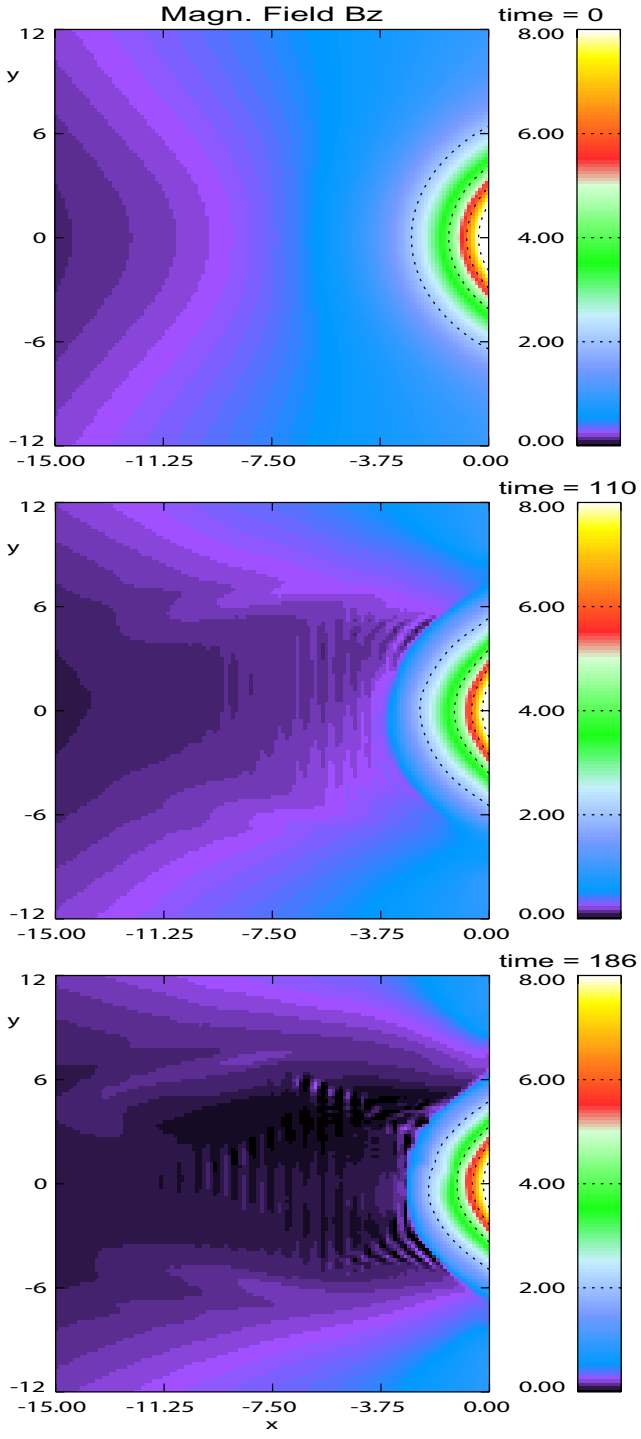

Figure 3.15. The format is the same as Figure 3.7, except for the asymmetric MFD run.

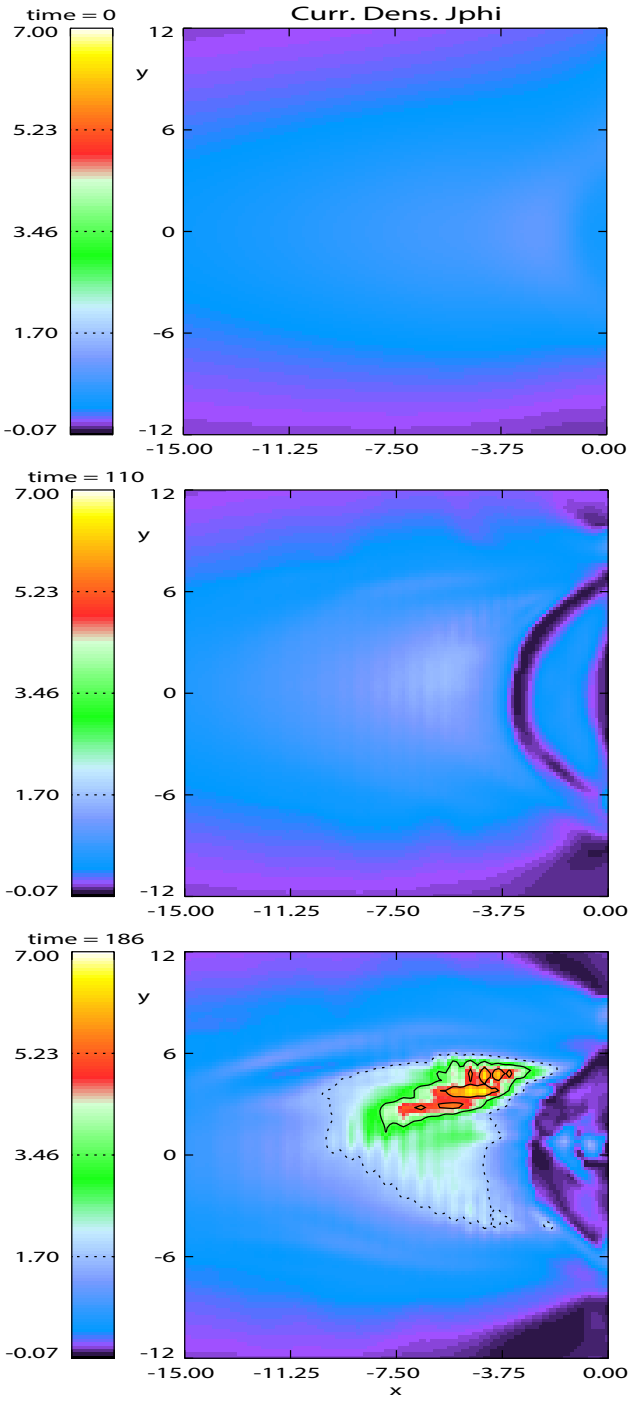

Figure 3.16. The format is the same as Figure 3.9, except for the asymmetric MFD run.

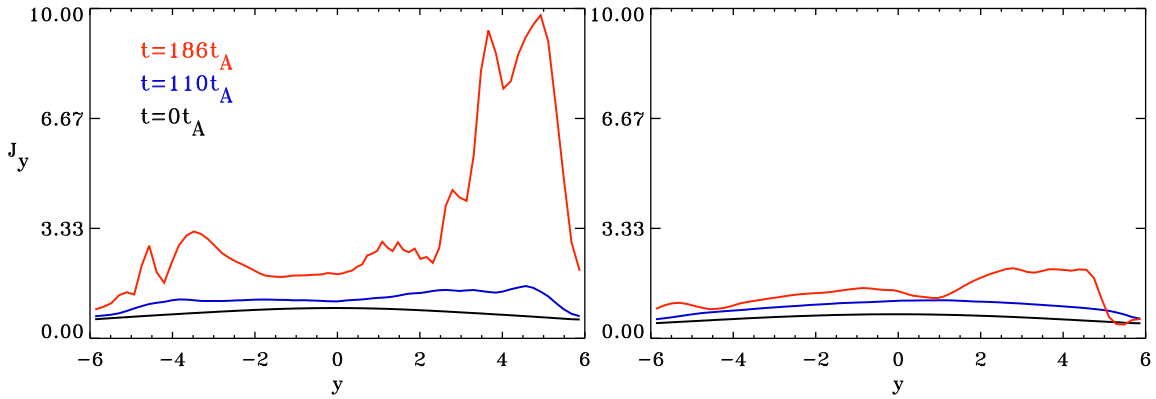

Figure 3.17. Current density at the radial distance (left) $x = -10\,R_E$ and (right) $x = -14\,R_E$ in the equatorial plane. Three different times (black) $t = 0t_A$, (blue) $t = 110t_A$, and (red) $t = 186t_A$ are shown here.

minimum of the current density near the midnight meridian plane was also presented by *Nakai et al.* [1997]. Figure 3.17 also illustrates that the strong crosstail current density distributes wider on the duskside. The strong asymmetry is more pronounced in the near-Earth region particularly in the late growth phase. The largest current density is located around $y = 4$ to 5 where one can expect the strongest thinning of the CS.

3.4 Discussion and Summary

This study investigates the evolution of the magnetotail for conditions that lead to a strong depletion of the near-Earth closed magnetic flux, which we termed midnight magnetic flux depletion (MFD). This midnight MFD in the near-Earth tail is caused by sunward convection to replenish magnetic flux that is eroded on the dayside magnetopause during periods of southward IMF. This convection is subject to adiabatic constraints which apply during the slowly evolving growth phase, that is, the depletion of magnetic flux in the tail is confined to the region of flux tube entropy which matches the entropy of recently reconnected flux tubes on the dayside. Midnight MFD leads to a strong reduction of B_z in a flux reservoir located in the near-Earth equatorial plane and results in strong CS thinning as well as a significant increase of the cross-tail and the azimuthal current densities in the center of the plasma sheet.

In the quasi-static evolution, the increase of current density depends only on the total amount of the depleted magnetic flux. The presented result shows that the current density increases almost linearly with the increase of total amount of the removed magnetic flux. This suggests that the duration of the growth phase depends on the average total removal rate of magnetic flux in the flux reservoir. Here the growth phase is regarded ending when the magnetic flux is almost depleted down to 1 nT (in the late of the simulations), i.e., $t \propto 1/\phi_{\rm t}$, where $\phi_{\rm t}$ (potential) is determined by the sunward flux transport rate. In steady state the sunward potential is approximately equal to the cross-polar cap potential ($\phi_{\rm pc}$), which implies $\frac{d\Phi_{\rm d}}{dt} = \phi_{\rm pc}$. That is, the duration of the growth phase is approximately

inversely-proportional to the cross-polar cap potential which is affected by the dayside reconnection rate. The simulation results of midnight MFD show that a very thin CS is formed within half an hour to one hour, which agrees well with the typical duration of the substrom growth phase.

In this study the thickness of the thin CS is found to decrease to $0.4\,R_E$ ($\sim$ 2500 km) estimated base on the Harris sheet model for a single CS. In observations, *Petrukovich et al.* [2007] showed that the CS thinness estimated from the Harris sheet profile reaches to $2500 \sim 3000$ km preceding the local magnetic reconnection. *Asano et al.* [2003] presented that the CS thickness is down to 3000 km before the onset of the expansion phase by employing the Ampére's law. Although the Harris sheet profile is restricted to the assumption of the Maxwell distribution of particles, it can still provide an overview of the evolution of CS thinning during the growth phase. Note, the strong embedded CS shown in the late growth phase (bottom panel of Figure 3.3) implies that the embedded CS can be much thinner. Figure 3.6 demonstrates that the half thickness of the embedded CS is about 600 km which is very close to the ion inertial length. This embedded thin CS thickness is comparable to the CS thickness that is estimated base on a modificated Harris Sheet model, with a considering of meandering ions in the very thin CS [*Zhou et al.*, 2009].

The presented results demonstrate that the strong thin CS is highly concentrated near the equatorial plane (center of the crosstail CS) and located between $x = -9\,R_E$ and $-15\,R_E$ in the simulation, suggesting that a current instability leads to the magnetic reconnection onset in the near-Earth tail. Satellite observations also presented examples of tailward plasma flows associated with the local near-Earth magnetic reconnection [*Sergeev et al.*, 1995; *Petrukovich and Yahnin*, 2006]. Note that this thin CS located at the radial region agrees well with many growth phase investigations, e.g., *Mitchell et al.* [1990], *Sergeev et al.* [1990], *Baker et al.* [1993], *Pulkkinen et al.* [1994], and *Asano et al.* [2003]. Midnight MFD in the simulation runs show a strong concentration of the current density for a large region of $\pm 6\,R_E$ or ± 3 hours from midnight that matches the region with a strong reduction of the closed magnetic flux. These results suggest that magnetic reconnection may occur not only close to the midnight meridian plane but also in the pre- and post midnight regions. The highest current density is off the midnight meridian plane in the late growth phase, where one can expect also the strongest thinning of the CS. This study also demonstrates that a strong asymmetric CS can be caused by the asymmetric depletion of the near-Earth closed magnetic flux.

Note that the presented results do not include a lobe driver (addition of magnetic flux to the tail lobes) which may also be important for the magnetotail evolution during the growth phase. In the presented simulation runs the lobe magnetic field in the near-Earth region is reduced by about 30% at the end of these simulations. The objective of this approach is to investigate the effects of magnetic flux depletion only, and including a lobe driver would have made it difficult or impossible to attribute configurational changes of the magnetotail to MFD or to the addition of lobe magnetic flux. The combined effects of the depletion and loading of magnetic flux will be investigated in Chapter 4. Also, the depletion of near-Earth magnetic flux can be expected to cause a concentration of magnetic field

line footpoints in the ionosphere. A more systematic examination of the ionospheric morphology that results from the MFD is presented in Chapter 5.

In summary, the midnight MFD is a highly efficient mechanism to generate a very thin CS near the equatorial plane. This MFD mechanism is strongly related to the southward IMF condition. The main effect of different potentials applied at the sunward boundary is a change of the temporal evolution of the magnetotail but the results are basically identical.

The influences of the midnight MFD on the magnetotail include:

- a strong thin CS formation in the near-Earth region ($x < -15\,R_E$);
- a strong depletion of the closed magnetic flux (B_z reduction) in the near-Earth region;
- a strong enhancement of the crosstail current and azimuthal current densities near the equatorial plane;
- the duration of the growth phase is proportional to $1/\phi_{\rm t}$.

Chapter 4

Thin Current Sheet Formation in Response to the Loading and the Depletion of Magnetic Flux during the Substorm Growth Phase

4.1 Introduction

The physics of the substorm onset and of the substorm growth phase is still not well understood. In particular, the growth phase thin CS formation is of major importance to understand the mechanism that leads to the expansion phase onset. In the previous chapter we have demonstrated that sunward convection can efficiently generate a very thin CS confined to the near-Earth magnetotail. The replenishment of closed magnetic flux toward dayside causes the strong crosstail and azimuthal current densities near the equatorial plane. In order to uniquely identify the influence of sunward convection on the CS thinning, an additional influence of a compression of the magnetotail lobes was not considered, however, this assumption is usually not satisfied during the substorm growth phase. This compression is addressed as a lobe driver in this chapter and it is caused by the transport of open magnetic flux from dayside reconnection to the magnetotail lobes. Such a lobe driver can be either characterized by a suitable convection profile at the lobe boundary or by a corresponding electric field. The latter has the advantage that an electric field directly measures the magnetic flux transport and can be used to infer the velocity perpendicular to the local magnetic field.

The lobe compression is supported by a slow increase of the lobe magnetic field during the growth phase [*Caan et al.*, 1975; *Wang et al.*, 2004; *Petrukovich et al.*, 2007]. However, *Snekvik et al.* [2012] found a considerable number of substorms where the lobe magnetic field does not increase in the near-Earth region. Note that the absence of a lobe field increase should not be considered an argument against the open magnetic flux transport from the day- to the night-side. The results in Chapter 4 demonstrate that the lobe field decreases significantly if only the transport of closed magnetic flux back to the dayside is considered. This implies that the open flux transport to the tail lobes is required to maintain the lobe field strength in the near-Earth tail. This also implies that the growth phase magnetotail properties should include both the loading of magnetic flux into the tail lobes and the depletion of the near-Earth magnetic flux.

Adiabatic lobe compression has been implemented to result in thin CSs formation starting with the quasi-static magnetotail [*Wiegelmann and Schindler*, 1995; *Ma et al.*, 1995; *Birn et al.*, 1998]. The addition of magnetic flux to the lobe through the presence of an electric field (E_y) has been found to locally redistribute the current and generate a localized thin CS. However, there is no specific model for the electric field profile because this profile depends on varying solar wind and magnetosphere properties in addition to the dayside reconnection rate. The driving electric field is often assumed as a profile that peaks in the near-Earth region and decreases with increasing radial distance, which is suitable if the solar wind conditions are approximately constant. However, this electric field is not only determined by the dayside reconnection rate but also by the total static pressure in the solar wind. An electric field which peaks in the near-Earth region is expected to favor a near-Earth location of thin CS formation

in the tail, associating with a stronger external driver [*Wiegelmann and Schindler*, 1995; *Ma et al.*, 1995]. This chapter examines CS formation under the influence of adiabatic lobe compression during the growth phase contrasted and in combination with the closed magnetic flux circulation considered in Chapter 3. For this purpose we assume an electric field that is uniformly distributed along the magnetotail lobe. This choice provides no bias to any particular location for CS formation and can be compared to results in the literature.

A thin CS formation is often found in the near-Earth tail [*Mitchell et al.*, 1990; *Sergeev et al.*, 1990; *Baker et al.*, 1993; *Pulkkinen et al.*, 1994]. However, such a near-Earth thin CS is difficult to explain sunward busty bulk flows (BBF's) tailward of the near-Earth region, implying an occurrence of multiple reconnection sites during the growth phase or in the early expansion phase. This chapter demonstrates that lobe compression favors the formation of a thin CS confined in the mid-tail region for a uniform electric field applied at the lobe boundary. In response to lobe compression in combination with sunward convection, a double-current sheet forms in the mid-tail region and in the near-Earth region. A gradient of electric field profile is also employed to examine the influence on a thin CS location.

4.2 The Influence of Lobe Compression on CS Formation

As a first step, we present the influence of adiabatic lobe compression only on the CS evolution. That is, the depletion of near-Earth magnetic flux is not considered here. A driving electric field is applied at the top boundary of the simulation box ($z = 12$), serving as the open magnetic flux loaded into the lobes during periods of the southward IMF. The uniform electric field is switched on starting from the magnetotail equilibrium generated by the relaxation method. By ignoring the tangential velocity v_x, the equatorward inflow v_z is determined by $-e_y/b_x$ in the lobe region. The electric field strength is normalized by $v_A b_0 \sim 8.6 \times 10^{-3}$ V/m. The results employ a three-dimensional mesoscale MHD simulation. The descriptions of model and boundary conditions have been presented in Chapter 2.

The primary effect of a lobe compression on the crosstail CS density is shown in Figure 4.1. Here the electric field strength is 0.015 which is applied to the entire lobe boundary yielding a potential (or flux transport rate) of about 25 kV. Three panels in the midnight meridian at times $t = 0t_A$, $t = 100t_A$, and $t = 202t_A$ are displayed. Note that our sunward boundary is at $x = -5\,R_E$ that corresponds to the simulation coordinate $x = 0$. Figure 1 shows that the CS density appears a clear enhancement, particularly in the region from $x = -17$ to -35 at time $t = 100t_A$. A strong and thin CS is embedded at the location around $x = -22$ to -29 at the later time ($t = 202t_A \sim 49$ minutes). This demonstrates an increase of mid-tail CS density associated with the loading of lobe magnetic flux. In comparison, the near-Earth bifurcated CS structure is not associated with any strong enhancement of the current density. The result indicates that thin CSs favor formation in a region where the magnetotail is sufficiently stretched when the lobe is driven by a uniform electric field. This result also demonstrates that lobe compression is insufficient to generate a thin CS close to Earth where the magnetic field is more dipolar. Note, the time evolution of a thin CS formation is strongly associated with the amount

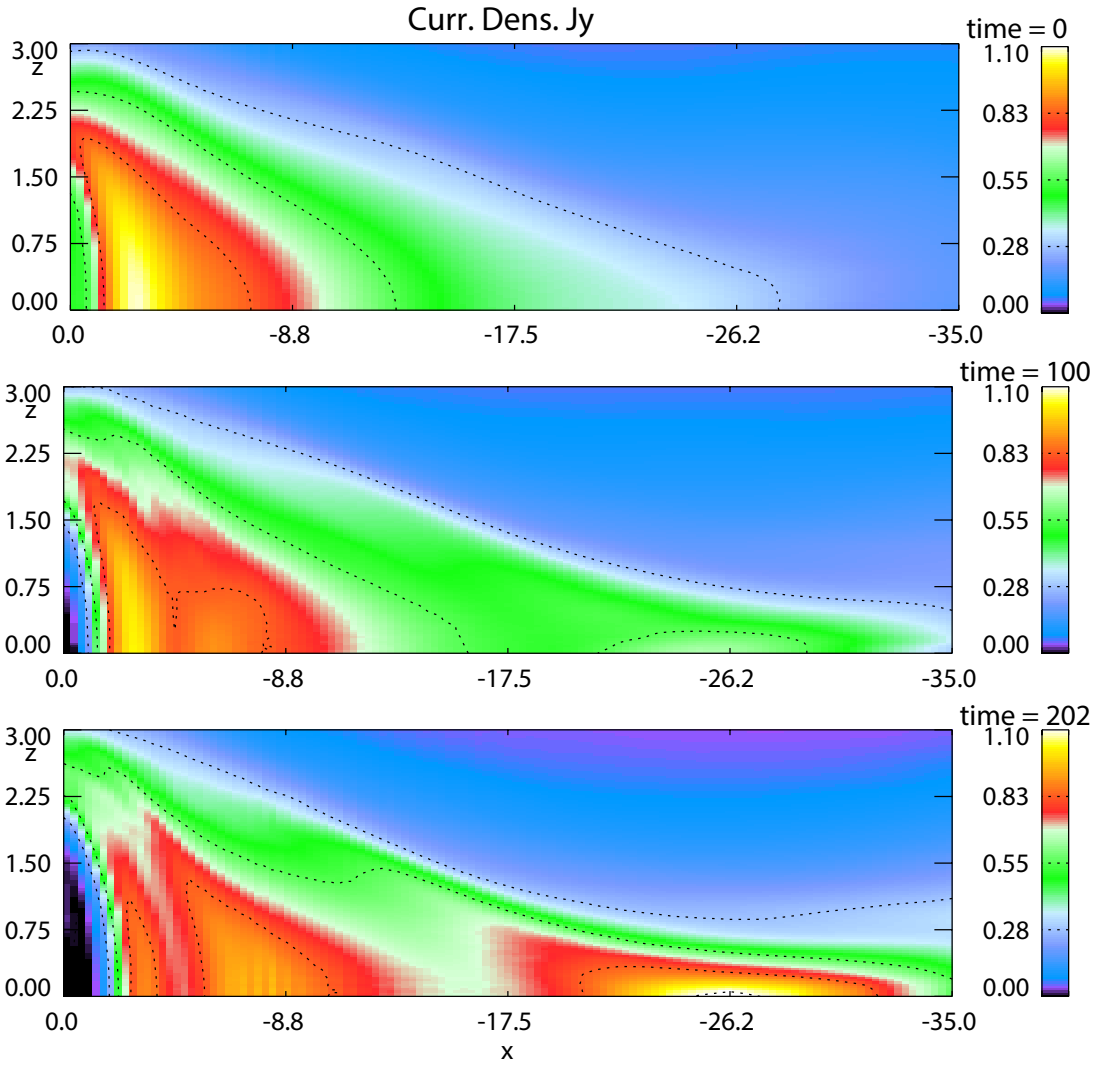

Figure 4.1. The influence of lobe compression on the crosstail current density in the midnight meridian plane at times (top) $t = 0t_A$, (middle) $t = 100t_A$, and (bottom) $t = 202t_A$.

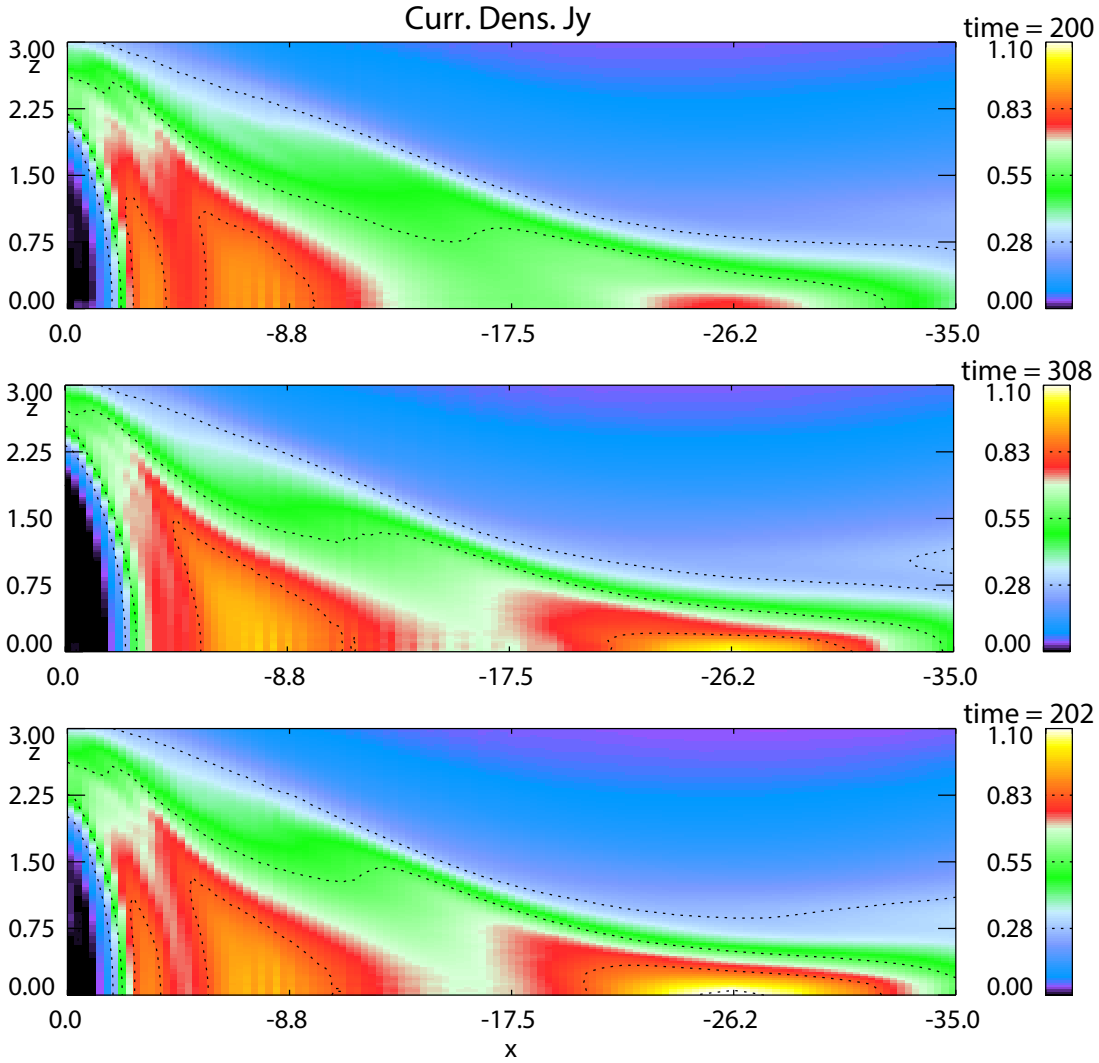

Figure 4.2. The format of each panel is the same as Figure 4.1. The top two panels show the slower lobe driver case, whereas the bottom panel shows the stronger lobe driver case.

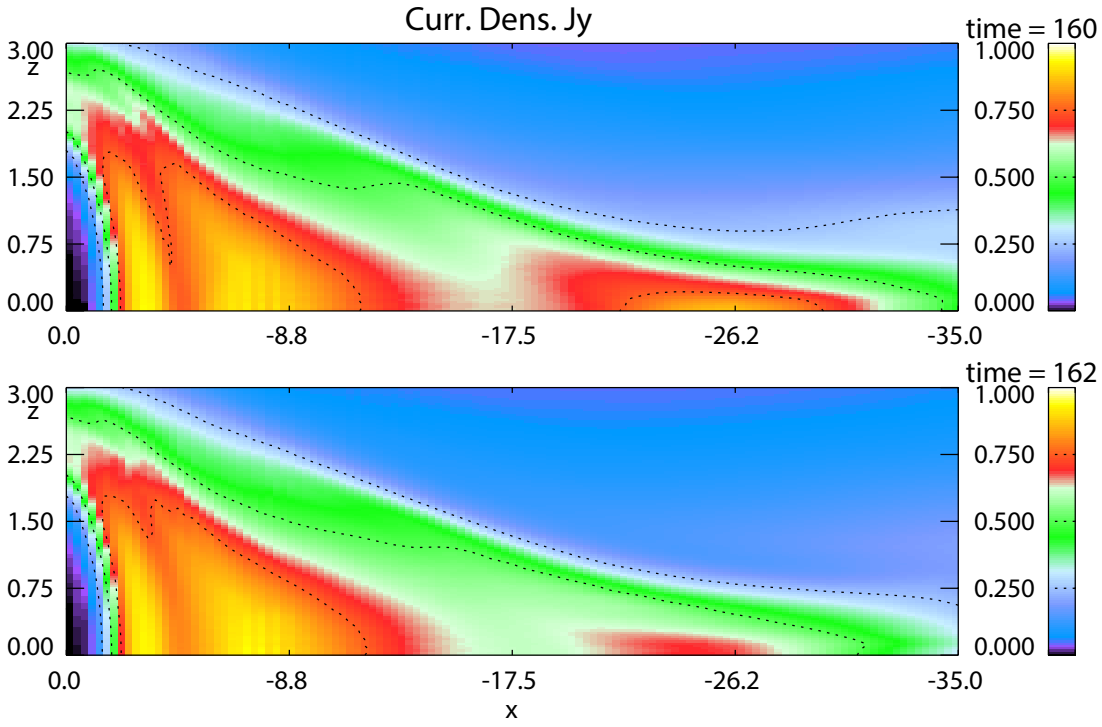

Figure 4.3. The format of each panel is the same as Figure 4.1. The top panel shows the case for a constant electric field, whereas the bottom panel shows the case for a gradient electric field.

of the added lobe magnetic flux. The top two panels of Figure 4.2 show results for which the electric field is reduced by about 30%. Comparing with the stronger lobe driver case, the near-Earth bifurcated CS forms at about the same time but the mid-tail thin CS appears at a later time (~ 74 minutes). By applying a constant electric field, Figures 4.1 and 4.2 demonstrate that a strong thin CS favors the generation in the mid-tail with a tailward edge at about $x = -28$.

The influence of the gradient of electric field on the CS formation is shown in Figure 4.3. Here the lobe electric field is applied by a function of the radial distance x as

$$e_y = 0.015 \times \{1 - \tanh(|x|/62)\}. \tag{4.1}$$

In comparison, the value of 0.015 is the strength of the constant electric field used in Figure 4.1. This function implements an electric field that peaks close to the Earthward boundary and gradually decreases with the radial distance (this electric field is maximum in the near-Earth region and is reduced by 60% close to the tailward boundary). The top (bottom) panel in Figure 4.3 shows the CS configuration for a constant (gradient) electric field. This figure shows that the near-Earth CS does not have an apparent difference in response to the profile of the electric field. However, the mid-tail CS evolution is strongly subjected to the strength of the electric field. With a decreasing electric field in the mid-tail region, a slower rate of the enhancement of the current density is expected. Note that the thin CS also favors the formation in the mid-tail region but with the tailward edge a few R_E inward for a gradient electric field.

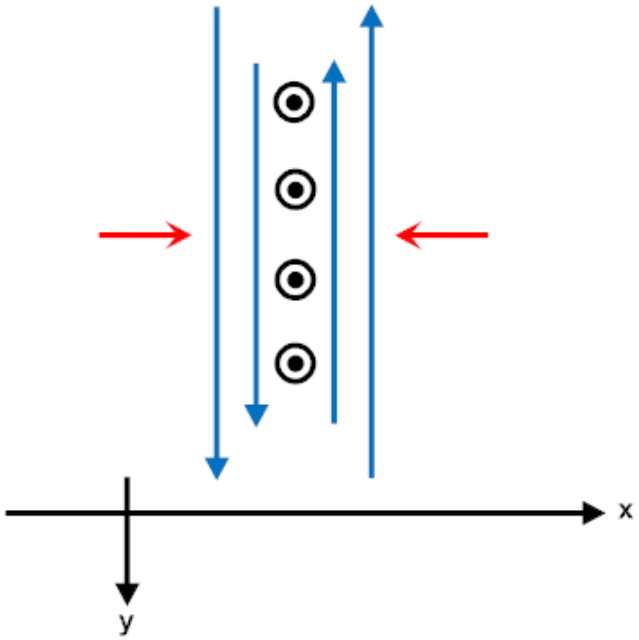

Figure 4.4. Sketch of one-dimensional Harris sheet compression. The blue lines represent magnetic field lines. The current density is out of the plane.

A frequent expectation is that thin CSs form by sufficiently compressing a pre-existing current layer. It is important to note that this expectation is simplistic and misleading. Therefore it is interesting to compare CS formation in a tail-like configuration with the simple case of compressing a one-dimensional Harris sheet. Figure 4.4 sketches the one-dimensional Harris sheet compression. The two red arrows represent the addition of magnetic flux at the boundaries. Figures 4.5 to 4.7 demonstrate the evolution of magnetotail properties in the one-dimensional (x) compression at times $t = 0$, $t = 200$, and $t = 400t_A$. The one-dimensional simulation uses different coordinates where y corresponds to x, z corresponds to y, and x corresponds to z in GSM coordinates. The MHD simulation is with 843 grids in the region between $x = -12$ to $12\,R_E$. Figure 4.5 shows the initial Harris sheet equilibrium with the magnetic field

$$b_y = b_0 \tanh(\frac{x}{l_0}). \tag{4.2}$$

By choosing $l_0 = 2.557$ (CS width) and $b_0 = 0.8$ (lobe magnetic field), the magnetic field profile yields an initial current density similar to the three-dimensional simulation. Note that $b_0 = 0.8$ (16 nT) is exactly the strength of lobe magnetic field at the radial location with the strongest enhancement of current density in the three-dimensional compression. The pressure p and the density ρ are determined by the forms

$$p = \frac{b_0^2}{2\mu_0}\mathrm{sech}^2(\frac{x}{l_0}) \quad \text{and} \tag{4.3}$$

$$\rho = \rho_0 + \mathrm{sech}^2(\frac{x}{l_0}), \tag{4.4}$$

with $\rho_0 = 1$. The velocity components v_y and v_z are set to zero in the one-dimensional simulation. The inflow v_x is determined by e_z/b_y at the boundaries. The electric field is kept at a constant value 0.015

(the same as e_y in the prior three-dimensional simulation) in the compression. Similar to the three-dimensional simulation, the electric field e_z at the boundaries represents the transport of magnetic flux into the system. A slow adiabatic compression is implemented through the inflow v_x at the boundaries. This velocity propagates as a low amplitude fast wave toward the center where it is reflected. An increase of lobe magnetic field that corresponds to the compression is shown in Figure 4.6 and 4.7. Note that the lobe magnetic field is strongly enhanced by about 50% (at time $t = 400t_A$), which is rarely shown in observations. Figures 4.5 to 4.7 demonstrate that the maximum current density j_z increases under the one-dimensional adiabatic compression.

Figure 4.8 presents the relation between the amount of magnetic flux transported into the simulation and the current density. The results for the one- and three-dimensional compression are represented by the blue and red lines, respectively. In three-dimensions we only consider the compression in the region where the strong thin CS is formed. In one and in two dimensions the electric field equals the magnetic flux transport per unit length along the invariant direction. In three-dimensions the total flux transport is the integral of the electric field along y. The three-dimensional flux transport has to be divided by the system size $2L_y$ in order to make these measurements comparable. The magnetic flux per unit length is denoted as Ψ. In one-dimension Ψ is represented as

$$\Psi = e_z \int dt, \tag{4.5}$$

and in three-dimensions Ψ is represented as

$$\Psi = \frac{1}{2L_y} \int_{-L_y}^{L_y} e_y dy dt = e_y \int dt, \tag{4.6}$$

with a uniform electric field e_z and e_y. Figure 4.8 shows that the current density increases approximately linearly with the added magnetic flux in both the one and the three-dimensional adiabatic compression. The result presents a steeper slope in the three-dimensional (red line) than in the one-dimensional (blue) compression. This demonstrates that the same amplification of the current density, for instance to a value of 1.2, requires only half magnetic flux increase in the three-dimensional simulation ($\Psi = 3.1$) than in the one-dimensional simulation ($\Psi = 6.2$). This result is not unexpected if one considers the freedom of the three-dimensional system. In one-dimension the magnetic field can change only subject to the compression while in three-dimensions magnetic flux can be transport also Earthward (tailward) or along the crosstail direction such that a locally depleted magnetic flux can also contribute to an increase of the current density. Therefore, the concept of a simple CS compression requires a huge and entirely unrealistic amount of magnetic flux added to the tail lobe in order to explain the observed thin CSs. This result also implies that a thin CS resulting from lobe compression would tend to be confined in a restricted radial region where the magnetopause flaring angle is not too small and the field is sufficiently stretched. In the distant tail the current sheet is almost one-dimensional and tail compression occurs only due to a total static pressure increase because of the balance between the tail magnetic field pressure and solar wind static total pressure. This case is similar to the one-dimensional compression for which we have demonstrated the problem to generate a thin CS.

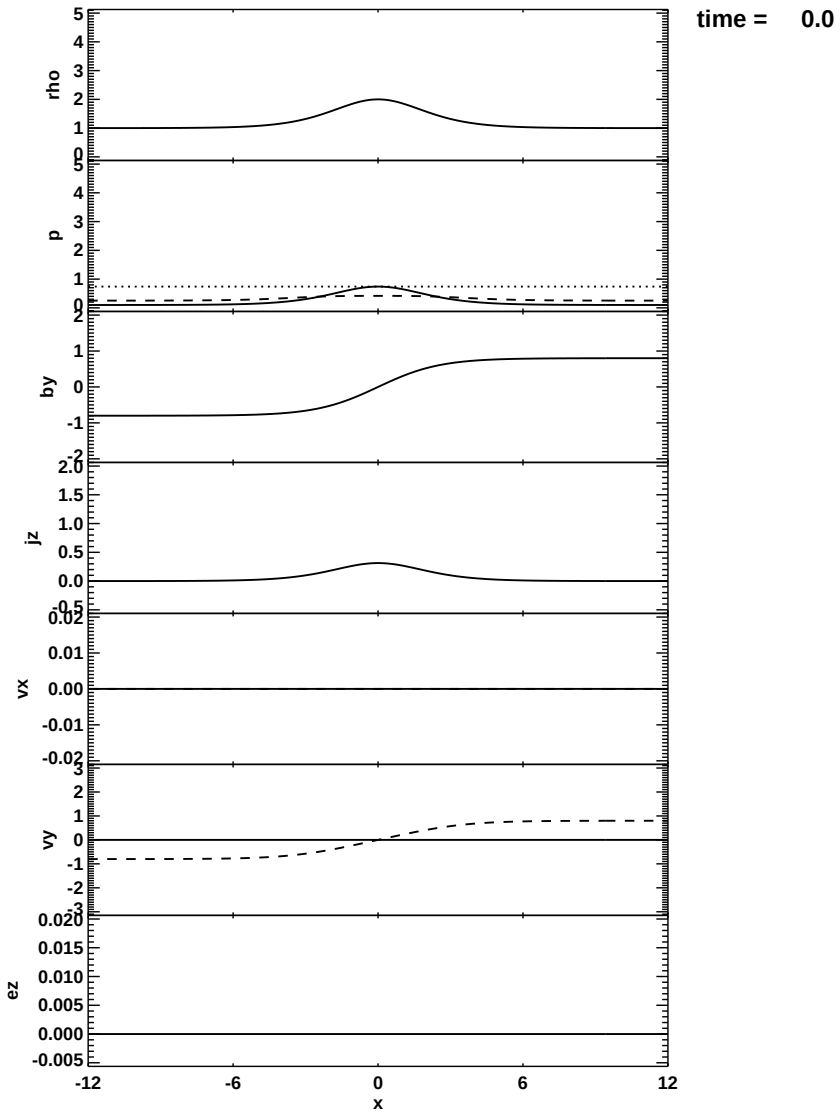

Figure 4.5. One-dimensional Harris sheet compression. From the top to bottom it shows the density, pressure, magnetic field, current density, velocity x component, velocity y component, and electric field. This figure shows the initial Harris sheet equilibrium.

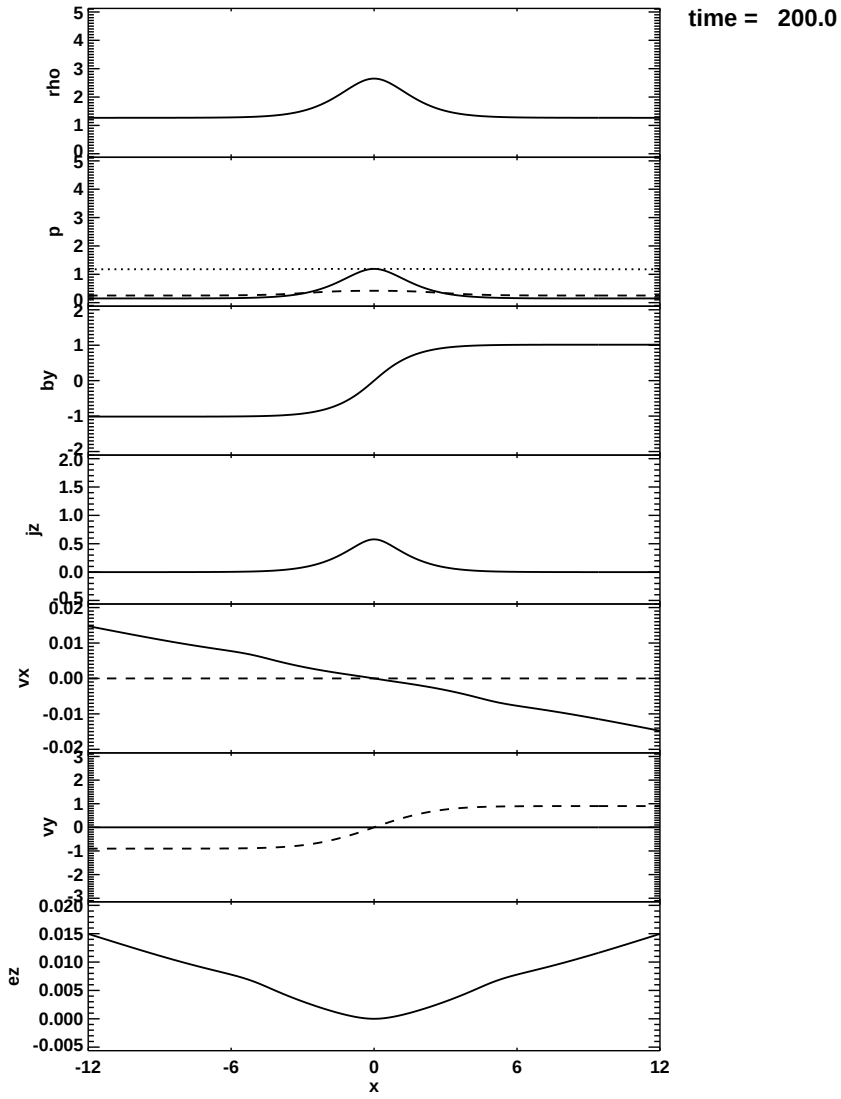

Figure 4.6. The format is the same as Figure 4.5, except for the time $t = 200t_A$.

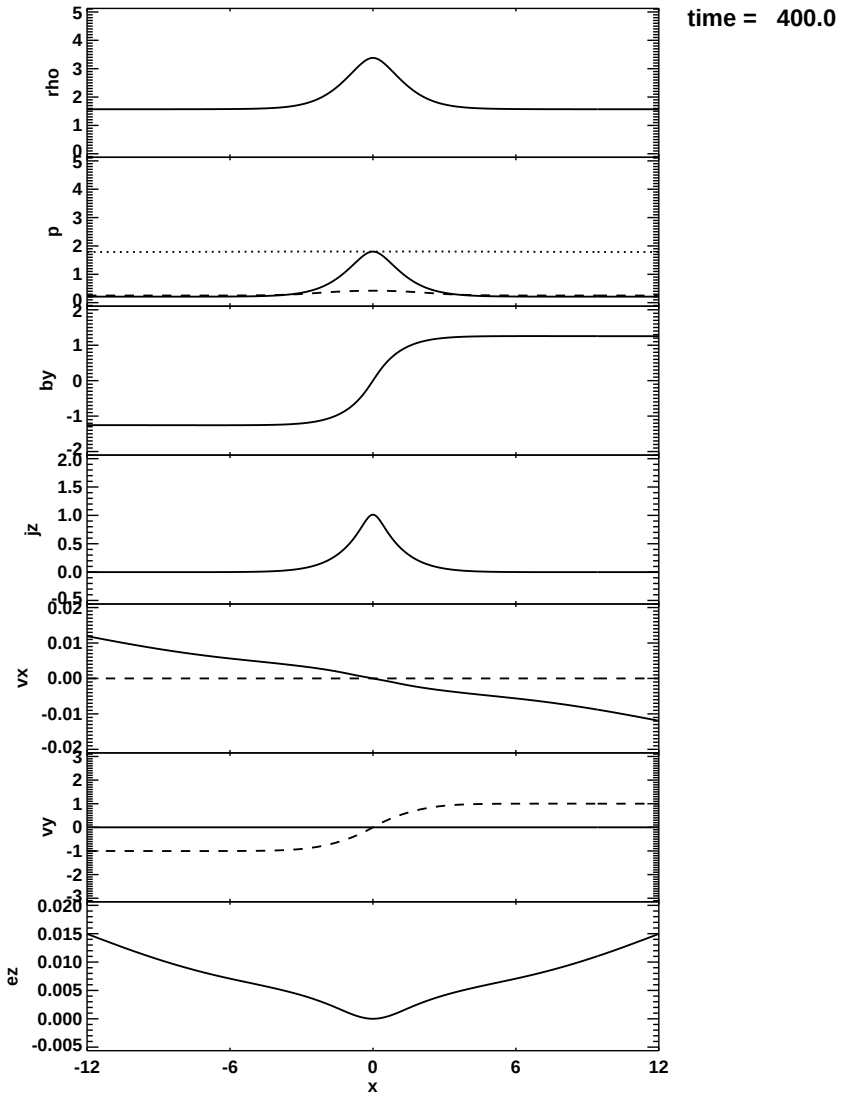

Figure 4.7. The format is the same as Figure 4.5, except for the time $t = 400t_A$.

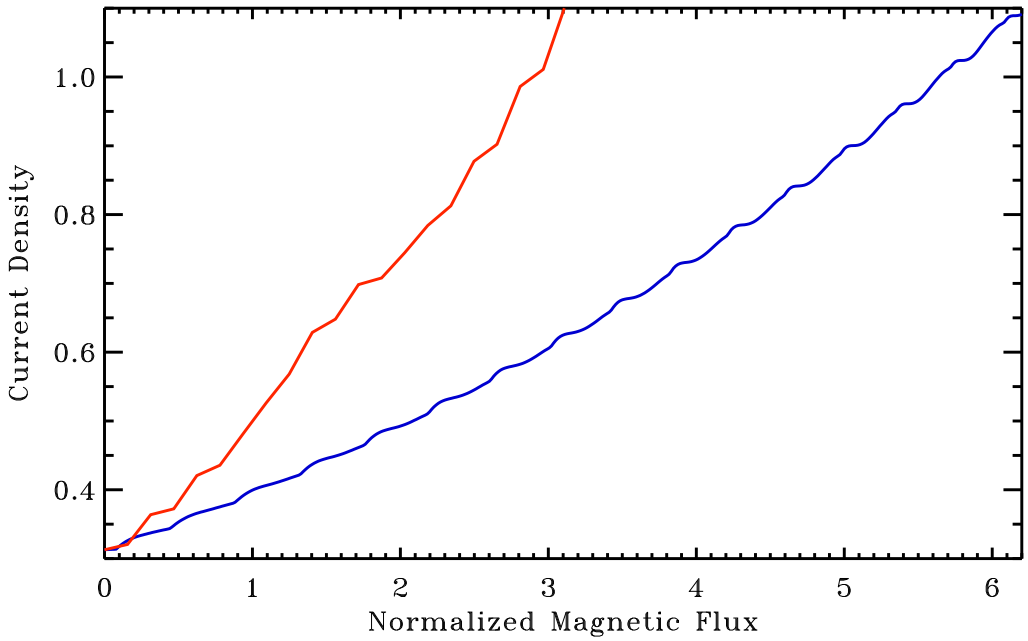

Figure 4.8. Relationship between the added magnetic flux and maximum current density. The blue and red line represent the compressed results in the one- and three- dimensional simulations, respectively.

4.3 CS Evolution in Response to MFD and Lobe Driver

Adiabatic compression has been demonstrated to favor the formation of a thin CS in the mid-tail. However, this localized current redistribution and concentration by adiabatic compression does not provide an explanation for the observed near-Earth thin CS possibly because the near-Earth dipole field is not easily to be compressed by the addition of open magnetic flux only. Chapter 3 has proposed a model of CS thinning based on the MFD, which is caused by sunward convection to replenish dayside magnetic flux to balance magnetic reconnection during periods of southward IMF. We have shown that midnight MFD is efficient to generate a strong thin CS in the near-Earth tail. Since either mechanism could result in the thin CS formation, it is important to consider both processes for a more realistic growth phase. In this section, the combined influence of MFD and lobe compression on the evolution of CS structure is examined.

Figure 4.9 shows a comparison of the two mechanisms for the crosstail current density in the midnight meridian. From the top to bottom the panels show the cases of lobe compression, MFD, and the combined physics at the time $t \sim 200t_A$ ($\sim$ 50 minutes). The result for the run with both, lobe compression, and MFD illustrates that the strong thin CS inside $x = -9$ is almost the same as in the case for MFD only and therefore caused by the removal of near-Earth magnetic flux. Similarly, the enhanced current density in the region from $x = -15$ to -30 is similar to the case with lobe compression only and therefore caused by this compression. It is not unexpected that the last panel shows the superposed CS configurations for both mechanisms. Both effects lead to a slow quasi-static evolution of sequences of force balanced equilibria, where any snapshot in time only depends on the entire magnetic flux added or removed. Therefore the combination of both effects can be expected to

yield a double CS (near-Earth tail and mid-tail) configuration that is close to the superposition of the individual CSs when the effects are considered separately. Note, however, that some difference may exist compared to a simple superposition because the changes for the magnetic field are nonlinear. Overall the combined effects yield an extended CS from $x = -3$ to $x = -30$ with local maxima in the near-Earth and mid-tail regions for times corresponding to the late growth phase. Such a radial extension is also reported by *Pulkkinen et al.* [1999] who found that the thin CS structure can form the near geosynchronous distances and extend to the mid-tail ($\sim x = -33R_E$).

Figure 4.10 quantitatively present the CS evolution in the near-Earth region at about $x = -7\,R_E$. The lobe compression, MFD, and the combined results are shown by the black, red, and blue lines respectively. In the case of adiabatic compression, the lobe magnetic field (B_x) enhances by about 20% in the late growth phase while the magnetic field for the MFD case decreases by 7%. Note that the instantaneous difference in B_x between the combined case and the lobe compression is close to the net decrease of the MFD case. The plots of CS width and maximum current density at $x = -7R_E$ show almost no change for lobe compression only. This demonstrates that lobe compression does not result in a significant increase of current density in the near-Earth region. In the MFD case, with a reduced lobe magnetic field, the CS thickness decreases to $0.4\,R_E$ toward the end of the growth phase. The current density increases up to 5.3 ($\sim$ 13 nA/m^2) toward the end of the simulation run. The blue line represents the combination of lobe driver and MFD. Note that the near-Earth current density does not evolve simply as the superposed effects of MFD and lobe compression. The current density increases similarly but with the lower rate compared to the MFD case. This comparison illustrates that the near-Earth thin CS can be attributed entirely to the removal of closed magnetic flux. It implies the importance of sunward convection for the near-Earth tail evolution during the substorm growth phase. The comparison suggests that the near-Earth magnetotail properties strongly depend on the competition of added open and depleted closed magnetic flux. This agrees and explains a considerable number of substorms where the lobe magnetic field does not increase in the near-Earth region [*Snekvik et al.*, 2012], i.e., where the loading and flux depletion appear to balance each other. We note that the lobe magnetic field decrease caused by MFD also depends strongly on distance along the tail where the decrease is largest in the near-Earth region and ceases in the mid-tail.

Figure 4.11 shows the equatorial plasma velocity corresponding to the three panels in Figure 4.9. No normal component of velocity is present in the equatorial plane ($v_z = 0$). For lobe compression, the top panel shows that the overall plasma velocity is very slow. In a quasi-static evolution the magnetotail configuration at every point of the evolution is in an equilibrium state. This is always satisfied if the velocity is much smaller than the Alfvén speed v_A [*Schindler and Birn*, 1982]. In our simulation the Earthward flow is $\sim 0.02v_A$ and $v_A \sim 430$ km/s (similar to the speed of sound). This illustrates that the configuration is force balanced and evolves in a quasi-static sense. Note that a steady state for the lobe electric field of 0.015 implies Earthward convection of about $0.3v_A$ or 130 km/s. If the Earthward flow is $0.02v_A$ then $(0.02v_A)^2/(0.3v_A)^2 \sim 1/15^2$ is much smaller than the unity. The fastest flows for the

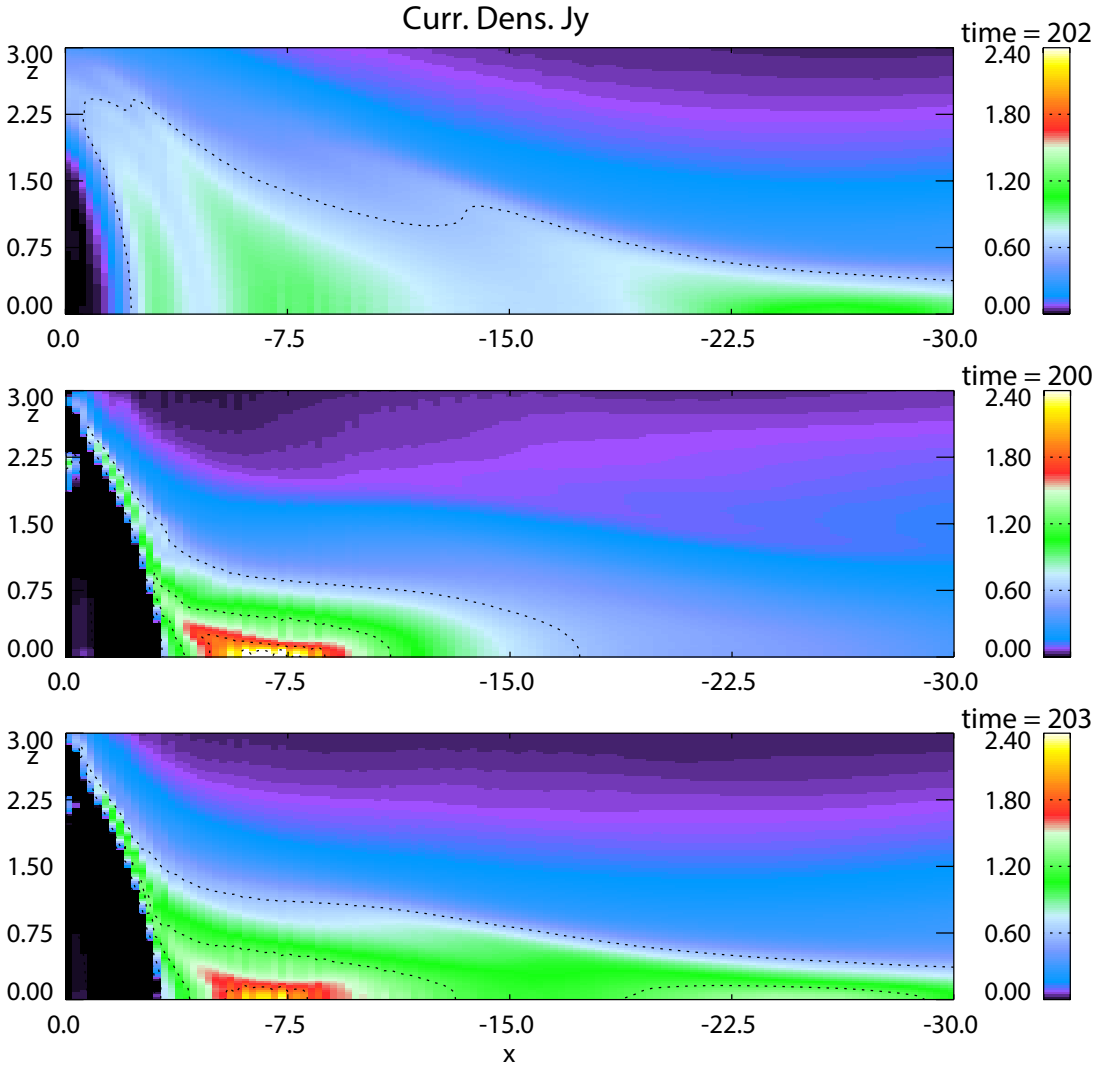

Figure 4.9. Crosstail current density in the midnight meridian plane at the time $t \sim 200 t_A$. The top, middle, and bottom panels show the influence of lobe compression, MFD, and the combination on the CS current density respectively.

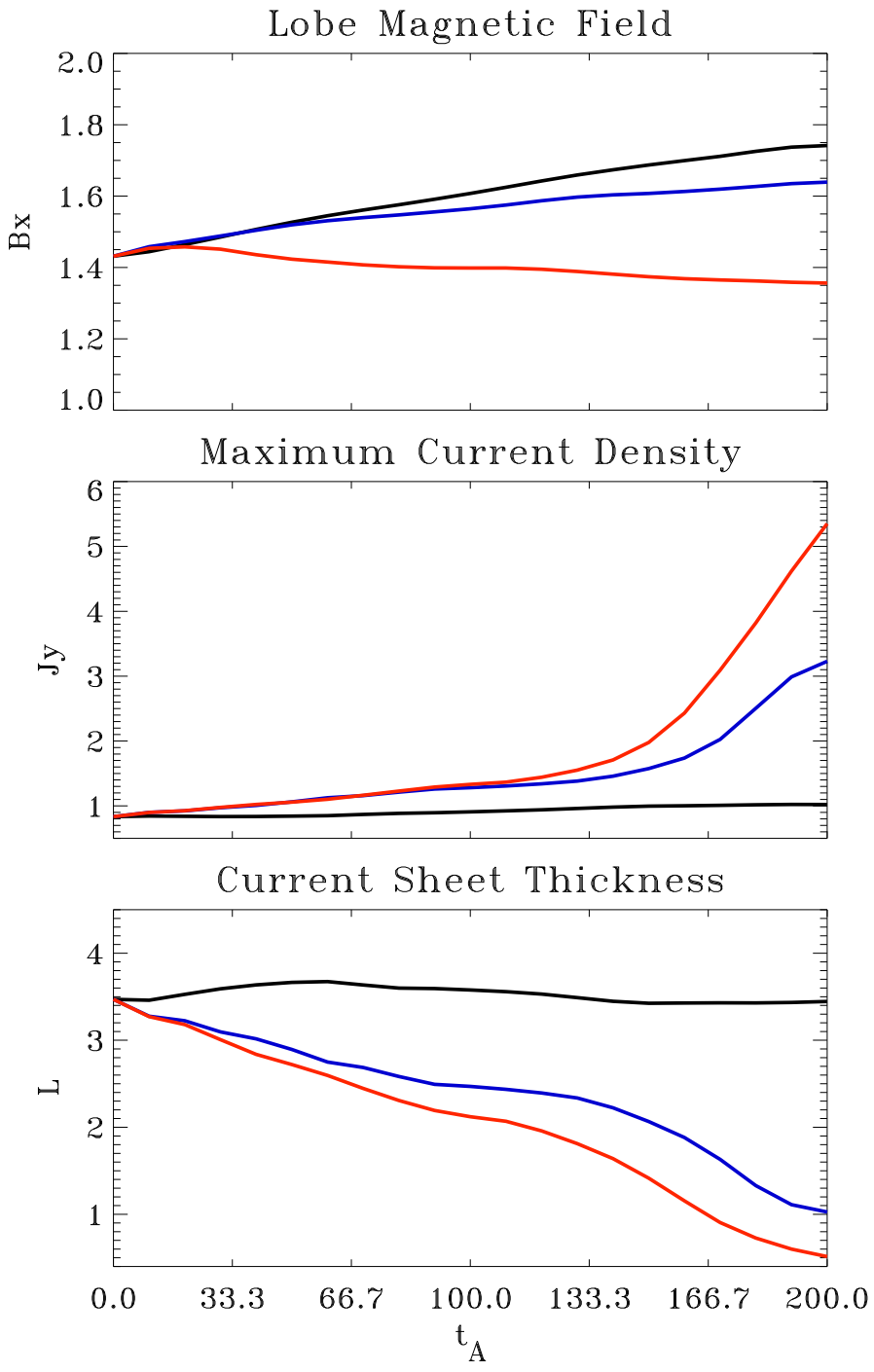

Figure 4.10. CS properties in the near-Earth region ($x \sim -7\,R_E$). From the top to bottom it shows the lobe magnetic field, the maximum current density, and the CS thickness. The black, red, and blue lines represent the case of lobe compression, MFD, and the combination respectively.

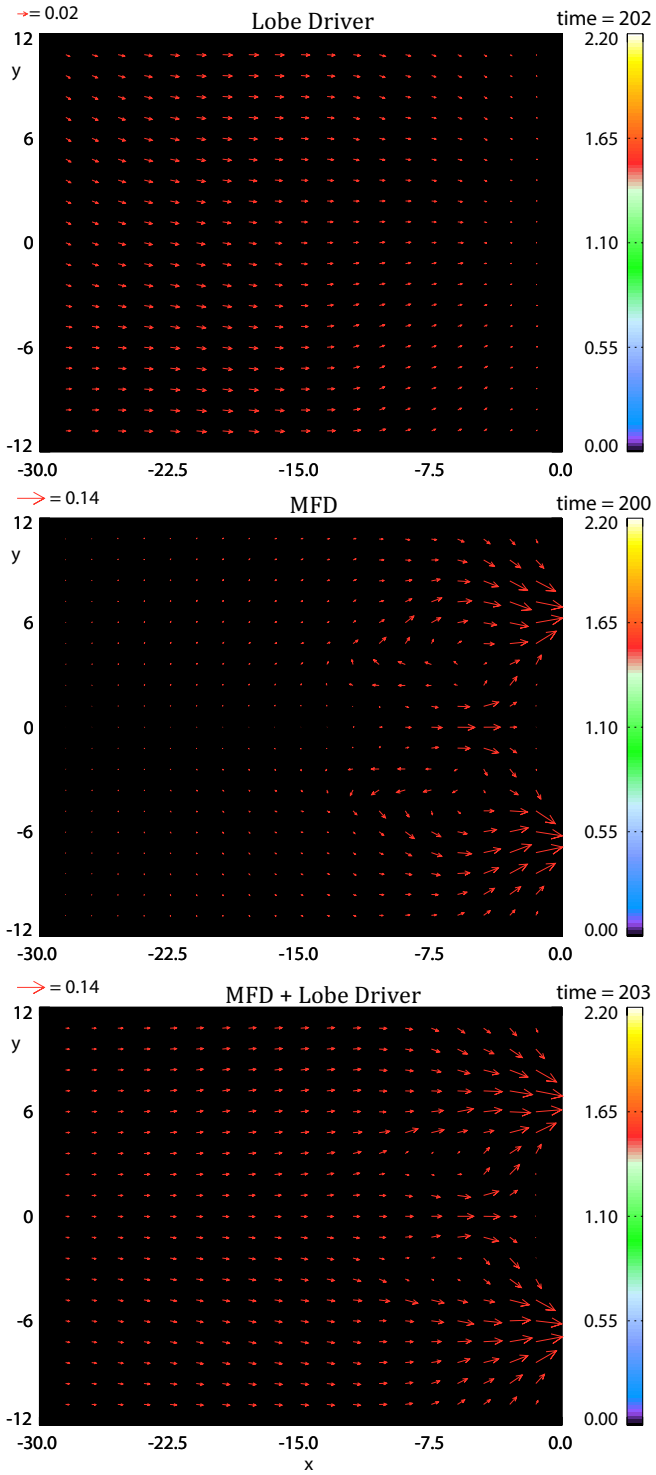

Figure 4.11. Plasma velocity in the equatorial plane. The three panels correspond to Figure 4.9. The color represents the normal component (v_z), and the arrow represents the tangential component of velocity, i.e., $v_x\hat{e_x} + v_y\hat{e_y}$.

MFD case (middle panel) are about 60 km/s with typical velocities of a few 10 km/s. This convection is dominant only in the near-Earth region ($x > -5$) with a strong divergence at about $x = -3$ to $x = -4$. This convection is driven by our sunward flow boundary condition, and this flow is associated with the near-Earth CS thinning and the generation of strong field-aligned currents. Convection for the combination of lobe compression and MFD again appears like a superposition of the convection for the two runs where these effects are considered separately. This is consistent with the comparison of the CS evolution.

The corresponding magnetic field strength in the equatorial plane is displayed in Figure 4.12. This figure shows that the magnetic field for lobe compression is still close to the dipole field in the near-Earth region. The magnetic field in the mid-tail region is reduced particularly in the vicinity of the mid-tail thin CS. For the MFD case, the magnetic flux is significantly depleted down to values of $B_z \sim 1$ nT in a large portion of the near-Earth plasma sheet, consistent with the divergent slow convection at $10\,R_E$ radial distance which forms in response to the sunward flow boundary condition. The reduction of magnetic field near geosynchronous distances is a typical property of the substorm growth phase [*McPherron*, 1972; *Kokubun and McPherron*, 1981], however, this reduction is not presented for lobe compression only. This strong reduction of the near-Earth magnetic field requires the divergent convection which is induced by sunward outflow boundary condition. The last panel of Figure 4.12 presents the combined effect of the lobe driver and MFD on the strength of equatorial magnetic field. The result indicates that the magnetic field slightly differs from a superposition of the first and second panels. The mid-tail magnetic field reduction extends over a wider crosstail region and extends further earthward for the case of lobe compression compared to the MFD case. This reduction is caused by the slow sunward convection in the mid-tail which also transports some magnetic flux into the near-Earth region. This transport is slow and insufficient to compensate the strong removal of near-Earth magnetic flux, however, it can explain the slower rate of the thin CS formation in the near-Earth region compared to the case of MFD only.

Figure 4.13 shows the crosstail current density distribution in the equatorial plane. It illustrates that the strong intensification of the near-Earth current coincides exactly with the depletion of near-Earth closed magnetic flux. The near-Earth current intensification is smaller if the lobe driver operates simultaneous with the sunward convection. As mentioned before, we attribute this to the slow transport of magnetic flux from the mid-tail to the near-Earth tail. The top panel shows that lobe compression results in the intensification of the crosstail current in the mid-tail region again coincident with the local reduction of B_z in this region. These results imply that the magnetic reconnection can possibly operate at the different radial locations in the near-Earth and the mid-tail region.

Figure 4.14 presents the sheet current density, which is the current density integrated from the equatorial plane to the lobe boundary. In the presence of a lobe driver only, the near-Earth current density appears strongest among the three cases. This result is not unexpected because the intensity of the integrated current should be determined only by the difference of the lobe magnetic field, i.e.,

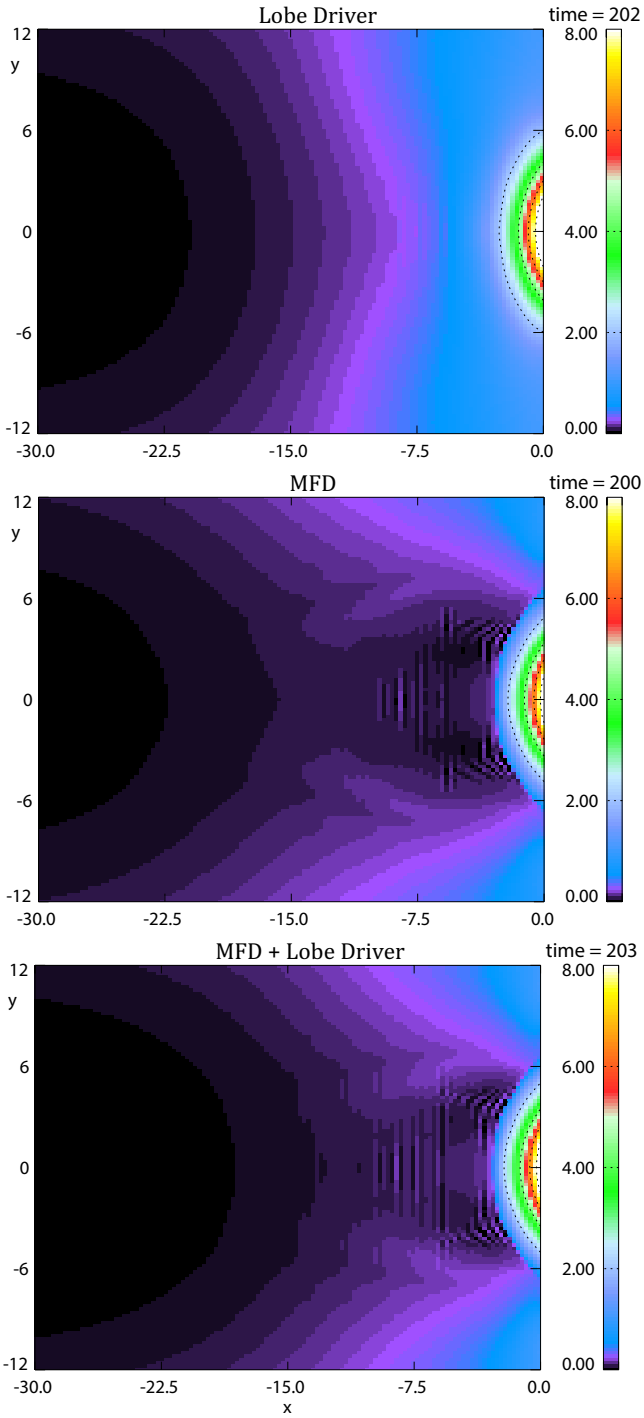

Figure 4.12. Magnetic field strength (B_z) in the equatorial plane. The three panels correspond to Figure 4.9

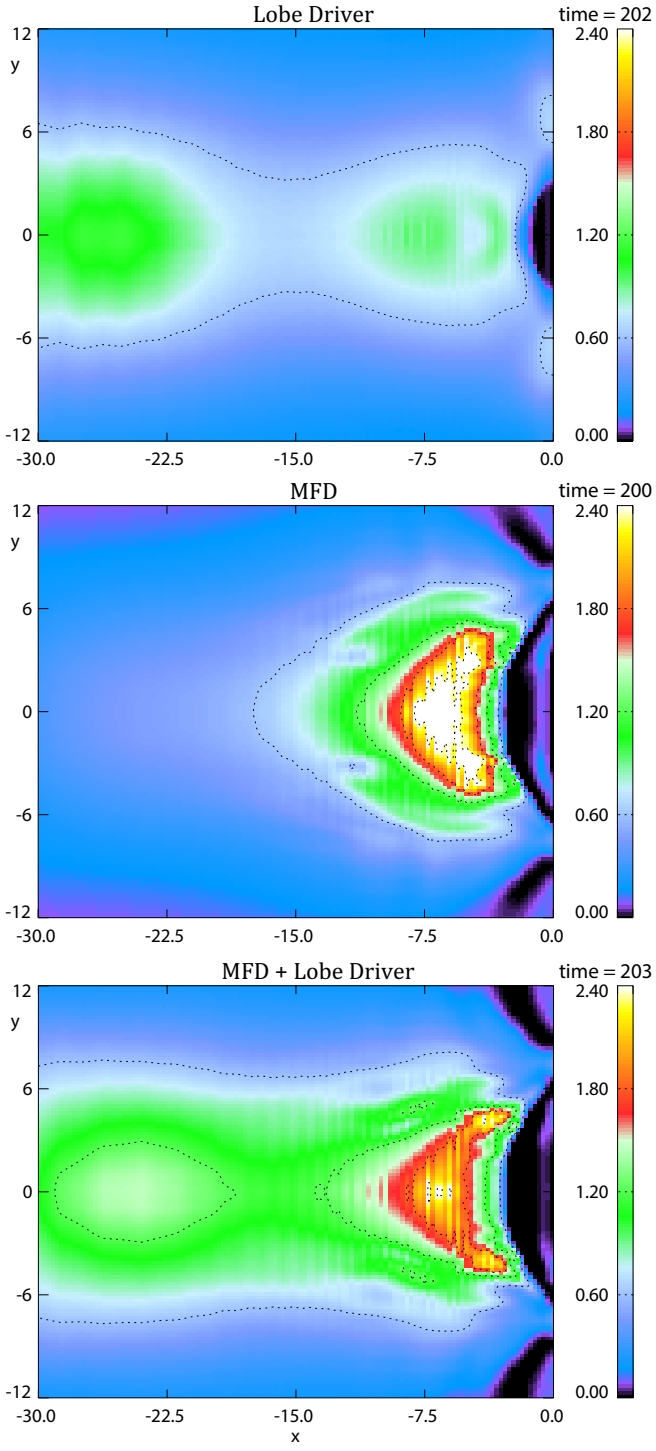

Figure 4.13. Crosstail current density in the equatorial plane. The three panels correspond to Figure 4.9.

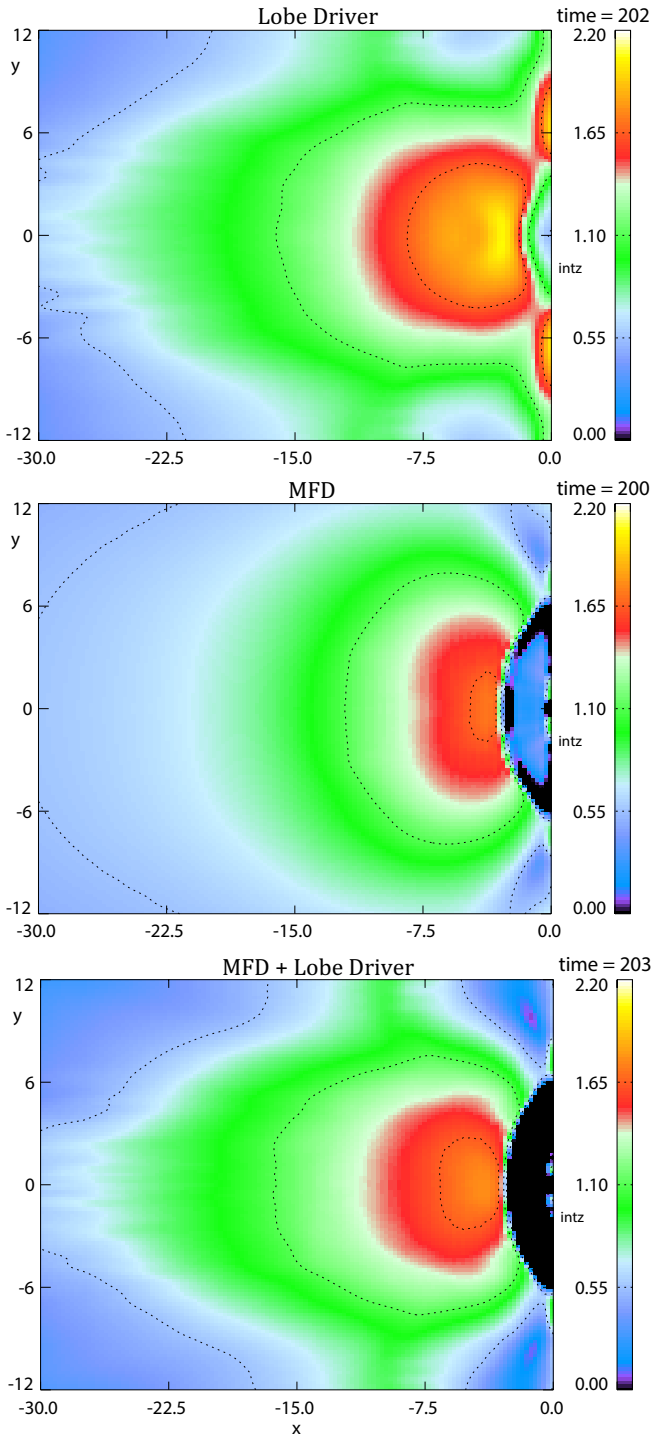

Figure 4.14. The format is the same as Figure 4.13, except for the integrated sheet current density from the equatorial plane to the lobe boundary.

$j_{int} \sim \Delta B_x$. MFD removes the near-Earth magnetic flux such that the lobe magnetic field is reduced (for the reduced magnetic field one can also see Figure 4.10). Figure 4.14 shows that the overall crosstail current density is enhanced everywhere under the influence of lobe compression. Again, the result demonstrates that the CS configuration depends strongly on both loading and depletion of magnetic flux.

In order to better understand the magnetic field changes, the evolution of magnetic field lines during each process is presented in Figures 4.15 to 4.17. Here field lines are computed for fixed location at $z = 0$ in the midnight meridian plane. Note that the scale along x is somewhat contracted with increasing distance from Earth for a better illustration of both the near-Earth and the mid-tail CS regions. We first demonstrate the case of lobe compression in Figure 4.15, which shows that magnetic field lines near mid-tail strongly converge toward the equatorial plane, which is associated with the finite mid-tail thin CS. The convergence toward the equatorial plane however is obvious only in the mid-tail region while the shape and location of field lines in the near-Earth region appears unaltered.

In comparison, Figure 4.16 shows the evolution of magnetic field lines for the MFD case. It illustrates that magnetic field lines in the dipole field and near-Earth region converge strongly toward the equatorial plane. This convergence is presented out to about $x = -15$ but is not apparent in the mid-tail region. In comparison to the prior results it is clear that this convergence is associated with the thin CS confined to the near-Earth tail. The MFD result also shows a strong convergence of magnetic field lines near the Earthward boundary. This is caused by the strong reduction of closed flux in the midnight meridian. The displacement of field lines toward lower z values at the Earthward boundary indicates that there would be an equatorward motion of field line footpoints in the ionosphere. Note, this convergence of magnetic field lines does not appear by only considering the lobe compression, which means the equatorward displacement of ionospheric properties likely requires a significant depletion of the near-Earth magnetic flux and cannot be explained by lobe compression.

The combined influence of lobe compression and MFD on the shape of magnetic field lines is shown in Figure 4.17. This figure illustrates that magnetic field lines converge both in the near-Earth and mid-tail region toward the equatorial plane, however, there are different physical causes for the convergence which are difficult to identify in observations.

4.4 Double-Current Sheet Model in Response to the Loading and Depletion of Magnetic Flux

We have found that a thin CS can be generated either in the near-Earth or in the mid-tail region in response to a lobe driver or sunward convection. The growth phase magnetotail properties are quite likely the result of a superposition of these two physical processes. It is shown that the lobe magnetic field changes in response to the balance of the added open and depleted closed magnetic flux. This section examines the CS evolution associated with the competition of the addition of open magnetic flux and the removal of closed magnetic flux. To achieve this goal, three comparisons between the amount

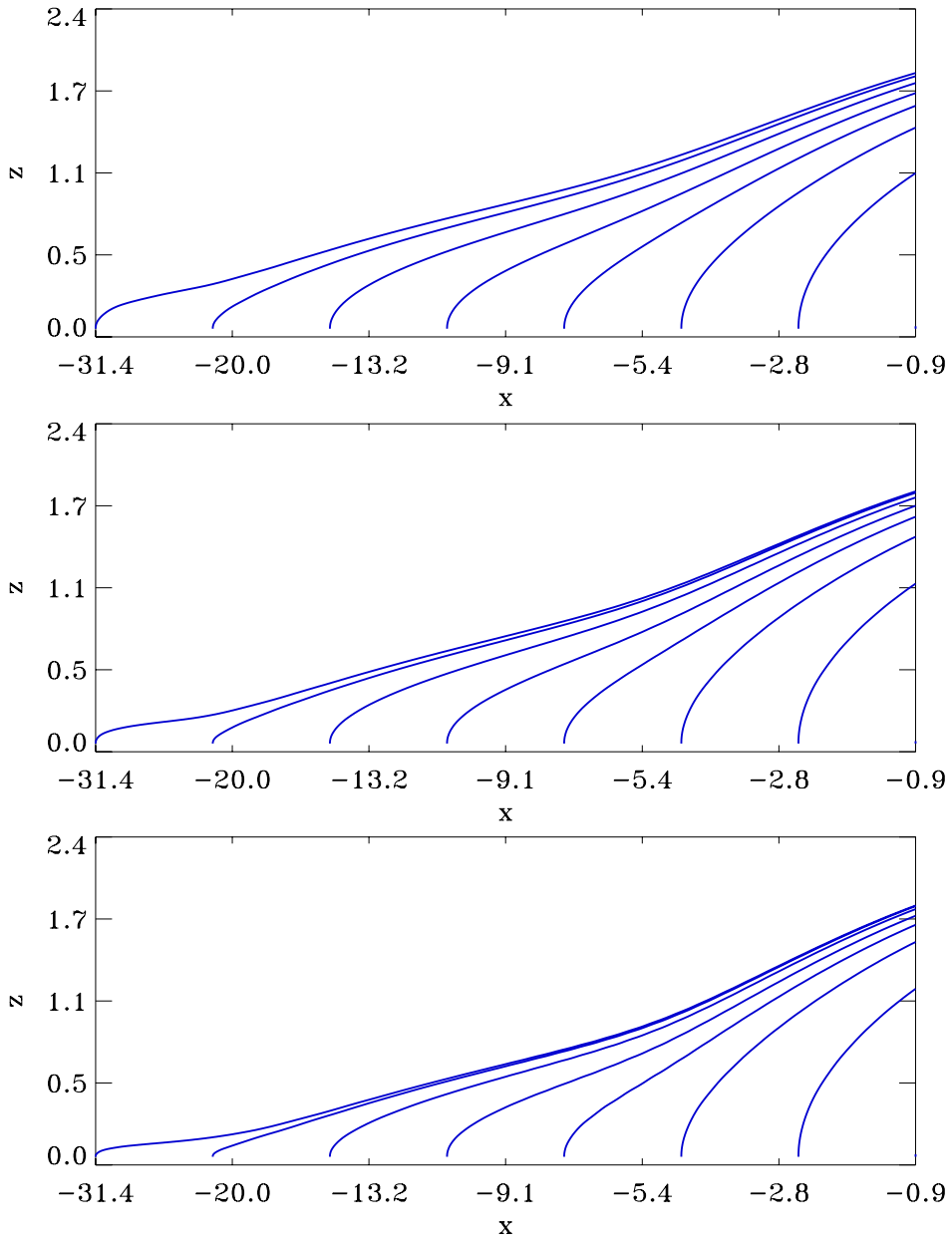

Figure 4.15. The evolution of magnetic field lines in the midnight meridian plane for lobe compression. The top, middle, and bottom panels are at times $t = 0t_A$, $t = 100t_A$, and $t = 200t_A$.

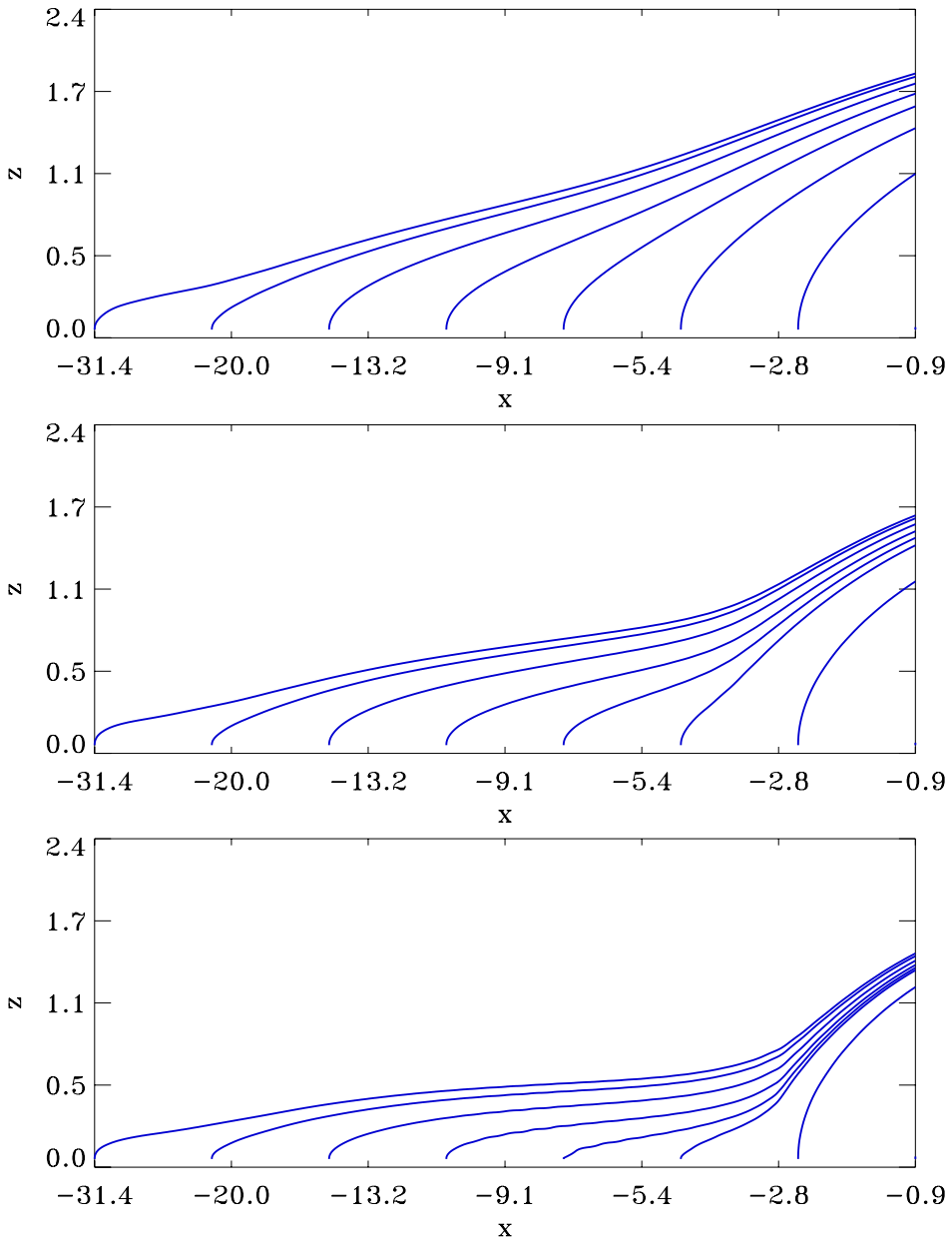

Figure 4.16. The format is the same as Figure 4.15, except for MFD case.

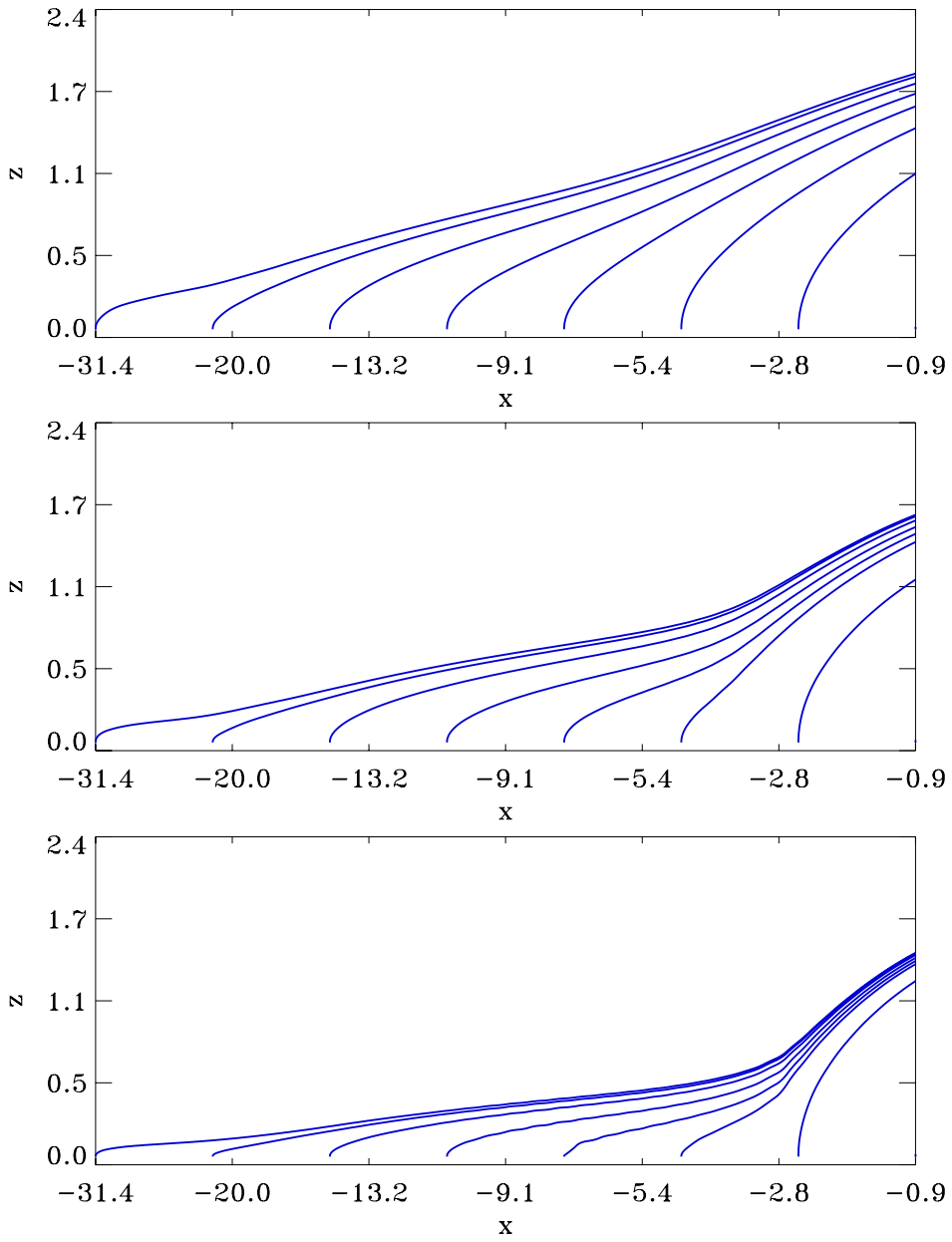

Figure 4.17. The format is the same as Figure 4.15, except for the combination case.

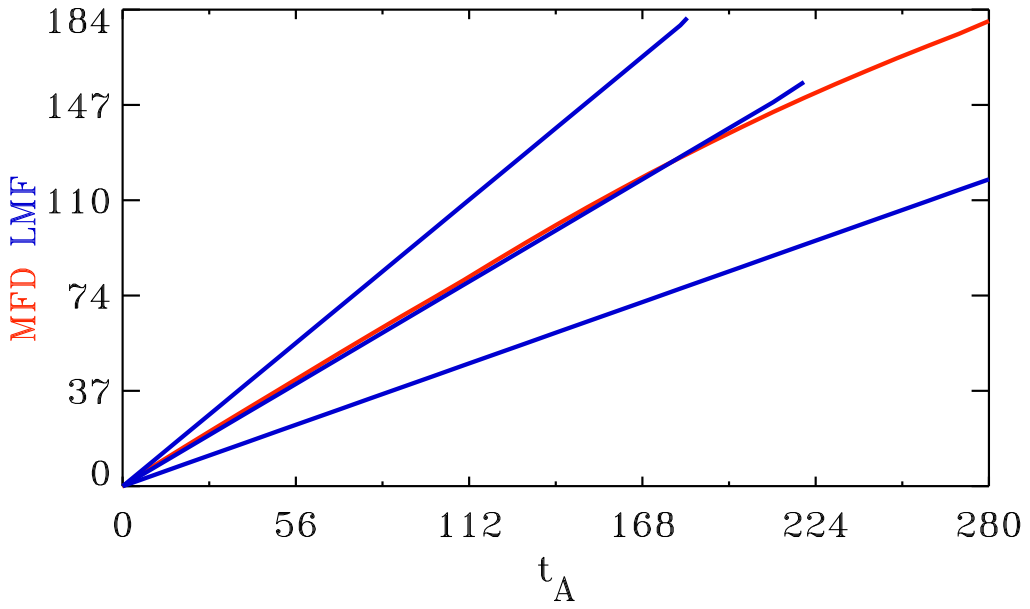

Figure 4.18. Competition between the addition of open magnetic flux and the depletion of closed magnetic flux. (blue lines) LMF is denoted as the total amount of the added magnetic flux while the (red line) MFD is denoted as the total amount of the depleted magnetic flux.

of open/closed magnetic flux are employed in our simulation, as shown in Figure 4.18. We denote MFD (red line) as the total amount of closed magnetic flux removed through the sunward boundary, while LMF (blue lines) measures the total amount of open lobe magnetic flux transported into the simulation box. Here the flux removal rate for MFD is kept the same for the three cases, that is, the sunward convection removes the near-Earth magnetic flux at the same rate (the average potential is ~ 40 kV). The different rates at which flux is added (LMF) are larger, approximately equal, and smaller than flux is removed by MFD, are designed to examine the CS response to the balance or inbalance between loading and depletion of magnetic flux. The applied electric fields (lobe potentials) in the three cases are 0.015 ($\sim$ 25 kV), 0.025 ($\sim$ 40 kV), and 0.035 ($\sim$ 58 kV). Note, the grid resolution used here is only half of our above results because the strong lobe driver makes it difficult to keep the simulation longer. One should notice that the CS current density is expected higher if the higher grid resolution were employed.

The CS configuration of the three comparisons is shown in Figure 4.19. The top panel assumes the smallest LMF rate and shows that there is a strong embedded thin CS in the near-Earth region where the MFD process is dominant. This implies that the reconnection would likely start to operate initially at a radial distance close to Earth. Note, the current density from $x = -10$ to $x = -25$ is not negligible, because it reaches about 5 nA/m^2 that could possibly cause onset of magnetic reconnection. When loading and depletion of magnetic flux almost balance each other, the second panel shows that the strongest CS first forms in the mid-tail. The near-Earth CS density evolves slower in response to the same amount of LMF and MFD, which implies that the magnetic reconnection would initially not occur in the near-Earth tail but rather in the mid-tail until the near-Earth current density reaches a

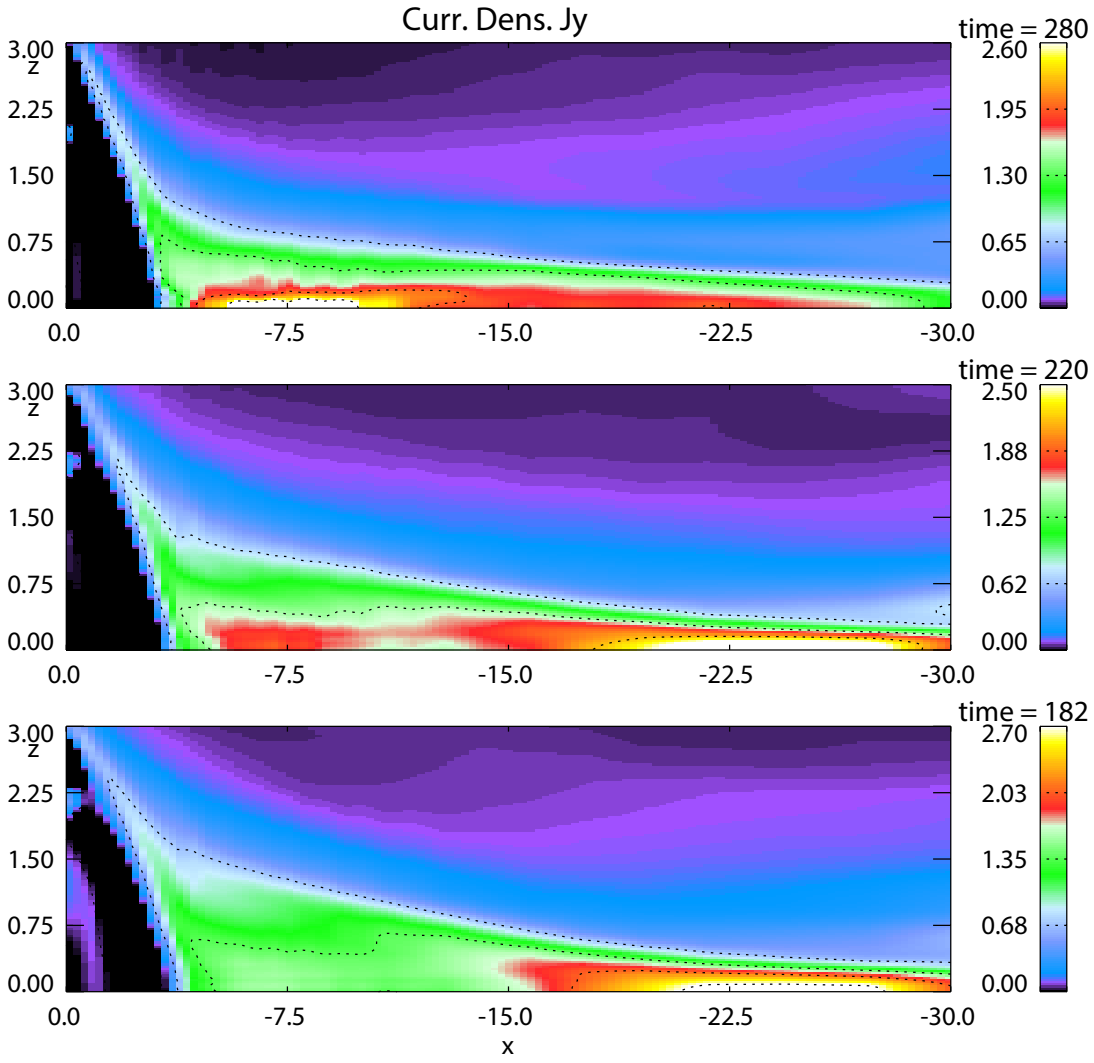

Figure 4.19. Crosstail current density in the midnight meridian plane. From the top to bottom it shows the case when the MFD is larger, comparable, smaller than the LMF.

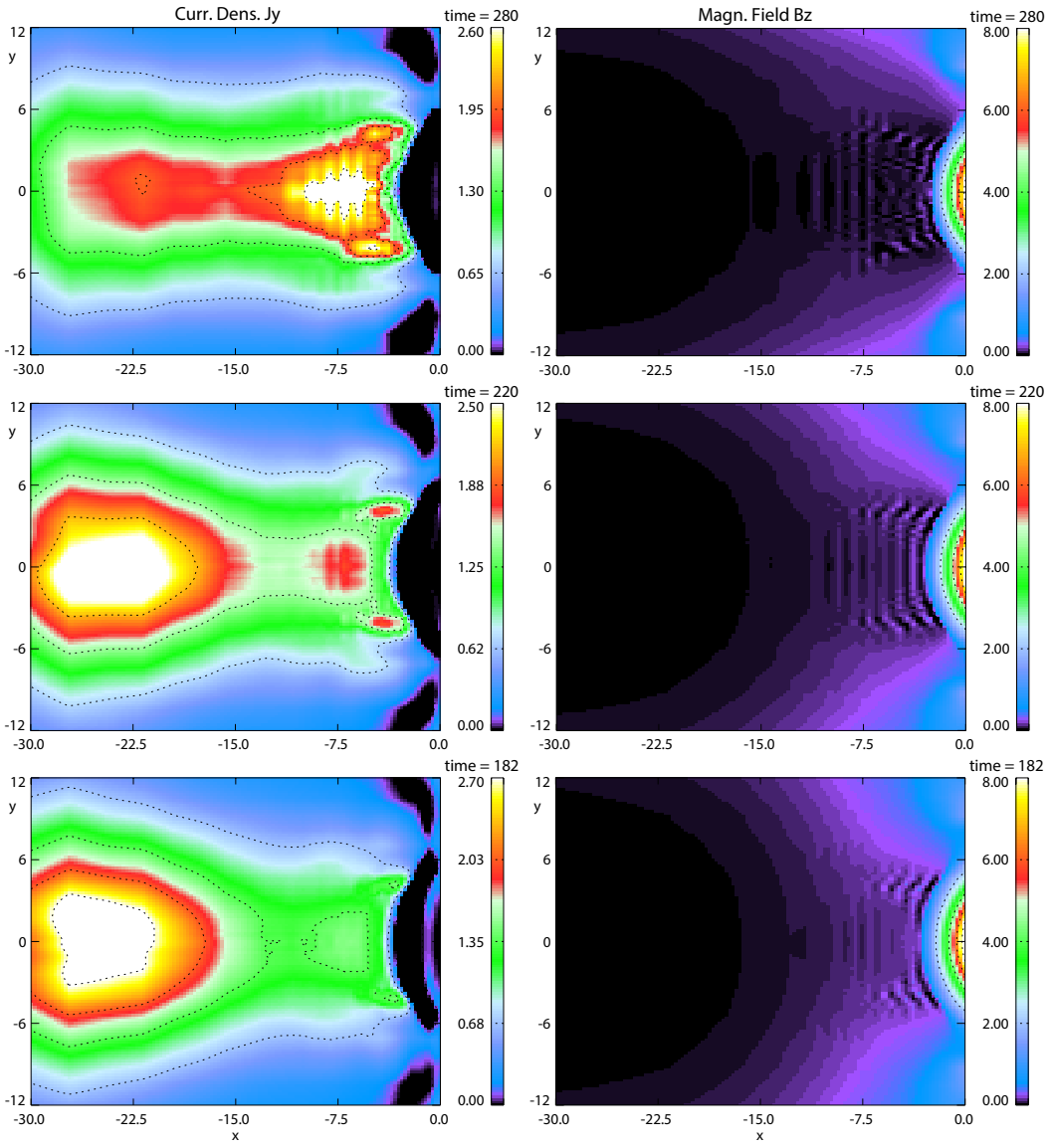

Figure 4.20. Crosstail current density and magnetic field strength in the equatorial plane. The three panels correspond to Figure 4.19.

sufficient intensity. The bottom panel of Figure 4.19 shows the CS density when the LMF flux transport is dominant. It is expected based on the balanced flux transport case that strong CS formation occurs first in the mid-tail for strong lobe compression. Although mid-tail reconnection may likely occur first, it is not necessarily associated with geosynchronous particle injection and therefore with the expansion phase onset. The corresponding equatorial current density and magnetic field are shown in Figure 4.20. The enhanced current is seen well associated with the region where the magnetic field is depleted. Figures 4.19 and 4.20 demonstrate a model of double-current sheet formation during the substorm growth phase. This result suggests the possibility of the multiple magnetic reconnection sites in the radial distance, however, does this imply that substorm expansion can be associated with reconnection onset at either location?

4.5 Discussion and Summary

Substorm physics has been highly debate for a long time (see Chapter 1). A major outstanding question is whether the mid-tail reconnection is the cause for the near-Earth plasma injection or not. To better understand this aspect, the presented study of the growth phase CS is of central importance because the thin and strong CS in the late growth phase most likely determines the conditions for magnetic reconnection and the expansion phase onset. This chapter demonstrates the growth phase CS configuration and provides a possible link to the magnetic reconnection. The growth phase considered in this study includes the loading of open magnetic flux into the tail lobes and the depletion of closed magnetic flux in the midnight near-Earth tail. When these two processes almost balance each other, the near-Earth lobe magnetic field would remain almost constant or increase only slowly depending on radial distance [*Snekvik et al.*, 2012].

This study demonstrates that a strong thin CS can be generated either in the near-Earth or the mid-tail in response to sunward convection or lobe compression. The lobe driver is applied through the presence of a constant electric field at the lobe boundary. This y component of the electric field equals the local transport rate of magnetic flux into the simulation. Although the assumption of the constant electric field is idealized, this approach still provides a basic reference and important insight into the influence of lobe compression. It is found that the magnetotail is more easily compressed and modified in the region where the magnetic fields are highly stretched, which is associated with a thin CS formation in the mid-tail.

In comparison to literatures, *Wiegelmann and Schindler* [1995] applied a nonuniform magnetic flux at the lobe boundary, and found that a maximum current density appears close to the Earthward boundary, with a strong gradient of flux tube volume. Such the near-Earth strong thin CS can be expected in an aspect to the strong lobe driver implemented near the Earthward boundary. The limitation of their model is that the model uses a weakly two-dimensional MHD assumption without the presence of the dipole field. The effect of a nonuniform electric field on CS formation is also investigated by *Ma et al.* [1995]. In their study, the tailward edge of the thin CS remains approximately

at $x = -30R_E$ because the electric field applied in the distant tail is relatively small. It is similar to our result that a strong thin CS favors the formation in the mid-tail with a tailward edge about $x = -33R_E$ for a constant electric field. An apparent difference between our results and *Ma et al.* [1995] is that they found the thin CS extending to the near-Earth region about $x = -7R_E$ for lobe compression. However, their study is based on a two-dimensional MHD simulation such that the condition of the near-Earth dipole field is much different from our model.

This chapter also presents the effect of a nonuniform electric field on the CS formation. It is found that a thin CS favors the formation in the mit-ail with a tailward edge a few R_E inward when the electric field smoothly decreases with the radial distance. The similar result is found by *Birn et al.* [1998] that the radial distribution of current density varies in response to the different gradient profiles of the electric field. Our results show that lobe compression has no significant effect on the CS configuration in the near-Earth tail where the magnetic field is more dipolar. This chapter also examines the importance of lobe compression in the one- and three-dimensional simulations for a constant electric field. It is found that the same enhancement of current density only requires a smaller amount of magnetic flux added into the lobe in the three-dimensional simulation. This result implies a favorable location of the mid-tail CS. We suggest that in the distant tail (where the magnetopause flaring angle is relatively small) the CS is almost one-dimensional compression for which we have demonstrated the problem to generate a thin CS.

In comparison, sunward convection depletes the closed magnetic flux at $x \sim -10R_E$ such that a thin CS forms in the near-Earth region. This convection is subject to the conservation of flux tube entropy, which implies that enhanced convection in the equatorial plane is more likely along contours of constant flux tube entropy. The depletion of closed magnetic flux also results in the convergence of the footpoints of magnetic field lines, however, this is not the case for the lobe compression. This result implies that the typical equatorward motion of ionospheric properties likely requires the removal of the large near-Earth magnetic flux. Also, the reduction of geosynchronous magnetic field during a typical growth phase can not easily to be caused by lobe compression. Thus our results demonstrate the importance of sunward convection for the near-Earth tail dynamics.

An important aspect of this chapter is that we examine the competition of the addition of open magnetic flux and the removal of closed magnetic flux associated with the CS configuration. It is found that a strong thin CS can form first either in the near-Earth or the mid-tail depending on whether the depleted closed or the added open magnetic flux is dominant. The near-Earth thin CS would take longer to pick up if the loading and the depletion of magnetic flux are approximately equal for a constant lobe electric field. This double-current sheet model implies the possibility of multiple magnetic reconnection sites in the magnetotail. Onset of reconnection can take place first either in the near-Earth or the mid-tail, or they can occur simultaneously when the current density reaches a sufficient intensity in both regions. Evidences of the near-Earth and the mid-tail magnetic reconnection have been reported in many papers by studying fast flows. However, not all fast flows can be associated

with the expansion phase onset [*Shue et al.*, 2003; *Ohtani et al.*, 2006]. Our results demonstrate that the mid-tail thin CS appears later than the near-Earth thin CS if MFD is dominant, which implies that the mid-tail reconnection would occur later than the near-Earth instability. In that case, the mid-tail reconnection cannot be the cause for the near-Earth plasma injection. The opposite case, initial onset of reconnection in the mid-tail, is highly interesting. Fast flows are frequently observed during the growth phase [*Baumjohann et al.*, 1990; *Angelopoulos et al.*, 1992; *Ma et al.*, 2009; *Juusola et al.*, 2011], implying that reconnection often occurs prior to the onset of the expansion phase. This is consistent with the onset of mid-tail reconnection. However, there are good physical arguments that the mid-tail reconnection onset may not be associated with the substorm expansion onset. Several recent studies [*Dubyagin et al.*, 2011; *Sergeev et al.*, 2012b] have shown that, although these fast flows are often entropy depleted (so-called plasma bubbles), this depletion is generally insufficient to explain penetration deep into the inner magnetosphere. Therefore, theses flows cannot explain a strong dipolarization in this region, and more importantly, they are unable to generate energetic particle injection at geosynchronous distances, which is one of the most characteristic signatures of the expansion phase onset. Our double-current sheet model demonstrates the formation of two thin CSs at distinct location in the near-Earth and in the mid-tail region also suggests that the substorm expansion onset is associated only with the near-Earth onset of magnetic reconnection, while the mid-tail reconnection causes BBF's and entropy bubbles.

In summary, this chapter studies the CS formation in response to lobe compression and sunward convection, i.e., loading and depletion of magnetic flux. The results include:

• a thin CS favors the formation in the mid-tail with a tailward edge about $x = -33R_E$ for a constant electric field;

• the CS current density increases approximately linearly with the added magnetic flux in both the one- and the three-dimensional adiabatic compression;

• a double-current sheet forms in the mid-tail and near-Earth regions for lobe compression in combination with sunward convection;

• the relative current densities in the double-current sheet configuration depends strongly on whether the added or the depleted magnetic flux dominates during periods of southward IMF.

Chapter 5

The Influence of Magnetic Flux Depletion on the Magnetotail and Auroral Morphology during the Substorm Growth Phase

5.1 Introduction

The breakup of the most equatorward preexisting auroral arc is described as the onset of the expansion of an auroral substorm [*Akasofu*, 1964]. During the growth phase, auroral arcs are observed moving equatorward close to or even into the region of the diffuse aurora characteristic of a dipolar magnetic field. The equatorward velocity of the growth phase arcs is about 100 to 200 m/s [*Aikio et al.*, 2002]. *Clausen et al.* [2012] suggested that the equatorward drift of auroral arcs is likely a result of the addition of open magnetic flux to the polar cap through the dayside reconnection such that the gradual increasing size of polar cap leads to an expansion of the region 1 currents moving toward lower latitudes. In this study, we demonstrate that the equatorward motion of the field-aligned currents is most likely caused by the removal of closed tail magnetic flux, which is also associated with the formation of a near-Earth thin CS, and not caused by an external compression of the magnetotail.

The prior chapters have examined a new model of CS thinning based on midnight magnetic flux depletion (MFD), which is caused by slow sunward convection to balance dayside magnetic reconnection during periods of southward IMF. A central aspect of any model for thin CS formation during the growth phase is the changes of the auroral morphology associated with the near tail evolution. Therefore, this chapter examines the near-Earth magnetotail features mapped into the auroral ionosphere. This mapping is based on the T96 magnetic field model used for the MHD simulations, corrected by the requirement of magnetic flux conservation. Of specific interest are the changes in magnetic flux, flux tube entropy, field-aligned currents, convection, and the size and location of the respective ionospheric footpoints of magnetotail structures and properties.

One of the main difficulties in identifying auroral signatures through any global or mesoscale fluid simulation is the lack of an explicit process for particle precipitation or particle acceleration in these simulations. This can at least in part be remedied by two aspects of such simulations that are related to particle precipitation. It is well established that discrete electron precipitation is strongly linked to the presence of strong upward field-aligned currents. Therefore the presence of such currents can serve as a proxy for the expected discrete electron precipitation. Another property linked to particle precipitation are the so-called isotropy boundaries. Equatorward of these boundaries the loss cone is empty while it is filled implying particle precipitation poleward of the isotropy boundary [*Sergeev and MalKov*, 1988; *Sergeev et al.*, 1993b; *Yahnin et al.*, 1997a]. These boundaries are different for electrons and ions, they depend on particle energy, and are easily identified by low altitude orbiting satellites.

The physics of these boundaries is relatively straightforward: On sufficiently dipolar field lines particles are largely adiabatic such that an empty loss cone is not easily refilled. In contrast, particles in the stretched plasma sheet undergo chaotic particle motion when the width of the CS becomes comparable to the gyro radius. The chaotic motion easily refills the loss cone and explains the energy

dependence of the associated isotropy boundary. The ion isotropy boundary is related to the so-called trapping boundary, which is used to characterize the outermost shell of the dipolar closed magnetic field by auroral observations. Isotropy boundaries are easily identified by the magnetic field configuration in the simulation and can therefore be used for comparison with auroral and satellite observations.

In this study both electron and ion isotropy boundaries are used and mapped into the ionosphere to provide a reference for the transition between dipolar and tail-like field, auroral observations, and ionospheric convection. We have conducted a range of simulation cases with varying values of the sunward magnetic flux transport rate (potential). However, the configurational changes of these different cases are, as shown in Chapter 3, almost identical and the exact value of the potential only stretches or contracts the timeline of the evolution. Therefore this chapter will focus mostly on a single case with an average potential of 40 kV to demonstrate fundamental properties of the thin CS formation and of the evolution of plasma sheet and field-aligned current properties mapped into the auroral ionosphere. The results are contrasted with a case of lobe compression to compare the impact of CS formation by MFD and lobe compression on the ionospheric evolution.

The results employ the same three-dimensional mesocale MHD simulation of the near-Earth tail. A typical substorm growth phase is characterized by the removal of closed magnetic flux in the near-Earth tail and the loading of energy and magnetic flux into the tail lobes. However, in order to clearly identify the influence of MFD on the auroral morphology, most of this study do not include the addition of lobe magnetic flux which can contribute to thin CS formation. By ignoring the presence of a lobe driver this chapter demonstrates that MFD is sufficient to generate the thin CS and to explain the typical equatorward motion of field-aligned currents and other ionospheric properties during the substorm growth phase. In the discussion, we contrast these results with a case including the additional lobe driver. The results demonstrate that the equatorward motion of growth phase arc is not likely caused by the addition of open magnetic flux to the tail lobes. This study suggests that all typical growth phase properties can be attributed to the depletion of near-Earth closed magnetic flux.

Often and intuitively the stretching of the tail magnetic field and the equatorward expansion are believed to be associated with Earthward or tailward flows in the plasma sheet. This notion is carefully examined and contradicted by a quantitative evaluation of the displacement of flux tubes in the magnetotail in the presented model. The results demonstrate that the depletion of the closed magnetic field in the near-Earth region implies a significant reduction of the size of the ionospheric magnetic footpoints of this region, which is sufficient to explain the observed equatorward motion of the aurora during the growth phase.

5.2 Near-Earth Tail Region Mapping

5.2.1 Mapping Method

Typical for the substorm expansion onset is the auroral brightening and poleward expansion of the bright discrete aurora mostly simultaneous with major changes and fast convection in the magnetotail.

During the growth phase, a characteristic feature is the equatorward motion of the midnight aurora, particularly of the most equatorward discrete arc (growth phase arc) and of the poleward boundary of the aurora often associated with the closed magnetic field or plasma sheet boundary. This study examines the evolution of the ionospheric changes in the near-Earth magnetotail by quantitatively mapping flux tube properties of the thin CS configuration from the Earthward boundary into the ionosphere. The employed mapping method is based on magnetic flux conservation combined with T96 magnetic field model.

While our initial configuration is still close to the T96 model used for the initial input, the evolution close to the Earthward boundary changes strength and orientation of the magnetic field such that it is not anymore consistent with the initial T96 configuration. Worse, a simple unaltered use of the initial T96 model does not conserve magnetic flux because the magnetic field decreases in magnitude and changes in direction such that the Earthward directed magnetic flux is much smaller than the corresponding flux into the ionosphere from the T96 model. In some regions of the Earthward boundary the magnetic field is tilted very strongly and actually shows a small negative B_x component. Therefore it is of importance to include magnetic flux conservation in the mapping. The basic procedure is as follows.

Attributing a certain ground truth to the statistical T96 mapping, the map in longitude is mostly preserved except for a small contraction factor measuring distance from midnight. This factor is 1 for our equatorward boundary and can be adjusted linearly going down with increasing latitude (reasonable values are between 0.7 and 0.9 at the poleward boundary). For the presented results the contraction factor is assumed to be 0.8 at the poleward boundary. Magnetic flux conservation implies that a smaller value (more contraction) would lead to reduced equatorial motion while unmodified longitudinal map would lead to a larger amplitude of the equatorial displacement of footpoints. By using this distribution of longitudinal coordinates for all boundary points, the latitudinal width of each ionospheric grid cell (corresponding to a boundary cell of the simulation) is adjusted such that the flux into the ionosphere equals the flux out of our Earthward boundary cell. Here the equatorward boundary of the simulation is kept fixed because changes are likely smaller at lower latitudes. Specifically, grid cell size in the ionosphere is converted from geographic/geomagnetic coordinates to length scales by

$$\frac{\Delta\lambda}{180^\circ}\pi = \frac{\Delta z_i}{1\,R_E} \quad \text{and} \tag{5.1}$$

$$\frac{\Delta\phi}{180^\circ}\pi = \frac{\Delta y_i}{1\,R_\lambda} \ = \frac{\Delta y_i}{1\,R_E\cos\lambda}, \tag{5.2}$$

where we denote latitude as λ, longitude as ϕ, and Δy_i (also Δz_i) as the grid point separation in the ionosphere. With magnetic flux conservation $\Phi_{msp} = \Phi_{io}$ ($\Phi_{msp} = \Delta y \Delta z B_x B_0$ and $\Phi_{io} = \Delta y_i \Delta z_i B_{io}$), the latitudinal width of each ionospheric grid cell becomes

$$\Delta\lambda \ = A_i \frac{180^{\circ 2}}{\pi^2 \Delta\phi\cos\lambda} \quad \text{and} \tag{5.3}$$

$$A_i = \frac{\Delta y \Delta z B_x B_0}{B_{io}}, \tag{5.4}$$

where B_0 is the normalization for the magnetic field (20 nT), A_i is the grid cell area mapped to the ionosphere, $\Delta\lambda$ is the corrected latitudinal width, and i is the grid cell index. Here Φ_{msp} and Φ_{io} represent the grid cell magnetic flux at the Earthward simulation boundary and the ionosphere, and $B_{io}\cos\lambda$ is the magnetic field normal to the ionosphere. Note, $\cos\lambda = 0.5$ for $\lambda = 60°$ and 0.34 for $\lambda = 70°$, i.e., there is a significant change in the area over a distance of 10° in latitude. Note also that B_x represents the magnetic field strength perpendicular to the grid cell cross section of the Earthward boundary. For cells with negative $B_x \leq 0$, the ionospheric crossectional area is set to 0, consistent with the absence of magnetic flux out of the simulation domain at this grid point. Here B_{io} is the magnetic field strength at the ionospheric surface based on the dipole field

$$B_{io} = B_E(\frac{R_E}{r})^3(1+3\sin^2\lambda)^{1/2} \quad \sim \quad 5.7\times10^4\mathrm{nT},$$

with $B_E = 3.11\times10^{-5}$ T, $r = 1\,R_E$ at the Earth surface, and the latitude λ at 64°.

The overall mapping from the simulation in many cases is a two step process: In the first step quantities within the simulation domain, such as the magnetic field in the equatorial plane, are mapped along magnetic field lines into the Earthward boundary of the simulation. This step is not needed for any quantity that is already computed at this boundary such as the field-aligned current density. The second step is the mapping from the Earthward boundary into the auroral ionosphere using the outlined mapping procedure.

5.2.2 Mapping of the Earthward Boundary

In this section we illustrate first mapping results applied to the midnight MFD. For references Figure 5.1 shows the CS evolution during the MFD considered in Chapter 3. The top and bottom panels present the CS configuration at $t = 5$ and $t = 45$ minutes after the sunward divergent flow is switched on. This sunward outflow is located at a radial distance of about $x = -10\,R_E$. This outflow causes the initially wide CS to become significantly concentrated into a thin and strongly bifurcated current near the equatorial plane after 45 minutes. The corresponding magnetic field and azimuthal current density in the equatorial plane are shown in Figure 5.2. The figure illustrates the azimuthal extend of the reduction of the equatorial B_z component and the rather thin transition from the "stretched" magnetic field to the dipolar field region. It also illustrates the spatial extent of the intensified azimuthal current which coincides with the small B_z region.

A first impression of basic properties of the mapping is given by Figure 5.3, which shows the ionospheric maps of the rectangular grid at the Earthward boundary of the simulation. The top and bottom panels show the map of the grids at $t = 5$ and $t = 45$ minutes (corresponding to the cases shown in Figures 5.1 and 5.2). Here only every 3th grid line is plotted to avoid an overly dense impression of the mapping. The two thick lines are introduced to guide the eye to an important aspect of the mapping and configurational change. These are lines of the same constant z coordinate at the Earthward boundary for the two plots and illustrate the apparent equatorward motion of magnetospheric structures

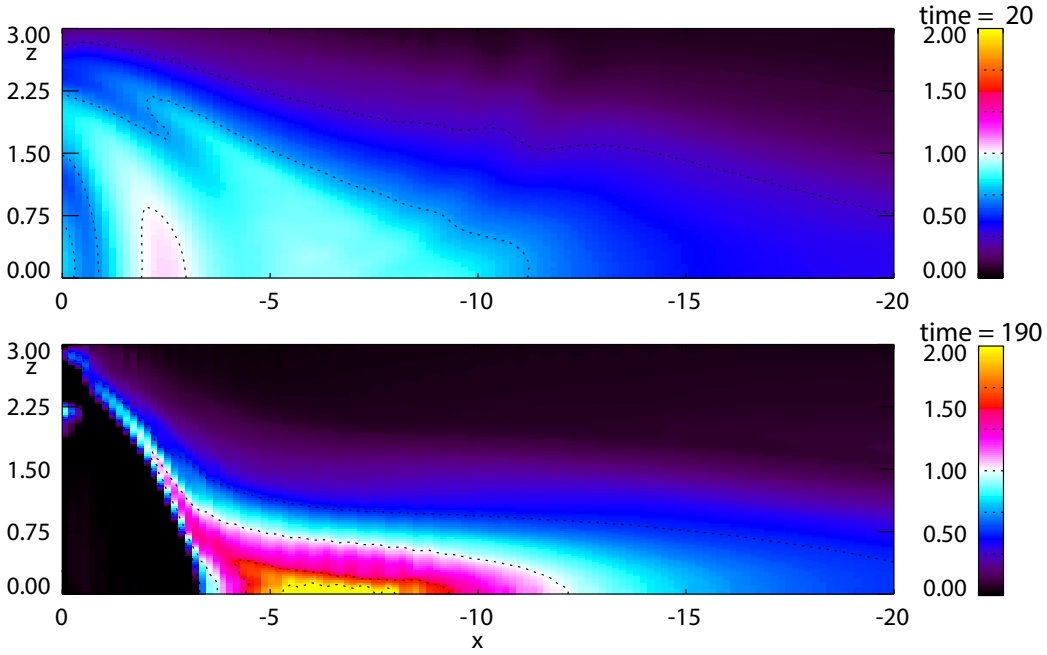

Figure 5.1. Crosstail current density in the midnight meridian plane. The top and bottom panels show j_y at $t = 5$ and $t = 45$ minutes after the sunward outflow is switched on.

(with a fixed location in z at our Earthward boundary) during the flux depletion. The cause for the equatorward expansion is in the region around 65° where many grid cells collapse to a zero area which maps to the region of divergent and sunward convection. The two thick lines in Figure 5.3 indicate that the equatorward expansion is about 2° in latitude close to the equatorward boundary of the divergent convection and can be up to 4° in the more poleward regions of the auroral ionosphere. Note, that structures at higher latitudes move further than at the lower latitudes because of the decreasing crossectional area with increasing latitude. This also implies that the poleward plasma sheet boundary converges toward the most equatorward boundary structures. Employing this map as illustrated in Figure 5.3, all properties of the near-Earth tail can be mapped along magnetic field lines first into our Earthward boundary and from there into the ionosphere. Note, that the latitude of grid cells which collapse to a zero area can vary depending on the radial distance of sunward convection, but the overall mapping properties would not change. Figure 5.4 shows that the strong flux depletion region moves further equatorward ($\sim 1°$) if the sunward convection is assumed closer to the Earth ($x = \sim -9\,R_E$).

The construction of this mapping is most reliable close to the midnight because of the fairly strong dipolar character of field lines (close to the midnight meridian) which constitute the equatorial boundary of our map. At larger distances from midnight and higher latitudes we expect increasing errors because of (1) the assumption to fix the mapping of the Earthward edge of the equatorial plane (equatorward ionospheric boundary) by the original Tsyganenko field, and because of (2) the assumption that the longitude of boundary grid coordinates is still mostly (except for the stretching factor) determined by the Tsyganenko field mapping. The disproportionate equatorward motion of the two reference lines at

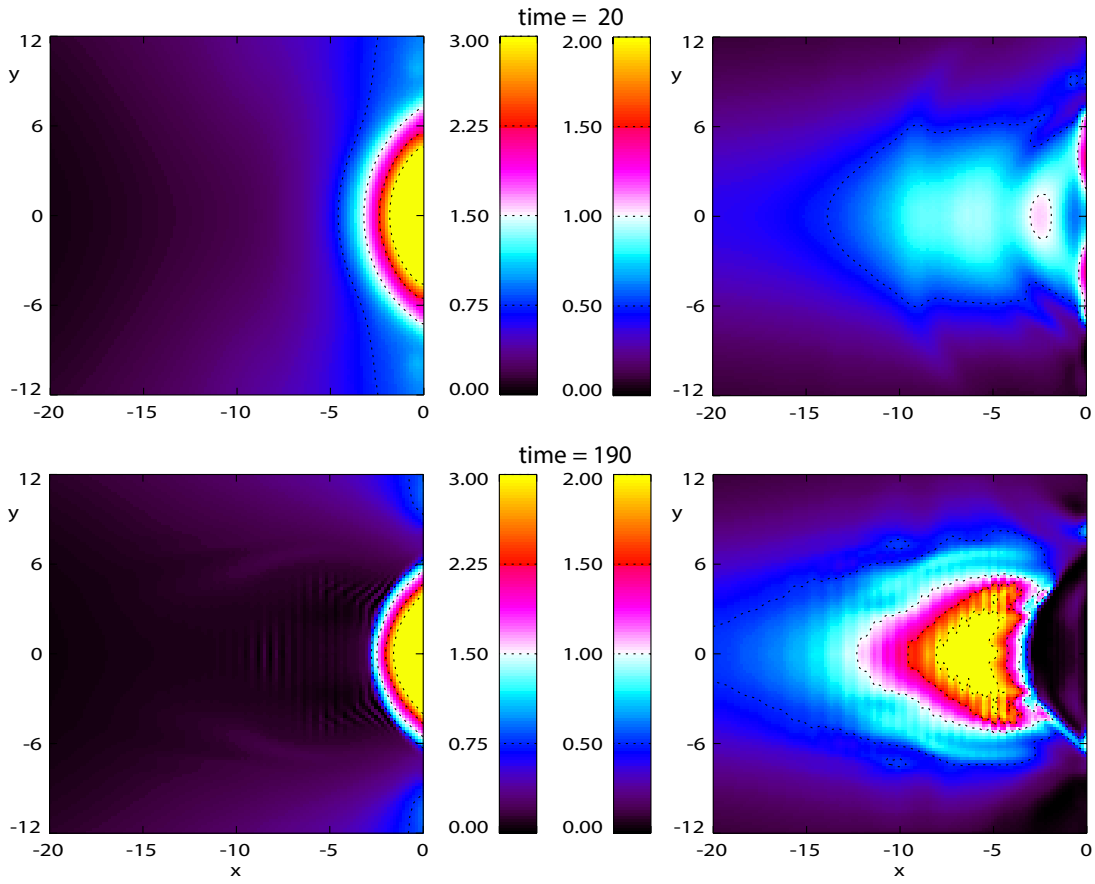

Figure 5.2. The left column presents the magnetic field strength B_z in the equatorial plane ($z = 0$), where the top (bottom) panel shows the magnetic field at $t = 5$ ($t = 45$) minutes after the sunward outflow is switched on. The format of the right column is the same as the left column, except for the azimuthal current density j_ϕ.

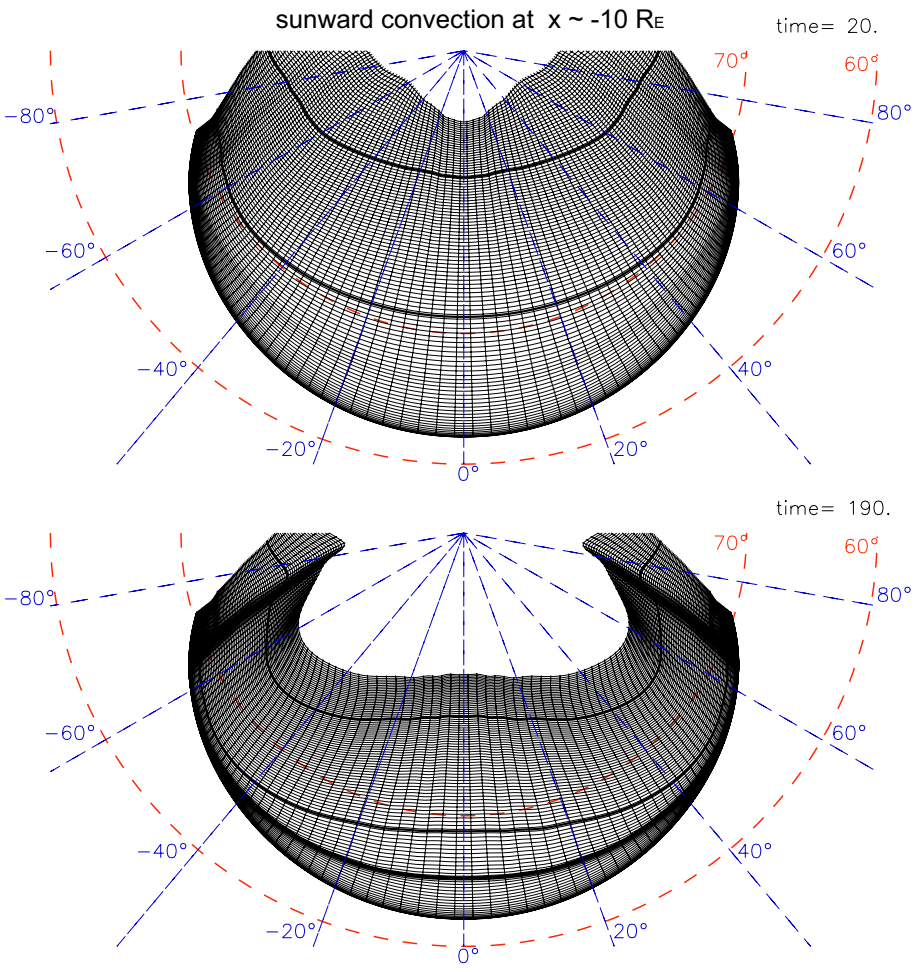

Figure 5.3. Grids of the Earthward boundary mapped into the ionosphere. The top and bottom panel show the ionospheric map at $t = 5$ and $t = 45$ minutes. The red dash lines mark the latitudes at 60° and 70° and the blue dash lines mark the longitudes from $-80°$ to 80°. Only every third boundary grid is plotted here because the actual grid is too dense for a good illustration.

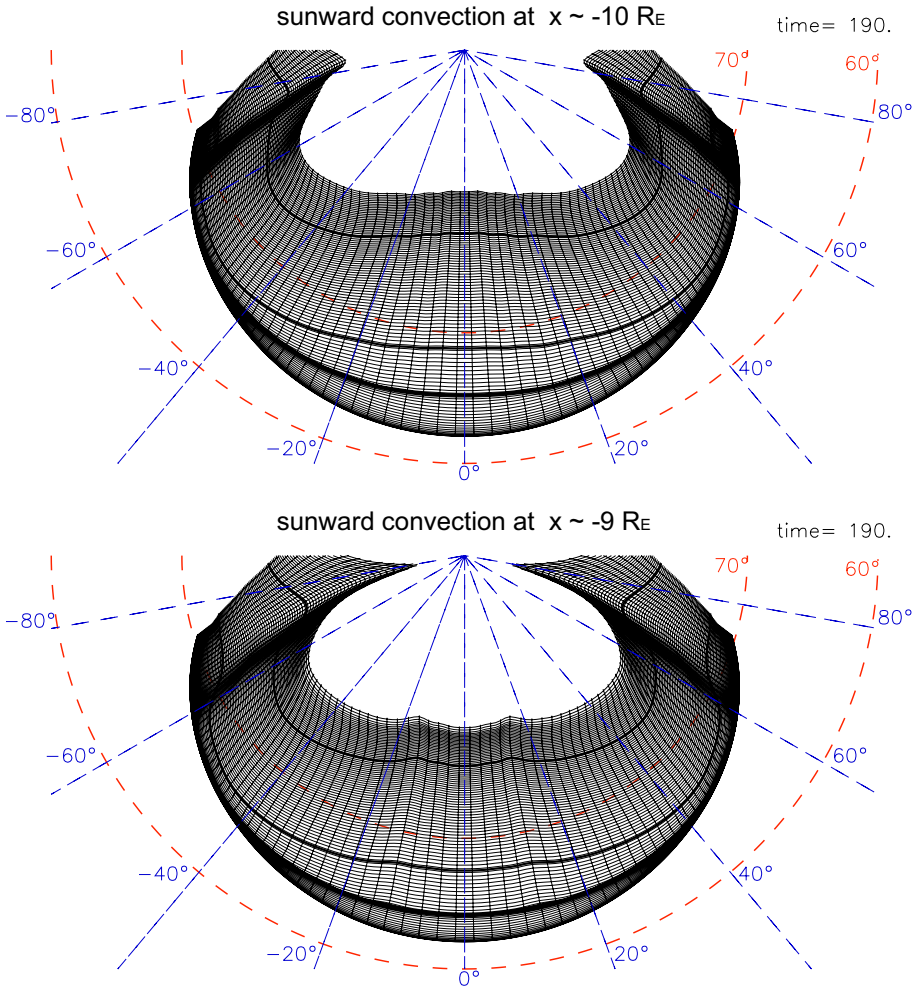

Figure 5.4. Grids of the Earthward boundary mapped into the ionosphere. The top and bottom panels show cases with sunward convection assumed at $x \sim -10R_E$ and $x \sim -9R_E$.

$\pm 40^\circ$ longitude from midnight might be an indication of the larger mapping error away from midnight at higher latitudes. Also, mapping results at high latitudes and large distance from midnight are less reliable because the corresponding field maps into one of the peripheral or lobe boundaries of the simulation.

It is instructive, to examine how the different simulation boundaries map along the magnetic field into the ionosphere. The map in Figure 5.5 shows the image of these boundaries in different colors for time $t = 5$ and $t = 45$ minutes. The ionospheric image of the equatorial plane is indicated in yellow and reconfirms that the amount of closed magnetic flux through the equatorial plane is significantly reduced. The remainder of this chapter focuses mostly on the mapping of a restricted region in latitude and around midnight because of the increasing errors at higher latitudes and further from midnight. It should be mentioned that the mapping close to midnight may slightly underestimate the equatorward expansion because the mapping assumes an unmodified magnetic field in the inner magnetosphere, but, it is well established that the magnetic field close to geosynchronous distances also decreases significantly during the expansion phase.

Figure 5.6 presents a first example of the magnetic field component B_x at the Earthward boundary mapped into the ionosphere. The latitude and longitude are plotted in polar coordinate in a region limited by 40° from midnight and from about 62° to 72° in latitude. It demonstrates a strong reduction of magnetic field in the region around 65° which is caused by MFD at times typical for the late growth phase. The following section is using ionospheric maps like this one to illustrate and characterize the evolution in the magnetotail simulation mapped into the auroral ionosphere.

5.2.3 Flux Tube Entropy

In order to examine the overall motion of plasma sheet boundaries, Figure 5.7 shows the ionospheric map of the magnetic flux tube entropy (at times $t = 5$ and $t = 45$ minutes) defined as

$$H = \int \frac{p^{\frac{1}{\gamma}} ds}{B},$$

where p is the thermal pressure, $\int \frac{ds}{B}$ is the magnetic flux tube volume, and $\gamma = 5/3$ for the adiabatic convection. The line integral of the flux tube entropy is integrated between the Earthward boundary and the equatorial plane (or one of the other boundaries) and is then mapped into the ionosphere to demonstrate the change of plasma sheet boundaries mapped into the ionosphere. The dot-dashed lines in Figure 5.7 indicate the location of the boundary edges of the simulation domain. The lower line (red) represents the intersection between Earthward boundary and equatorial plane, the middle line (black) indicates the intersection between equatorial plane and tailward boundary, and the top line (black) represents the intersection between tailward and lobe boundary. These lines are chosen to provide information on the endpoints of the field line integration.

We note the flux tube entropy very close to the Earthward boundary has a larger entropy error because of the limited length of magnetic field lines within the simulation domain. Similarly the

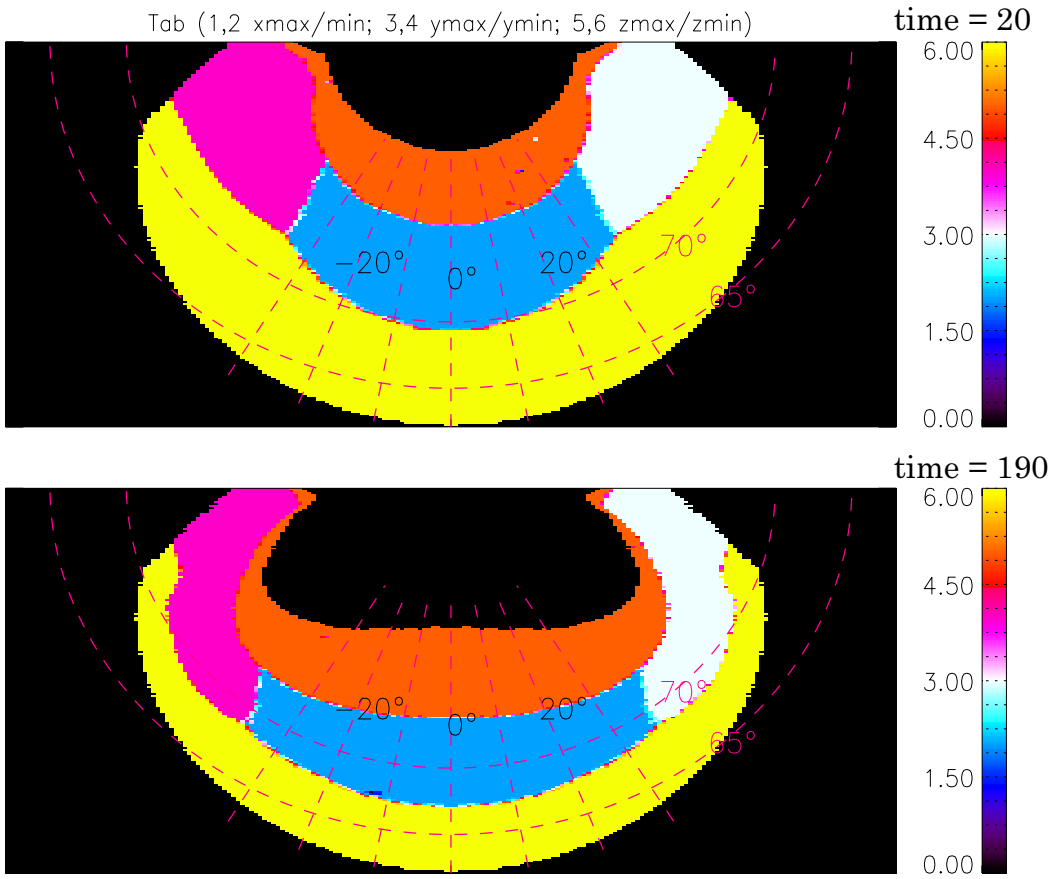

Figure 5.5. Endpoints of the magnetic field lines traced from the Earthward boundary at (top) $t = 5$ and (bottom) $t = 45$ minutes. The values 2, 3, 4, 5, and 6 represents the endpoints of magnetic field lines connected to the x_{min}, y_{max}, y_{min}, z_{max}, and z_{min} boundaries.

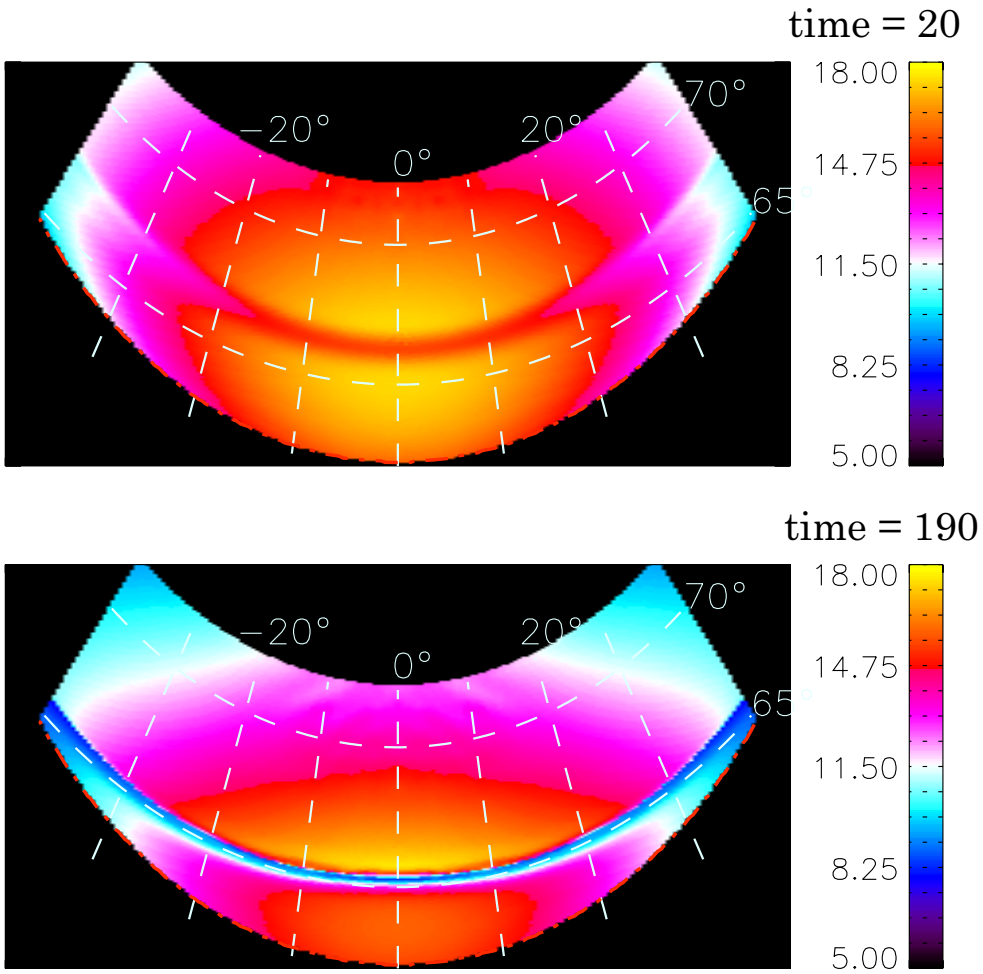

Figure 5.6. Ionospheric maps of magnetic field component B_x at the Earthward boundary. The top and bottom panels show the map at $t = 5$ and $t = 45$ minutes. The white dash lines mark the latitudes and longitudes, where the map is within the range from $-40°$ to $40°$ in longitude and $62°$ to $72°$ in latitude.

entropy at high latitudes is misleading and an artifact of the simulation because the length of field lines is limited by the simulation boundaries but more importantly flux tube entropy is ill defined for high latitude open field lines. The dark region in the figure corresponds to the dipolar field with a very low entropy. The location of the near-Earth plasma sheet and mid-tail plasma sheet are the blue and yellow region, respectively. The flux tube entropy decreases at higher latitudes, where magnetic field lines are connected to the tail- or lobeward boundary of the simulation domain, and because the plasma pressure decreases for lobe field lines. The edge between equatorial and tailward boundary is located at $x = -45\,R_E$ in the simulation and it moves from about 69° to 66.5° in latitude.

Although the simulation does not contain explicitly the open/closed boundary, the plasma sheet boundary has to be slightly equatorward of the intersection between tail- and lobeward boundary (about 1° to 2° poleward of the maximum field line entropy). This implies a motion from about 71° to 68° for the lobeward plasma sheet boundary. The near-Earth plasma sheet location is somewhat diffuse initially but is clearly indicated by the transition from dark to purple at $t = 45$ min, indicative for a steeper gradient at this time. Overall the figure demonstrates a clear equatorward motion of the entropy distribution by 2° to 3°, moving with a velocity about 100 m/s which is slow and comparable with the drift velocity of growth phase arcs found by *Aikio et al.* [2002]. Note that the equatorward motion of the open/close boundary is not caused by magnetic flux added to the magnetotail for the presented results because this simulation includes no such transport. The removal of magnetic flux by the sunward divergent flow is sufficient to cause a realistic equatorward motion of typical tail properties.

5.2.4 Crosstail Plasma Sheet Current and Field-Aligned Currents

Figure 5.8 presents the ionospheric maps of crosstail plasma sheet current and is obtained by mapping the crosstail current density from the equatorial plane along field lines into the ionosphere using the outlined mapping procedure. The larger current close to our equatorward boundary (yellow) is likely a numerical artefact and is present only on the first few grid points (from the Earthward boundary) of our simulation. It is shown that an initially wide CS develops into a thin intense current layer, located in the region where the magnetic flux is strongly depleted by the sunward divergent flow. The most intense current toward the end of the growth phase is confined to a narrow latitudinal extent of about 1°.

Figure 5.9 shows the ionospheric maps of field-aligned currents (FAC's). In the absence of divergent perpendicular currents along a magnetic field line, $\frac{J_{//}}{B}$ is a conserved quantity on magnetic flux tubes. Therefore the mapped field-aligned current $J_{//}$ is given by

$$J_{//} = \frac{J_{//msp}}{B_{msp}} B_{io},$$

where $J_{//msp}$ (B_{msp}) is the field-aligned current density (magnetic field) at the Earthward boundary. It is shown that the intensity of field-aligned currents increases about 6 fold and reaches 10^5 nA/m^2 in the late growth phase. The width of these intense FAC's decreases to a rather small fraction of the initial

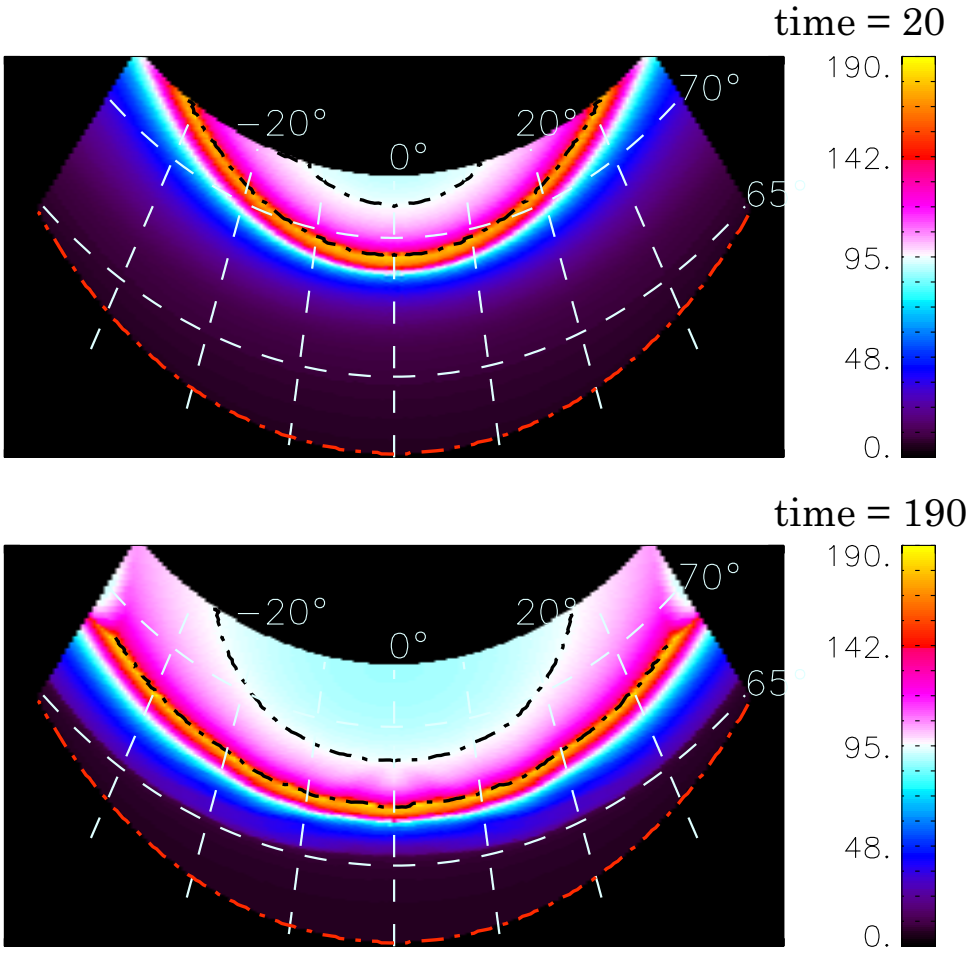

Figure 5.7. The format is the same as Figure 5.6, for the flux tube entropy. The red dot-dash line represents the intersection between the Earthward boundary and the equatorial plane.

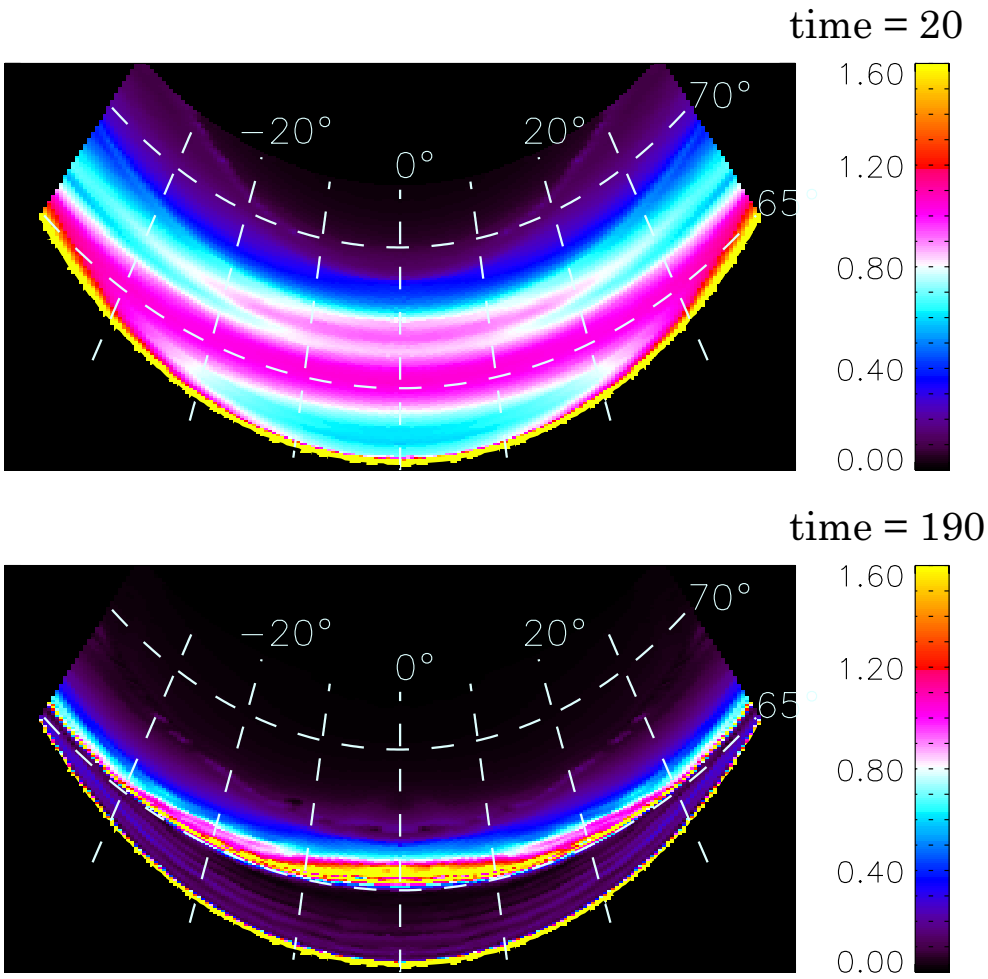

Figure 5.8. The format is the same as Figure 5.6, except for the crosstail plasma sheet current.

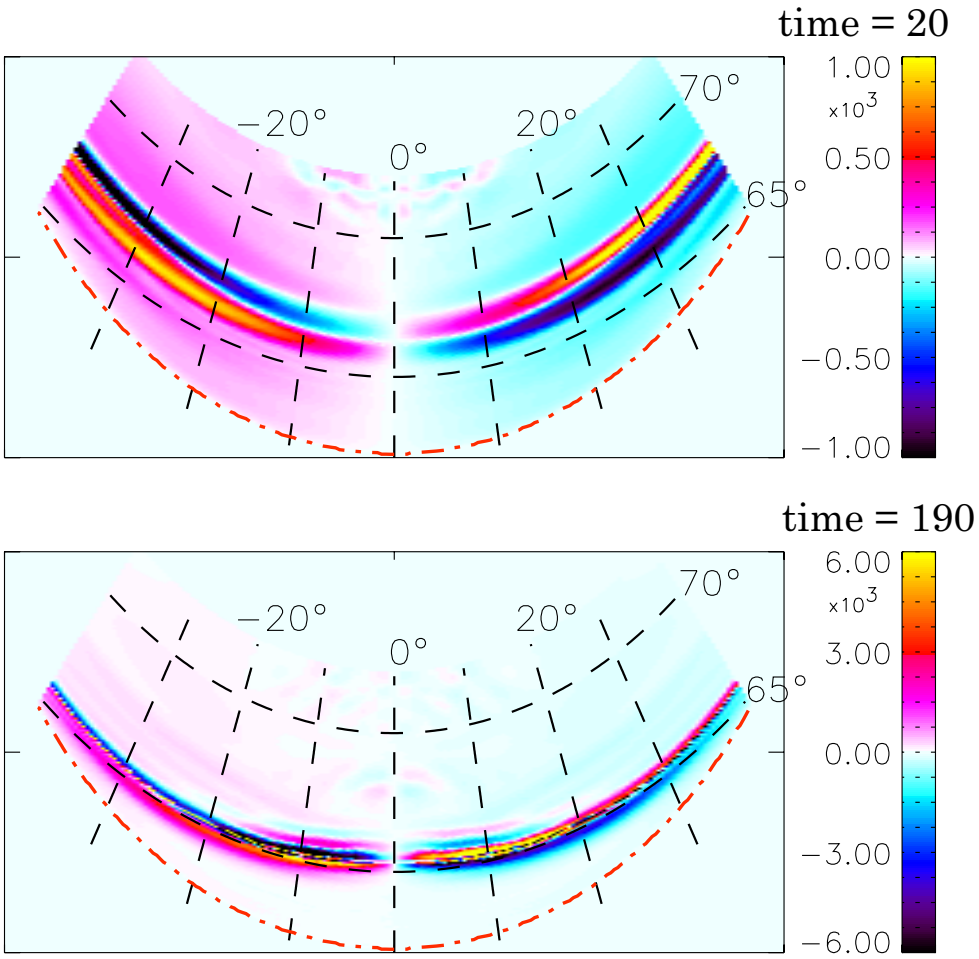

Figure 5.9. The format is the same as Figure 5.6, except for the field-aligned currents.

distribution during the evolution. These strong field-aligned currents are directly associated with the region of the thin CS (see also Figure 5.8) because the sunward divergent flow bends the magnetic field lines in a narrow magnetic flux region, thereby, inducing the current density enhancement. The region 1 and region 2 currents (hereafter denoted as R1 and R2) are located in close proximity of the outer and inner boundary of the return flow, respectively. The R2 current is located directly equatorward of the R1 and the intense crosstail current. The R1 current maps into the region of the most intense crosstail current.

Figure 5.9 illustrates an evolution of thinning and convergent motion of R1 and R2 currents during the growth phase. The spatial thinning of the field-aligned currents is likely also a result of the magnetic flux depletion. The strongly reduced B_z in the near-Earth tail requires a larger sunward flow in order to maintain an approximately constant flux transport rate ($E_y \sim v_x B_z$). This explains a narrower flow channel and an increasing convection velocity for consistency with an approximately constant magnetic flux transport rate (potential). Therefore faster convection in a narrower channel can be expected in the ionosphere, consistent with more intense and narrower FAC distributions. Figure 5.9 also shows a clear equatorward motion of the R1 and R2 current system approximately consistent with the overall equatorward motion. The maximum R2 current moves by about 1° and the R1 current by about 2° equatorward. The distribution of field-aligned currents suggests that the growth phase arc is moving close to (or possibly into) the dipolar field region (typically characterized by diffuse aurora region) in the late growth phase.

5.2.5 Electron and Ion Isotropy Boundaries Superposed on the Field-Aligned Currents and Plasma Sheet Magnetic Field

Figure 5.10 shows the 100 keV electron and 30 keV ion isotropy boundaries (IB's) mapped into the ionosphere superposed to maps of different simulation variables at time $t = 45$ minutes. The IB's are the boundaries characterized by the adiabatic/chaostic motions as well as the regions characterized by particle precipitations. In this study the IB's are chosen by a threshold value of $R_c/r_{gi} \sim 8$ in the equatorial plane [*Sergeev and Tsyganenko*, 1982], where R_c is the curvature radius of magnetic field lines and r_{gi} is the gyro radius of species. The 100 keV electron and 30 keV ion IB is represented as the yellow and black line, which is first mapped from the equatorial plane to the Earthward boundary and then into the ionosphere. Both figures present a magnified view of the mapping to better identify structures and latitudinal distances.

The top and bottom panels of Figure 5.10 show the IB's superposed on the ionospheric maps of field-aligned current density and magnetic field strength in the equatorial plane (or other boundary planes if the field line ends at any other simulation boundary). The magnetic field B_z in the equatorial plane is again determined by a field line integration from the Earthward boundary into the tail. Figure 5.10 demonstrates that the electron IB maps almost exactly to the boundary between R1 and R2 currents and to the transition region from depleted to dipolar field, implying that the substorm growth phase

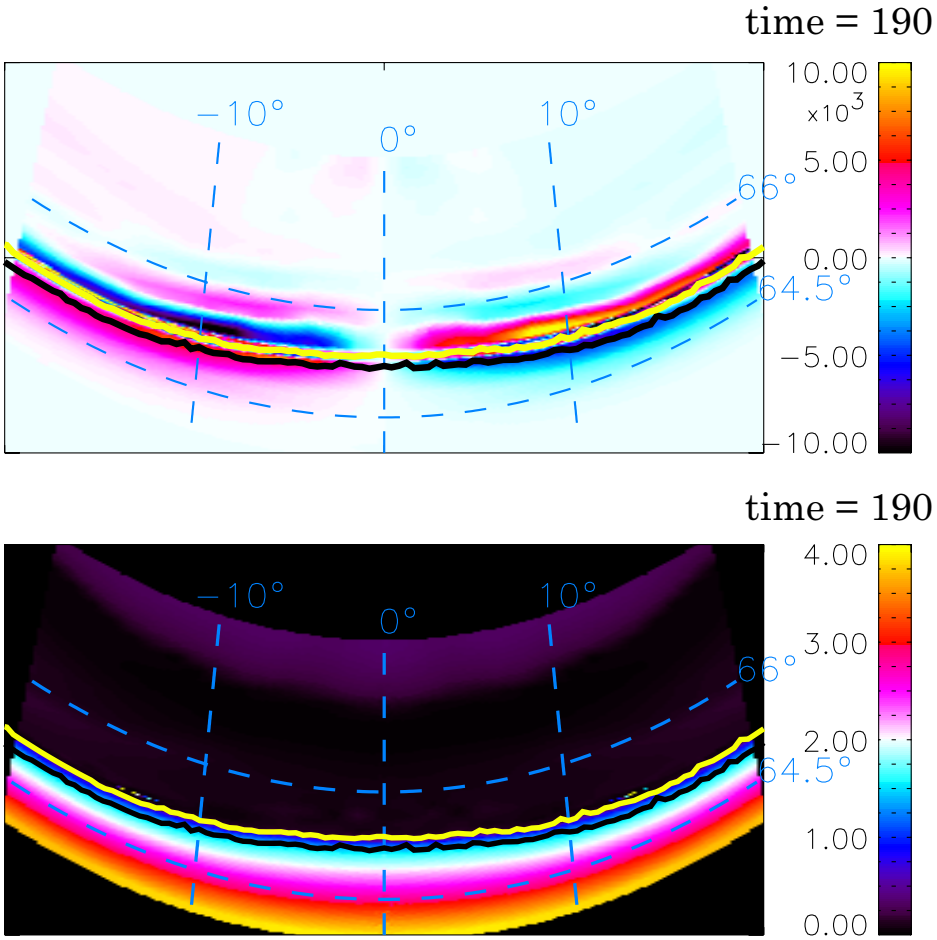

Figure 5.10. Ionospheric maps of isotropy boundaries. The yellow line presents 100 keV electron IB and the black line presents 30 keV ion IB. Top and bottom panels show the IB's superposed on the ionospheric maps of field-aligned current density and plasma sheet magnetic field strength. The maps are within the range from $-20°$ to $20°$ in longitude and $64°$ to $68°$ in latitude.

is characterized by the equatorward motion of the auroral arc very close to the region of diffuse aurora characteristic for a dipolar magnetic field. The ion IB maps into the R2 current region and the dipolar field region about 0.3° equatorward of the electron IB. The transition between dipole/stretched field is at a latitude about 65°. Note that if the dipole field equation is considered, i.e., $L = 1/\cos^2\Lambda$ (Λ is invariant latitude), the dipole field boundary should trace to $L = 5.6$ in the magnetotail. However, the dipole field boundary is located at $L \sim 7.8$ in our simulation because of the reduction of the size of the ionospheric footprints caused by the depleted magnetic flux in the near-Earth tail. The equatorward expansion, the location of the IB's, and the convergence and intensification of the R1 and R2 currents in the midnight region in the simulation as illustrated in Figure 5.10 provide a basic growth phase morphology that agrees well with typical properties of the auroral ionosphere [*Sergeev et al.*, 1993b; *Yahnin et al.*, 1997b; *Ohtani et al.*, 2010; *Sergeev et al.*, 2012a].

A comparison of the the location of the R1 current at the beginning and the end of the growth phase indicates that the amplitude of the equatorward motion of the peak current location is slightly larger away from midnight. In fact Figure 5.10 indicates that the actual location of the thin R1 current layer and of the IB is marginally further equatorward away from midnight (by $< 1/4°$). However, it may be interesting to note that the IB and the R1 current peak are at an almost constant magnetic latitude. This is somewhat counterintuitive because on a global scale one would expect the largest amplitude at midnight. We do not know if this result is an artifact of our mapping but we note that for instance *Xing et al.* [2010] showed several examples where the growth phase or onset arc appears to be on an almost constant latitude within 15° to 30° from midnight. The ion isotropy boundary corresponds well to the latitude of the maximum ion energy flux precipitation [*Newell et al.*, 1998].

5.2.6 Electron and Ion Isotropy Boundaries Superposed on a Quasi Convection Potential

Figures 5.11 and 5.12 show the IB's superposed on the ionospheric maps of a quasi convection potential. The potential calculation is a challenge and associated with several uncertainties because of a number of reasons: First, the electric field in the simulation is not a potential field. Most of the electric field in and close to the equatorial plane is associated with the change of the magnetic field $\partial B/\partial t$ and is therefore inductive. Second, we specify the outflow condition at the Earthward boundary such that the electric field at the Earthward boundary may have numerical artifacts. Third, the present model does not consider effects from finite ionospheric conductance. However, the changes in the magnetic field and the electric field are slow such that the electric field close to the Earthward boundary may at least indicate some basic insight into changes of the ionospheric convection. Figure 5.13 shows the variation of electric field at the boundary close to the Earth, which is very slow and different from the electric field associated with propagating Alfvén waves.

We select a crosstail cut at $x = -6\,R_E$ close to the Earthward boundary, and the quasi-potential is calculated in this plane and the small part of the equatorial plane between $-5\,R_E$ and $-6\,R_E$. In comparison, we select another cut at $x = -16\,R_E$ and the equatorial plane between $-5\,R_E$ and

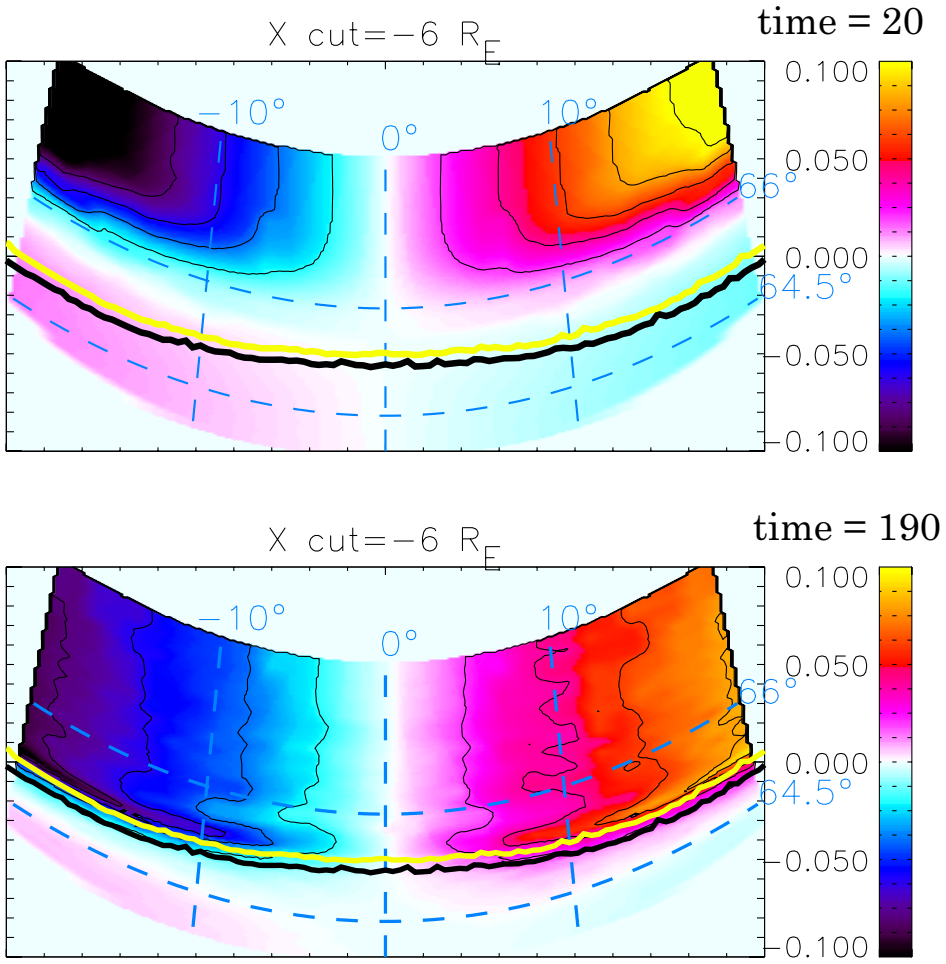

Figure 5.11. Ionospheric maps of isotropy boundaries superposed on the quasi convection potential maps. The format of each panel is the same as Figure 5.9, except for the quasi-potential for the x cut$=-6R_E$.

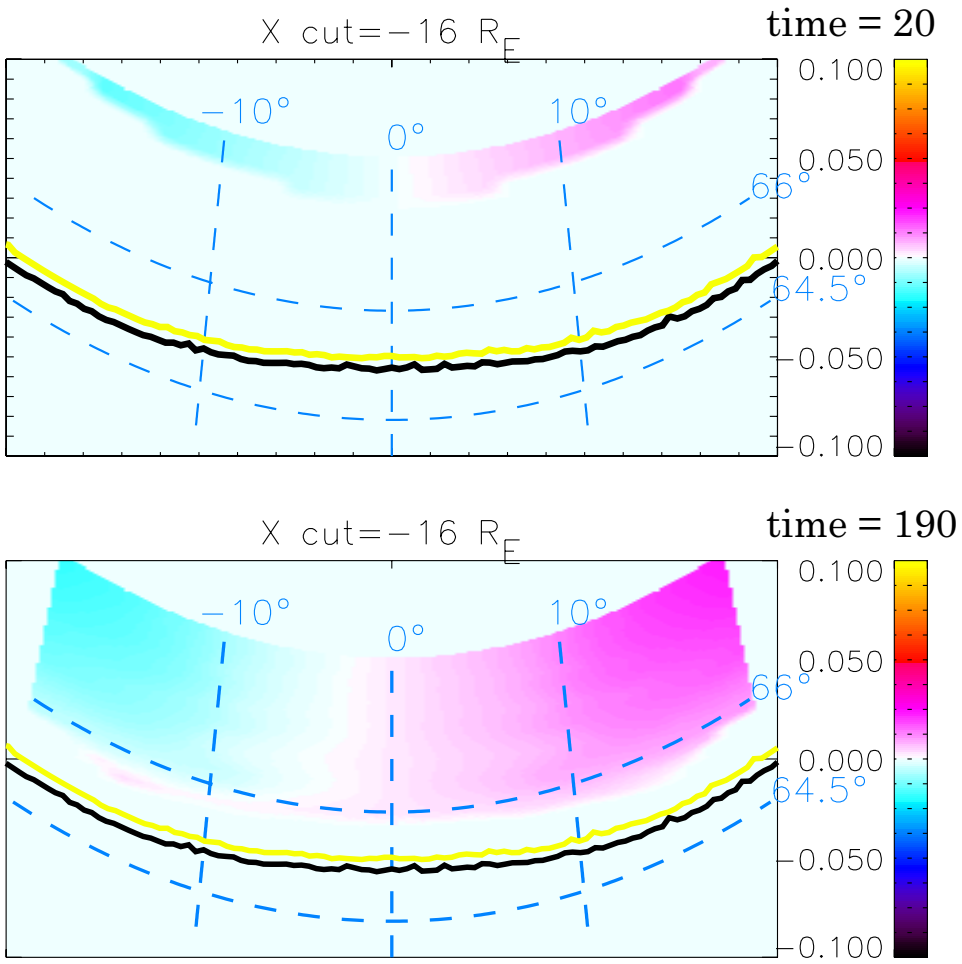

Figure 5.12. The format of each panel is the same as Figure 5.11, except for the quasi-potential for the x cut=$-16R_E$.

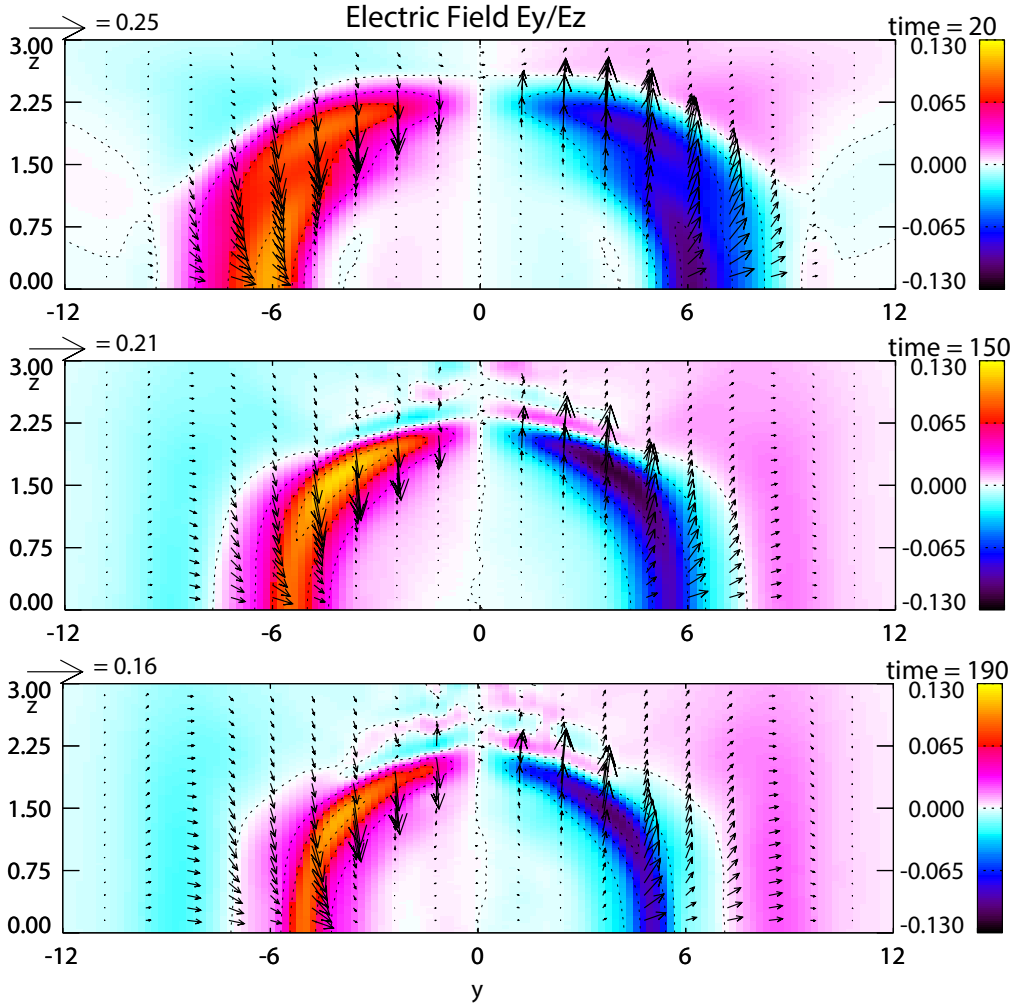

Figure 5.13. Electric field close to the Earthward boundary at times $t = 20$, $t = 150$, and $t = 190t_A$. The color represents the normal component of electric field (E_x), and the arrow represents the tangential component of electric field ($E_y\hat{e_y} + E_z\hat{e_z}$).

$-16\,R_E$ further away from the Earthward boundary as shown in Figure 5.12. The purpose of the quasi-potential map is twofold. (a) The mapped potential provides at least qualitatively insight into the expected changes for ionospheric convection and also a reference relative to the location of the convection reversal and the isotropy boundaries and field-aligned current regions. (b) It is sometimes believed the plasma sheet electric field can be mapped into the ionosphere, and we demonstrate by comparison with a different reference plane for the potential calculation that this is not the case in the simulation. Both of these points are difficult to make without this map.

The thin black lines in Figure 5.11 represent contour lines of the potential which can also be interpreted as flow lines. It is shown that the overall convection propagates equatorward during the CS thinning. A clear pair of west- and eastward flows are seen away from the midnight, which is associated with the sunward divergent outflows. As shown in the bottom panel, the equatorward gradient of the quasi-potential steepens toward the end of the growth phase (at $\sim 65°$), implying an increasing velocity of west- and eastward flows very close to the electron IB. In comparison with the top panel in Figure 5.10, the flow channels are approximately coincident with the boundary of R1 and R2 currents. This result implies the location of pre-onset arc is likely inside the channel of westward flows at the pre-midnight region, which is consistent with the ionospheric observation from *Bristow et al.* [2003]. It is also worth mentioning that the quasi-potential shows an apparent change with the choice of the x location of the plane to evaluate the electric field. Note, the quasi-potential is calculated from the cut and the equatorial section between the cut and $x = -5\,R_E$, i.e., a larger contribution of plasma sheet electric field is involved when the cut in x moves further tailward. Figure 5.12 indicates that the overall plasma sheet potential is very low implying that plasma sheet convection is very slow. This result is expected because the magnetotail changes are subject to a slow adiabatic evolution and thereby the convection is slow, i.e., small convective electric fields consistent with many results of quasi-static evolution [*Erickson and Wolf*, 1980; *Schindler and Birn*, 1993; *Birn et al.*, 1998]. It is shown that the quasi-potential highly increases by a factor up to 9 when it is evaluated closer to Earth. The strong increase of the quasi-potential is caused by the change of the magnetic field associated with significant inductive electric fields. Finally, it should be mentioned that the strong gradient of the flow toward the equatorward edge is caused by our assumption of the outflow channels in the simulation. This gradient would disappear for rather slow sunward convection in the dipolar region because of the different mapping properties comparing dipolar and thin CS regions.

5.3 Flux Tube Displacement in the Magnetotail

The previous section has demonstrated a clear equatorward motion of all of magnetotail properties mapped into the ionosphere during the growth phase. The removal of magnetic flux in the tail results in the contraction of ionospheric flux tube footpoints such that all of the mapped magnetotail structures move equatorward. Often the equatorward expansion is believed to be associated with Earthward or tailward flows in the plasma sheet. Here we quantitatively examine the motion of flux tubes in

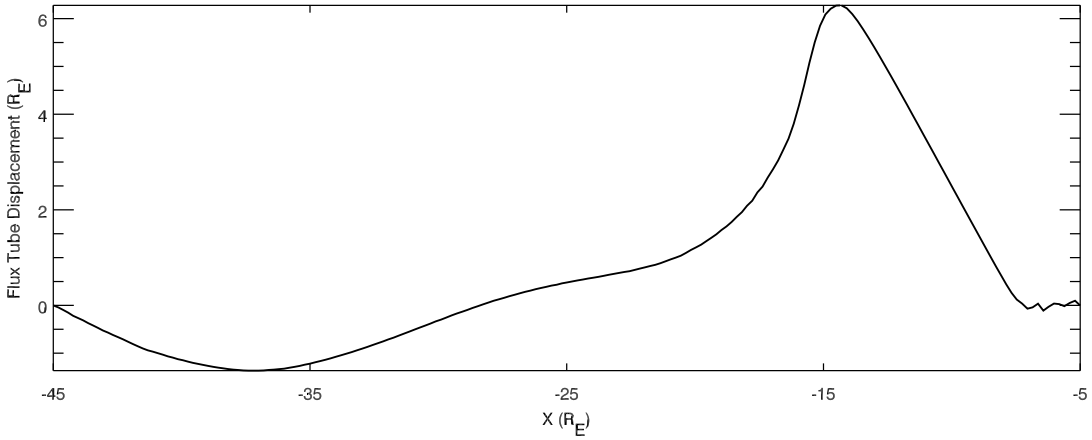

Figure 5.14. Flux tube displacement in the midnight magnetotail based on the tracing of plasma elements in the equatorial plane. The x axis is the radial distance in the magnetotail within the simulation domain. The y axis is flux tube deviations from the initial position, which positive (negative) values corresponding to the Earthward (tailward) motion.

the magnetotail to provide further insight into the cause for the equatorward motion of ionospheric footpoints and the role of magnetic flux depletion rather than a simple stretching of the magnetic field lines by divergent Earthward convection.

Figure 5.14 shows the radial displacement of the footpoints of flux tubes (along x in the midnight) in the equatorial plane based on the tracing of plasma elements in the magnetotail from $t = 20$ to $t = 190t_A$. Here a positive (negative) value corresponds to Earthward (tailward) displacement of the flux tube along the radial direction. The radial displacement of equatorial footpoints is generally small and negligible except for a region between $-18\,R_E$ and $-8\,R_E$. The largest displacement is positive with a value of about $6\,R_E$ for an initial flux tube footpoint at about $-15\,R_E$. Closer to Earth the gradient is negative implying converging motion along the x direction. Tailward the gradient is positive implying that flux tubes starting tailward of the maximum have smaller displacements implying divergent motion or stretching. However, the stretching factor is only approximately 2 in the very limited region between $\sim -15\,R_E$ and $-18\,R_E$, i.e., the flux tube footpoints that are initially separated by $3\,R_E$, are finally separated by about $6\,R_E$ at the end of the growth phase. Ignoring any crosstail variation, the stretching would only reduce the equatorial magnetic field by about 50%. While this is not negligible, it is insufficient to explain the actual reduction of the magnetic field in the midnight region which requires the divergent flow away from the midnight plane.

Furthermore, the convergent motion of equatorial footpoints Earthward of the maximum in Figure 5.14 implies an increase of the equatorial field at the associated location opposite to observational evidence and opposite to our model properties. This demonstrates that CS thinning and the mapping properties of our model cannot be attributed to simple notion of field line stretching which within our model is not negligible but an effect secondary to the divergent flow along the crosstail direction.

5.4 Discussion and Summary

This study examines the evolution of the magnetotail and the associated ionospheric signatures for conditions that lead to a strong depletion of the near-Earth closed magnetic flux. The midnight MFD is caused by sunward convection to replenish magnetic flux which is eroded on the dayside magnetopause during periods of southward IMF. This convection is subject to adiabatic constraints during the slowly evolving growth phase, that is, the depletion of magnetic flux in the tail is confined to the region of flux tube entropy which matches the entropy of recently reconnected flux tubes on the dayside. The MFD leads to a strong reduction of B_z in a flux reservoir located in the midnight equatorial plane and results in strong CS thinning as well as a significant increase of the cross-tail current density.

This chapter examines the evolution of the auroral ionosphere associated with the changes of magnetotail structure by mapping tail properties from the Earthward boundary into the ionosphere. Our results show that overall plasma sheet features move equatorward by 2° to 3° caused by the depletion of closed magnetic flux. Figure 5.15 illustrates the MFD and the associated equatorward motion during the growth phase. Closed magnetic flux is removed by the sunward divergent convection in the near-Earth tail (red arrows in the equatorward plane), and therefore causes a contraction of the ionospheric footpoints of this tail region. The magnetic field line (a) located equatorward is approximately stationary, and the ionospheric footpoints of the magnetic field lines (b) and (c) converge toward lower latitudes even though their Earthward motion in the tail is small. This convergent motion results in a sharp transition from the dipole to stretched magnetic field as well as strong CS thinning during the growth phase.

The results of the MFD show that the sunward divergent flow is associated with the source region of field-aligned currents. The evolution of R1 and R2 currents are associated with the changes of outer and inner boundaries of the return convection channel. In the late growth phase, magnetic field lines are highly deformed by a faster divergent convection in a narrower channel such that the strong field-aligned currents develop within a very thin region of about 1° in latitude. Also, the R1/R2 boundary is approximately coincident with the electron isotropy boundary in the late growth phase. A plausible proxy of the pre-onset arc may be the location of the highest intensity R1 currents. The presented results suggest that this region is located in close proximity just poleward of the 100 keV electron IB and in close proximity to the intensified R2 currents. Our model results indicate that the distance between the maximum R1 intensity, the electron IB, and the R2 current is smaller than 1° toward the end of the CS thinning. Considering either the R2 current region or a small region poleward of the ion IB as proxies for ion precipitation, it is conceivable that the onset arc is either just poleward of the diffuse aurora or even within the region of diffuse proton aurora considering the several 10 km broadening of it by charge exchange collisions. This is consistent with results from *Newell et al.* [1998] which demonstrate that the 30 keV ion isotropy boundary corresponds well to the latitude of the maximum ion energy flux precipitation. These results agree well with many observational studies and may shed light on the controversy regarding the location of the late growth phase arc relative to the diffuse proton aurora.

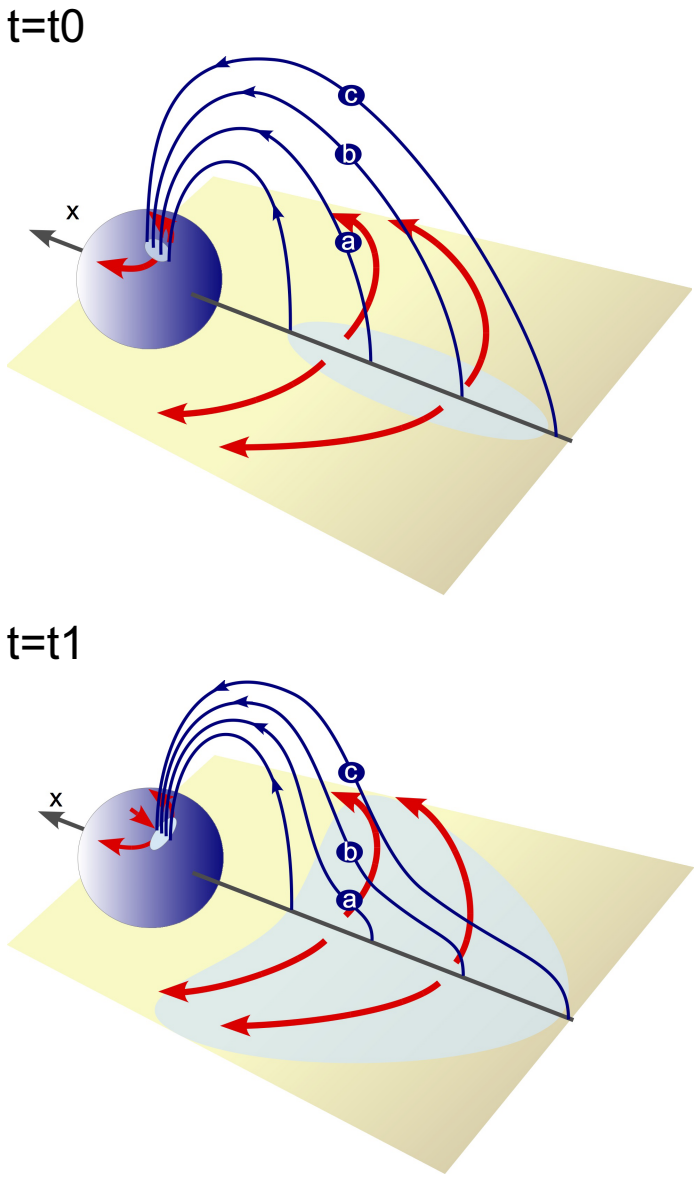

Figure 5.15. Illustration of MFD and the associated equatorward motion in the ionosphere. The top and bottom panel is at times $t = t_0$ (initial) and $t = t_1$ (growth phase). The points (a), (b), and (c) represent different magnetic field lines. The sunward divergent flow is present as red arrows in the equatorward plane.

The physics of substorm onset has been highly debated for a long time, i.e., outside-in and inside-out models (see Chapter 1). The detailed observational confirmation of either model is not easy and depends heavily on the exact relative locations of satellites and ground observations. It is also not unambiguous because of the incomplete knowledge of the magnetospheric configuration which determines the mapping. Close to the end of the CS thinning in our simulation, field lines originating from $8\,R_E$ and $20\,R_E$ in the magnetotail (in the midnight meridian) map to the latitudes of 65.3° and 66.0° respectively, which is less than 1° latitudinal separation in the ionosphere. The result suggests that the distinction between the inside-out and outside-in hypotheses is even more challenging than conventionally assumed, because the intense field-aligned currents and IB's develop in a very narrow latitudinal region, which makes it difficult to attribute any ionospheric observations in this region to a specific magnetotail location between 8 and $20\,R_E$. A less than 1° separation is also well within the uncertainty of the mapping of traditional magnetic field models [*Shevchenko et al.*, 2010]. Furthermore the transition to the dipolar magnetic field boundary in our simulation would map to $L = 5.6$ based on a dipole field while it is actually located at $L = 7.8$ in the simulation. These examples make it very obvious that dipole or T96 magnetic field model are incapable to characterize magnetotail locations properly and a Tsyganenko magnetic field require a significant correction that depends on the actual tail dynamics during the growth phase.

All of the presented results have been obtained by considering only the depletion of closed magnetic flux in the midnight region without adding magnetic flux and energy to the lobes. The objective of this approach was to examine the effects of magnetic flux depletion, and including a lobe driver would have made it difficult or impossible to attribute configurational changes of the magnetotail or of the mapping to either cause. Finally we demonstrate the influence of the addition of open magnetic flux on the auroral ionosphere without the presence of the depletion of closed magnetic flux. The ionospheric grid map of the Earthward boundary in shown in Figure 5.16 at times (top) $t = 5$ and (bottom) $t = 45$ minutes. It illustrates that the grid is significantly distorted at high latitudes during the evolution but there is no overall equatorward motion at latitudes corresponding to the location of the plasma sheet mapped into the ionosphere. In Chapter 4 we also demonstrate that the magnetic field lines do not converge significantly equatorward for lobe compression. Another important aspect of the tail dynamics is the slow intensification and equatorward motion of the R1 and R2 currents. Figure 5.17 shows the field-aligned currents for the case of lobe compression only at times $t = 5$ and $t = 45$ minutes. The scale for these currents is the same that is used in Figure 5.9 for MFD. Figure 5.17 demonstrates that lobe compression does not lead to a clearly identifiable R1 and R2 current system, and field aligned current intensity is generally small compared to MFD. The figure also gives no indication of an equatorward motion of any current system. This illustrates that the divergent flow is a central element for the evolution of field-aligned current and for the equatorward motion of these currents. This demonstrates the importance of MFD for the growth phase auroral evolution.

In summary this study examines the changes of magnetotail structures mapped into the ionosphere

during the growth phase based on a mesoscale tail simulation of magnetic flux depletion. In this example depletion of magnetic flux is caused by azimuthal sunward flow out of the simulation domain with a flux transport rate of 40 kV. Overall the results demonstrate an ionospheric equatorward motion of about 2° to 3° associated with the evolution of CS thinning caused by midnight MFD. The removal of magnetic flux in the near-Earth tail causes a contraction of the ionospheric footpoints of this tail region such that all of the mapped magnetotail quantities participate in the equatorward motion. It is found that the mapped thin CS is located in the region where magnetic flux is strongly depleted, and in close proximity with strong and narrow R1 and R2 sense field-aligned currents which are separated by less than 1° in latitude at the end of the CS thinning. The presented results also show a sharp transition between the dipole and stretched magnetic field and an evolution of thinning and convergent motion of field-aligned currents in the late growth phase.

All of the presented results have been obtained without considering the addition of magnetic flux and energy to the lobes. This does not imply that a lobe driver is unimportant for the evolution during the growth phase. Chapter 4 has demonstrated that a lobe driver can also cause a thin CS formation. Note, however, that a lobe driver alone can only locally re-distribute the equatorial magnetic field in the tail such that the significant equatorward displacement of ionospheric boundaries likely requires significant magnetic flux depletion as considered in the presented results.

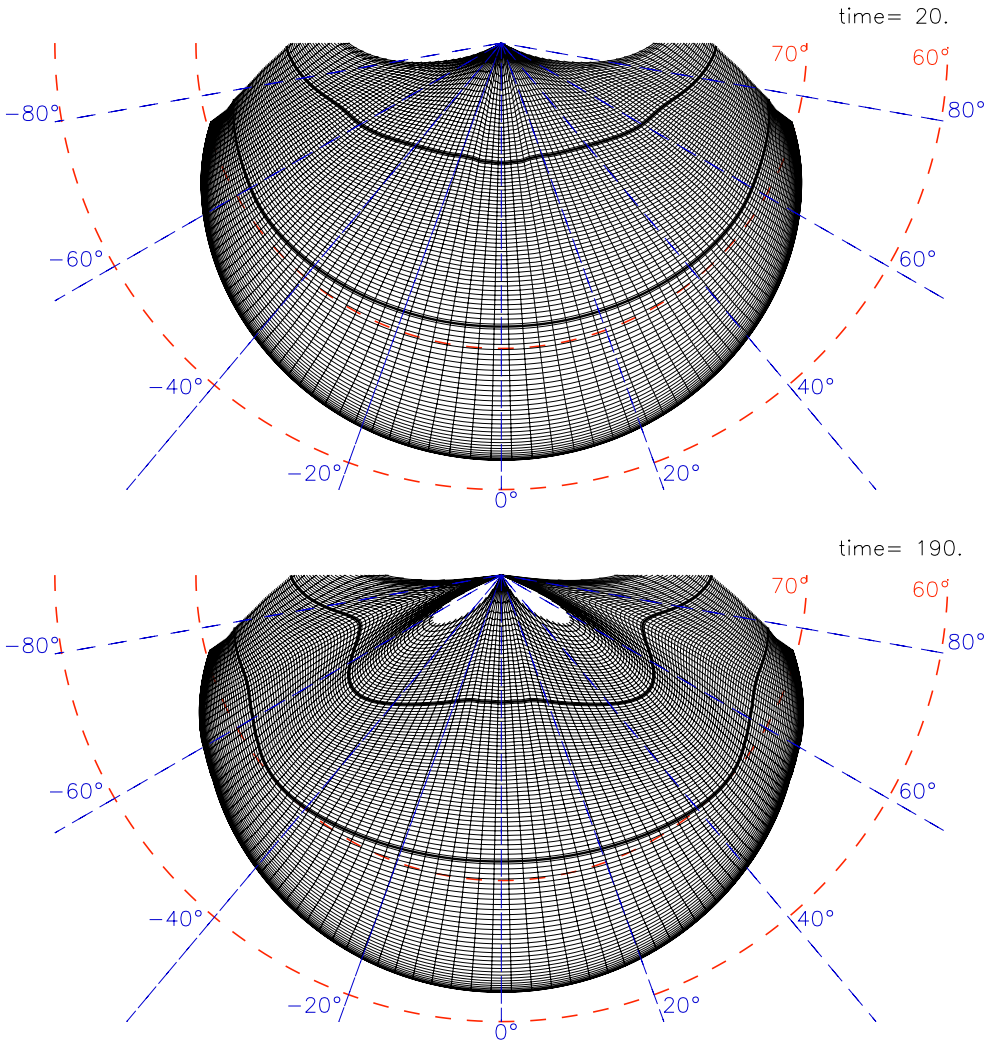

Figure 5.16. Grids of the Earthward boundary mapped into the ionosphere. The format of each panel is the same as Figure 5.3, except for lobe compression.

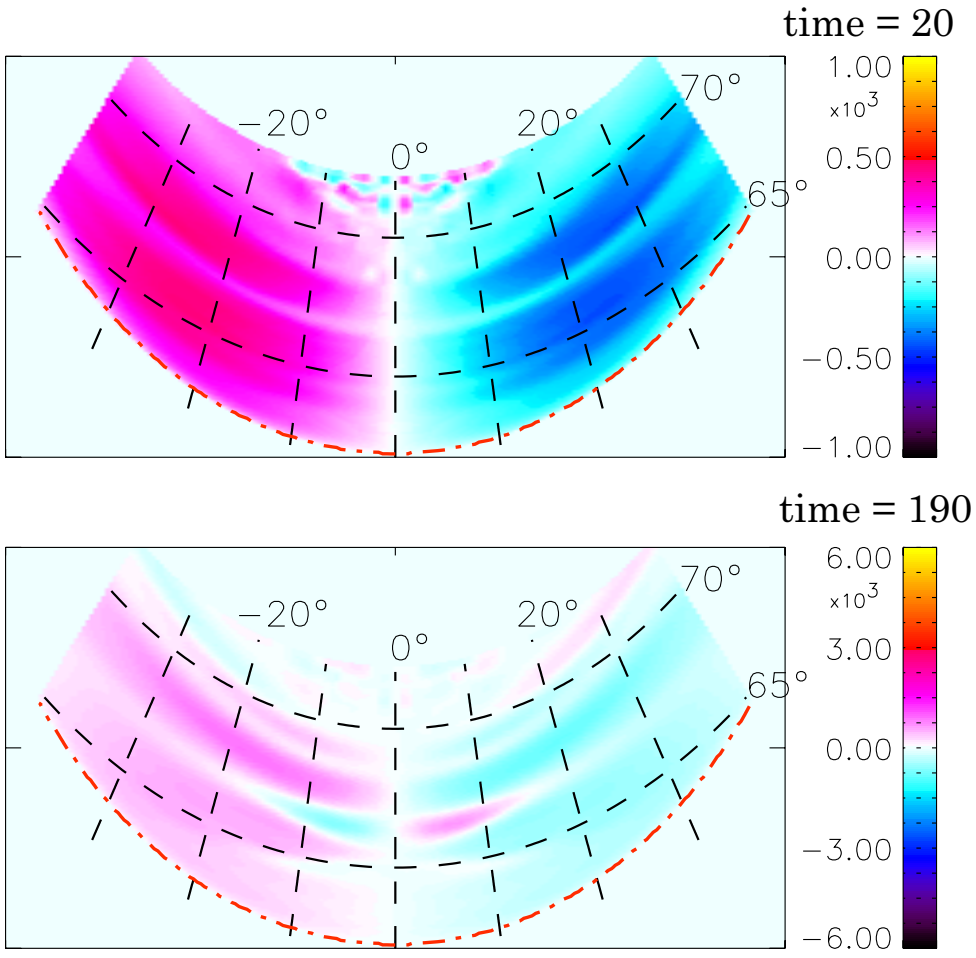

Figure 5.17. Ionospheric map of the field-aligned currents. The format of each panel is the same as Figure 5.9, except for lobe compression.

Chapter 6
Discussion and Conclusions

6.1 Magnetotail Evolution

This study examines physical processes which are critical for the understanding of the evolution of the magnetotail and auroral ionosphere during the substorm growth phase. A centrally important and poorly understood property of this evolution is the formation of a thin CS in the near-Earth magnetotail. This formation is characteristic of the growth phase and represents a critical element to understand the physics of geomagnetic substorms. A drastic thinning of a CS is often observed preceding the expansion phase onset, implying that either a possible loss of the equilibrium or micro-instabilities associated with the large current density could cause the onset of the expansion phase. Either way, the very thin and intense CS sets the stage for the expansion phase onset. Although previous studies have proposed that a thin CS can be generated by means of boundary deformations or of entropy anti-diffusion, such approaches do not explain well the specific location of the thin CS or its obvious association with dayside magnetic reconnection during periods of southward IMF. Furthermore, none of the proposed models can predict the typical duration of the growth phase. It is also important to note that no model to date can predict the typical ionospheric evolution of the substorm growth phase and shed light on the role and location of the growth phase arc.

This dissertation proposes a new CS thinning mechanism based on midnight magnetic flux depletion (MFD) to replenish the magnetic flux that is eroded by reconnection at dayside magnetopause for southward IMF. It is proposed that midnight MFD is caused by sunward convection subject to the adiabatic constraint of flux tube entropy conservation in the slowly evolving magnetotail. In the quasi-static evolution of the magnetotail, the depletion of magnetic flux in the tail is confined to the region of flux tube entropy which matches the entropy of recently reconnected flux tubes on the dayside. The presented model specifies an outflow condition at the Earthward boundary to prescribe the rate of sunward magnetic flux transport by mapping an azimuthally divergent convection at $x \sim -10\,R_E$ from the equatorial plane into the Earthward boundary. It is found that a very thin CS forms in the near-Earth tail within about half an hour to an hour, consistent with the typical duration of the growth phase. In the quasi-static evolution the current density increases almost linearly with the amount of depleted magnetic flux, suggesting that the duration of the growth phase can be determined by the sunward transport rate of magnetic flux.

In response to the prescribed sunward boundary condition strong crosstail current and azimuthal current densities are distributed over a range of about 3 hours from local midnight, associated with the azimuthal depletion of the near-Earth magnetic flux. Note, the reduction of the near-Earth equatorial magnetic flux is also a typical signature during the growth phase. In the process of midnight MFD, the lobe magnetic field in the near-Earth region is reduced by about 30 % in an hour. This reduction of lobe magnetic field can be compensated by the addition of magnetic flux to the lobes through the presence of a driving electric field. An increase of the lobe magnetic field is a frequently but not always

observed magnetotail property during the growth phase.

This dissertation implements a uniform electric field at the lobe boundary, different from several previous studies that employ an electric field decreasing with the radial distance. This uniform electric field considers the importance of both the dayside reconnection rate and the total static pressure in the solar wind rest frame during periods of southward IMF. The results demonstrate that a strong thin CS is generated in the mid-tail under the influence of the lobe compression. It is found that the thin CS forms in a region where the magnetotail is significantly stretched. The tailward edge of this CS is located at about $x = -33\,R_E$. Often and intuitively the tailward edge of the mid-tail CS is believed to be associated with a decreasing magnitude of the lobe electric field profile which should approach zero where the flaring of the lobe boundary is negligible (here the solar wind dynamic pressure is negligible). By assuming a uniform electric field, our results suggest a new interpretation for the location of the thin CS formation. By excluding the electric field profile as the cause for the CS location, we conclude that the location is determined by the structure of the magnetotail magnetic field. It is demonstrated that thin CS formation requires a much larger compression in a one-dimensional Harris sheet. Since the distant magnetotail is approximately one-dimensional, any CS must form sufficiently close to Earth. Note that *Wiegelmann and Schindler* [1995] implemented a magnetic field profile that peaks at the near-Earth lobe boundary based on a weakly two-dimensional MHD tail model and found that a strong thin CS forms close to the Earthward boundary. However, their model was restricted by the absence of a dipole field. Somewhat similarly, *Becker et al.* [2001] found that the formation of a thin CS requires the transition region between a dipolar and a highly stretched magnetic field.

In order to examine the influence of the electric field profile, this dissertation also studied CS formation for a lobe electric field with an Earthward gradient. The result demonstrates an almost unaltered location of mid-tail CS formation. In summary of these results, it should be emphasized that both MFD and the transport of flux into the lobes cause CS formation, however, at separate locations in the magnetotail.

6.2 Evolution in the Auroral Ionosphere

Some of the most typical substorm and growth phase signatures are observed in the auroral ionosphere. Therefore, this study also constructs ionospheric maps of tail properties based on the T96 magnetic field model combined with magnetic flux conservation. By mapping magnetotail structures from the Earthward boundary into the ionosphere, we find that all of the mapped properties move equatorward by 2° to 3° during the growth phase. This equatorward motion of the ionospheric footpoints requires a large depletion of the closed near-Earth magnetic flux. The results illustrate that the midnight MFD causes a strong convergence of the ionospheric footpoints of field lines that are separated by a large distance in the tail. This poses a big problem to any attempt of mapping observed auroral structures into the near-Earth tail using typical magnetic field models. At times corresponding to the end of the growth phase field lines between $x = -8\,R_E$ and $x = -20\,R_E$ in the simulation (in the midnight

meridian) map to the latitudes from 65.3° to 66.0°. This narrow latitude range is indeed smaller than the uncertainty of the mapping in conventional empirical magnetic field models [*Shevchenko et al.*, 2010]. Note, the equatorward motion of the ionospheric footpoints implies an increase of open magnetic flux in the polar cap, consistent with an increase of the polar cap size during the growth phase [*Weimer et al.*, 1992; *Milan et al.*, 2003, 2008; *Aikio et al.*, 2013].

The presented mapping results are consistent with many of the growth phase observations in the auroral ionosphere, such as the equatorward motion of the growth phase arcs [*Aikio et al.*, 2002], the concentration of the R1 and R2 currents [*Mende et al.*, 2001], and the location of the growth phase arcs relatively close to the ion and electron isotropy boundaries. Midnight MFD is of particular importance for the evolution of field-aligned currents. Field-aligned currents are likely associated with convection channels, implying the importance of the sunward convection for the substorm dynamics. In the simulation R1 and R2 currents move equatorward, intensify, and converge toward each other when a large amount of magnetic flux has been depleted in the late growth phase. This convergent motion of field-aligned currents suggests the possibility that the onset arc is close to or even within the proton aurora region because they are separated only by a few 10 km at the late growth phase time in the simulation, which is comparable to the typical broadening of proton aurora by charge exchange collisions. Corresponding observations have been reported by *Vallance Jones et al.* [1982], *Samson et al.* [1992], and *Mende et al.* [2001].

In our simulation the electron isotropy boundary maps into the boundary between the R1 and R2 currents, and is located by about 0.3° poleward of the ion isotropy boundary. This also implies that the onset arc should be located relatively close to the dipole field region. In fact in our simulations the onset arc maps exactly to the transition between the dipolar field and thin CS. This result agrees with *Jayachandran et al.* [2002] who have examined 96 onset arcs in a statistical study and found that the onset arc locations are near the equatorward edge of the proton aurora (ion isotropy boundary) when the IMF is predominantly southward prior to the substorm onset. We also find that the strong field-aligned currents map into the region coincident with the very thin CS layer, which agrees well with *Zaharia and Cheng* [2003] who use a three-dimensional equilibrium model based on solving the force-balance equation with realistic pressure distributions in the near-Earth tail.

This dissertation demonstrates that midnight MFD is a highly efficient mechanism to generate a very thin CS in the near-Earth tail, and the location of this thin CS is consistent with typical auroral ionospheric features during the growth phase. Table 6.1 lists the results in the MFD model compared with the previous studies. The MFD mechanism is denoted as M1, the lobe compression approach is represented as M2, and the anti-entropy diffusion mechanism is denoted as M3.

In this table question marks indicate a model parameter dependence that can be adjusted but has no obvious physical motivation for any particular choice. For instance, pressure diffusion (M3) could be turned on at any time independent of whether the IMF has been southward, and the location of the diffusion determines the location of the thin CS, posing the question of why pressure diffusion would

occur about an hour after the southward turning of the IMF and only close to the inner magnetosphere at about 10 to $15R_E$. A similar ambiguity applies to lobe compression (M2). The precise CS location depends on the choice of the electric field at the lobe boundary and the resulting CS forms preferably tailward of about $25R_E$. We note that the electric field at the lobe boundary does not only depend on the dayside reconnection rate but also on other changes in the solar wind such as dynamic and static pressure changes. A "$\times$" in the table indicates that the model appears incapable to provide an explanation for the observed growth phase signature based on the results of this dissertation.

These results demonstrate that MFD is the first model that can consistently explain and predict the typical magnetotail and ionospheric evolution during the substorm growth phase and shed light on the physics of the growth phase aurora.

Table 6.1. Comparison of different CS thinning mechanisms. The MFD mechanism is denoted as M1, the lobe deformation is represented as M2, and entropy anti-diffusion approach is denoted as M3. Several growth phase magnetotail and ionospheric properties are listed in the left column.

	M1	M2	M3
• Thin CS formation	$\surd$	$\surd$	$\surd$
• Strong relation with the southward IMF	$\surd$	$\surd$	?
• Thin CS location prediction	$\surd$	?	?
• Growth phase duration prediction	$\surd$	?	?
• B_z reduction near geosynchronous distances	$\surd$	$\times$	?
• Equatorward motion of the growth phase arc • Gradual increase of the polar cap size • Reduction of the closed magnetic flux	$\surd$	$\times$	?
• Convergent motion of the most equatorward discrete arc and the diffuse aurora	$\surd$	$\times$	?

6.3 Double-current Sheet Considerations

It is generally believed that energetic particle injection at geosynchronous distances is indicative for the substorm expansion onset. The source region of the injected plasma is often studied by investigating the locations of fast flows and is still highly debated. In response to the depletion of the near-Earth magnetic flux or the addition of lobe magnetic flux, this study demonstrates that there can be two separate thin CS forming during the growth phase. Strong thin CSs can evolve either in the near-Earth region or in the mid-tail region depending on the relative magnitude of the potential transporting closed magnetic flux sunward or adding open flux to the lobes. By combining both effects, a thin CS structure extends from near-geosynchronous distances to the mid-tail region, however, with two local maxima in the current density. A thin CS forms slightly faster in the mid-tail region when the removal of closed magnetic flux and the loading of open magnetic flux almost balance each other (for the case of a

uniform lobe electric field). The near-Earth CS develops faster when the MFD rate is larger than the flux transport into the lobes and the opposite is the case if the MFD rate is smaller. This double-current sheet model clearly allows for two separate reconnection sites during the growth phase or in the early expansion phase. A highly important question regarding this possibility of two reconnection sites is: Can either CS be associated with the expansion phase onset? In order to shed some light on this issue we have conducted three additional simulations.

Figure 4.17 has shown that the CSs can evolve differently in response to the competition between the midnight MFD and the lobe compression during the growth phase. Figures 6.1 to 6.3 show the evolution of reconnection and fast flows for the case (a) that MFD dominates, (b) the MFD flux transport is approximately equal to the lobe transport, and (c) that the lobe transport dominates. The arrows in these plots show plasma velocity in the x, y plane and color represents the z component of the velocity. The cut is taken just above the equatorial symmetry plane and a negative z component can be indicative for a reconnection site because flow converges toward the symmetry plane. The three plots show snapshots after about 7, 19, and 29 minutes. The Earthward boundary in the plots is located at $x = -5R_E$ and in the following we will use GSM coordinates to refer to distances in the tail. The magnitude of the flow is indicated by the length of the arrows which is scaled by the arrow in the upper left corner of the plots. A value of 1 corresponds to 440 km/s.

The fast flows are the outflows caused by the magnetic reconnection. In this simulation reconnection is triggered by a localized resistivity applied when the current density is higher than a critical value about $1.5\, j_0$. When midnight MFD is dominant, a strong thin CS is generated in the near-Earth tail such that magnetic reconnection is triggered at about $x = -11\, R_E$, as shown in the top panel of Figure 6.1. Later, the x-line retreats about $5\, R_E$ tailward, and the channel of the tailward flows extends over a wide region from $y = -6\, R_E$ to $6\, R_E$. At $t = 130\, t_A$, the x-line stays at about $x = -18\, R_E$ and the Earthward flows penetrate into $x = -8\, R_E$ with a velocity about 0.6 ($\sim$ 260 km/s). The associated tailward flow velocity reaches to 0.87 ($\sim$ 370 km/s).

Figure 6.2 shows that the x-line first forms at about $x = -27\, R_E$ when the depletion and the loading of magnetic flux almost balance each other. At $t = 80\, t_A$, the Earthward flows evolve in a region from $x = -25$ to $x = -19\, R_E$ and divert in the near-Earth tail. A second reconnection site is formed later at about $x = -11\, R_E$, i.e., at the location of the near-Earth CS, with most of the Earthward flows diverted around the Earth. Figure 6.3 presents the magnetotail flows when a strong mid-tail CS is generated (flux transport into the lobes is dominant). The figure shows that most of the Earthward flows are located tailward of $x = -13\, R_E$, and the flow does not penetrate as far into the near-Earth region as in the first case. This result indicates the difficulty to obtain near-Earth plasma injection associated with the mid-tail magnetic reconnection while the near-Earth reconnection in Figure 6.1 shows that convection can penetrate significantly closer to Earth.

To appreciate these results it is important to summarize observations and physics of fast convection in the magnetotail. Transient fast flows termed bursty bulk flows (BBF's) are observed at all times

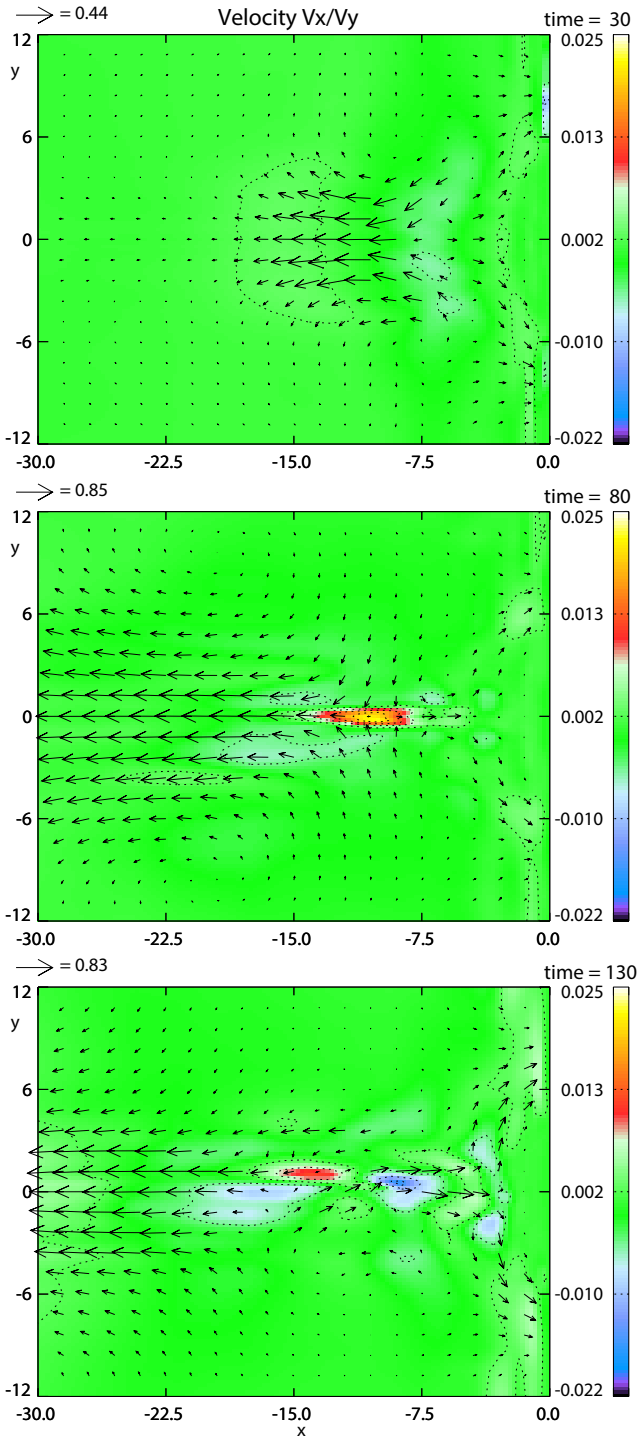

Figure 6.1. Evolution of equatorial flows at times (top) $t = 30\,t_A$, (middle) $t = 80\,t_A$, and (bottom) $t = 130\,t_A$ when MFD is dominant. The color shows the value of v_z, and the vector indicates $v_x\hat{e_x}+v_y\hat{e_y}$.

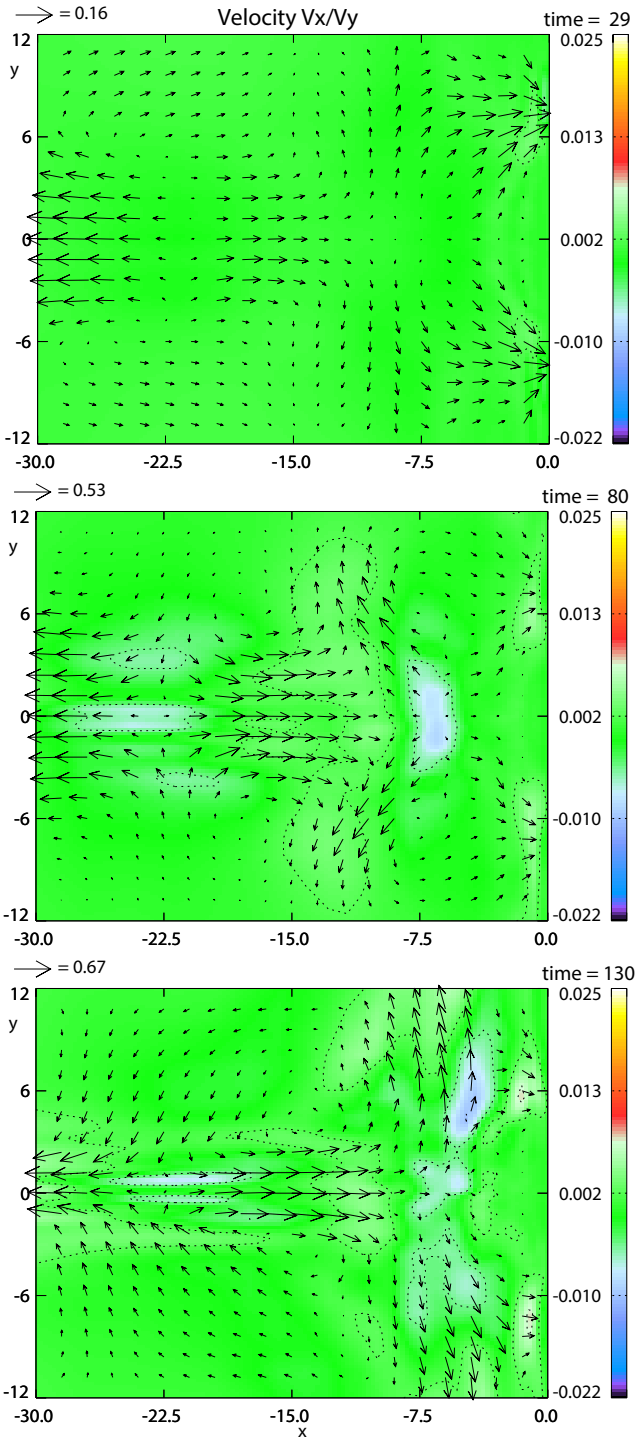

Figure 6.2. Evolution of equatorial flows when MFD and lobe compression almost balance each other. The format is the same as Figure 6.1.

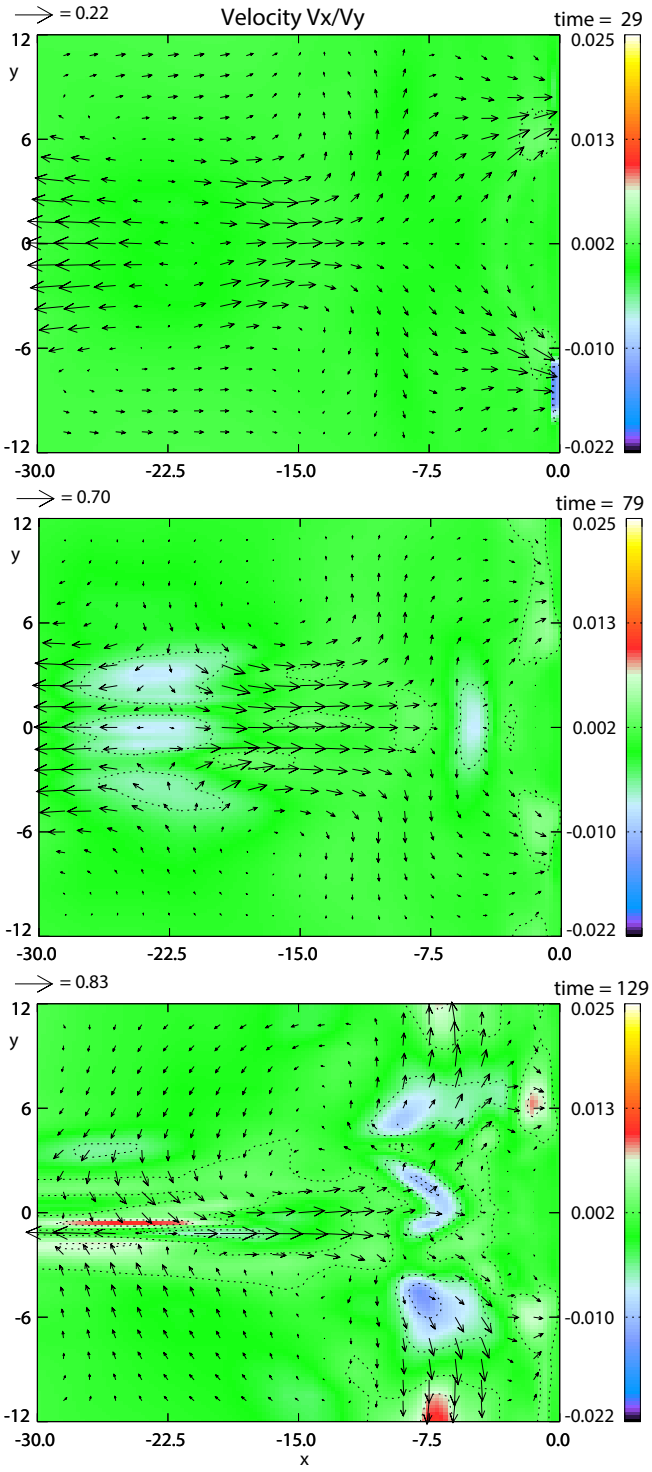

Figure 6.3. Evolution of equatorial flows when lobe compression is dominant. The format is the same as Figure 6.1.

in the Earth's magnetotail but are more frequent during the growth phase of substorms [*Baumjohann et al.*, 1990]. Generally these flows have velocities of 100's of km/s and durations of several minutes (up to about 10 minutes) in the satellite locations. The cause for these flows is most likely magnetic reconnection. In recent years several papers have interpreted these fast flows as so-called plasma bubbles [*Birn et al.*, 2011; *Dubyagin et al.*, 2011; *Sergeev et al.*, 2012b] which represent entropy depleted magnetic flux tubes. The low flux tube entropy of these magnetic flux tubes requires them to move Earthward into regions which match the flux tube entropy of the plasma bubbles.

This interpretation of BBF's as entropy deleted flux tubes is confirmed by observations but leaves the question of the cause of the entropy depletion unaddressed. The most plausible cause for such an entropy depletion is again magnetic reconnection where the newly formed magnetic flux tubes have a much reduced flux tube entropy when low plasma beta lobe magnetic flux is reconnected. Note that both BBF's and plasma bubbles are also often associated with so-called dipolarization fronts. These are structure in the fast flow where the magnetic field abruptly increases to much higher values explaining the terminology "dipolarization front". While these fronts carry magnetic flux, it is unresolved if and how much they contribute to the dipolarization of the near-Earth magnetic field in the substorm expansion.

Several studies in recent years have examined the question whether BBF's and entropy bubbles can cause particle injection and dipolarization at geosynchronous distances. Both of these observation are considered typical to identify substorms although a general definition of substorms is somewhat vague in terms of required ground and satellite signatures. *Ohtani et al.* [2006] and *Takada et al.* [2006] found that not all fast flows can cause a strong dipolarization near the geosynchronous distances. *Dubyagin et al.* [2011] have shown that only fast flows with suitably small entropy can reach the inner magnetosphere and produce an increase of energetic particles flux. Similar result is also presented by *Sergeev et al.* [2012b]. In fact, these authors conclude that fast flows can penetrate into geosynchronous distances only very rarely. They have also demonstrated that the flux tube entropy is the most important factor for the penetration depth into the inner magnetosphere. However, this penetration is required to cause energetic particle injection at geosynchronous distances. *Wolf et al.* [2009] have shown that plasma flux tube entropy increases monotonically with the distance downtail, suggesting that the importance of the onset of near-Earth reconnection on the plasma injection near the geosynchronous distances. Mid-tail reconnection creates larger flux tube volume and entropy flux tubes. In addition *Ma* [2012] has shown that nonadiabatic heating can strongly increase the flux tube entropy for an extended reconnection outflow region. These are strong arguments to suggest that any reconnection which causes flux tube to penetrate deep into the magnetosphere is much more likely to occur in the near-Earth region consistent with the convection shown in Figures 6.1 to 6.3.

Recent studies have suggested that plasma intrusion associated with equatorward moving auroral arcs (streamers) can lead to auroral substorms. The sequence is initiated by poleward boundary intensifications (PBI's) followed by auroral arcs moving equatorward toward the onset latitude, leading

to the substorm onset when they reach the onset arc location [*Nishimura et al.*, 2010, 2011]. This equatorward motion of auroral arcs has been suggested to be associated with fast Earthward flows with reduced entropy (bubble) penetrating into the inner magneotosphere. However, *Xing et al.* [2010] found that similar flow channels correlated equatorward moving auroral arcs can appear during quiet times and not lead to the substorm onset, implying that the earthward penetration of reduced-entropy fast flow channels is not a sufficient condition for an onset to occur. It is also noted that *Mende et al.* [2011] demonstrated that many subsorms onsets occur without the presence of a so-called streamer, concluding that streamers are also not sufficient conditions for the onset of the expansion phase. In fact streamers are frequently observed during the growth phase consistent with the high likelihood of a mid-tail CS formation and associated reconnection as demonstrated in this dissertation.

This dissertation presents a double-current sheet evolution during the growth phase and suggests that substorm expansion onset is associated only with the onset of near-Earth magnetic reconnection, while mid-tail reconnection causes bursty bulk flows or bubbles. To test this double-current sheet hypothesis, satellite observations at distinct locations in the near-Earth region and mid-tail region are highly desired. For instance *Shue et al.* [2008] have studied the relationship between nightside auroral power and two classes of Earthward fast flows. The class (1) flows were observed near $x = -10R_E$, whereas the class (2) flows were found at $x < -15R_E$. They found that the class (1) fast flows can be associated with an auroral substorm bulge developing on the nightside, while class 2 fast flows are more often associated with PBI's and pseudobreakups. Their results indicate that auroral activity can be much different in response to the onset of magnetic reconnection at the distinct locations. More statistical studies in the future are necessary to examine this double-current sheet hypothesis.

6.4 Summary

This dissertation investigates the magnetotail and ionospheric evolution during the substrom growth phase. The physics of MFD and the effects of lobe compression on the magnetotail evolution are examined as possible cause for thin CS formation in the magnetotail. In addition, this study examines the changes of auroral morphology associated with the magnetotail evolution by mapping magnetospheric changes into the auroral ionosphere. The results are summarized below.

1. MFD is a highly efficient mechanism to generate a very thin CS in the near-Earth tail.

Sunward convection removes a large portion of the near-Earth closed magnetic flux and causes strong crosstail and azimuthal current densities near the equatorial plane. In a quasi-static evolution, the current density increases almost linearly with the amount of the depleted magnetic flux. In the simulation the thin CS forms in the near-Earth tail within about half an hour to one hour, consistent with the typical duration of the growth phase. The depletion of the near-Earth magnetic flux results in the reduction of lobe magnetic field in the near-Earth tail.

2. MFD is a central element for the evolution of field-aligned current and for the equatorward motion of these currents.

MFD causes a contraction of the ionospheric footpoints of the near-Earth region such that all of the mapped magnetotail structures move equatorward by about 2° to 3°. Sunward divergent flow is associated with the source region of field-aligned currents. In the late growth phase, the strong field-aligned currents develop within a very narrow region of about 1° in latitude. The R1/R2 boundary is approximately coincident with the electron isotropy boundary in the late growth phase.

3. Lobe compression through the presence of an electric field can generate a strong thin CS in the mid-tail region.

A thin CS favors the formation in the mid-tail with a tailward edge about $x = -33R_E$ for a uniform electric field at the lobe boundary. The CS current density increases approximately linearly with the addition of magnetic flux accompanied by a slow increase of the lobe magnetic field in the near-Earth tail.

4. A double-current sheet evolves in response to MFD in combination with lobe compression.

A double-current sheet evolves at distinct locations in the near-Earth region and mid-tail region in response to MFD and the addition of lobe magnetic flux. The relative current densities in the double-current sheet configuration depend strongly on whether the added or the depleted magnetic flux dominates during periods of southward IMF. The evolution of distinctly different CS's suggests two preferable locations for tail reconnection. Only the near-Earth CS appears likely to be associated with expansion phase onset. The mid-tail CS may explain the more frequent occurrence of BBF's and streamers during the substorm growth phase.

5. No clearly identifiable equatorward expansion of open/close field boundary and intensification of field-aligned currents can be caused by lobe compression.

Although lobe compression can cause a strong mid-tail CS, it is incapable of explaining the equatorward motion of the poleward auroral boundary and the growth phase arc, the slow intensification and equatorward motion of R1 and R2 currents, and the increase of ionospheric convection during the growth phase.

Appendix A

Harris Sheet Derivation

To derive the one-dimensional Harris sheet profile, we first start from the Ampére's law

$$-\nabla^2 A_y = \mu_0 j_y. \tag{A.1}$$

The current density along the y direction can be formally computed from the integral of Maxwellian (symmetric) distribution function shifted by the the bulk velocity u_s in the v_y direction such as

$$\vec{j_s} = q_s n_{0s} h_s(\phi, A_y)\hat{e_y}, \quad \text{with} \tag{A.2}$$

$$h_s(\phi, A_y) = \exp\{\{-\frac{q_s}{k_B T_s}(\phi - u_s A_y)\}\}. \tag{A.3}$$

Assuming the plasma of single charged ions and electrons yields the current density

$$j_y = e\{n_{0i} u_i \exp\{\frac{-e}{k_B T_i}(\phi - u_i A_y)\} - n_{0e} u_e \exp\{\frac{e}{k_B T_e}(\phi - u_e A_y)\}\}, \quad \text{with} \tag{A.4}$$

$$n_{0i} = n_{0e} = n_0, \quad \kappa = \frac{k_B T_i}{e u_i}, \quad u_e = -\frac{T_e}{T_i} u_i, \quad \text{and} \quad \phi = 0. \tag{A.5}$$

Now one can rewrite equation (A.1) into

$$-\nabla^2 A_y = \mu_0 e n_0 u_i (1 + \frac{T_e}{T_i}) \exp\{\frac{A_y}{\kappa}\} = -\lambda \exp\{\frac{A_y}{\kappa}\}. \tag{A.6}$$

Solving equation (A.6), one could get

$$-\bigtriangledown^2 A_y = -\lambda \exp\{\frac{A_y}{\kappa}\} \tag{A.7}$$

$$\Longrightarrow \frac{d^2 A_y}{dx^2} = \lambda \exp\{\frac{A_y}{\kappa}\} \tag{A.8}$$

$$\Longrightarrow \frac{dA_y}{dx}(\frac{d}{dx}\frac{dA_y}{dx}) = \lambda \exp\{\frac{A_y}{\kappa}\}\frac{dA_y}{dx}. \tag{A.9}$$

Because of

$$\frac{d}{dx}(\frac{dA_y}{dx})^2 = 2(\frac{dA_y}{dx})\{\frac{d}{dx}(\frac{dA_y}{dx})\}$$

$$\Longrightarrow \frac{dA_y}{dx}(\frac{d}{dx}\frac{dA_y}{dx}) = \frac{1}{2}\frac{d}{dx}(\frac{dA_y}{dx})^2 \quad \text{and}$$

$$\frac{d}{dx}(\exp^{\frac{-A_y}{\kappa}}) = -\frac{1}{\kappa}\exp^{\frac{-A_y}{\kappa}}\frac{dA_y}{dx}$$

$$\Longrightarrow \exp^{\frac{-A_y}{\kappa}}\frac{dA_y}{dx} = -\kappa\frac{d}{dx}(\exp^{\frac{-A_y}{\kappa}}),$$

equation (A.9) turns into

$$\frac{1}{2}\frac{d}{dx}(\frac{dA_y}{dx})^2 = -\lambda\kappa\frac{d}{dx}(\exp^{\frac{-A_y}{\kappa}}) \tag{A.10}$$

$$\Longrightarrow \frac{d}{dx}\{\frac{1}{2}(\frac{dA_y}{dx})^2 + \lambda\kappa\exp^{\frac{-A_y}{\kappa}}\} = 0 \tag{A.11}$$

$$\Longrightarrow \frac{1}{2}(\frac{dA_y}{dx})^2 + \lambda\kappa\exp^{\frac{-A_y}{\kappa}} = const \tag{A.12}$$

$$\Longrightarrow \frac{1}{2}(\frac{dA_y}{dx})^2 + \lambda\kappa\exp^{\frac{-2A_y}{A_0}} = const. \tag{A.13}$$

With the normalization

$$\kappa = \frac{A_0}{2} \quad \text{and} \quad P_0 = \frac{\lambda\kappa}{\mu_0},$$

equation (A.13) is equivalent to the force balance equation $\frac{{B_z}^2}{2\mu_0} + \frac{\lambda\kappa}{\mu_0} = P_{total}$ as

$$\begin{aligned}
&\frac{1}{2}(\frac{dA_y}{dx})^2 + \mu_0 P_0 \exp^{\frac{-2A_y}{A_0}} = \mu_0 P_{total} \\
\Longrightarrow &\frac{1}{2}(\frac{dA_y}{dx})^2 = \mu_0(P_{total} - P_0 \exp^{\frac{-2A_y}{A_0}}) \\
\Longrightarrow &\frac{dA_y}{dx} = \sqrt{2\mu_0(P_{total} - P_0 \exp^{\frac{-2A_y}{A_0}})} \\
\Longrightarrow &\frac{1}{\sqrt{2\mu_0}} \int_0^{A_y} \frac{dA_y}{\sqrt{P_{total} - P_0 \exp^{\frac{-2A_y}{A_0}}}} = \int_0^x dx.
\end{aligned}$$

Now we let

$$\begin{aligned}
&P' = P_0 \exp^{\frac{-2A_y}{A_0}} \\
\Longrightarrow &\frac{dP'}{dA_y} = P_0(\frac{-2}{A_0}) \exp^{\frac{-2A_y}{A_0}} = \frac{-2}{A_0} P' \\
\Longrightarrow &dA_y = \frac{-A_0}{2} \frac{dP'}{P'},
\end{aligned}$$

therefore,

$$\frac{1}{\sqrt{2\mu_0}} \int_0^{A_y} \frac{dA_y}{\sqrt{P_{total} - P_0 \exp^{\frac{-2A_y}{A_0}}}} = \int_0^x dx \tag{A.14}$$

$$\Longrightarrow \frac{1}{\sqrt{2\mu_0}}(\frac{-A_0}{2}) \int_{P_0}^{P'} \frac{dP'}{P'} \frac{1}{\sqrt{P_{total} - P'}} = \int_0^x dx, \tag{A.15}$$

with

$$\int \frac{dP'}{P'} \frac{1}{\sqrt{P_{total} - P'}} \tag{A.16}$$

$$= \frac{1}{\sqrt{P_{total}}} \ln\left(\frac{\sqrt{P_{total} - P'} - \sqrt{P_{total}}}{\sqrt{P_{total} - P'} + \sqrt{P_{total}}}\right) \tag{A.17}$$

$$= \frac{1}{\sqrt{P_{total}}} \ln\left(\frac{\sqrt{\frac{P_{total}}{P'} - 1} - \sqrt{\frac{P_{total}}{P'}}}{\sqrt{\frac{P_{total}}{P'} - 1} + \sqrt{\frac{P_{total}}{P'}}}\right) \tag{A.18}$$

$$= \frac{1}{\sqrt{P_{total}}} \left\{ \ln\left(\sqrt{\frac{P_{total}}{P'} - 1} - \sqrt{\frac{P_{total}}{P'}}\right) - \ln\left(\sqrt{\frac{P_{total}}{P'} - 1} + \sqrt{\frac{P_{total}}{P'}}\right) \right\} \tag{A.19}$$

$$= \frac{1}{\sqrt{P_{total}}} \left\{ \ln\left(\sqrt{\frac{P_{total}}{P'} - 1} - \sqrt{\frac{P_{total}}{P'}}\right) - \cosh^{-1}\left(\sqrt{\frac{P_{total}}{P'}}\right) \right\}. \tag{A.20}$$

Employing the boundary condition:

$A_y = 0$,

$$\frac{{B_z}^2}{2\mu_0} = 0,$$
$$P_{total} = P_0$$
$$\Rightarrow \frac{P_{total}}{P'} = \frac{P_0}{P_0} = 1;$$

$A_y = A_y$,

$$P_{total} = P_{total}(A_y = 0) = P_0$$
$$\Rightarrow \frac{P_{total}}{P'} = \frac{P_0}{P_0 \exp^{\frac{-2A_y}{A_0}}} = \exp^{\frac{2A_y}{A_0}},$$

equation (A.16) turns into

$$\int_{P_0}^{P'} \frac{dP'}{P'} \frac{1}{\sqrt{P_{total} - P'}}$$
$$= \frac{1}{\sqrt{P_0}}\{(\ln(\sqrt{\exp^{\frac{2A_y}{A_0}} - 1} - \sqrt{\exp^{\frac{2A_y}{A_0}}})$$
$$- \cosh^{-1}(\sqrt{\exp^{\frac{2A_y}{A_0}}})) - (\ln(\sqrt{1-1} - \sqrt{1}) - \cosh^{-1}(\sqrt{1}))\}$$
$$= \frac{1}{\sqrt{P_0}} \left\{ (\ln(\sqrt{\exp^{\frac{2A_y}{A_0}} - 1} - \sqrt{\exp^{\frac{2A_y}{A_0}}}) - \cosh^{-1}(\exp^{\frac{A_y}{A_0}})) - (\ln(-1) - 0) \right\}.$$

Substituting this into equation (A.15) yields

$$\frac{1}{\sqrt{2\mu_0}}(\frac{-A_0}{2}) \int_{P_0}^{P'} \frac{dP'}{P'} \frac{1}{\sqrt{P_{total} - P'}} = \int_0^x dx \tag{A.21}$$
$$\Rightarrow -\frac{A_0}{2\sqrt{2\mu_0 P_0}} \left\{ \ln(\sqrt{\exp^{\frac{2A_y}{A_0}} - 1} - \sqrt{\exp^{\frac{2A_y}{A_0}}}) - \ln(-1) - \cosh^{-1}(\exp^{\frac{A_y}{A_0}}) \right\} = x. \tag{A.22}$$

Note that

$$\ln(\sqrt{\exp^{\frac{2A_y}{A_0}} - 1} - \sqrt{\exp^{\frac{2A_y}{A_0}}})$$

and $\ln(-1)$ are all imaginary numbers.

Therefore, equation (A.21) becomes

$$\frac{1}{\sqrt{2\mu_0}}(\frac{-A_0}{2}) \int_{P_0}^{P'} \frac{dP'}{P'} \frac{1}{\sqrt{P_{total} - P'}} = -\frac{A_0}{2\sqrt{2\mu_0 P_0}}(-\cosh^{-1}(\exp^{\frac{A_y}{A_0}})) = x$$
$$\Longrightarrow \cosh^{-1}(\exp^{\frac{A_y}{A_0}}) = \frac{2\sqrt{2\mu_0 P_0}}{A_0} x$$
$$\Longrightarrow \exp^{\frac{A_y}{A_0}} = \cosh(\frac{2\sqrt{2\mu_0 P_0}}{A_0} x)$$
$$\Longrightarrow \frac{A_y}{A_0} = \ln(\cosh(\frac{2\sqrt{2\mu_0 P_0}}{A_0} x)).$$

With the normalization

$$P_0 = \frac{\lambda\kappa}{\mu_0} = \frac{\frac{A_0}{L^2}\frac{A_0}{2}}{\mu_0} = \frac{{A_0}^2}{2\mu_0}\frac{1}{L^2}$$
$$\Longrightarrow \frac{1}{L} = \frac{\sqrt{2\mu_0 P_0}}{A_0},$$

$$\frac{1}{L_0} = \frac{\sqrt{\mu_0 P_c}}{A_0}, \quad \text{and} \quad P_c = \frac{P_0}{2},$$

the potential vector becomes

$$A_y = A_0 \ln(\cosh(\frac{x}{L_0})). \tag{A.23}$$

The Harris sheet profile can be assumed as the equations (1.7) to (1.9) in Chapter 1 based on the equation (A.23).

Appendix B

Adiabatic Constraint

Starting from a plasma parcel with a fixed volume, the first law of thermodynamics [*Marion and Hornyak*, 1982] can be expressed as

$$dQ = nC_v dT + pdV, \tag{B.1}$$

where dQ is the heat added to the parcel and pdV is the differential work done by the parcel. Here C_v is the molar specific heat for a constant volume, which is represented as

$$C_v = (\frac{1}{n})(\frac{dQ}{dT})\Big|_V. \tag{B.2}$$

Here dQ is

$$\begin{aligned}
&dQ = nC_v dT + pdV \\
&\Longrightarrow \frac{1}{n}\frac{dQ}{dT} = C_v\frac{dT}{dT} + \frac{p}{n}\frac{dV}{dT} \\
&\Longrightarrow \frac{1}{n}\frac{dQ}{dT} = C_v + \frac{p}{n}\frac{dV}{dT} \\
&\Longrightarrow C_p = \frac{1}{n}\frac{dQ}{dT}\Big|_p = C_v + \frac{p}{n}\frac{dV}{dT}\Big|_p = C_v + R,
\end{aligned}$$

where C_p is the molar specific heat for a constant pressure, which can be expressed as

$$C_p = C_v + R. \tag{B.3}$$

Employing the ideal gas law

$$pV = nRT, \tag{B.4}$$

where n is the number of moles and R is the universal gas constant 8.31 J/mol $\cdot$ K.

By assuming constant n

$$ndT = (\frac{1}{R})(pdV + Vdp), \tag{B.5}$$

we can rewrite equation (B.1) as

$$\begin{aligned}
dQ &= nC_v dT + pdV \\
&= C_v\frac{1}{R}(pdV + Vdp) + pdV \\
&= nC_v\frac{pV}{nR}\left(\frac{dV}{V} + \frac{dp}{p} + \frac{RdV}{C_v V}\right) \\
&= nC_v T\left(\frac{dp}{p} + \frac{dV}{V}\left(\frac{C_v + R}{C_v}\right)\right) \\
&= nC_v T\left(\frac{dp}{p} + \frac{dV}{V}\left(\frac{C_p}{C_v}\right)\right) \\
&= nC_v T\left(\frac{dp}{p} + \frac{dV}{V}\gamma\right),
\end{aligned}$$

with $\gamma = C_p/C_v$.

Therefore, equation (B.1) becomes

$$dQ = nC_vT(d\ln(pV^\gamma)). \tag{B.6}$$

The entropy is defined as

$$dS = \frac{dQ}{T} \tag{B.7}$$

such that

$$dS = nC_v(d\ln(pV^\gamma)). \tag{B.8}$$

For the adiabatic change, $dS = 0$, therefore

$$nC_v(d\ln(pV^\gamma)) = 0. \tag{B.9}$$

Since nC_v is non-zero, finally one gets

$$pV^\gamma = const. \tag{B.10}$$

Equation (B.10) means that the flux tube entropy $S = pV^\gamma$ should remain constant for the adiabatic constraint.

Appendix C

Energy Equation

Let $h = p^{\frac{1}{\gamma}}$, the energy equation becomes

$$\frac{\partial h}{\partial t} = -\nabla \cdot (h\vec{u}) + \left\{ \left[\frac{(\gamma - 1)}{\gamma} \right] h^{1-\gamma} \eta \vec{j}^2 \right\} \tag{C.1}$$

$$\implies \frac{\partial}{\partial t}(p^{\frac{1}{\gamma}}) = -\nabla \cdot (p^{\frac{1}{\gamma}} \vec{u}) + \left[\frac{(\gamma - 1)}{\gamma} \right] (p^{\frac{1}{\gamma}})^{1-\gamma} \eta \vec{j}^2 \tag{C.2}$$

$$\implies \frac{1}{\gamma} p^{\frac{1}{\gamma}-1} \frac{\partial p}{\partial t} = -\vec{u} \cdot \nabla p^{\frac{1}{\gamma}} - p^{\frac{1}{\gamma}} \nabla \cdot \vec{u} + p^{\frac{1}{\gamma}^{1-\gamma}} \frac{(\gamma - 1)}{\gamma} \eta \vec{j}^2. \tag{C.3}$$

This is equivalent to the pressure equation

$$\frac{\partial p}{\partial t} + \vec{u} \cdot \nabla p + \gamma p \nabla \cdot \vec{u} = (\gamma - 1) \eta \vec{j}^2 \tag{C.4}$$

$$\implies p^{\frac{1}{\gamma}-1} \frac{\partial p}{\partial t} = -p^{\frac{1}{\gamma}-1} \vec{u} \cdot \nabla p - \gamma p^{\frac{1}{\gamma}} \nabla \cdot \vec{u} + p^{\frac{1}{\gamma}-1} (\gamma - 1) \eta \vec{j}^2 \tag{C.5}$$

$$\implies \frac{1}{\gamma} p^{\frac{1}{\gamma}-1} \frac{\partial p}{\partial t} = -\frac{1}{\gamma} p^{\frac{1}{\gamma}-1} \vec{u} \cdot \nabla p - p^{\frac{1}{\gamma}} \nabla \cdot \vec{u} + p^{\frac{1}{\gamma}-1} \frac{(\gamma - 1)}{\gamma} \eta \vec{j}^2, \tag{C.6}$$

with

$$\vec{u} \cdot \nabla p^{\frac{1}{\gamma}} = \vec{u} \cdot \nabla (p^{\frac{1}{\gamma}}) = \vec{u} \cdot (\frac{1}{\gamma} p^{\frac{1}{\gamma-1}} \nabla p) = \frac{1}{\gamma} p^{\frac{1}{\gamma-1}} \vec{u} \cdot \nabla p.$$

References

Aikio, A. T., T. Lakkala, A. Kozlovsky, and P. J. S. Williams (2002), Electric fields and currents of stable drifting auroral arcs in the evening sector, *jgr*, *107*, 1424, doi:10.1029/2001JA009172.

Aikio, A. T., T. Pitkänen, I. Honkonen, M. Palmroth, and O. Amm (2013), IMF effect on the polar cap contraction and expansion during a period of substorms, *Annales Geophysicae*, *31*, 1021–1034, doi:10.5194/angeo-31-1021-2013.

Akasofu, S.-I. (1964), The development of the auroral substorm, *planss*, *12*, 273, doi:10.1016/0032-0633(64)90151-5.

Angelopoulos, V., W. Baumjohann, C. F. Kennel, F. V. Coronti, M. G. Kivelson, R. Pellat, R. J. Walker, H. Luehr, and G. Paschmann (1992), Bursty bulk flows in the inner central plasma sheet, *jgr*, *97*, 4027–4039, doi:10.1029/91JA02701.

Asano, Y., T. Mukai, M. Hoshino, Y. Saito, H. Hayakawa, and T. Nagai (2003), Evolution of the thin current sheet in a substorm observed by Geotail, *jgr*, *108*, 1189, doi:10.1029/2002JA009785.

Baker, D. N., T. A. Fritz, R. L. McPherron, D. H. Fairfield, Y. Kamide, and W. Baumjohann (1985), Magnetotail energy storage and release during the CDAW 6 substorm analysis intervals, *jgr*, *90*, 1205–1216, doi:10.1029/JA090iA02p01205.

Baker, D. N., et al. (1993), CDAW 9 analysis of magnetospheric events on May 3, 1986 - Event C, *jgr*, *98*, 3815–3834, doi:10.1029/92JA02475.

Baker, D. N., T. I. Pulkkinen, V. Angelopoulos, W. Baumjohann, and R. L. McPherron (1996), Neutral line model of substorms: Past results and present view, *jgr*, *101*, 12,975–13,010, doi:10.1029/95JA03753.

Baumjohann, W., R. J. Pelunent, H. J. Opgenoorth, and E. Nielsen (1981), Joint two-dimensional observations of ground magnetic and ionospheric electric fields associated with auroral zone currents: Current systems associated with local auroral break-ups currents., *Planetary and Space Science*, *29*, 431–447.

Baumjohann, W., G. Paschmann, and H. Luehr (1990), Characteristics of high-speed ion flows in the plasma sheet, *jgr*, *95*, 3801–3809, doi:10.1029/JA095iA04p03801.

Becker, U., T. Neukirch, and K. Schindler (2001), On the quasistatic development of thin current sheets in magnetotail-like magnetic fields, *jgr*, *106*, 3811–3826, doi:10.1029/2000JA900141.

Birkeland, K. (1908), The norwegian aurora polaris expedition 1902-1903, *Aschhoug, Oslo*, *1*, 785V801.

Birn, J., and K. Schindler (2002), Thin current sheets in the magnetotail and the loss of equilibrium, *jgr*, *107*, 1117, doi:10.1029/2001JA000291.

Birn, J., M. F. Thomsen, J. E. Borovsky, G. D. Reeves, D. J. McComas, and R. D. Belian (1997), Characteristic plasma properties during dispersionless substorm injections at geosynchronous orbit, *jgr*, *102*, 2309–2324, doi:10.1029/96JA02870.

Birn, J., M. Hesse, and K. Schindler (1998), Formation of thin current sheets in space plasmas, *jgr*, *103*, 6843–6852, doi:10.1029/97JA03602.

Birn, J., R. Nakamura, E. V. Panov, and M. Hesse (2011), Bursty bulk flows and dipolarization in MHD simulations of magnetotail reconnection, *jgr*, *116*, A01210, doi:10.1029/2010JA016083.

Bristow, W. A., G. J. Sofko, H. C. Stenbaek-Nielsen, S. Wei, D. Lummerzheim, and A. Otto (2003), Detailed analysis of substorm observations using SuperDARN, UVI, ground-based magnetometers, and all-sky imagers, *jgr*, *108*, 1124, doi:10.1029/2002JA009242.

Caan, M. N., R. L. McPherron, and C. T. Russell (1975), Substorm and interplanetary magnetic field effects on the geomagnetic tail lobes, *jgr*, *80*, 191–194, doi:10.1029/JA080i001p00191.

Clausen, L. B. N., J. B. H. Baker, J. M. Ruohoniemi, S. E. Milan, and B. J. Anderson (2012), Dynamics of the region 1 Birkeland current oval derived from the Active Magnetosphere and Planetary Electrodynamics Response Experiment (AMPERE), *jgr*, *117*, A06233, doi:10.1029/2012JA017666.

Coroniti, F. V. (1985), Explosive tail reconnection - The growth and expansion phases of magnetospheric substorms, *jgr*, *90*, 7427–7447, doi:10.1029/JA090iA08p07427.

Coroniti, F. V., and C. F. Kennel (1973), Can the ionosphere regulate magnetospheric convection?, *jgr*, *78*, 2837, doi:10.1029/JA078i016p02837.

Courant, R., K. Friedrichs, and H. Lewy (1967), On the Partial Difference Equations of Mathematical Physics, *IBM Journal of Research and Development*, *11*, 215–234, doi:10.1147/rd.112.0215.

Davis, T. N., and M. Sugiura (1966), Auroral electrojet activity index AE and its universal time variations, *jgr*, *71*, 785V801, doi:10.1029/JZ071i003p00785.

Dubyagin, S., V. Sergeev, S. Apatenkov, V. Angelopoulos, A. Runov, R. Nakamura, W. Baumjohann, J. McFadden, and D. Larson (2011), Can flow bursts penetrate into the inner magnetosphere?, *grl*, *38*, L08102, doi:10.1029/2011GL047016.

Dungey, J. W. (1963), The structure of the exosphere or adventures in velocity, in: Geophysics: The Earth's Environment, C. Dewitt, J. Hieblot and A. Lebeau, eds., *New York, Gordon and Breach*, pp. 505–550.

Erickson, G. M., and R. A. Wolf (1980), Is steady convection possible in the earth's magnetotail, *grl*, *7*, 897–900, doi:10.1029/GL007i011p00897.

Fletcher, C. A. J. (1988), Computational Techniques for Fluid Dynamics, *Berlin: Springer-Verlag.*

Grad, H., and H. Rubin (1958), Hydromagnetic equilibria and force-free fields, *Proc. 2nd Intern. Conf. on Peaceful Uses Atomic Energy*, *31*, 190V197.

Hall (2006), *A Mechanism for Current Sheet Thinning in the Growth Phase of Magnetospheric Substorms*, Ph.D. thesis, University of Alaska Fairbanks.

Harris, E. G. (1962), On a plasma sheath separating regions of oppositely directed magnetic field, *Nuovo Cimento*, *23*, 155.

Hesse, M., and J. Birn (1993), Three-dimensional magnetotail equilibria by numerical relaxation techniques, *jgr*, *98*, 3973–3982, doi:10.1029/92JA02905.

Hones, E. W., Jr., et al. (1984), Structure of the magnetotail at 220 earth radii and its response to geomagnetic activity, *grl*, *11*, 5–7, doi:10.1029/GL011i001p00005.

Hsu, T., and R. L. McPherron (2004), Average characteristics of triggered and nontriggered substorms, *jgr*, *109*, A07,208, doi:DOI: 10.1029/2003JA009933.

Jayachandran, P. T., J. W. MacDougall, D. R. Moorcroft, J.-P. St-Maurice, K. Liou, and P. T. Newell (2002), Substorm onset location and the equatorward boundary of the proton auroral oval, *grl*, *29*, 2159, doi:10.1029/2002GL015484.

Juusola, L., N. ØStgaard, E. Tanskanen, N. Partamies, and K. Snekvik (2011), Earthward plasma sheet flows during substorm phases, *jgr*, *116*, A10228, doi:10.1029/2011JA016852.

Kan, J. R. (1990), Tail-like reconfiguration of the plasma sheet during the substorm growth phase, *grl*, *17*, 2309–2312, doi:10.1029/GL017i013p02309.

Kokubun, S., and R. L. McPherron (1981), Substorm signatures at synchronous altitude, *jgr*, *86*, 11,265–11,277, doi:10.1029/JA086iA13p11265.

Le, G., J. A. Slavin, and R. J. Strangeway (2010), Space Technology 5 observations of the imbalance of regions 1 and 2 field-aligned currents and its implication to the cross-polar cap Pedersen currents, *jgr*, *115*, A07202, doi:10.1029/2009JA014979.

Lee, L. C., L. Zhang, A. Otto, G. S. Choe, and H. J. Cai (1998), Entropy antidiffusion instability and formation of a thin current sheet during geomagnetic substorms, *jgr*, *103*, 29,419–29,428, doi:10.1029/97JA02141.

Lui, A. T. Y. (1996), Current disruption in the Earth's magnetosphere: Observations and models, *jgr*, *101*, 13,067–13,088, doi:10.1029/96JA00079.

Lyons, L. R., G. T. Blanchard, J. C. Samson, R. P. Lepping, T. Yamamoto, and T. Moretto (1997), Coordinated observations demonstrating external substorm triggering, *jgr*, *102*, 27,039–27,052, doi: 10.1029/97JA02639.

Ma, X. (2012), Kelvin-Helmholtz instability and magnetic reconnection at the Earth's magnetospheric boundary, Ph.D. thesis, University of Alaska Fairbanks.

Ma, Y. D., J. B. Cao, R. Nakamura, T. L. Zhang, H. Reme, I. Dandouras, E. Lucek, and M. Dunlop (2009), Statistical analysis of earthward flow bursts in the inner plasma sheet during substorms, *jgr*, *114*, A07215, doi:10.1029/2009JA014275.

Ma, Z. W., X. Wang, and A. Bhattacharjee (1995), Growth, sudden enhancement, and relaxation of current sheets in the magnetotail: Two-dimensional substorm dynamics, *grl*, *22*, 2985–2988, doi: 10.1029/95GL02937.

Marion, J. B., and W. F. Hornyak (1982), Physics for Science and Engineering, Parts 1 and 2 Combined, *Saunders College Publishing, Philadelphia.*

McPherron, R. L. (1972), Substorm related changes in the geomagnetic tail: The growth phase, *planss*, *20*, 1521–1539, doi:10.1016/0032-0633(72)90054-2.

Mcpherron, R. L. (1997), Magnetospheric dynamic, *Introduction of Space Physics, edited by Kivelson, M. G. and Russell, C. T.*, pp. 208–211.

McPherron, R. L., C. T. Russell, and M. P. Aubry (1973), Satellite studies of magnetospheric substorms on August 15, 1968: 9. Phenomenological model for substorms, *jgr*, *78*, 3131, doi: 10.1029/JA078i016p03131.

McPherron, R. L., T. Terasawa, and A. Nishida (1986), Solar wind triggering of substorm onset, *J. Geomagn. Geoelectr.*, *38*, 1089, doi:10.1029/93JA01151.

Mende, S. B., H. U. Frey, M. Lampton, J.-C. Gerard, B. Hubert, S. Fuselier, J. Spann, R. Gladstone, and J. L. Burch (2001), Global observations of proton and electron auroras in a substorm, *grl*, *28*, 1139–1142, doi:10.1029/2000GL012340.

Mende, S. B., H. U. Frey, V. Angelopoulos, and Y. Nishimura (2011), Substorm triggering by poleward boundary intensification and related equatorward propagation, *jgr*, *116*, A00I31, doi: 10.1029/2010JA015733.

Milan, S. E., M. Lester, S. W. H. Cowley, K. Oksavik, M. Brittnacher, R. A. Greenwald, G. Sofko, and J.-P. Villain (2003), Variations in the polar cap area during two substorm cycles, *Annales Geophysicae*, *21*, 1121–1140, doi:10.5194/angeo-21-1121-2003.

Milan, S. E., P. D. Boakes, and B. Hubert (2008), Response of the expanding/contracting polar cap to weak and strong solar wind driving: Implications for substorm onset, *jgr*, *113*, A09215, doi: 10.1029/2008JA013340.

Mitchell, D. G., D. J. Williams, C. Y. Huang, L. A. Frank, and C. T. Russell (1990), Current carriers in the near-earth cross-tail current sheet during substorm growth phase, *grl*, *17*, 583–586, doi: 10.1029/GL017i005p00583.

Mozer, F. S. (1971), Origin and effects of electric fields during isolated magnetospheric substorms, *jgr*, *76*, 7595–7608, doi:10.1029/JA076i031p07595.

Nagai, T., and S. Machida (2013), Magnetic Reconnection in the Near-Earth Magnetotail, in New Perspectives on the Earth'S Magnetotail(eds A. Nishida, D.N. Baker and S.W.H. Cowley), *American Geophysical Union, Washington, D. C.*, doi:10.1029/GM105p0211.

Nakai, H., Y. Kamide, and C. T. Russell (1997), Statistical nature of the magnetotail current in the near-Earth region, *jgr*, *102*, 9573–9586, doi:doi:10.1029/97JA00136.

Nakamura, R., T. Oguti, T. Yamamoto, and S. Kokubun (1993), Equatorward and poleward expansion of the auroras during auroral substorms, *jgr*, *98*, 5743–5759, doi:10.1029/92JA02230.

Nakamura, R., et al. (2002), Fast flow during current sheet thinning, *grl*, *29*, 2140, doi: 10.1029/2002GL016200.

Newell, P. T., V. A. Sergeev, G. R. Bikkuzina, and S. Wing (1998), Characterizing the state of the magnetosphere: Testing the ion precipitation maxima latitude (b2i) and the ion isotropy boundary, *jgr*, *103*, 4739–4746, doi:10.1029/97JA03622.

Nishimura, Y., L. Lyons, S. Zou, V. Angelopoulos, and S. Mende (2010), Substorm triggering by new plasma intrusion: THEMIS all-sky imager observations, *jgr*, *115*, A07222, doi:10.1029/2009JA015166.

Nishimura, Y., L. R. Lyons, V. Angelopoulos, T. Kikuchi, S. Zou, and S. B. Mende (2011), Relations between multiple auroral streamers, pre-onset thin arc formation, and substorm auroral onset, *jgr*, *116*, A09214, doi:10.1029/2011JA016768.

Ohtani, S., F. Creutzberg, T. Mukai, H. Singer, A. T. Y. Lui, M. Nakamura, P. Prikryl, K. Yumoto, and G. Rostoker (1999), Substorm onset timing: The December 31, 1995, event, *jgr*, *104*, 22,713–22,728, doi:10.1029/1999JA900209.

Ohtani, S., H. J. Singer, and T. Mukai (2006), Effects of the fast plasma sheet flow on the geosynchronous magnetic configuration: Geotail and GOES coordinated study, *jgr*, *111*, A01204, doi: 10.1029/2005JA011383.

Ohtani, S., S. Wing, P. T. Newell, and T. Higuchi (2010), Locations of night-side precipitation boundaries relative to R2 and R1 currents, *jgr*, *115*, A10233, doi:10.1029/2010JA015444.

Otto, A. (1990), 3D resistive MHD computations of magnetospheric physics, *Comput. Phys. Commun.*, p. 185.

Petrukovich, A. A., and A. G. Yahnin (2006), The Substorm Onset Location Controversy, *ssr*, *122*, 81–87, doi:10.1007/s11214-006-7022-8.

Petrukovich, A. A., W. Baumjohann, R. Nakamura, A. Runov, A. Balogh, and H. RèMe (2007), Thinning and stretching of the plasma sheet, *jgr*, *112*, A10213, doi:10.1029/2007JA012349.

Pulkkinen, T. I., D. N. Baker, D. G. Mitchell, R. L. McPherron, C. Y. Huang, and L. A. Frank (1994), Thin current sheets in the magnetotail during substorms: CDAW 6 revisited, *jgr*, *99*, 5793–5803, doi:10.1029/93JA03234.

Pulkkinen, T. I., et al. (1999), Spatial extent and dynamics of a thin current sheet during the substorm growth phase on December 10, 1996, *jgr*, *104*, 28,475–28,490, doi:10.1029/1999JA900240.

Russell, C. T. (2000), How northward turnings of the IMF can lead to substorm expansion onsets, *grl*, *27*, 3257–3259, doi:10.1029/2000GL011910.

Russell, C. T., and J. G. Luhmann (1997), Earth: Magnetic field and magnetosphere, *Encyclopedia of Planetary Sciences, edited by J. H. Shirley and R. W. Fainbridge, Chapman and Hall, New York*, pp. 208–211.

Saito, M. H., D. Fairfield, G. Le, L.-N. Hau, V. Angelopoulos, J. P. McFadden, U. Auster, J. W. Bonnell, and D. Larson (2011), Structure, force balance, and evolution of incompressible cross-tail current sheet thinning, *jgr*, *116*, A10217, doi:10.1029/2011JA016654.

Samson, J. C., L. R. Lyons, P. T. Newell, F. Creutzberg, and B. Xu (1992), Proton aurora and substorm intensifications, *grl*, *19*, 2167–2170, doi:10.1029/92GL02184.

Sanny, J., R. L. McPherron, C. T. Russell, D. N. Baker, T. I. Pulkkinen, and A. Nishida (1994), Growth-phase thinning of the near-Earth current sheet during the CDAW 6 substorm, *jgr*, *99*, 5805–5816, doi:10.1029/93JA03235.

Schindler, K., and J. Birn (1982), Self-consistent theory of time-dependent convection in the earth's magnetotail, *jgr*, *87*, 2263–2275, doi:10.1029/JA087iA04p02263.

Schindler, K., and J. Birn (1993), On the cause of thin current sheets in the near-Earth magnetotail and their possible significance for magnetospheric substorms, *jgr*, *98*, 15,477, doi:10.1029/93JA01047.

Sergeev, V., Y. Nishimura, M. Kubyshkina, V. Angelopoulos, R. Nakamura, and H. Singer (2012a), Magnetospheric location of the equatorward prebreakup arc, *jgr*, *117*, A01212, doi:10.1029/2011JA017154.

Sergeev, V. A., and M. V. MalKov (1988), Diagnostics of the magnetic configuration of the plasma sheet according to measurements of energetic electrons above the ionosphere, *Geomagnetism and Aeronomy*, *28*, 649–654.

Sergeev, V. A., and N. A. Tsyganenko (1982), Energetic particle losses and trapping boundaries as deduced from calculations with a realistic magnetic field model, *planss*, *30*, 999–1006, doi:10.1016/0032-0633(82)90149-0.

Sergeev, V. A., P. Tanskanen, K. Mursula, A. Korth, and R. C. Elphic (1990), Current sheet thickness in the near-earth plasma sheet during substorm growth phase, *jgr*, *95*, 3819–3828, doi:10.1029/JA095iA04p03819.

Sergeev, V. A., D. G. Mitchell, C. T. Russell, and D. J. Williams (1993a), Structure of the tail plasma/current sheet at ˜11 R_E and its changes in the course of a substorm, *jgr*, *98*, 17,345–17,366, doi:10.1029/93JA01151.

Sergeev, V. A., M. Malkov, and K. Mursula (1993b), Testing the isotropic boundary algorithm method to evaluate the magnetic field configuration in the tail, *jgr*, *98*, 7609–7620, doi:10.1029/92JA02587.

Sergeev, V. A., V. Angelopoulos, D. G. Mitchell, and C. T. Russell (1995), In situ observations of magnetotail reconnection prior to the onset of a small substorm, *jgr*, *100*, 19,121–19,134, doi:10.1029/95JA01471.

Sergeev, V. A., I. A. Chernyaev, S. V. Dubyagin, Y. Miyashita, V. Angelopoulos, P. D. Boakes, R. Nakamura, and M. G. Henderson (2012b), Energetic particle injections to geostationary orbit: Relationship to flow bursts and magnetospheric state, *jgr*, *117*, A10207, doi:10.1029/2012JA017773.

Shevchenko, I. G., V. Sergeev, M. Kubyshkina, V. Angelopoulos, K. H. Glassmeier, and H. J. Singer (2010), Estimation of magnetosphere-ionosphere mapping accuracy using isotropy boundary and THEMIS observations, *jgr*, *115*, A11206, doi:10.1029/2010JA015354.

Shue, J.-H., et al. (1998), Magnetopause location under extreme solar wind conditions, *jgr*, *103*, 17,691–17,700, doi:10.1029/98JA01103.

Shue, J.-H., S. Ohtani, P. T. Newell, K. Liou, C.-I. Meng, A. Ieda, and T. Mukai (2003), Quantitative relationships between plasma sheet fast flows and nightside auroral power, *jgr*, *108*, 1231, doi:10.1029/2002JA009794.

Shue, J.-H., A. Ieda, A. T. Y. Lui, G. K. Parks, T. Mukai, and S. Ohtani (2008), Two classes of earthward fast flows in the plasma sheet, *jgr*, *113*, A02205, doi:10.1029/2007JA012456.

Slavin, J. A., E. J. Smith, B. T. Tsurutani, D. G. Sibeck, H. J. Singer, D. N. Baker, J. T. Gosling, E. W. Hones, and F. L. Scarf (1984), Substorm associated traveling compression regions in the distant tail - ISEE-3 geotail observations, *grl*, *11*, 657–660, doi:10.1029/GL011i007p00657.

Snekvik, K., E. Tanskanen, N. Østgaard, L. Juusola, K. Laundal, E. I. Gordeev, and A. L. Borg (2012), Changes in the magnetotail configuration before near-Earth reconnection, *jgr*, *117*, A02219, doi:10.1029/2011JA017040.

Takada, T., et al. (2006), Do BBFs contribute to inner magnetosphere dipolarizations: Concurrent Cluster and Double Star observations, *grl*, *33*, L21109, doi:10.1029/2006GL027440.

THEMIS Scientific Aims (2007), Graph Illustration the Development of Substorms, *retrieved from http:www.igep.tu-bs.de/forschung/weltraumphysik/projekte/themis/wissziel_en.html*.

Vallance Jones, A., F. Creutzberg, R. L. Gattinger, and F. R. Harris (1982), Auroral studies with a chain of meridian-scanning photometers. I - Observations of proton and electron aurora in magnetospheric substorms, *jgr*, *87*, 4489–4503.

Wang, C.-P., L. R. Lyons, T. Nagai, and J. C. Samson (2004), Midnight radial profiles of the quiet and growth-phase plasma sheet: The Geotail observations, *jgr*, *109*, A12201, doi:10.1029/2004JA010590.

Weimer, D. R., J. R. Kan, and S.-I. Akasofu (1992), Variations of the polar cap potential measured during magnetospheric substorms, *jgr*, *97*, 3945–3951, doi:10.1029/91JA03159.

Wiegelmann, T., and K. Schindler (1995), Formation of thin current sheets in a quasistatic magnetotail model, *grl*, *22*, 2057–2060, doi:10.1029/95GL01980.

Wiens, R. G., and G. Rostoker (1975), Characteristics of the development of the westward electrojet during the expansive phase of magnetospheric substorms, *jgr*, *80*, 2109–2128, doi:10.1029/JA080i016p02109.

Williams, D. J. (1981), Energetic ion beams at the edge of the plasma sheet - ISEE 1 observations plus a simple explanatory model, *jgr*, *86*, 5507–5518, doi:10.1029/JA086iA07p05507.

Wolf, R. A. (1995), Electric Fields and Magnetospheric Convection, *Introduction of Space Physics, edited by Kivelson, M. G. and Russell, C. T.*, p. 303.

Wolf, R. A., Y. Wan, X. Xing, J.-C. Zhang, and S. Sazykin (2009), Entropy and plasma sheet transport, *jgr*, *114*, A00D05, doi:10.1029/2009JA014044.

Xing, X., L. Lyons, Y. Nishimura, V. Angelopoulos, D. Larson, C. Carlson, J. Bonnell, and U. Auster (2010), Substorm onset by new plasma intrusion: THEMIS spacecraft observations, *jgr*, *115*, A10246, doi:10.1029/2010JA015528.

Yahnin, A. G., V. A. Sergeev, B. B. Gvozdevsky, and S. Vennerstrøm (1997a), Magnetospheric source region of discrete auroras inferred from their relationship with isotropy boundaries of energetic particles, *Annales Geophysicae*, *15*, 943–958, doi:10.1007/s00585-997-0943-z.

Yahnin, A. G., V. A. Sergeev, B. B. Gvozdevsky, and S. Vennerstrøm (1997b), Magnetospheric source region of discrete auroras inferred from their relationship with isotropy boundaries of energetic particles, *Annales Geophysicae*, *15*, 943–958, doi:10.1007/s00585-997-0943-z.

Zaharia, S., and C. Z. Cheng (2003), Near-Earth thin current sheets and Birkeland currents during substorm growth phase, *grl*, *30*, 1883, doi:10.1029/2003GL017456.

Zhou, X.-Z., et al. (2009), Thin current sheet in the substorm late growth phase: Modeling of THEMIS observations, *jgr*, *114*, A03223, doi:10.1029/2008JA013777.